



**HAL**  
open science

# Few-body Förster resonances in Rydberg atoms for the implementation of quantum computing

Ivan Ashkarin

► **To cite this version:**

Ivan Ashkarin. Few-body Förster resonances in Rydberg atoms for the implementation of quantum computing. Atomic Physics [physics.atom-ph]. Université Paris-Saclay, 2023. English. NNT : 2023UPASP199 . tel-04549470

**HAL Id: tel-04549470**

**<https://theses.hal.science/tel-04549470>**

Submitted on 17 Apr 2024

**HAL** is a multi-disciplinary open access archive for the deposit and dissemination of scientific research documents, whether they are published or not. The documents may come from teaching and research institutions in France or abroad, or from public or private research centers.

L'archive ouverte pluridisciplinaire **HAL**, est destinée au dépôt et à la diffusion de documents scientifiques de niveau recherche, publiés ou non, émanant des établissements d'enseignement et de recherche français ou étrangers, des laboratoires publics ou privés.

# Few-body Förster resonances in Rydberg atoms for the implementation of quantum computing

*Résonances de Förster à quelques corps dans  
les atomes de Rydberg pour la mise en oeuvre  
de l'informatique quantique*

**Thèse de doctorat de l'université Paris-Saclay**

École doctorale n° 572, Ondes et Matière (EDOM)

Spécialité de doctorat : Physique

Graduate School : Physique

Référent : Faculté des Sciences d'Orsay

Thèse préparée dans le **Laboratoire Aimé Cotton (Université Paris-Saclay, CNRS)**, sous la direction de **Patrick CHEINET**, Chargé de recherche et la co-direction de **Ilya BETEROV**, Chargé de recherche

**Thèse soutenue à Paris-Saclay, le 18 Décembre 2023, par**

**Ivan ASHKARIN**

## Composition du jury

Membres du jury avec voix délibérative

**Christoph WESTBROOK**  
Directeur de Recherche CNRS,  
LCF/ Université Paris-Saclay

Président

**Christiane KOCH**  
Professeure des Universités,  
QDC/Freie Universität Berlin

Rapporteur & Examinatrice

**Guido PUPILLO**  
Professeur des Universités,  
ISIS/Université de Strasbourg

Rapporteur & Examineur

**Martin ROBERT-DE-ST-VINCENT**  
Chargé de Recherche CNRS,  
LPL/Université Sorbonne Paris Nord

Examineur

**Titre:** Résonances de Förster à quelques corps dans les atomes de Rydberg pour la mise en oeuvre de l'informatique quantique

**Mots clés:** Informatique quantique, Résonance de Förster, Porte quantique, Atome de Rydberg, Porte de Toffoli, Porte de phase

**Résumé:** L'application des résonances de Förster à plusieurs corps est étudiée pour réaliser des circuits de portes quantiques multi-qubits. Deux nouveaux schémas de transitions borroméennes à trois atomes utilisant un atome relais ont été proposées et étudiées numériquement. En particulier, une résonance de Förster à trois atomes, non isolée des interactions à 2-corps et contrôlée par effet Stark entre des états  $S$  et  $P$  de niveaux élevés  $n = 80, 81, 82$  avec des atomes de Rb piégés dans des pinces optiques a été modélisée. Une résonance de Förster isolée à trois atomes a également été démontrée pour les états  $n = 70, 71$  des atomes Rb. Les résonances ont été étudiées dans une configuration spatiale fixe, ce qui nous a permis de démontrer l'évolution cohérente de la population et de la phase des états collectifs impliqués.

Des schémas de portes de Toffoli à trois qubits ont été développés et modélisés numériquement sur la base des résonances démontrées dans des ensembles à trois atomes. En outre, un schéma généralisé de porte de phase doublement contrôlée *CCPHASE* a été développé sur la base de la résonance de Förster à trois corps induite par radiofréquence. De plus, un schéma de porte quantique similaire a été proposé sur la base de la résonance de Förster induite par radiofréquence à deux atomes avec un déplacement contrôlé par interaction avec le troisième. Les performances de vitesse et de fidélité des schémas proposés, ainsi que leur robustesse potentielle aux erreurs, nous permettent d'espérer le succès d'une réalisation expérimentale prochainement.

**Title:** Few-body Förster resonances in Rydberg atoms for the implementation of quantum computing

**Keywords:** Quantum computing, Förster resonance, Quantum gate, Rydberg atoms, Toffoli gate, Phase gate

**Abstract:** Application of few-body Förster resonances for the implementation of multiqubit quantum gate circuits has been investigated. New schemes of three-atom Borromean transitions based on a relay atom have been proposed and numerically studied. In particular, a Stark-controlled three-atom Förster resonance, non-isolated from two-body processes, between high-lying  $n = 80, 81, 82$   $S$  and  $P$  states of Rb atoms held in individual optical traps has been modeled. Isolated three-atom Förster resonance has also been demonstrated for  $n = 70, 71$   $S$  and  $P$  states of Rb atoms. The resonances were investigated in a fixed spatial configuration, allowing us to demonstrate the coherent population and phase dynamics

of the collective states involved.

Three-qubit Toffoli gate schemes have been developed and numerically modeled based on the demonstrated resonances. Also, a generalized doubly controlled *CCPHASE* phase gate scheme has been developed based on the radiofrequency-induced three-body Förster resonance. Additionally, a similar quantum gate scheme has been proposed based on two-atom RF-induced Förster resonance with controlled displacement. The performance in terms of speed and fidelity of the proposed schemes, as well as their potential robustness to errors, allow us to expect a successful experimental implementation in the near future.

Dedicated to Dmitry Kolker and all repressed Siberian scientists.



# Contents

<b>Acknowledgements</b>	<b>9</b>
<b>1 Introduction</b>	<b>13</b>
1.1 Historical background . . . . .	13
1.2 Quantum computation efficiency . . . . .	15
1.3 Quantum computation criteria and paradigms . . . . .	16
1.4 Quantum hardware platforms . . . . .	17
1.5 Neutral-atom-based quantum computing . . . . .	19
1.6 Quantum algorithms for atomic hardware . . . . .	22
1.7 Gate fidelity problem . . . . .	23
1.8 Thesis topic and structure . . . . .	25
<b>2 Theoretical foundations</b>	<b>27</b>
2.1 Quantum information basics . . . . .	27
2.1.1 Qubits . . . . .	27
2.1.2 Quantum gates . . . . .	29
2.1.3 Quantum circuits . . . . .	34
2.1.4 Quantum algorithms . . . . .	36
2.1.5 Gate fidelity . . . . .	37
2.2 Rydberg atoms . . . . .	38
2.2.1 Historical background . . . . .	38
2.2.2 Alkali atoms . . . . .	39
2.2.3 Atom-light interaction . . . . .	44
2.2.4 Dipole-dipole interaction . . . . .	45
2.2.5 Förster resonance . . . . .	49
2.3 Rydberg quantum computing . . . . .	52
2.3.1 Atomic ensemble preparation . . . . .	54
2.3.2 Rydberg excitation . . . . .	54
2.3.3 Quantum computations . . . . .	56
2.3.4 Ensemble readout . . . . .	59
<b>3 Few-body Förster resonances: Early-stage studies</b>	<b>61</b>
3.1 Four-body Förster resonances in Cs ensembles . . . . .	62
3.1.1 Four-body resonance proposal . . . . .	62
3.1.2 Experimental results . . . . .	63
3.1.3 Conclusion . . . . .	65
3.2 Borromean Förster resonances in Cs ensembles . . . . .	66
3.2.1 Three-body Förster resonance . . . . .	66
3.2.2 Experimental results . . . . .	68
3.2.3 Conclusion . . . . .	71
3.3 Three-body Förster resonances in Rb ensembles . . . . .	72
3.3.1 Three-body resonance scheme . . . . .	73

3.3.2	Experimental results . . . . .	74
3.3.3	Analytical model . . . . .	76
3.3.4	Resonance analysis . . . . .	78
3.3.5	Numerical simulations . . . . .	81
3.3.6	Disordered ensemble simulation . . . . .	84
3.3.7	Coherent oscillations in various spatial configurations . . . . .	85
3.3.8	Coherence dependence on atomic position variations . . . . .	88
3.3.9	Conclusion . . . . .	89
<b>4</b>	<b>Results</b>	<b>91</b>
4.1	Toffoli gate: First proposal . . . . .	91
4.1.1	New Förster resonance scheme . . . . .	92
4.1.2	Numerical simulations . . . . .	94
4.1.3	Resonance simulation results . . . . .	98
4.1.4	Toffoli gate proposal . . . . .	102
4.1.5	Numerical optimization . . . . .	106
4.1.6	Gate fidelity . . . . .	107
4.1.7	Conclusion . . . . .	108
4.2	FSSC three-body Förster resonances . . . . .	109
4.2.1	Resonant scheme description . . . . .	110
4.2.2	FSSC resonance study . . . . .	112
4.2.3	Quasi-forbidden resonances . . . . .	113
4.2.4	Numerical simulations . . . . .	120
4.2.5	Conclusion . . . . .	124
4.3	FSSC-based Toffoli gate . . . . .	125
4.3.1	Numerical model . . . . .	125
4.3.2	Toffoli gate proposal . . . . .	128
4.3.3	Phase and population dynamics . . . . .	130
4.3.4	Optimization of gate parameters . . . . .	132
4.3.5	Conclusion . . . . .	134
4.4	CCPHASE gate based on RF-induced FSSC resonances . . . . .	135
4.4.1	Introduction to CCPHASE gates . . . . .	137
4.4.2	RF-induced Förster resonances . . . . .	138
4.4.3	Numerical simulations . . . . .	140
4.4.4	CCPHASE gate proposal . . . . .	146
4.4.5	Gate fidelity . . . . .	151
4.4.6	Conclusion . . . . .	152
<b>5</b>	<b>Summary and Outlook</b>	<b>155</b>
5.1	Summary . . . . .	155
5.1.1	First stage . . . . .	155
5.1.2	Second stage . . . . .	156
5.1.3	Third stage . . . . .	157
5.1.4	Fourth stage . . . . .	158
5.1.5	Results . . . . .	159
5.2	Outlook . . . . .	160
5.2.1	Fidelity improvement . . . . .	160

5.2.2	Sensitivity to atomic positions . . . . .	162
5.2.3	Förster blockade gates . . . . .	162
5.2.4	Experiment proposal . . . . .	163
5.3	Afterword . . . . .	164
<b>Appendix</b>		<b>165</b>
A	Alkali wave functions and radial matrix elements . . . . .	165
A.1	Wave functions . . . . .	165
A.2	Matrix elements . . . . .	166
B	RF-induced resonance model . . . . .	168
C	Analytical model of three-body Förster resonances . . . . .	170
<b>List of Publications</b>		<b>175</b>
<b>Resume</b>		<b>177</b>
I	Première étape . . . . .	178
II	Deuxième étape . . . . .	179
III	Troisième étape . . . . .	180
IV	Quatrième étape . . . . .	181
V	Conclusion . . . . .	182
<b>Bibliography</b>		<b>183</b>



# Acknowledgements

This manuscript describes my doctoral research conducted between October 2020 and December 2023. I spent this time working in the wonderful research teams of Aime Cotton Laboratory (France) and Rzhanov Institute of Semiconductor Physics (Russia). My greatest privilege was the opportunity to realize my doctoral project under joint international scientific supervision, getting the chance to gain valuable experience of both research teams. I was also lucky to have two supervisors, each of whom was willing to support me and share their knowledge and research experience with me.

The realization of my doctoral project was complicated by many significant challenges. Between 2020 and 2022, the world experienced the COVID-19 pandemic, which led to a change in the original research plan. Then, Russia's military invasion of Ukraine began, causing, among other sad consequences, a significant disruption of international scientific cooperation. After the outbreak of the war, the realization of a joint project between our laboratories became impossible due to politically motivated restrictions. Nevertheless, it is precisely the troubling circumstances that allow us to fully appreciate the fundamental value that allows humanity to successfully develop and overcome any difficulties - the value of kind, sincere human support. In this preamble, I would like to express my deepest gratitude to all the people who participated in successful implementation of this research project.

The main person behind the success of this project is my thesis director Dr. Patrick Cheinet. Patrick is a brilliant scientist who inspires others with his optimistic attitude and passion for research. We met during his visit to ISP in 2019, and I remember my excitement when, after a few weeks of working together, he suggested that I write my thesis under his supervision. I agreed immediately, and I still think it was one of the best decisions of my life. I found it very easy and comfortable to work with Patrick. His numerous insights and guidance were always extremely helpful and resulted in consistent success in producing important and valid scientific results. He was always willing to take the time to answer my many questions in detail and was also available for open and fruitful scientific discussion. Also, Patrick was always around to help with any difficulties I had. I can't count the number of times I have asked him for help with a variety of issues, from dealing with administrative tasks and searching for funding to my accommodation and residency problems. Each time his help has been priceless. I am grateful to Patrick for the guidance during the project and for sharing his immense knowledge with me. I also deeply appreciate his scientific pragmatism and his ability to choose research priorities that allow to successfully organize the research process and achieve the desired results in a rapidly changing environment. Without these skills, the realization of this research project would be absolutely impossible.

An exceptionally important contribution to the implementation of this project was made by my thesis co-director Dr. Ilya Beterov. I started working under his supervision at ISP SB RAS in August 2017, and it became a great fortune for me. Ilya introduced me for the first time to the fascinating world of Rydberg physics and quantum computing, instilling in me a craving

for research and exploration of the mysteries of nature. It was thanks to him that I decided to write my master's thesis and afterwards to enter PhD program. Ilya is an excellent scientist, prone to deep and thoughtful analysis, and he passes these qualities on to his students. During my studies at Novosibirsk State University, he was always there for me, ready to help with any problem that arose. He set the course of our joint research, opening for me new aspects of modern quantum computing problems, and motivating me to constantly develop and persevere in new scientific disciplines. Thanks to his support, I received numerous scholarships and grants, without which successful scientific work would be absolutely impossible. He also supported my decision to participate in this doctoral project and agreed to be my supervisor at ISP. Although our project no longer formally exists due to politically motivated restrictions, we continue to collaborate, work on cooperative projects and publish joint articles. I am deeply grateful for the knowledge and experience he has shared with me and for all the opportunities he has opened up for me. I was extremely fortunate to have such a great mentor at the beginning of my scientific career, and I hope that we will continue to work together.

I would like to express my deep appreciation to Dr. Olivier Dulieu, Director of the Aime Cotton Laboratory, and Dr. Igor Ryabtsev, Director of the ISP Laboratory №32. The wonderful working atmosphere they have been able to create in the laboratories contributes a lot to productive scientific work. Their assistance in all aspects of scientific and administrative activities allowed me to concentrate on the research process, shifting many other concerns to them. At the same time, both of them have extensive scientific experience and are willing to share it. I am convinced that prudent and confident leadership is the foundation of successful teamwork. In this regard, I would like to thank Olivier and Igor for their wisdom and knowledge, which allowed our teams to successfully achieve all the objectives.

Throughout my work, I was surrounded by wonderful colleagues. In Russian language, there is an expression "to gnaw the granite of science", which shows how hard new knowledge can be to master. I can say with certainty that in good company "granite of science" turns into a delicacy, which is much more convenient and pleasant to consume. I thank Dr. Steven Lepoutre for showing me how interesting experimental work can be. I hope to learn more by working with him as a postdoc after my thesis defense. I am appreciative to Dr. Daniel Comparat, who leads our research group, for the interesting scientific discussions we have weekly in the lab as part of our group meetings. I am grateful for the interesting conversations and friendly atmosphere to the other doctoral students and postdocs, as well as to the entire LAC team. Thank you Charbel, Clelia, Alex, Thibault, Thomas, Sebastian, Lucas and all the rest! Special thanks go to Christine, who helps us all with administrative problems, and to Laurence, whose positive energy keeps our whole lab going! I also thank Dr. Denis Tretyakov, Lena and Kirill from ISP, for their optimism and love of science, as well as for our fruitful scientific discussions.

It is necessary to express my gratitude for all help that I received after the outbreak of the war in Ukraine. Although our joint research project was closed, all the people who were directly involved in it gave me great support and helped me to stay in France, where I was able to continue my research in a peaceful scientific environment. Patrick and Olivier helped me with all the administrative work, seeking for funding, obtaining a residence permit, and many other aspects of life so important in emigration. Their advice and sympathy for me in this horrible situation

inspired me and allowed me to survive this difficult period. In turn, Ilya and Igor helped me with a huge number of administrative issues in Russia, and offered possible solutions to difficulties that arose. I am incredibly grateful to Patrick, Ilya, Olivier and Igor for everything they have done for me. I am also grateful to my colleagues at LAC for their support. It was a great honor and good fortune for me to work with you!

This project would not have been possible without receiving sufficient funding. I thank the Embassy of France in Moscow and the Collège de France for their grant support.

Finally, I would like to thank my parents for their love and care throughout my life. Thanks to their invaluable support, attention and kindness, I always feel that life is beautiful and any problems are temporary. Their interest in life and curiosity is what inspires me to overcome any obstacles. Thank you! I hope to see you soon.



# Chapter 1

## Introduction

This chapter provides a brief introduction to the field of Rydberg quantum computing. In particular, Section 1.1 provides an overview of the historical background to the development of quantum computing. Section 1.2 gives a brief description of the efficiency of quantum computing in the context of computational complexity theory. Section 1.3 describes the DiVincenzo criteria as well as different paradigms of quantum computing. Section 1.4 gives an overview of leading quantum computing platforms. Section 1.5 presents quantum registers based on neutral atoms and their advantages and disadvantages for quantum computing compared to the other leading platforms. Section 1.6 gives several examples of quantum algorithms for which neutral-atom-based quantum computing shows a significant advantage in implementation efficiency. Section 1.7 describes the problem of insufficient quantum gate fidelities in neutral-atom-based quantum registers and possible approaches to its solution. Finally, Section 1.8 summarizes the research topics of this thesis and gives a description of the manuscript structure.

### 1.1. Historical background

The technological revolution of the 20<sup>th</sup> century is inextricably linked with the development of information technologies, including new approaches to the representation, storage and processing of information. In 1936, Alan Turing, who is rightfully considered the father of modern computer science, formulated the concept of an information processing device, later named the universal Turing machine. According to the presented concept, a universal Turing machine can be used to simulate any other Turing machine, as well as to implement any possible algorithmic computation. Famous Church-Turing thesis states that, if a certain task can be solved algorithmically on a physical device, then there is an equivalent algorithm for a universal Turing machine that solves this task [1]. A theoretical model for the implementation of a universal Turing machine was proposed by John Von Neumann, and began to develop actively after the invention of the first prototype transistor by Bardeen, Brattain and Shockley in 1947 [1, 2]. Transistors later became the main logical units for storing and processing information in computing devices. As a result of all these great discoveries, modern programmable computers were built, and the world entered a new age of information.

Nevertheless, the model of classical computing devices has a number of disadvantages. First of all, the Church-Turing thesis has no indication of the implementation efficiency for computational algorithms. To compensate for this gap, in the early 1970s, this thesis was reformulated. The new formulation claimed that any algorithmic process can be efficiently modeled on a Tur-

ing machine, and was called the “strong Church-Turing thesis”. Also, according to the statement of the new formulation, if the problem does not have an efficient algorithmic solution on a Turing machine, it cannot be solved efficiently using any physical device [1].

The concept of efficiency in the strengthened version of Church-Turing thesis implies the possibility of solving any presented algorithmic task using the amount of computational resources, which scales polynomially with the “size” (or complexity) of the task. Computational resources can be represented, in particular, by the calculation time, the number of necessary computational components in the physical implementation of a Turing machine (for example, the number of transistors in a classical processor), or the number of necessary logical operations. Thus, the strong Church-Turing thesis postulates the existence of an absolutely universal paradigm of algorithmic computing based on the use of a Turing machine [1].

As it became clear in the following decades, a number of important algorithmic tasks do not fit into the framework of the presented model. For example, the simulation of any quantum system obviously require an exponential amount of computational resources. The number of complex amplitudes in the wavefunction of a multiparticle quantum system, where each particle has  $A$  energy eigenstates scales as  $A^n$  with the number  $n$  of particles involved. Thus, in order to find an effective algorithmic solution to this problem, as well as a number of other important tasks, a transition to a fundamentally different computing paradigm based on probabilistic description is necessary.

Another important reason for the development of alternative concepts of information processing is that all classical computation schemes have finite scalability, thus failing to meet the increasing demand for computational power. According to the law of computational system scaling, empirically derived by Gordon Moore in 1965, the number of transistors in modern integration circuits should double every two years [1]. A similar trend is also observed for the computational performance progression, leading to the conclusion that computing power is linearly related to the number of available processors. However, with the increasing miniaturization of computing devices, Moore’s law ceases to be observed. The size of modern transistors is typically a few nanometers, and therefore their further miniaturization is impossible due to the significant influence of quantum effects on the interaction of individual logic blocks. For 2023, there is no clear consensus in the industry about whether the violation of Moore’s law is being observed or not. So, in September 2022, the NVIDIA Corp. CEO Jensen Huang stated that Moore’s law is no longer applicable [3], while the INTEL Corp. CEO Pat Gelsinger had the opposite point of view [4]. Nevertheless, all experts agree that the presence of transistor miniaturization limit will lead to the violation of Moore’s law in the short term [1, 5].

One of the possible alternatives to the modern digital computing paradigm based on bitwise representation of information is the concept of quantum computing. Quantum computing involves the use of quantum resources, such as quantum entanglement and quantum parallelism, and provides an extension for the concept of a universal Turing machine [1, 6, 7]. It has been repeatedly demonstrated that quantum computers are able to efficiently solve complex tasks that do not have an efficient algorithmic solution on a universal Turing machine. Thus, the first proposal of a quantum algorithm formulated by David Deutsch in 1985, along with the first concept of a quantum computer, consisted in solving the problem of checking a Boolean function

for constancy (presentation of the same result for all possible arguments) or balance (equilibrium distribution of the bitwise result for two equally large sets of arguments) [1]. This problem, which requires  $2^{n-1} + 1$  number of calls to the classical algorithmic oracle, is solved in the quantum computing paradigm in just one call! This algorithm was later implemented on different quantum computing platforms, including trapped ions [8], single electron spins in diamonds [9] and polarisation qubits [10]. Among other tasks that have generated extensive interest in quantum computer science, one need to highlight Shor's factoring algorithm [11], as well as Grover's algorithm [12] for efficient element search in unstructured ensembles.

## 1.2. Quantum computation efficiency

To date, the class of problems that have an effective solution in the quantum computing paradigm has significantly expanded. In order to describe this class, we need to introduce some definitions from computational complexity theory. So, we define **P** as a class of all problems for which solutions can be found effectively on a classical computing device. We also assert that **P** is a subclass of a broader class of **NP** problems, for which a proposed solution can be efficiently verified using a classical computer. For example, the problem of finding prime divisors of an integer, in general, has no effective solution on a classical computer. Nevertheless, if the solution to such a task is known in advance, it can be easily verified [1, 13].

Currently, computational complexity theory does not provide a clear relation between **P** and **NP** classes. Nevertheless, most researchers believe that  $\mathbf{P} \neq \mathbf{NP}$ . Thus, **P** must be included into **NP** as its subclass. Another important class of problems included into **NP** is a class of **NP**-complete problems. The problem is defined to be **NP**-complete, if the algorithm for solving this problem can be efficiently transformed into an algorithm for solving any **NP**-problem. If  $\mathbf{P} \neq \mathbf{NP}$ , it is obvious that the solution of any **NP**-complete problem is impossible in the classical computing paradigm, and thus no intersections between **P** and **NP**-complete exist [1, 14].

Unfortunately, the efficiency of quantum computing for solving **NP**-complete problems has not yet been proven, although it is obvious that some problems from **NP** that are not included in **P** have effective solutions in quantum paradigm. Defining more broadly the class of **PSPACE** tasks (tasks that require small processing resources, but can use unlimited time resources), we can say with confidence that quantum computers cannot effectively solve problems that go beyond **PSPACE**. Ultimately, **BQP** (a class of problems, whose solutions can be obtained efficiently by using quantum computational paradigm) occupies parts of **NP** and **PSPACE**, including all classical **P** problems [15]. The relation between different complexity classes is presented in Fig. 1.1.

It is also useful to make a link between the results given by the theory of computational complexity and real-world problems. Problems related to **NP** include, in particular, the integer factorization problem and the "traveling salesman problem". Efficient solutions to both of these problems are of great practical interest for modern information science and for practical applications. For example, factorization of integers is widely used in modern encryption algorithms, in particular the RSA algorithm. In turn, solving the traveling salesman problem can be applied

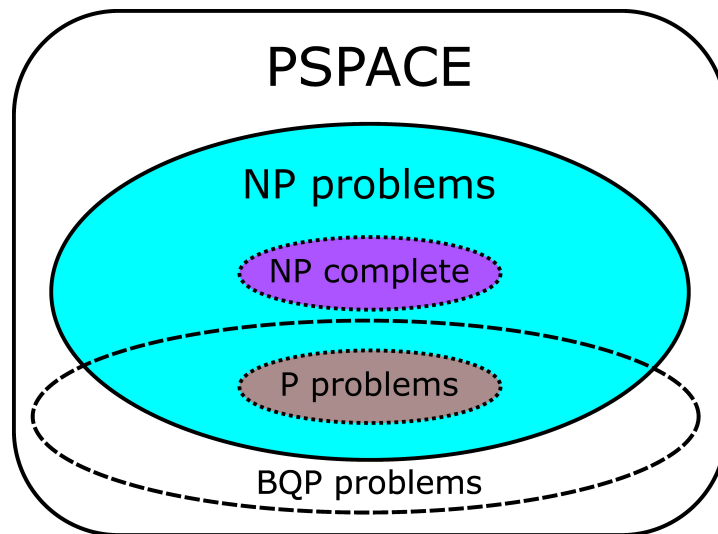


**Figure 1.1 :** Complexity class diagram for **P**, **NP**, **NP-complete** and **BQP** problems. According to [1], **BQP** class includes all **P**-class and occupies a parts of **NP** and **PSPACE**.

to efficiently construct logistic routes. Quantum computing can potentially provide solutions to both of these problems [11, 16, 17]. Thus, continuing research in quantum computing, one can expect to find solutions to other important problems from **NP** advancing the capabilities of modern computing systems!

### 1.3. Quantum computation criteria and paradigms

The physical implementation of quantum computing (QC) devices requires the use of elementary quantum objects as its logic elements. This idea, expressed by Richard Feynman in 1982, still remains relevant. It is customary to describe the advantages and disadvantages of QC experimental setups in terms of compliance with the “DiVincenzo criteria” formulated in 2000 by David P. DiVincenzo [7]. According to these criteria, a device for quantum information processing must:

- Be a scalable physical system with well-characterized qubits
- Allow to initialize each qubit into a simple fiducial state
- Have high stability (i.e., long decoherence times for logical elements)
- Have a universal set of quantum gates performed with high fidelity
- Give ability to measure the qubit states

To ensure the ability of quantum information transmission, two additional requirements arise:

- The ability to interconvert stationary and moving qubits
- The ability to faithfully transmit moving qubits between specified locations

Along with the DiVincenzo criteria, it is also important to consider the ability of the quantum computational device to support various paradigms of quantum computing. Among different paradigms, one can distinguish digital quantum computing (DQC) [18], analog quantum computing (AQC) [19], measurement-based quantum computing (MBQC) [20] and quantum annealing (QA) [21]. In digital quantum computing, the computational task is translated into a discretized algorithm, which is divided into logical blocks consisting of individual quantum gates. Theoretically, any calculation process can be represented in this form, so digital quantum computing provides a universal tool to solve any **BQP** problems. Nevertheless, some types of tasks, such as simulation of quantum systems, as well as solving complex topological problems, can be effectively emulated by the internal interactions of controllable quantum systems. Analog quantum computing is based on the use of analogies between the Hamiltonian of the problem under consideration and the Hamiltonian of the quantum computational system used to solve it [22]. In turn, measurement-based quantum computing relies on the preparation of highly entangled states called cluster or graph states. The subsequent measurement has a quantum gate effect and allows to realize quantum algorithms, for example, quantum error correction algorithm [23]. Finally, quantum annealing represents the quantum computing paradigm oriented to solve optimisation problems which require the minimization of specific cost functions. These cost functions generally correspond to the energy of an Ising spin glass, and quantum annealing provide a solution by adiabatic passage of a quantum register into the ground state of Ising Hamiltonian [24].

## 1.4. Quantum hardware platforms

Currently, different physical platforms are used for quantum computing implementation. In particular, superconducting quantum circuits based on Josephson junctions demonstrate high compliance with the DiVincenzo criteria. Superconducting quantum computational devices are actively developed by academic institutions, as well as private companies such as Google, IBM, Rigetti, IQM and many others. In particular, IBM's "*Osprey*" quantum processor, shown in 2022, consists of 433 superconducting qubits. According to the IBM announcement, in 2023 the research team plans to demonstrate a "*Condor*" quantum processor with 1121 qubits. Quantum operations in such registers have high fidelity ( $\sim 99.85\%$  for two-qubit operations), and can also be implemented very quickly ( $\sim 10 - 60$  nanoseconds) [25]. Nevertheless, a number of significant issues persist in this field, presenting hard challenges for the researchers [26]. First of all, to implement complex quantum algorithms, it is necessary to significantly increase the coherence times in superconducting quantum processors. This task is extremely difficult, and remains unsolved to the best of the author's knowledge. Secondly, the need to use ultra-low

**Table 1.1:** Comparison of the performance characteristics between three different QC platforms: superconducting quantum circuits, ion-based quantum circuits and neutral-atom-based quantum circuits. Significant part of the table data was recollected from [28].

Platform	Number of qubits	Coherence time	Gate fidelity & time	
			One-qubit	Two-qubit
SC	53 [29] 54 [30] 433 [31, 32]	70 $\mu$ s [33]	0.9992; 10 ns [34]	0.997; 60 ns [35] 0.998; 25 ns [36] 0.99922; 50 ns [37]
Trapped ions	32 [38], 53 [39]	50 s [40]	0.999999; 12 $\mu$ s [40]	0.9992; 30 $\mu$ s [41]
Neutral atoms	219 [42] 256 [43] 324 [44]	48 s [45]	0.99986 ; 31 $\mu$ s [46]	0.991; 59 ns [45] 0.974 ; $\sim$ 400 ns [47] 0.98; 2 $\mu$ s [48] 0.995 ; $\sim$ 200 ns [49]

temperatures in the register to maintain superconductivity complicates the implementation of circuits. Although modern cryostatic systems are quite efficient, registers that are unstable to temperature deviations are difficult to scale up. Also, when scaling up to a larger number of qubits, problems of spatial coherence, effective verification and validation of system parameters, calibration of parameters and maintenance of interconnectivity throughout the register inevitably arise [27]. Finally, the main problem of superconducting quantum schemes is the lack of natural qubit universality. Superconducting qubits are created artificially, which means they are not ideal, and may differ in their properties. The deviation of the logical element properties in the computational system, in turn, can have an unpredictable effect on the result of the calculation.

Another promising approach is the implementation of quantum processors based on ions [50]. Ion quantum computing is usually based on the use of long ionic chains (also called ionic crystals) [51]. Alternatively, quantum registers could also be implemented using isolated modules with shuttling trapped ions, where individual ionic qubits are physically transferred between isolated quantum processor modules, performing quantum entanglement between them [52]. In both approaches, each ion acts as a separate qubit [53]. At the moment, the largest “*Forte*” quantum register [38] based on a chain of 32 cold Ytterbium ions is registered by IonQ Inc. Cold ion-based quantum registers demonstrate the highest accuracy of quantum operations among all available platforms ( $> 99.9\%$  for two-qubit gates), as well as high register coherence times, allowing up to  $10^6$  quantum operations to be implemented, while for superconducting qubits this number is 1000 times less. Additionally, high-precision preparation ( $> 99.93\%$  accuracy [54, 55]) and readout ( $> 99.99\%$  accuracy [40]) were shown for ion qubit states. Unlike superconducting qubits, ions are natural objects, which means they are completely identical. The lifetimes of ions in individual traps are shockingly high – each ion can live in a trap for hours, days or even months! Thus, ionic quantum computers are extremely demanded nowadays. However, ionic platform also demonstrate significant drawbacks [53].

While high ion lifetimes allow a large number of gates to be implemented, it should be noted that such gates require several microseconds of realization time each, which is approximately a 1000 times larger compared to the superconducting circuits. A recent analysis has shown that the task of factorizing 1024 and 2048-bit numbers will require  $\sim 10$  and  $\sim 100$  days, respectively, on the ionic quantum computer [52]. This example clearly shows the issues for the implementation of complex quantum algorithms. Apart from that, the scaling of ionic registers presents a separate challenge [53]. While capturing several thousands of ions into an individual RF trap is not troubling for modern experimental setups, controlling individual qubits in such large registers presents a number of unsolved issues, thus making huge ionic ensembles practically useless for quantum computation. The realization of coherent control in long ion chains is a big practical challenge for the ionic quantum technology research. A possible solution to the scaling problem is the use of registers based on shuttling trapped ions [56]. Nevertheless, this technology is rather new and, although promising, has not demonstrated significant superiority over ion crystal-based computing yet.

Revising the previous examples, we can ask ourselves whether the described approaches for quantum computation are excessively overcomplicated? Perhaps natural systems that interact weakly with each other in natural conditions will present an ideal choice to implement quantum schemes? This exact reasoning inspire research teams studying the application of neutral atoms to quantum computing!

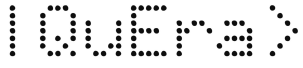
## 1.5. Neutral-atom-based quantum computing

Neutral atoms represent one of the most promising and modern platforms for quantum computing. Registers of individual ultracold atoms isolated in arrays of optical dipole traps give access to wide computational capabilities, allowing both analog and numerical computational algorithms to be implemented. Figure 1.2 shows a list of 6 commercial companies that currently have leading positions in the field. Each of these companies was founded by prominent researchers from the world's leading universities, and in a short time they managed to attract multi-million investments in their projects [57].

Atomic registers have a number of important advantages compared to other quantum computing platforms:

- **Extremely high lifetimes and coherence times**

In recent experiments, the atomic lifetimes in dipole traps of  $\sim 10 - 60$  s were demonstrated in room temperature setup [28]. At the same time, using a cryostat, these lifetimes can be significantly increased. The record lifetime of an individual atom in an optical trap is currently  $\sim 6000$  s [58]. Also, coherence time of  $\sim 40$  s in an atomic register was recently demonstrated [45]. Such long coherence allows to perform  $\sim 10^6$  gate operations in quantum registers, thus paving a way towards implementation of complex quantum algorithms.

Company	Modality	Status
 IQM	Analog	256 qubit quantum processor with public online access
 PASQAL	Analog	324 qubit processor not yet available for public access
 planqc	Analog	Early stage startup, no quantum register available
 atom computing	Digital	100 qubit processor providing beta-version of public access
 Infleqtion	Digital	100 qubit processor providing beta-version of public access
 ColdQuanta	Digital	100 qubits with public remote access

**Figure 1.2:** A list of the most successful commercial startups in Rydberg quantum computing for 2023. Second column indicates the computational mode under development. Development status is described in the third column. Substantial part of the information in the table was recollected from [57].

- **Scalability of registers**

Since atoms are natural objects, they can be obtained absolutely identical in any quantities necessary for quantum computing. Also, since atoms are neutral, the interactions between them are much weaker than between individual ions. Thus, it is possible to produce very compact registers with interqubit distances of about 1 – 5 microns [59]. To date, the available quantum devices based on alkali neutral atoms contain several hundred qubits (see Table 1.1), and scaling to several thousand qubits is expected in 2024.

- **Connectivity of registers**

An important factor is the ability to implement quantum operations between remote qubits. In atomic registers consisting of individual optical tweezers or dipole traps, a 20 : 1 connectivity was already implemented [60], and current research focuses on creating a connectivity of at least 100 : 1 [61]. A possible approach to create “all-to-all” connectivity is based on the qubit rearrangement during the calculation process. Atomic registers can also be linked to each other, allowing for “horizontal scaling” [61]. Also, the creation of three-dimensional quantum registers is possible employing optical tweezers [62].

- **Universal gate sets**

Recently, universal sets of single-qubit and multi-qubit gates have been demonstrated in atomic registers, including single-qubit rotational gates, as well as two-qubit *CNOT*,

*CZ*, *CPHASE* and *SWAP* gates [28, 63, 64]. Three-qubit Toffoli gates were also implemented, even while their fidelity remains relatively low [47, 49]. Parallel implementation of gates in large-scale quantum registers is also possible.

- **High-quality ensemble preparation and readout**

For alkali-atom registers, individual qubit preparation fidelity of about 98.8% was demonstrated [65]. Also, the state readout fidelity is competitive with the other leading platforms, amounting to  $\sim 95\%$  [66].

- **A large number of programming paradigms available**

Atomic registers are suitable both for analog quantum computing and quantum simulations (AQC, QS), and for digital quantum computing (DQC) [67]. Implementation of mixed-type computing (DAQC) and quantum annealing-based computing (QA) is also possible [18, 28].

- **Easy control**

Atomic registers are controlled by external radiation that induces transitions between individual atomic states [59]. Unlike superconducting qubits, no individual wires are required for each qubit.

- **No general cooling requirements**

Atomic registers operate at room temperature, which significantly facilitates the experimental implementation of calculations. However, to increase the qubit lifetimes and coherence times of quantum register states, one can use cryogenic-based setup [63].

High-fidelity quantum operations, comparable to those of other leading platforms, have been demonstrated for neutral-atom-based quantum computing setups. While single-qubit gates are easily executed with  $\sim 99.98\%$  fidelity [28], the maximum fidelities of  $\sim 97.4\%$  [47] and  $\sim 99.5\%$  [49] are demonstrated for two-qubit quantum gates. The maximum Bell state generation fidelity is  $\sim 99.1\%$  [45]. These values already exceed the threshold for modern quantum error correction algorithms, which means that the task of constructing effective neutral-atom-based quantum computation schemes becomes technically feasible [49]. Nevertheless, further improvements in quantum gate fidelity are necessary to efficiently implement complex quantum algorithms in accessible quantum registers. At the moment, the deficient precision of quantum operations can be considered as one of the limiting factors for neutral-atom-based quantum computing.

Another factor hindering the rapid development of atomic QC is the long duration of qubit preparation times. For registers containing about a thousand atoms, such times are measured in hundreds of milliseconds, which reduces the total time allotted for the execution of any quantum computation, due to the limited atomic lifetime. Moreover, when the number of atoms in individual register will increase to  $\sim 10^4$  or more, the state preparation will take significantly longer times. Nevertheless, efforts are being made to overcome these issues: schemes for deterministic loading of optical tweezers have been implemented in order to surpass the stochastic nature of individual trap loading [44, 63].

Based on the presented information, one can conclude that neutral atoms represent a promising platform for quantum computing. The natural properties of atoms, coupled with the ability to precisely control interatomic interactions, allow atomic quantum registers to exhibit capabilities unavailable to other leading quantum computing platforms. Nevertheless, such registers have a number of drawbacks that need to be compensated for.

### 1.6. Quantum algorithms for atomic hardware

Considering a quantum computing setup, it is very important to determine which class of problems can be effectively solved with it. As mentioned earlier, quantum registers based on neutral atoms can support both AQC and DQC computational paradigms, which means that their field of application is potentially unlimited. Moreover, currently such registers are considered as the most effective tool for solving a number of practical issues, surpassing in this sense other leading QC platforms. According to [61], three groups of tasks are proven to be solved by neutral-atom-based quantum computing systems with superior efficiency:

- **Quantum simulation**

Analog quantum simulations have been implemented in atomic quantum registers to solve various problems in materials science and statistical physics [68], including high-temperature superconductivity [69–72], simulation of new phases of matter [43], simulation of spin systems [42, 73–75], as well as problems of high-energy physics and astrophysics [76–78]. Nevertheless, effective analog quantum computations are possible only if the Hamiltonian of the modeled system and the Hamiltonian of the quantum register are essentially similar [60]. Thus, to solve the issues raised in materials science by analog simulation, individual atoms in optical traps mimic electrons in the nodes of the crystal lattice. More complex tasks can potentially be implemented using digital quantum simulations [61].

- **Machine learning**

Machine learning is an extremely promising branch, which provides many issues to be potentially solved by quantum computations [60]. For example, exponential acceleration was shown for the QSVM (Quantum Support Vector Machine) algorithm [79]. Additionally, classification problems that are inaccessible to classical calculations can be efficiently solved on quantum computers [80].

An important class of machine learning tasks used in computational physics are the tasks of identifying the physical laws that determine the behavior of the systems under consideration, based on large data arrays. Physics-Informed Machine Learning (PIML) approximators present a tool for solving such problems [81]. The experts from Pasqal Inc. state that the class of techniques available to modern quantum machine learning can be expanded to these tasks. Moreover, according to experts, atomic quantum registers can demonstrate the greatest success in building PIML approximators. However, this issue has not yet been widely investigated [61].

- **Combinatorial optimization**

Combinatorial optimization tasks efficiently solved by modern QC often become native for atomic registers [61]. The universality of neutral atom interactions, coupled with the possibility of exciting individual atoms into Rydberg states to enhance these interactions, allows, in particular, to address a wide class of problems - problems of finding the maximal independent set (MIS) on a unit disk graph [82]. The solution of MIS tasks, in turn, finds application in finance, bioinformatics, medicine, logistics, etc [83]. This class of problems can also potentially be extended to maximally weighted independent set problems on a unit disk graph [84]. The basis for the effective solution of the MIS tasks is represented by variational quantum algorithms [81, 85]. Quantum Approximate Optimization Algorithms (QAOA) and quantum annealing can also be used [61]. All these techniques were effectively demonstrated in the neutral-atom-based registers. In the future, the growth of quantum registers will significantly expand the range of efficiently solvable combinatorial optimization problems, and many industrial and scientific projects will benefit from it.

## 1.7. Gate fidelity problem

The implementation of complex quantum algorithms requires a large number of quantum gates to be implemented. In this regard, the central problem when scaling such algorithms to a large number of qubits is the lack of accuracy of individual gates. Generally, any quantum algorithm can be implemented with one- and two- qubit gates forming universal gate sets. Nevertheless, in the presence of the slightest individual gate errors, the cumulative error leads to the destruction of coherence in the computational process. There are several approaches to solve this problem. Firstly, quantum error correction algorithms can be used. Unfortunately, such algorithms require additional qubits and quantum gates, significantly reducing the useful quantum volume of the register. For example, the famous Shor-code-based error correction technique requires the use of nine qubits and several dozen one- and two-qubit operations to correct errors in one qubit [86], assuming those operations to be perfectly implemented. Such significant amounts of additional resources are needed because the quantum bit state cannot be perfectly copied according to the so-called “No-Cloning Theorem” [1]. One thus cannot use the same error correction techniques as in classical computer science.

A second solution is to increase the fidelity of individual one-qubit and two-qubit operations. Currently, many scientific groups are proposing new approaches to the high-fidelity quantum gate implementation [28, 63, 67]. Although recent advances have brought the accuracy of quantum operations in atomic registers to values compatible with quantum error correction, further development in this area is necessary to improve the efficiency of implementing complex quantum algorithms with a limited number of available qubits.

**Table 1.2:** Theoretical proposals for multi-qubit gate implementations in Rydberg systems. First column indicate the used approach, presented in the publications listed in the second column. Second column also describes the type of the implemented multi-qubit operation and its fidelity. Significant part of the information in this table was recollected from [28].

Dipole blockade	
Basic blockade gates	0.9997 $C_3NOT$ gate [91]
	0.982 Deutsch gate [92]
Asymmetric interaction	0.96 Three-qubit gate [93]
Pulse shaping	0.998 Toffoli gate [94]
	0.997 Toffoli gate [95]
	0.999 $C_{46}NOT$ [96]
	0.998 $C_2Z$ gate [64]
	0.902 Toffoli gate [97]
Multiqubit Rydberg excitation	
Rabi-like rotations via Förster resonance	0.983 Toffoli gate [98]
Dark states formed via Förster resonance	0.999 Toffoli gate [99]
Heteronuclear Förster resonance	$\sim 0.98 CNOT^N$ and $C_2NOT^2$ gates [100]
Two-photon adiabatic passage	0.995 $C_kZ$ gates [101]
Rydberg Antiblockade	
High-order $\Omega$ via matching the detuning in laser fields with Rydberg interactions	0.9887 Toffoli gate [102]
	0.9965 Toffoli gate [103]
Dissipation via asymmetric interactions	0.9947 3-qubit entanglement [104]
Dissipation	0.9924 3-qubit entanglement [105]
	0.99 6-qubit entanglement [106]

A very promising approach towards facilitating the implementation of complex quantum computations is thus the development of native schemes of multi-qubit quantum gates. Such gates, which allow operations on  $n$  qubits in a quantum register, can significantly reduce the total number of operations required to implement quantum algorithms. For example, the well-known three-qubit Toffoli gate is an essential element of many algorithms, including Shor's algorithm [11], Grover's algorithm [12, 87], as well as quantum error correction [88, 89] and Takahashi adders [90] implementation. Under normal conditions, 6 two-qubit gates and 9 additional one-qubit rotations are required to perform the Toffoli gate. Thus, assuming the typical fidelities of this single- and two-qubit gates to be  $\sim 99.9\%$  and  $\sim 99.5\%$  for neutral-atom registers, one achieve the final Toffoli gate fidelity of  $\sim 96\%$ , which is relatively low for efficient quantum computation. The implementation of a high-precision multi-qubit quantum gate in one shot thus presents a desired goal for many research teams.

Currently, many proposals are presented for the implementation of high-fidelity multiqubit gates in Rydberg systems (see Table 1.2). Among them Rydberg-blockade-based schemes represent the mostly developed and widely used group. Such schemes are native to the implementation of quantum computing and were well investigated during the last decades. Nevertheless, the maximum three-qubit gate fidelity obtained using the dipole blockade effect so far is  $\sim 97.9\%$  [49]. The main disadvantage of the dipole blockade effect for Rydberg quantum computing is the impossibility to implement gates between far isolated qubits using this approach. The dipole blockade is based on the van der Waals interaction, which strength decreases with distance as  $1/R^6$ . Consequently, such gates cannot be implemented between distant atoms, which is necessary to create high-precision entanglement in large ensembles. To compensate for this effect, it is necessary to strengthen the interatomic interactions [28].

Förster resonances (described in detail in Subsection 2.2.5) provide a reasonable alternative to the dipole blockade effect for Rydberg quantum gate implementation. While the dipole blockade effect prevents the excitation of several atoms into Rydberg states, schemes based on Förster resonances assume simultaneous ensemble excitation [59, 107]. By compensating for the Förster defect, one can achieve a significant increase in interaction strength. So, when realizing the resonance between the collective atomic Rydberg states, the dipole-dipole interaction is proportional to  $1/R^3$ , thus allowing the implementation of quantum gates between further distant atoms! While the typically allowed interatomic distance for blockade-based two-body gate implementation is  $\sim 5$  microns, the Förster interaction enables the gate implementation at distances of up to  $\sim 25$  microns for the same Rydberg levels. This significant increase paves a way to create full interconnectivity in quantum registers, and thus is promising for the implementation of multi-qubit quantum entanglement and quantum gates!

## 1.8. Thesis topic and structure

The research presented in this thesis relates to the study of three-body Förster resonances and their applications in Rydberg quantum computing. We have developed and numerically investigated various schemes of three-body resonances in structured and unstructured ensembles of Rydberg Rb atoms. A study of quasi-forbidden two-body resonance processes in ensembles of Rb and Cs atoms has also been carried out. New methods for the resonant control in Rydberg systems have also been proposed to ensure the immunity of computed gates to unwanted interaction channels. In particular, the use of an external magnetic field for the separation of resonant channels has been proposed. Also, RF-induced Förster resonances have been considered, which provided an opportunity to isolate the resonance channel of interest and gave us extensive interaction control possibilities.

We have proposed and numerically simulated several variants of implementation of multiqubit quantum gates based on Förster resonances. In particular, two different Toffoli gate schemes have been presented based on three-body resonance transitions in structured Rb registers. Also, doubly controlled phase gate implementation schemes have been proposed based on two- and three-body RF-induced Förster resonances. The quantum gates demonstrate high

## Chapter 1. Introduction

---

theoretical fidelity values within our numerical simulations. The simplicity of the experimental implementation of the suggested phase gates should be considered as a separate advantage.

This thesis is divided into 5 chapters. A broad introduction giving an overview of the current status of quantum computer science, concentrating on neutral-atom-based quantum computing, is provided in current chapter (Chapter 1). Chapter 2 describes the theoretical background to this thesis, including the Rydberg physics of alkali atoms, the foundations of quantum computing, and the basics of modern Rydberg quantum computing. Chapter 3 presents the results of the research on many-body Förster resonances obtained in Aime Cotton Laboratory (LAC) and the Institute of Semiconductor Physics (ISP SB RAS) before 2018. Although the author of this thesis was an employee of both institutions, the results of Chapter 3 were obtained without his participation. Nevertheless, these results are directly relevant to the subject of this thesis and should be considered as the basis of the conducted research. Chapter 4 presents the results of the research carried out by the author during his doctoral studies. Each of the sections in Chapter 4 describes a different study, and is based on the results presented in the articles produced (fully or partially) by the author of this thesis. In general, each section corresponds to the results of a single article. The exception is Section 4.1, where results from two articles are presented. Finally, Chapter 5 provides conclusions on the results presented in this thesis and suggests possible directions for future research.

# Chapter 2

## Theoretical foundations

Rydberg quantum computing is a young field of science covering the application of neutral atoms to quantum computing problems. It combines many aspects of atomic physics and quantum computation theory. This chapter will provide an overview of the theoretical foundations needed to describe the conducted research. Specifically, in Section 2.1, the basics of quantum computer science are described, including the concepts of quantum gates and quantum algorithms. Section 2.2 deals with the physics of Rydberg alkali atoms, including the peculiarities of atomic structure and interatomic interactions, as well as the interactions of atoms with external radiation. Also in this section, Förster resonances, the study of which forms the subject of this thesis, are discussed in detail. In Section 2.3, the fundamentals of Rydberg quantum computing are explained, including peculiarities of the structure of atomic registers, as well as details of the implementation of quantum computations with Rydberg atoms.

### 2.1. Quantum information basics

This section will describe the basics of quantum computing and quantum information processing. It includes the definition of fundamental concepts such as qubits and quantum gates, as well as descriptions of quantum algorithms. We also discuss here the three-qubit quantum gates and their applicability to quantum algorithms.

#### 2.1.1. Qubits

A qubit is a logical unit of quantum information. Unlike the classical bit, which has a binary discrete spectrum, the qubit is represented by a two-level quantum system, and thus potentially contains an infinite amount of information. However, since each qubit measurement results in a collapse of the quantum state, only a small fraction of this potential becomes available to the final user. In this subsection, we will briefly describe the concept of a qubit in terms of quantum mechanics.

##### 2.1.1.1. Single-qubit states

As stated before, any qubit can be represented as a two-level quantum system:

$$|\psi\rangle = \alpha|0\rangle + \beta|1\rangle \quad (2.1)$$

Here  $\alpha$  and  $\beta$  are the complex amplitudes of basis states  $|0\rangle$  and  $|1\rangle$ , respectively. Thus, the

qubit can persist in an arbitrary superposition of its logical states [1].

According to the probability conservation principle, all qubit states are normalized  $|\alpha|^2 + |\beta|^2 = 1$ . Note that the total qubit phase is immeasurable and can be omitted in quantum state representation. Thus, one can parametrise the qubit state with two real numbers and the relative phase between two basis states. A convenient visual representation for pure qubit states is given by a point on a Bloch sphere surface (see Fig.2.1). In such a representation, the coefficients  $\alpha$  and  $\beta$  are replaced by the cosine and sine of the polar angle, preserving the norm of the vector to be unit (see Eq. 2.2). The relative phase is described by the azimuthal angle  $\phi$ . In the case of dissipation, mixed states can also be described in terms of the Bloch vector. Such a vector will lie inside the surface of the Bloch sphere, and its length is determined by the population of logical states.

$$|\psi\rangle = \cos(\theta/2)|0\rangle + \sin(\theta/2)e^{i\phi}|1\rangle \quad (2.2)$$

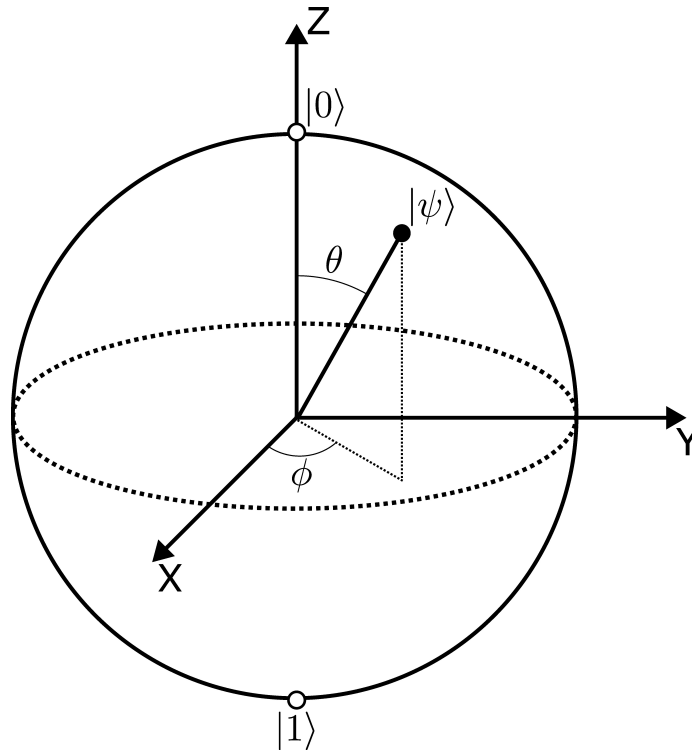


**Figure 2.1 :** Bloch sphere representation of qubit state  $|\psi\rangle$ .

In Eq.(2.2),  $0 \leq \theta \leq \pi$  and  $0 \leq \phi \leq 2\pi$ . With the common notation  $|0\rangle = \begin{pmatrix} 1 \\ 0 \end{pmatrix}$  and  $|1\rangle = \begin{pmatrix} 0 \\ 1 \end{pmatrix}$  the vector representation of qubit state is

$$|\psi\rangle = \begin{pmatrix} \cos(\theta/2) \\ e^{i\phi} \sin(\theta/2) \end{pmatrix} \in \mathbb{C}^2 \quad (2.3)$$

Thus, a state  $|0\rangle$  is in the north pole of the Bloch sphere, while a state  $|1\rangle$  is in the south pole.

### 2.1.1.2. Multi-qubit collective state

Similarly, any collective  $n$ -qubit state in  $\mathbb{C}^{2^n}$  space can be described as a linear combination of tensor products of the  $n$  individual qubit states [108].

$$\left\{ \begin{array}{l} |\Psi\rangle_n = \sum_{x_1, x_2, \dots, x_n \in \{0,1\}} \alpha_{x_1 x_2 \dots x_n} |x_1 x_2 \dots x_n\rangle \in \mathbb{C}^{2^n} \\ \sum_{x_1, x_2, \dots, x_n \in \{0,1\}} |\alpha_{x_1 x_2 \dots x_n}|^2 = 1 \end{array} \right. \quad (2.4)$$

In accordance with the presented description, the basis states of an  $n$ -qubit system are tensor products of the basis states of individual qubits. As an example, consider a state of a two-qubit system (2.5). The system is described by a complex vector in a four-dimensional Hilbert space  $\mathbb{C}^4$  with basis states (2.6). Unfortunately, multi-qubit quantum systems do not have an intuitive geometric interpretation [1].

$$|\Psi\rangle_2 = \alpha_{00}|00\rangle + \alpha_{01}|01\rangle + \alpha_{10}|10\rangle + \alpha_{11}|11\rangle \quad (2.5)$$

$$|00\rangle = \begin{pmatrix} 1 \\ 0 \\ 0 \\ 0 \end{pmatrix}, \quad |01\rangle = \begin{pmatrix} 0 \\ 1 \\ 0 \\ 0 \end{pmatrix}, \quad |10\rangle = \begin{pmatrix} 0 \\ 0 \\ 1 \\ 0 \end{pmatrix}, \quad |11\rangle = \begin{pmatrix} 0 \\ 0 \\ 0 \\ 1 \end{pmatrix} \quad (2.6)$$

When considering the states of multi-qubit systems, it is important to distinguish between entangled states and separable states. Separable states of an  $n$ -qubit system can be represented as a tensor product of the states of  $k$  individual subsystems of this system containing  $n_i$  qubits each.

$$|\Psi\rangle_n = \bigotimes_{i=1}^k |\Psi\rangle_{n_i}, \quad \sum_{i=1}^k n_i = n \quad (2.7)$$

Alternatively, entangled states can be represented as a superposition of such products, and cannot be described by equation (2.7). A well-known example of entangled states is given by Bell states (2.8), which represent four maximally entangled two-qubit states.

$$\begin{aligned} |\Phi^+\rangle &= \frac{|00\rangle + |11\rangle}{\sqrt{2}}, & |\Phi^-\rangle &= \frac{|00\rangle - |11\rangle}{\sqrt{2}} \\ |\Psi^+\rangle &= \frac{|01\rangle + |10\rangle}{\sqrt{2}}, & |\Psi^-\rangle &= \frac{|01\rangle - |10\rangle}{\sqrt{2}} \end{aligned} \quad (2.8)$$

## 2.1.2. Quantum gates

Analogous to classical computing systems, the states of quantum information units are transformed by the action of logical operators in digital quantum computing. Such operators can act on either one or several qubits, thus forming single- or multi-qubit quantum gates.

Any quantum system evolution can be described by the evolution operator  $U(t)$ . According to the principle of probability conservation, as well as the principle of reversibility, this operator must be unitary [1].

$$|\psi(t + t_0)\rangle = U(t)|\psi(t_0)\rangle \quad (2.9)$$

Thus, quantum gates are described by unitary transformations of quantum register states. In this subsection we will describe the basic concept of such gates, as well as some specific examples of gates that are widely used in quantum computer science.

### 2.1.2.1. Single-qubit gates

Unitary quantum operations acting on the states of individual qubits in a quantum register are called single-qubit quantum gates. Since a qubit is a two-level quantum system, the operator acting on 1 qubit is a superposition of the outer products of the qubit basis states, and is represented by a  $2 \times 2$  matrix.

The simplest set of logical quantum operations is provided by the Pauli group  $\{I, \sigma_x, \sigma_y, \sigma_z\}$  [109]:

$$I = \begin{pmatrix} 1 & 0 \\ 0 & 1 \end{pmatrix}, \quad \sigma_x = \begin{pmatrix} 0 & 1 \\ 1 & 0 \end{pmatrix}, \quad \sigma_y = \begin{pmatrix} 0 & -i \\ i & 0 \end{pmatrix}, \quad \sigma_z = \begin{pmatrix} 1 & 0 \\ 0 & -1 \end{pmatrix} \quad (2.10)$$

Pauli gates satisfy  $\sigma_j^2 = -i\sigma_x\sigma_y\sigma_z = I$  relation, commutation relations  $[\sigma_j, \sigma_k] = 2i \sum_l \epsilon_{jkl}\sigma_l$ , and anticommutation relations  $\{\sigma_j, \sigma_k\} = 2\delta_{jk}I$ . The operators are presented in the standard basis of states  $|0\rangle$  and  $|1\rangle$  ( $Z$ -basis), described in the previous section. Hereinafter, we will adhere to this basis when describing any quantum gates and quantum algorithms, unless specified otherwise [1, 109].

The impact of single-qubit quantum gates can be visualized as vector rotations on the Bloch sphere. So, the application of  $\sigma_x, \sigma_y, \sigma_z$  operations corresponds to  $\pi$  rotations around the  $X, Y, Z$  axes, respectively. In this regard, operators are often referred to by a letter denoting the axis of rotation. Thus,  $\sigma_x$  is denoted as  $X$ ,  $\sigma_y$  as  $Y$ , and  $\sigma_z$  as  $Z$ . Generalizing rotation operations by applying Euler's formula  $e^{i\theta\mathbf{A}} = \cos(\theta)\mathbf{I} + i\sin(\theta)\mathbf{A}$ , one can provide the following notation [1, 109]:

$$R_x(\theta) = e^{-i\sigma_x\theta/2} = \cos(\theta/2)I - i\sin(\theta/2)\sigma_x = \begin{pmatrix} \cos(\theta/2) & -i\sin(\theta/2) \\ -i\sin(\theta/2) & \cos(\theta/2) \end{pmatrix} \quad (2.11)$$

$$R_y(\theta) = e^{-i\sigma_y\theta/2} = \cos(\theta/2)I - i\sin(\theta/2)\sigma_y = \begin{pmatrix} \cos(\theta/2) & -\sin(\theta/2) \\ \sin(\theta/2) & \cos(\theta/2) \end{pmatrix} \quad (2.12)$$

$$R_z(\theta) = e^{-i\sigma_z\theta/2} = \cos(\theta/2)I - i\sin(\theta/2)\sigma_z = \begin{pmatrix} e^{-i\theta/2} & 0 \\ 0 & e^{i\theta/2} \end{pmatrix} \quad (2.13)$$

Note that an arbitrary one-qubit unitary gate  $U$  can be represented as a combination of rotations around two arbitrary orthogonal axes on the Bloch sphere. Omitting the detailed description, we provide here two frequently used decompositions:  $Z - Y$  decomposition on a rotation thread (2.14) and  $AB$  decomposition (2.15) [1]. In the  $ABC$  decomposition the operators  $A$ ,  $B$  and  $C$  are unitary and satisfy  $ABC = I$ .

$$U = e^{i\alpha} R_z(\beta) R_y(\gamma) R_z(\delta) \quad (2.14)$$

$$U = e^{i\alpha} A X B X C \quad (2.15)$$

Among other single-qubit quantum gates, it is important to mention three frequently occurring operations - Hadamard gate  $H$ , phase gate  $S$  and  $T$  gate [1]. The importance of these gates is emphasized by the fact that they do not have counterparts in classical computer science. They are necessary for realization of universal quantum computations and also for generation of entangled multiqubit states. Further, we will use some of these gates to describe three-qubit gates decompositions.

$$H = \frac{\sigma_x + \sigma_z}{\sqrt{2}} = \frac{1}{\sqrt{2}} \begin{pmatrix} 1 & 1 \\ 1 & -1 \end{pmatrix} \quad (2.16)$$

$$S = e^{i\pi/4} R_z(\pi/2) = \begin{pmatrix} 1 & 0 \\ 0 & e^{i\pi/2} \end{pmatrix} \quad (2.17)$$

$$T = e^{i\pi/8} R_z(\pi/4) = \begin{pmatrix} 1 & 0 \\ 0 & e^{i\pi/4} \end{pmatrix} \quad (2.18)$$

### 2.1.2.2. Multi-qubit gates

To implement complex circuits and high-level quantum algorithms, it is necessary to perform logic operations involving several qubits. Thus, in addition to single-qubit gates, multi-qubit gates are also needed for quantum computing. Such gates can be described as unitary transformations over collective states of multiple qubits.

In general, the unitary evolution of a system of  $n$  qubits under the action of  $U_1 \dots U_k$  operators acting on subsystems with  $n_1 \dots n_k$  qubits, respectively, can be represented as a tensor product of individual operators acting on the complete system. Thus, multiqubit gates can be represented as compositions of single-qubit quantum gates, in particular Pauli gates along with the single-qubit state projectors.

$$\left( \bigotimes_{i=1}^k U_i \right) |\Psi\rangle_n = \bigotimes_{i=1}^k U_i |\Psi\rangle_{n_i}, \quad \sum_{i=1}^k n_i = n \quad (2.19)$$

An important special case of multi-qubit gates are controlled  $C^k U$  gates. These gates apply unitary transformation  $U$  to a subset of the quantum register (target subset), if the controlling subset  $C^k$  resides in a certain logical state.

• **Two-qubit controlled gates**

$CNOT$  and  $CZ$  gates are the most important and frequently used examples of single-controlled gates for two-qubit quantum systems. Thus, the  $CNOT$  gate applies a negation operation to the target qubit if the control qubit is in the  $|1\rangle$  state. The negation operation is described by a Pauli  $X$ -gate producing transitions  $|0\rangle \rightarrow |1\rangle$  and  $|1\rangle \rightarrow |0\rangle$ . The  $CZ$ -gate, in turn, is a controlled version of the Pauli  $Z$ -gate.

$$CNOT = |0\rangle\langle 0| \otimes I + |1\rangle\langle 1| \otimes X = \begin{pmatrix} 1 & 0 & 0 & 0 \\ 0 & 1 & 0 & 0 \\ 0 & 0 & 0 & 1 \\ 0 & 0 & 1 & 0 \end{pmatrix} \quad (2.20)$$

$$CZ = |0\rangle\langle 0| \otimes I + |1\rangle\langle 1| \otimes Z = \begin{pmatrix} 1 & 0 & 0 & 0 \\ 0 & 1 & 0 & 0 \\ 0 & 0 & 1 & 0 \\ 0 & 0 & 0 & -1 \end{pmatrix} \quad (2.21)$$

Two-qubit quantum gates are widely used in quantum computing. It is known that a universal set of quantum gates can be formed from one- and two-qubit gates, thus allowing to decompose any quantum computation into a sequence of such gates. We will discuss the universality of quantum gates in the Subsection 2.1.3.2.

In general, an arbitrary controlled gate can be represented by a matrix of the form (2.22). According to  $ABC$ -decomposition (2.23), we can represent such a gate by unitary  $ABC$ -operators separated with two  $CNOT$  gates and an additional controlled phase gate (2.24) needed to verify the global phase  $\alpha$ .

$$CU = \begin{pmatrix} 1 & 0 & 0 & 0 \\ 0 & 1 & 0 & 0 \\ 0 & 0 & U_{00} & U_{01} \\ 0 & 0 & U_{10} & U_{11} \end{pmatrix} \quad (2.22)$$

$$CU = A \otimes CNOT \otimes B \otimes CNOT \otimes C \otimes Ph(\alpha) \quad (2.23)$$

$$Ph(\alpha) = \begin{pmatrix} 1 & 0 & 0 & 0 \\ 0 & 1 & 0 & 0 \\ 0 & 0 & e^{i\alpha} & 0 \\ 0 & 0 & 0 & e^{i\alpha} \end{pmatrix} = \begin{pmatrix} 1 & 0 \\ 0 & e^{i\alpha} \end{pmatrix} \otimes I \quad (2.24)$$

Another convenient decomposition of controlled gates exploits the fact that an arbitrary unitary quantum operation  $U$  is analogous to a rotation on a Bloch sphere around an arbitrary axis. Then,

$$CU = CR_{\vec{n}}(\theta)Ph(\alpha) \quad (2.25)$$

$$CR_{\vec{n}} = R_z(+\alpha)R_y(+\beta) \otimes CR_z(\theta) \otimes R_y(-\beta)R_z(-\alpha) \quad (2.26)$$

Thus, we can realize an arbitrary unitary operation by performing a controlled  $Z$ -rotation. This fact gives ample opportunities for decomposition of gates, and will be useful for the subsequent analysis of the research results.

### • Three-qubit controlled gates

The main subject of this thesis is three-qubit quantum gate implementation. Therefore, we will describe such gates separately. The study of three-body gates has its origins in classical theory of computation [1]. Such gates involving 3 bits simultaneously can be both universal and reversible in classical computation. Universality is understood here in the sense that with some three-bit gates one can perform any classical logical operations, if given the ability to initialize the computational register to arbitrary states. Nevertheless, quantum three-qubit gates are not necessarily universal, and need additional one-qubit gates to maintain the universality of quantum computation.

### • Toffoli gate

The Toffoli gate ( $CCNOT$ ) is a generalization of the  $CNOT$  gate to the case of a three-qubit quantum register. This gate applies a negation operation to the target qubit if both controlling qubits are in the  $|1\rangle$  state. Toffoli gate is widely used in quantum algorithms, in particular in quantum error correction algorithms, Shor's algorithm, Grover's algorithm, and many others [1].

In principle, decomposition of the Toffoli quantum gate is possible using one-qubit and two-qubit quantum gates. According to [1], a minimum of 6 two-qubit and 9 one-qubit operations are needed to decompose a Toffoli gate.

$$CCNOT = \begin{pmatrix} 1 & 0 & 0 & 0 & 0 & 0 & 0 & 0 \\ 0 & 1 & 0 & 0 & 0 & 0 & 0 & 0 \\ 0 & 0 & 1 & 0 & 0 & 0 & 0 & 0 \\ 0 & 0 & 0 & 1 & 0 & 0 & 0 & 0 \\ 0 & 0 & 0 & 0 & 1 & 0 & 0 & 0 \\ 0 & 0 & 0 & 0 & 0 & 1 & 0 & 0 \\ 0 & 0 & 0 & 0 & 0 & 0 & 0 & 1 \\ 0 & 0 & 0 & 0 & 0 & 0 & 1 & 0 \end{pmatrix} \quad (2.27)$$

### • $CCZ$ gate

The  $CCZ$ -gate is a double-controlled version of the previously mentioned Pauli  $Z$ -gate. Similar to the Toffoli gate, it applies the Pauli  $Z$ -gate operation to the target qubit only if the controlling qubits are in the  $|1\rangle$  logical state. Note that these two gates can be transformed into each other by applying Hadamard gates to the target qubit.

$$CCZ = \begin{pmatrix} 1 & 0 & 0 & 0 & 0 & 0 & 0 & 0 \\ 0 & 1 & 0 & 0 & 0 & 0 & 0 & 0 \\ 0 & 0 & 1 & 0 & 0 & 0 & 0 & 0 \\ 0 & 0 & 0 & 1 & 0 & 0 & 0 & 0 \\ 0 & 0 & 0 & 0 & 1 & 0 & 0 & 0 \\ 0 & 0 & 0 & 0 & 0 & 1 & 0 & 0 \\ 0 & 0 & 0 & 0 & 0 & 0 & 1 & 0 \\ 0 & 0 & 0 & 0 & 0 & 0 & 0 & -1 \end{pmatrix} \quad (2.28)$$

$$CCZ = (I \otimes I \otimes H) \otimes CCNOT \otimes (I \otimes I \otimes H) \quad (2.29)$$

Principally, a large number of useful three-qubit quantum gates exist. In particular, Fredkin [110] and Peres [111] gates are often used in complex quantum algorithms, providing advantages in speed and accuracy of computation [1]. However, we do not consider all examples of complex quantum gates here, focusing on the Toffoli and  $CCZ$  gates, which are critical for our study.

### 2.1.3. Quantum circuits

#### 2.1.3.1. Quantum circuit composition

The quantum circuits required to perform complex quantum algorithms are constructed from sequences of single-qubit and multiqubit quantum gates. Before we proceed to the quantum algorithms description, it is necessary to consider the standard graphical representation used for quantum registers and quantum operations.

Individual qubits in the quantum register are represented as horizontal parallel wires [108]. We assume, that prior to the computation all qubits are prepared in  $|0\rangle$  logical states, unless specified otherwise. Quantum operations are depicted as boxes arranged on top of a single wire (single-qubit gate) or a group of wires (multi-qubit gate). The scheme is read from left to right, in such a way that at each moment of time the states of the quantum register are described by the tensor product of the states of all individual qubits (the tensor product is carried out vertically throughout the scheme).

Gates have a special representation on the quantum circuit. To show control connections, vertical wires are used linking the controlling qubits to the box of the operator displaying the controlled operation. Controlling qubits are denoted by a bullet ( $\bullet$ ). Also, the sign  $\oplus$  is used to denote the action of controlled negation operations (for example, in  $CNOT$  and Toffoli gates). In Figure 2.2, you can see an example of the simplest quantum algorithm, which creates the Bell states.

#### 2.1.3.2. Universal gate sets

Robust and reproducible implementation of arbitrary quantum circuits is a central issue in quantum computer science. According to [1, 109], a set of quantum gates is considered uni-

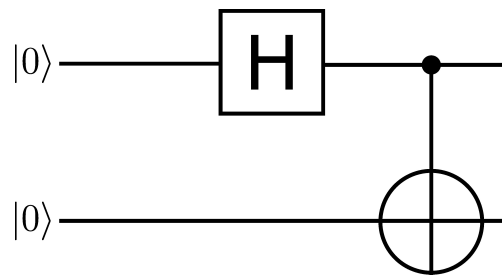


**Figure 2.2:** Quantum scheme for the Bell state creation. If initialized with the input  $|00\rangle$  (as presented here), this quantum scheme provides an  $|\Phi^+\rangle$  Bell state. Nevertheless, different inputs will allow the creation of any desired Bell state.

versal if any unitary operation on a quantum register can be arbitrarily precisely approximated using gates from this set alone.

There are several widely known universal sets of quantum gates. Such sets may consist of one- and two-qubit operations, or may also include three-qubit operations. Nevertheless, an essential requirement is the presence of “sufficiently entangled and universal gates” in the set. Consider this property in the examples below [108].

- **Clifford gate set**

Clifford set is a well-known gate set, consisting of  $\{H, S, CNOT\}$  gates. According to the Gottesman-Knill theorem [1], any quantum computation performed using gates from this set can be efficiently modeled on a classical computer. Thus, this set is not universal, although the included gates are capable of producing entanglement. Note that the universality of the Clifford set would denote that any quantum operations can be efficiently emulated on a classical computer.

- **Standard gate set**

The standard set  $\{H, S, CNOT, T/CCNOT\}$  is a discrete version of a more general  $CNOT + SU(2)$  set and is widely used in fault-tolerant quantum computing. It consists of a Clifford set, supplemented by one of the gates that guarantees the computation universality -  $T$  gate or Toffoli gate [109]. This example states that the implementation of gates that can guarantee universality is critically important for the construction of universal quantum computing schemes.

- **“Toffoli +  $H$ ” set**

In principle, the standard gate set can be reduced to two gates, the Toffoli gate and the Hadamard gate. As it was proved in [112], this gate set retains universality. The Hadamard gate is used to create superposition states and guarantee the possibility of generating entanglement in a quantum register, whereas the Toffoli gate allows controlled quantum operations in the register. Nevertheless, such a gate set is not very convenient for practical use, and the standard one is used more often.

### 2.1.4. Quantum algorithms

The main advantage of quantum computing over classical computing is its potential in solving part of the **NP** class of computational problems. Such problems belong to the **BQP** class, whose boundaries in the space of **NP** problems have not yet been defined. Currently, there are 4 classes of quantum algorithms that are proven to be superior to their classical counterparts in terms of efficiency [1, 113, 114].

#### • Quantum random walk-based algorithms

Quantum walks represent quantum counterparts to classical random walks. While classical random walks involve walkers occupying distinct states, and randomness emerges from stochastic transitions between these states, quantum walks differ in how randomness arises. The randomness in quantum walks results from:

- the quantum superposition of states
- non-random and reversible unitary evolution
- the wave function collapse triggered by state measurements

Similar to classical random walks, quantum walks can be formulated in both discrete time and continuous time.

Quantum walks have gained recognition for their ability to achieve exponential speedups in certain black-box problems. The list of tasks solved by quantum walk - based algorithms includes Boson sampling problem [115], element distinctness problem [116] and triangle finding problem [117].

#### • Amplitude amplification-based algorithms

Amplitude amplification-based quantum algorithms were proposed originally by Gilles Brassard and Peret Hoyer in 1997 [118]. The proposed technique allows to amplify the projection of the quantum system state into the desired subspace of its state space. Due to this amplification, a quantum search in an unstructured ensemble can be performed, as proposed by Lov Grover in 1996 [12]. Grover's algorithm allows one to search in an unstructured database of  $N$  objects in  $O(\sqrt{N})$  steps, giving a quadratic acceleration compared to standard algorithms. Another important algorithm of this class is the generalized quantum counting algorithm.

#### • Hybrid quantum-classical algorithms

Hybrid quantum-classical algorithms present an actively developing class of algorithms. They combine quantum computing protocols with classical subroutines. Most often, the classical subroutine provides an opportunity to adapt the parameters of the algorithm in the optimization process. Quantum Approximate Optimization Algorithm (QAOA) [119] and Variational Quantum Eigensolver (VQE) [120] are among the most important examples of this algorithm class.

### • QFT-based algorithms

The quantum Fourier transform was discovered in 1994 by Don Coppersmith [121]. This transformation is analogous to the discrete Fourier transform applied to a quantum register containing  $n$  qubits (and hence  $N = 2^n$  complex amplitudes). For the  $n$ -qubit state  $|\Psi\rangle_n = \sum_{i=0}^N \alpha_i |x_i\rangle$  the result of QFT is a state  $|\Psi'\rangle_n = \sum_{k=0}^N \alpha'_k |x_k\rangle$  with the coefficients [1]:

$$\alpha'_k = \frac{1}{\sqrt{N}} \sum_{j=0}^{N-1} e^{2i\pi jk/N} \alpha_j \quad (2.30)$$

The classical discrete Fourier transform is an exponentially complex problem requiring at least  $O(n2^n)$  logical gates for  $N$  complex amplitudes (here  $n$  is the number of classical bits). At the same time, the quantum Fourier transform for  $n$  qubits requires only a polynomial number of quantum gates ( $O(n \log(n))$  or  $O(n^2)$ ), which can be reduced to linear amount  $O(n)$  in specific cases.

Among the most important examples of the algorithms of this class one could mention the Deutsch-Jozsa algorithm [122], the Bernstein-Vazirani algorithm [123], Shor's algorithm [11], Simon's algorithm [124] and Quantum Phase Estimation (QPE) [125]. Note that the alternative QPE algorithm optimised for Rydberg registers was developed by the author of this thesis as part of his master research at NSU. Since this algorithm is not relevant to the subject of this study, it is not represented in this thesis. Nevertheless, the interested reader can review it in the article [126].

### 2.1.5. Gate fidelity

Quantum operation fidelity determination is critical for the evaluation of the gate implementation quality. However, there is currently no single standard of fidelity, and different research goals requires different fidelity definitions. Below we present commonly used approaches to the fidelity calculation, provided in [1, 28].

Since any quantum operation can be represented as a unitary transformation of a multi-qubit register, one of the commonly used methods for the fidelity calculation is to evaluate the similarity of the unitary transformation operator with its ideal analogue [28]. In particular, for two-qubit *CNOT* operators, the measure presented in Eq. (2.31) is often used, where  $U_{id}$  is the ideal gate operator, and  $U$  is the operator which corresponds to the actual gate implementation [47, 127]. Obviously, these two operators will differ significantly due to the presence of errors in the gate implementation. This approach was also adapted in order to better account for phase errors in gates, as well as to obtain an average value of gate fidelity [128].

$$F = Tr \left( U_{id}^\dagger U \right) \quad (2.31)$$

It can also be useful to estimate the fidelity by defining the "distance" between operators  $\rho$  and  $\rho_{id}$  [28, 129]. Specifically, one can define an operator  $D(\rho, \rho_{id}) = |\rho - \rho_{id}|/2$ , where  $|A| = \sqrt{A^\dagger A}$  for arbitrary operator  $A$ . One thus calculate the gate fidelity as  $F = 1 - D$ . When the operators  $\rho$  and  $\rho_{id}$  are completely identical,  $D(\rho, \rho_{id}) = 0$  and fidelity  $F = 1$ . Note that the

distance-defined fidelity is essentially sensitive to the dephasing errors when compared with the metric (2.31), and thus could be useful in various applications [130].

$$F = \text{Tr} \sqrt{\sqrt{\rho_{id}} \rho \sqrt{\rho_{id}}} \quad (2.32)$$

A natural method of measuring fidelity is to estimate the gate effect on the states of the system under study and to compare this effect with the ideal gate counterpart. A commonly used metric is then (2.32), described in [45, 47, 131]. Here  $\rho_{id}$  is the density matrix of the quantum register state after applying the ideal gate operator, and  $\rho$  is the density matrix resulted from the application of actual gate. Averaging the value of  $F$  over a large array of register initial states, one finds the actual fidelity of the quantum operation. This method is universal, and we will use it extensively to characterize quantum gates in this thesis [28].

## 2.2. Rydberg atoms

Neutral atoms present a convenient platform for the implementation of quantum computing. In this section, we discuss the properties of Rydberg atoms, along with strong interatomic interactions needed for quantum gate implementation in neutral-atom-based registers. We also consider the peculiarities of the interaction of atoms with external radiation. Finally, a detailed description of Förster resonances, which constitute the main subject of this thesis, is given in this section.

### 2.2.1. Historical background

Studies of atomic spectra conducted throughout the 18<sup>th</sup> century revealed the discreteness of absorption and emission lines for various chemical elements. The equation describing the wavelengths for these lines was empirically discovered by Johann Balmer in 1885 [132]. In 1888, this equation was reformulated by Johannes Rydberg [133, 134] in the form (2.33), where  $\lambda$  denotes a wavelength,  $n_1$  and  $n_2$  are integer numbers and the coefficient  $R$  is a Rydberg constant [135].

$$\frac{1}{\lambda} = R \left( \frac{1}{n_1^2} - \frac{1}{n_2^2} \right) \quad (2.33)$$

Rydberg's formula showed striking agreement with the experimental data available at the time of its presentation. However, its nature remained a mystery. In 1913, the Bohr atom model [136] explained the Rydberg formula and gave an expression for the Rydberg constant  $R$  in terms of fundamental physical constants. Since the energy of the Hydrogen atom in the Bohr model can be expressed as  $E_n = \frac{-hcR}{n^2}$ , it is obvious that the spectral lines of atoms correspond to transitions between the energy levels  $|n_1\rangle$  and  $|n_2\rangle$ , where the Rydberg constant is  $R = \frac{mq^4}{4\pi ch^3}$ , with  $q = \frac{e}{\sqrt{4\pi\epsilon_0}}$ . Thus, Bohr's theory provided a quantum mechanical explanation for the atomic structure, paving the way for the quantum-based theory of matter composition.

The development of the Bohr model led to the creation of modern atomic physics. It also delivered the prerequisite for the active investigation of Rydberg atoms. Rydberg atoms are highly excited atoms containing one (or more) electrons in states with high  $n$  values. They exhibit exaggerated properties, in particular, long lifetimes, as well as enhanced sensitivity to electric and magnetic fields. In this thesis, we will discuss in detail the physics of alkali Rydberg atoms, as well as their application in modern quantum computing.

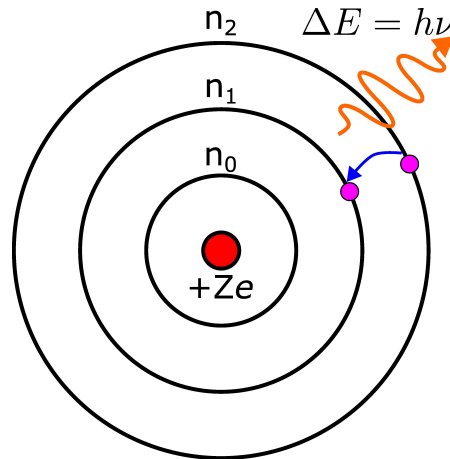


**Figure 2.3 :** Hydrogen-like ion model.

### 2.2.2. Alkali atoms

Alkali metal atoms are the basic building blocks for modern atomic quantum registers. Such atoms contain one valence electron on their outer orbital and are located in the first column of the Mendeleev's periodic table (thus including  ${}^3\text{Li}$ ,  ${}^{11}\text{Na}$ ,  ${}^{19}\text{K}$ ,  ${}^{37}\text{Rb}$ ,  ${}^{55}\text{Cs}$  and  ${}^{87}\text{Fr}$ ) [137]. These atoms exhibit high reactivity and are readily amenable to optical manipulation, which made them convenient objects of study in the early days of atomic spectroscopy. Note that alkali atoms also demonstrate the absence of autoionization due to two-electron excitation, when compared, for example, with alkaline earth metal atoms of  ${}^{38}\text{Sr}$ , or lanthanide atoms of  ${}^{70}\text{Yb}$  [138]. Both Yb and Sr are also used in modern quantum computing schemes, but their complex level structure is not always fully understood, thus complicating the construction of quantum registers [137]. In this subsection, we will review the basic properties of alkali atoms, as well as the peculiarities of their interaction with external electric and magnetic fields.

#### 2.2.2.1. Alkali-atom model and quantum defect theory

The presence of a single valence electron makes alkali atoms similar in their behavior to hydrogen atoms. The electrons of the inner atomic orbitals form a “closed shell” that shields the charge of the nucleus. Thus, the valence electron is placed in the central field of the nucleus with a unit effective charge in a rough approximation.

To understand the properties of alkali atoms, drawing analogies with the properties of the hydrogen atom will be instinctive. As a preliminary exemplar model we describe here an ion-like system with a heavy core of charge  $+Ze$ , with a single orbiting electron. Note that if  $Z = 1$ , the described system acquires the characteristics of the hydrogen atom. The Hamiltonian of this hydrogen-like ion thus can be expressed as [135]:

$$\hat{H} = -\frac{\hbar^2}{2\mu}\nabla^2 - \frac{Ze^2}{4\pi\epsilon_0 r} \quad (2.34)$$

where  $\mu = \frac{m_e m_n}{m_e + m_n}$  is the reduced mass of the electron with the mass  $m_e$  and the composite core with the mass  $m_n$ .

The spatial dependence of the atomic potential  $\sim 1/r$  is central. Thus, the angular momentum of the electron  $\hat{L}$  is preserved for this model, and the spherical symmetry is obvious [139]. By choosing the ansatz of the wave function as  $\psi = R(r)Y_{l,m}(\theta, \phi)$ , we can separate the Hamiltonian into angular and radial parts. Here  $Y_{l,m}$  represent the well known spherical harmonics, which are the eigenfunctions for both  $\hat{L}^2$  and  $\hat{L}_z$  operators [139]:

$$\begin{cases} \hat{L}^2 Y_{l,m} = l(l+1)\hbar^2 Y_{l,m} \\ \hat{L}_z Y_{l,m} = m\hbar Y_{l,m} \end{cases} \quad (2.35)$$

Introducing nabla operator in spherical coordinates, we can thus express the radial Schrödinger equation as

$$-\frac{\hbar^2}{2\mu} \frac{1}{r^2} \frac{d}{dr} \left( r^2 \frac{d}{dr} \right) R(r) + \left( -\frac{Ze^2}{4\pi\epsilon_0 r} + \frac{\hbar^2 l(l+1)}{2\mu r^2} \right) R(r) = ER(r) \quad (2.36)$$

Solution for the radial part of the wavefunction can be expressed in terms of associated Laguerre polynomials [135] as (2.37).

$$R_{n,l}(r) = \left( \frac{4Z^3(n-l-1)!}{a_\mu^3 n^4 (n+l)!} \right)^{1/2} e^{-\frac{Zr}{na_\mu}} \left( \frac{2Zr}{na_\mu} \right)^l L_{n-l-1}^{2l+1} \left( \frac{2Zr}{na_\mu} \right) \quad (2.37)$$

Here,  $a_\mu = \hbar^2/(\mu q^2)$  represent the reduced Bohr radius. Thus, we can represent the final wavefunction as a combination of radial and angular parts:

$$\psi_{n,l,m}(r, \theta, \phi) = R_{n,l}(r)Y_{l,m}(\theta, \phi) \quad (2.38)$$

Substituting the obtained wave functions into the Schrödinger equation, we can find the energy eigenvalues that coincide with the prediction of the Bohr model, corrected by the reduced mass and the core charge.

$$E_n = \frac{-Z^2 \mu E_H}{2m_e n^2} \quad (2.39)$$

Here  $E_H = 2hcR$  corresponds to the Hartree energy.

Note that  $\psi$  acquired a dependence on the discrete coefficients  $n, l$  and  $m$ , known as quantum numbers. Specifically,  $n$  is the principal quantum number, which is a positive integer,  $l$  is the angular momentum number, restricted by integer numbers between 0 and  $n - 1$ , and  $m$  is the  $l$  momentum projection, thus acquiring an integer value from  $-l$  to  $l$ . It can be seen, that all of these three values relate to quantum observables (energy, momentum and momentum projection, respectively), given by a complete set of commuting operators  $\{\hat{H}, \hat{L}^2, \hat{L}_z\}$  [140].

The described behavior characterizes ions having an infinitesimally small nucleus and a single electron on the outer shell. However, for alkali atoms, the presented model is not reliable. As described above, an alkali atom consists of a positively charged nucleus along with a closed electron shell and an outer shell containing one valence electron. The total charge of the nucleus and closed electron shell is  $Z - (Z - 1) = 1$ . Thus, at a large distance from the nucleus, the electron is placed in an effective field of unit charge, and its behavior can be described by the model presented above with  $Z = 1$ . However, the closed shell of the atom has a finite size. In turn, the valence electron with a low orbital momentum value can penetrate the inner shell. In this case, the charge shielding effect decreases, and the effective potential of the electron can increase up to  $-Zq^2/r$ . Atomic potential thus can be described by a smooth "effective charge function"  $Z_{eff}(r)$ , which tends to  $Z$  as  $r \rightarrow 0$  and tends to 1 as  $r \rightarrow \infty$  [135].

$$\hat{V}_{eff} = -\frac{Z_{eff}(r)q^2}{r} \quad (2.40)$$

The effective potential enhances the coupling of low-orbital electrons with the nucleus, reducing the energies of atomic levels compared to the hydrogen-like model. However, as the orbital quantum number increases, this correction quickly disappears, since the electron probability density near the nucleus decreases. This is intuitively understandable, since as the value of  $l$  increases, the electron's orbit evolves from elliptical to circular shape. At the same time, the value of the effective charge changes slightly with the principal quantum number, since the probability density outside the isolated shell is large compared to the internal probability density for any value of  $n$  possible for the outer electron.

It can be demonstrated that the alkali potential adjustment caused by the influence of the nucleus can be described in terms of quantum defect  $\delta_{nlj}$  [137, 141] for sufficiently high principal quantum numbers. Since the effective potential reduces the energy of a low-orbital electron, we can introduce an amendment to the principal quantum number  $\nu = n - \delta_{nlj}$ . Thus, the energy spectra of the alkali atoms are represented by the following equation:

$$E_\nu = -\frac{E_H}{2(n - \delta_{nlj})^2} = -\frac{E_H}{2(\nu)^2} \quad (2.41)$$

Positive quantum defects can be described by the Rydberg-Ritz formula (2.42), which takes into account a residual energy dependence of the quantum defect by Taylor expansion. The coefficients  $\delta_i$  are obtained from microwave and laser spectroscopy for  $S, P, D$  [142] and  $F$  [143] states [138]. According to [137], quantum defects are negligible for higher- $l$  states, and

**Table 2.1:** Leading-order coefficients of Rydberg-Ritz formula (2.42) for  $^{85}\text{Rb}$  [138].

State	$n^2 s_{1/2}$	$n^2 p_{1/2}$	$n^2 p_{3/2}$	$n^2 d_{3/2}$	$n^2 d_{5/2}$	$n^2 f_{5/2}$	$n^2 f_{7/2}$
$\delta_0$	3.1312	2.6549	2.64138	1.3481	1.3465	0.01652	0.01654
$\delta_2$	0.1784	0.2900	0.2950	-0.6029	-0.5960	-0.085	-0.086

the experimental results correlate well with the hydrogen model. Note that the quantum defect also depends on the total moment of the atom  $j$ . Thus, due to the penetration of the closed shell, the orbital symmetry is broken for the quantum defect model, and a new choice of reliable quantum numbers is required for system description. In the following, a set of  $n, l, j, m_j$  quantum numbers will often be used to describe the basis states of atomic Hamiltonians.

$$\delta_{nlj} = \delta_0 + \frac{\delta_2}{(n - \delta_0)^2} + \dots \quad (2.42)$$

### 2.2.2.2. Stark effect

One of the unique properties of the hydrogen atom is the linearity of its energy levels Stark shifts in the presence of external electric field. Since the atomic energies depend only on the principal quantum number, states with different values of the orbital moment  $l$  are degenerate [144]. Thus, a hydrogen atom can have a constant dipole moment for each of its energy levels, and, consequently, calculating the interaction of an atom with an external field  $F$  provides non-zero result in the first-order perturbation theory [135].

The situation is drastically changed for alkali atoms. Due to the presence of the quantum defect  $\delta_{nlj}$ , the atomic level energies are now  $l$ -dependent. Consequently, due to the absence of degeneracy, the levels are no longer mixed, and a certain energy level doesn't have a permanent dipole moment. Then, the second-order perturbation theory calculation for the Hamiltonian  $\hat{H} = \hat{H}_0 - \hat{d}\vec{F}$  gives

$$\Delta E = \sum_{n'l'm'} \frac{|\langle nlm | \hat{d} | n'l'm' \rangle|^2}{E_{nl} - E_{n'l'}} F^2 \quad (2.43)$$

The acquired energy shift is usually expressed in terms of polarizability  $\alpha$  as

$$\Delta E = -\frac{\alpha F^2}{2} \quad (2.44)$$

We thus can derive the polarizability from the expression (2.45):

$$\alpha = 2 \sum_{n'l'm'} \frac{|\langle nlm | \hat{d} | n'l'm' \rangle|^2}{E_{n'l'} - E_{nl}} \quad (2.45)$$

It is known that the polarizabilities of alkali atom states grow rapidly with the principal quantum number. To estimate the extent of this growth, we assume that the main contribution for the polarizability of a certain state comes from the closest spectral state of the opposite parity. Thus, we assume that this state has the same value of the principal quantum number  $n' = n$  and an angular momentum  $l' = l \pm 1$ . Note that while  $n' = n$ , the quantum defects of these two states are not the same. To account for the quantum defects, we denote the corrected  $n$  value as  $\nu$  [137].

The value of the dipole moment matrix element  $\langle n'l' | \hat{d} | nl \rangle$  is proportional to  $r$ , which means it has the same dependence on the principal quantum number as  $r \sim \nu^2$ . In turn, the energy difference in the limit  $n \rightarrow \infty$  is scaled as  $\Delta E \sim \nu^{-3}$ . Thus, the overall scaling of the Rydberg atom polarizability is  $\alpha \sim \nu^7$ . This extremely strong dependence motivates the widespread use of Rydberg atoms as electric field sensors [137, 145].

The above description well characterizes the Stark effect in Rydberg alkali atoms when the values of the orbital momentum are  $l < 4$ . In turn, for  $l \geq 4$ , the quantum defect becomes negligibly small, which means that the atomic spectrum becomes hydrogen-like. It is also important to note that the described approach works only in cases when the interaction induced by the external field is small compared to the energy difference between the considered dipole-paired states. To calculate the interaction, it is necessary to evaluate the matrix elements of the dipole moment by numerical methods, or to approximate them analytically. A detailed algorithm for calculating matrix elements used for the purposes of this thesis is given in the Appendix A.

### 2.2.2.3. Zeeman effect

The interaction of an atom with an external magnetic field can be described by the Hamiltonian  $\hat{H}_B = -\hat{\mu}\vec{B}$ . Here  $\hat{\mu} = -\mu_B(g_l\hat{L} + g_S\hat{S})$  is the total magnetic moment of the atom [139], with  $\mu_B$  representing the Bohr magneton. The gyromagnetic ratio factors have the values  $g_l = 1$  and  $g_S \approx 2$ . In weak fields, the energy correction due to Zeeman effect can be described by the equation (2.46):

$$\Delta E = g_j m_j \mu_B B \quad (2.46)$$

where the Lande factor  $g_j$  is defined as

$$g_j = \frac{3}{2} + \frac{s(s+1) - l(l+1)}{2j(j+1)} \quad (2.47)$$

As can be seen from the expression (2.46), the Zeeman effect depends on the momentum projection  $m_j$ , and leads to splitting of spectral lines, which scales linearly with  $B$ .

In the course of this study, we operate with relatively weak fields (typically, of  $\sim 3.5$  G), thus causing modest Zeeman shifts. However, if the Zeeman shift is comparable to the energy difference between undisturbed atomic levels under consideration, numerical diagonalization of the complete Hamiltonian is necessary to calculate the effect [138, 144].

### 2.2.3. Atom-light interaction

The excitation of atoms into Rydberg states occurs due to the interaction with external laser radiation. Microwave or radio frequency radiation can also be used to control resonant dynamics in Rydberg systems. In this regard, it is necessary to describe here the atom-light interaction model that was used in this study.

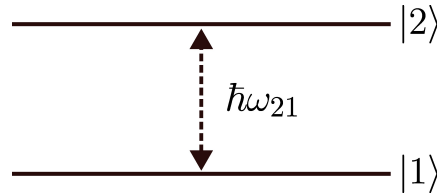


**Figure 2.4:** Two-level atom scheme.

We consider the semiclassical atom-light interaction model, which implies that radiation is a classical electromagnetic plane wave, while the atomic states are quantized. It is assumed that the wave is monochromatic, and the radiation frequency is close to the transition frequency between the atomic states under consideration. Since the transition frequency between the ground and Rydberg states is  $\sim 1000$  THz, while the detuning value does not exceed several MHz in typical experiments, the latter assumption is justified [138]. The assumption of monochromaticity is justified when narrow-band laser setup is used [144]. We thus can consider the atom-light interaction in rotating wave approximation.

To simplify the description, we present here the results for a two-level atom model with a ground state  $|1\rangle$  and an excited state  $|2\rangle$  (see Fig. 2.4). We assume that the states have different parity, and therefore dipole transitions in the system are allowed. The wave function of an atom can be written as (2.48), where  $\omega_{1(2)} = E_{1(2)}/\hbar$ .

$$|\psi(t)\rangle = c_1(t)e^{-i\omega_1 t}|1\rangle + c_2(t)e^{-i\omega_2 t}|2\rangle \quad (2.48)$$

The interaction of a two-level atom with radiation can be described as the interaction of a dipole with an external time-dependent electromagnetic field. The Hamiltonian of the atom-light system can be thus represented as

$$\hat{H} = \hat{H}_0 - \hat{d}\vec{F}(t) \quad (2.49)$$

According to the semiclassical model, the radiation is an unquantized electromagnetic wave, which means it can be described as a periodic cosine dependence

$$\vec{F}(t) = \vec{\epsilon}F_0 \cos(\omega t) \quad (2.50)$$

Here  $\vec{\epsilon}$  is the polarization vector,  $F_0$  is the amplitude of the electric field, and  $\omega$  is the radiation frequency. Then, from the Schrodinger equation we get

$$\begin{cases} \dot{c}_1 = i \frac{d_{12}^c F_0}{\hbar} e^{-i\omega_{21}t} \cos(\omega t) c_2(t) \\ \dot{c}_2 = i \frac{d_{12}^c F_0}{\hbar} e^{i\omega_{21}t} \cos(\omega t) c_1(t) \end{cases} \quad (2.51)$$

where  $d_{12}^c$  is the dipole matrix element between atomic states. Using the Euler decomposition, we can rewrite expressions (2.51) as

$$\begin{cases} \dot{c}_1 = i \frac{d_{12}^c F_0}{2\hbar} e^{-i\omega_{21}t} (e^{i\omega t} + e^{-i\omega t}) c_2(t) \\ \dot{c}_2 = i \frac{d_{12}^c F_0}{2\hbar} e^{i\omega_{21}t} (e^{i\omega t} + e^{-i\omega t}) c_1(t) \end{cases} \quad (2.52)$$

According to the rotating wave approximation, we can neglect the rapidly oscillating radiation components in comparison with the slow components. We thus neglect the terms proportional to the exponentiation of the sum frequency  $\omega + \omega_{21}$ . Introducing the notation  $\delta = \omega - \omega_{21}$ ,  $\tilde{c}_{1(2)} = c_{1(2)} e^{\mp i\delta t/2}$  we get the following equation system:

$$\begin{cases} \frac{d}{dt} \begin{pmatrix} \tilde{c}_1 \\ \tilde{c}_2 \end{pmatrix} = \frac{i}{2} \begin{pmatrix} -\delta & \Omega_0 \\ \Omega_0 & \delta \end{pmatrix} \begin{pmatrix} \tilde{c}_1 \\ \tilde{c}_2 \end{pmatrix} \\ \Omega_0 = \frac{d_{12}^c F_0}{\hbar} \end{cases} \quad (2.53)$$

Here  $\Omega_0$  denotes the well-known Rabi frequency. Diagonalizing the Hamiltonian, we can now determine the probability of finding the system in an excited state.

$$\begin{cases} |\tilde{c}_2(t)|^2 = \frac{\Omega_0^2}{2\Omega^2} (1 - \cos(\Omega t)) \\ \Omega = \sqrt{\Omega_0^2 + \delta^2} \end{cases} \quad (2.54)$$

We thus can state, that the population of atomic states oscillates between the states  $|1\rangle$  and  $|2\rangle$  under the action of external field with the effective Rabi frequency  $\Omega$ , which denotes the strength of atom-light interaction.

In this research, we will use the presented quasiclassical description when considering the interaction between the light and the atomic ensemble. Since the Rydberg levels are well isolated in the absence of a strong mixing external field, this model is relevant.

### 2.2.4. Dipole-dipole interaction

Interatomic interactions in Rydberg ensembles represent the basis of this thesis. Due to these interactions, one can achieve the correct phase and population dynamics of atomic qubits necessary for quantum operations. In this section we will consider the dipole-dipole interactions between Rydberg alkali atoms. Note that here a qualitative model of the interatomic dipole-dipole interactions based on the multipole decomposition of the atomic potential is described.

We intentionally do not give here the exact form of atomic wave functions or dipolar matrix elements, leaving their full description for the Appendix A.

As it was shown previously in Subsection 2.2.2.2, the polarizability of Rydberg alkali atoms increases rapidly with the effective principal quantum number  $\nu$ . Consequently, the atoms exhibit a strong interaction with an external electric field. Consider two atoms located at a distance  $R$  from each other (see Figure 2.5), with dipole moments  $\hat{d}_1$  and  $\hat{d}_2$ , respectively. We can then assume that the atoms influence each other due to the electric field produced by the oscillating dipoles. Thus, the dipole-dipole interaction occurs.

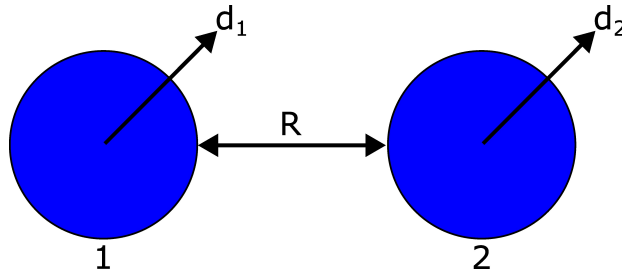


**Figure 2.5 :** Two atoms isolated on distance  $R$  from each other. Vectors  $d_{1(2)}$  represent the dipole moments of the first and second atom, respectively.

When describing the dipole-dipole interaction, we assume that the atoms are strongly isolated from each other, so that their Rydberg wave functions do not intersect. The minimum distance satisfying this requirement for Rydberg atomic states  $|\psi_1\rangle = |n_1, l_1, j_1\rangle$  and  $|\psi_2\rangle = |n_2, l_2, j_2\rangle$ , is given by LeRoy radius  $R_{LR}$  [137, 145]:

$$R_{LR} = 2 \left( \langle r_1^2 \rangle^{1/2} + \langle r_2^2 \rangle^{1/2} \right) \quad (2.55)$$

Here,  $\langle r_i^2 \rangle = \langle \psi_i | r^2 | \psi_i \rangle$ .

The electrostatic interaction between atoms can then be represented by a Taylor series of the Coulomb potential. Since the considered charge systems are isolated, the potential depends on the interatomic distance  $R = |\vec{r}_1 - \vec{r}_2|$  for two atoms 1 and 2 and on the dipole momentum orientation of each atom. The first two terms in the Taylor expansion describe the charge-charge interaction (Coulomb potential) and the charge-dipole interaction. Assuming the two atoms to be neutral and strongly isolated ensures these two terms to be zero. Thus, according to [137, 146], the leading term can be represented as:

$$\hat{V}_{dd}^{12}(r) = \frac{1}{4\pi\epsilon_0} \frac{\left( \hat{d}_1 \hat{d}_2 - 3 \left( \hat{d}_1 \hat{n} \right) \left( \hat{d}_2 \hat{n} \right) \right)}{R^3} \quad (2.56)$$

We can also express this formula in a more appropriate form

$$\begin{aligned} \hat{V}_{dd}^{12}(r) = \frac{1}{4\pi\epsilon_0 R^3} & \left[ S_1(\theta) \left( \hat{d}_{1+}\hat{d}_{2-} + \hat{d}_{1-}\hat{d}_{2+} + 2\hat{d}_{1z}\hat{d}_{2z} \right) \right. \\ & + S_2(\theta) \left( \hat{d}_{1+}\hat{d}_{2z} - \hat{d}_{1-}\hat{d}_{2z} + \hat{d}_{1z}\hat{d}_{2+} - \hat{d}_{1z}\hat{d}_{2-} \right) \\ & \left. - S_3(\theta) \left( \hat{d}_{1+}\hat{d}_{2+} + \hat{d}_{1-}\hat{d}_{2-} \right) \right] \end{aligned} \quad (2.57)$$

with the  $\hat{d}_{k,\pm}$  being the spherical components of the dipole moment operator and the  $S_i$  being the angular coefficients

$$\hat{d}_{k,\pm} = \mp \frac{\hat{d}_{k,x} \pm i\hat{d}_{k,y}}{\sqrt{2}} \quad (2.58)$$

$$\begin{cases} S_1 = \frac{1 - 3\cos^2(\theta)}{2} \\ S_2 = \frac{3\sin(\theta)\cos(\theta)}{\sqrt{2}} \\ S_3 = \frac{3\sin^2(\theta)}{2} \end{cases} \quad (2.59)$$

The dipole-dipole interaction operator  $\hat{V}_{dd}$  can provoke transitions between the collective states of the diatomic system. For simplicity, we will consider the situation of the interaction of two atoms, when each of them has only two Rydberg levels. Let atom 1 be in the Rydberg state  $|r_a\rangle$ , with additional Rydberg level  $|r_s\rangle$  of the opposite parity. Atom 2, in turn, is in the state  $|r_b\rangle$ , and also has a Rydberg level  $|r_t\rangle$ . Then we can describe a diatomic system in the basis of its collective states  $|r_a, r_b\rangle = |r_a\rangle \otimes |r_b\rangle$  and  $|r_s, r_t\rangle = |r_s\rangle \otimes |r_t\rangle$  (see Fig. 2.6). Note that we restrict the description to the states with the same collective parity. We thus assume that the transitions  $|r_a\rangle \rightarrow |r_s\rangle$  and  $|r_b\rangle \rightarrow |r_t\rangle$  are dipole allowed. We do not specify here the exact form of the atomic wavefunctions, keeping the form  $|r_i\rangle = |n_i l_i j_i m_{j_i}\rangle$  throughout this section. The dipole-dipole matrix elements can be described as  $U(r) = \langle r_s, r_t | \hat{V}_{dd} | r_a, r_b \rangle = \frac{C^3}{R^3}$  [138, 144]. Note that the detailed algorithm for calculating the wave functions and matrix elements of alkali atoms will be given in Appendix A.

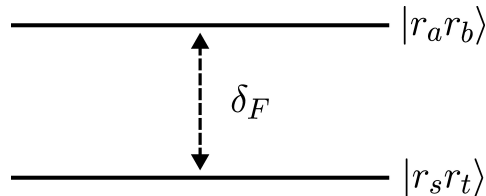


**Figure 2.6 :** Two-level representation of collective atomic states. Here  $|r_a\rangle$  and  $|r_s\rangle$  denote the state of the first atom, while  $|r_b\rangle$  and  $|r_t\rangle$  represent the states of the second atom. Thus, collective states are described as tensor products of the relevant single-atom states.

The Hamiltonian of a two - level system in the collective state basis can be presented as

$$\begin{pmatrix} 0 & U(r) \\ U(r) & \delta_F \end{pmatrix} \quad (2.60)$$

with the corresponding eigenvalues

$$\lambda_{1,2} = \frac{1}{2} \left( \delta_F \pm \sqrt{\delta_F^2 + 4U^2} \right) \quad (2.61)$$

Here we took the energy of the initial state  $|r_a, r_b\rangle$  as a reference. The energy difference between two basis states is  $\delta_F = E_{r_a, r_b} - E_{r_s, r_t}$ . This difference is called Förster defect.

The ratio between the interaction force expressed by the matrix element  $U(r)$  and the Förster defect  $\delta_F$  determines the behavior of the system. So, if the collective atomic levels are strongly isolated, and the Förster defect is large compared to the interaction potential  $\delta_F \gg U(r)$ , we can represent the Hamiltonian eigenvalues as

$$\begin{aligned} \lambda_{1,2} &= \frac{1}{2} \left( \delta_F \pm \delta_F \sqrt{1 + \frac{4U^2}{\delta_F^2}} \right) \approx \frac{1}{2} \left( \delta_F \pm \delta_F \left( 1 + \frac{2U^2}{\delta_F^2} \right) \right) \\ \lambda_1 &= \delta_F + \frac{U^2}{\delta_F} \\ \lambda_2 &= -\frac{U^2}{\delta_F} \end{aligned} \quad (2.62)$$

Thus, the collective state energy depend on the interatomic distance as  $\sim 1/R^6$ . This interaction regime is called the van der Waals regime, and we often refer to it as “off-resonant interaction”. The induced dipole-dipole interaction in this case can be obtained in the second order of perturbation theory. This effect is easily understood from a simple reasoning within the framework of classical electrodynamics. In this case, we consider the interaction to be small compared to the energy difference in the spectrum  $\delta_F$ . This means that the electric field created by the oscillating atomic dipole  $\hat{d}_{1(2)}$  did not have sufficient force to mix the energy levels of atom 2(1) with different values of  $l$ . Since these levels were not originally degenerated due to the presence of a quantum defect, the Stark interaction is zero in the first order of perturbation theory. Thus, the interaction force will depend on the square of the dipole matrix element  $\left| \langle r_s, r_t | \hat{V}_{dd} | r_a, r_b \rangle \right|^2$ , and, therefore, will be inversely proportional to the sixth power of the interatomic distance ( $R^{-6}$ ) [145].

Van der Waals regime is widely used to implement quantum gates in atomic registers. In particular, van der Waals interactions induce the dipole blockade effect, which does not allow more than one atom to be excited into the Rydberg state within a small volume. The implementation of quantum gates in Rydberg systems will be discussed in Subsection 2.3.3.

Consider the case of the strong interatomic interaction (or, equivalently, of small detuning)  $\delta_F \ll U(r)$ . The Hamiltonian eigenvalues thus are  $\lambda_{1,2} \simeq \pm U$ , providing the system with a strong interaction  $\sim 1/R^3$ . In this case, the quantum levels are quasi-degenerate, which means that the energy of the dipole-dipole interaction is calculated in the first order of perturbation theory. In the case of complete degeneracy  $\delta_F = 0$ , a resonant interaction occurs, which is called the Förster resonance.

Since the interaction energy depends on the interatomic distance, we can describe at which distance the exchange from the van der Waals interaction to the Förster interaction occurs. The transition between two different regimes of interaction arises when  $\delta_F \approx U(r)$ . Thus, the transition distance, which we will call the crossover radius  $R_c$ , is equal to [137]

$$R_c = \sqrt[3]{\frac{C_3}{\delta_F}} \quad (2.63)$$

Note that in addition to the dipole interaction, the quadrupole-quadrupole interaction for atoms with a non-zero momentum also persists [145]. It scales as  $1/R^5$ , so even though its strength is very small, it becomes comparable to the van der Waals interaction for long distances. However, for a typical distance of  $\sim 10$  microns considered in this manuscript, these effects remain negligible. We also do not take into account any dipole-quadrupole interactions, due to the same reasoning [147, 148].

Finally, it is useful to estimate how the strength of the interaction depends on the principal quantum number for each of the modes. In the case of van der Waals interactions, the second order of perturbation theory gives  $\lambda \sim \frac{U}{\delta_F} \sim \frac{((\hat{d}_1 \hat{d}_2))^2}{\delta_F}$ , where  $d_i \sim \nu^2$  and  $\delta_F \sim \nu^{-3}$ . Thus, the interaction strength scales as  $\nu^{11}$ ! This abnormally fast growth makes it possible to multiply the van der Waals interaction, and partially compensates for its drastic decay with distance.

For the Förster interaction, the same reasoning gives  $\lambda \sim U \sim \nu^4$ . We thus see that the strength of the Förster resonance is much less dependent on the principal quantum number than the strength of the van der Waals interaction.

## 2.2.5. Förster resonance

### 2.2.5.1. General properties

Dipole-dipole interaction, which we described in the previous section, can lead to non-radiative transitions between collective states of various quantum systems. In this section, we will consider strong dipole-dipole interactions, provided that the energy separation of collective levels is much less than the interaction energy of the system elements. Transitions caused by such interactions are called FRET, an abbreviation for fluorescence resonant energy transfer, or Förster resonant energy transfer [140]. The initial recorded instances of this phenomenon can be traced back to 1922 [149], when it was observed during the dissociation of hydrogen with mercury. It was discovered that the transfer of energy occurred through dipole-dipole coupling between the particles, and Theodor Förster was the pioneer in devising an effective theoretical approach [150]. Interactions of this kind have also been widely studied in biology when describ-

ing non-radiative transport between isolated chromophores. Presently, FRET is widely applied, particularly in molecular biology as a spectroscopic method [151]. One such application involves the use of quantum dots for investigating biomolecular interactions [152].

Förster resonances can significantly enhance the interaction, and make it possible to create quantum entanglement between isolated atoms. This is a priority for the implementation of quantum gates in neutral-atom-based register. In this thesis, we study the realization of quantum gates based on few-atom coherent Förster resonances. While the multiatom resonance model will be presented later, we focus here on the description of the simplest two-body Förster resonances in systems of two isolated atoms.

Note that non-radiative transfer occurs at near-field distances where the transition wavelength  $\lambda$  is much bigger than the distance between dipole-coupled systems  $R$ . For the typical atomic ensemble separation of  $\sim 10 \mu\text{m}$ , one thus assumes a possibility of FRET for the transition frequencies  $\omega < 10 \text{ THz}$ . Transitions from the ground state of an atom to the Rydberg state, in turn, require the use of high-energy radiation ( $\sim 100 - 1000 \text{ THz}$ ). Consequently, the radiation wavelengths are shorter than the distances between the atoms, which makes ground-Rydberg Förster transfer unprobable. We thus consider the Förster resonances between the Rydberg states of alkali atoms. The frequencies of such transitions are shifted to the microwave range. This places the Rydberg atoms deep into the near field limit, and makes Förster resonances possible [138].

To achieve Förster resonance, it is crucial to fulfill the condition that the Förster defect is much smaller than the interatomic interaction energy. Nevertheless, in alkali atoms, the degeneracy of collective energy levels of opposite parity is unlikely due to the presence of quantum defects. To overcome this limitation, an external influence is required to compensate for the quantum defect and enable Förster resonance.

Resonance induction can be achieved by the application of external electromagnetic field. Thus, the resonance is induced due to the Stark shift of the levels [59, 67]. If a DC field is applied, the Stark shift  $\Delta E = -\frac{1}{2}\alpha F^2$  can lead to the degeneracy of the initial and final states. Note that since we are considering the interaction of two atoms, the polarizabilities of collective states in this case will consist of the individual contributions of each atomic state. The strong dependence of the polarizabilities on the principal quantum number  $n$  leads to high requirements for the field control accuracy.

Resonances induced by microwave or radio frequency fields are also often used [153, 154]. As shown in the Appendix B, additional groups of Förster resonances could appear due to the application of external radiation, associated with the resonant Floquet sidebands.

Generally, two-body Förster resonance can be represented as a transition  $|n_1 l_1; n_2 l_2\rangle \rightarrow |n_3 l_3; n_4 l_4\rangle$ . Due to the dipolar nature of the resonant interaction, only transits with  $\Delta l = \pm 1$  are possible for each atom, leaving  $|l_1 - l_3| = |l_2 - l_4| = 1$ . The lift of magnetic sublevel degeneracy in external electromagnetic field can also provoke transition strength dependence on total momentum  $j$  and its projection  $m_j$  for both atoms.

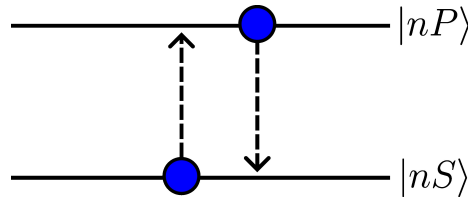
### 2.2.5.2. Experimental demonstration

Coherent electrically induced Förster resonance in Rydberg system was experimentally demonstrated in 2014 by Ravets et. al [155]. The resonance  $|dd\rangle \rightarrow \frac{|pf\rangle + |fp\rangle}{\sqrt{2}}$  was shown between two  $^{87}\text{Rb}$  Rydberg atoms, with  $|p\rangle = |61P_{1/2}, m_j = 1/2\rangle$ ,  $|d\rangle = |59D_{3/2}, m_j = 3/2\rangle$ ,  $|f\rangle = |57F_{5/2}, m_j = 5/2\rangle$ . Two individual  $^{87}\text{Rb}$  atoms were isolated at a distance of  $\sim 10$  microns from each other in microscopic optical tweezers. An external controlling constant electric field of 32 mV/cm, co-directed with the interatomic axis  $Z$ , was used to compensate for the Förster defect. Additional 3 G magnetic field, also aligned along  $Z$ , was used to split the Zeeman sublevels. Atoms were optically excited from the  $|5S_{1/2}, F = 2, m_F = 2\rangle$  Rb ground states to Rydberg  $|dd\rangle$  states by two-photon excitation technique. Avoided crossing was demonstrated by scanning of the laser detuning in the vicinity of resonance, displaying thus the predicted Förster resonance was found. High-contrast Rabi-oscillations of the collective  $|dd\rangle$  state population were demonstrated for different interatomic separation in a range of 9 – 12  $\mu\text{m}$ , showing an excellent agreement with theoretical predictions. This experiment confirmed the possibility of implementing highly coherent resonant interactions in Rydberg systems.

### 2.2.5.3. Low- $L$ Förster resonances

In this work, we consider mostly transitions between the  $S$  and  $P$  states of Rb atoms. Thus, the main types of Förster resonances under consideration can be divided into 2 categories:

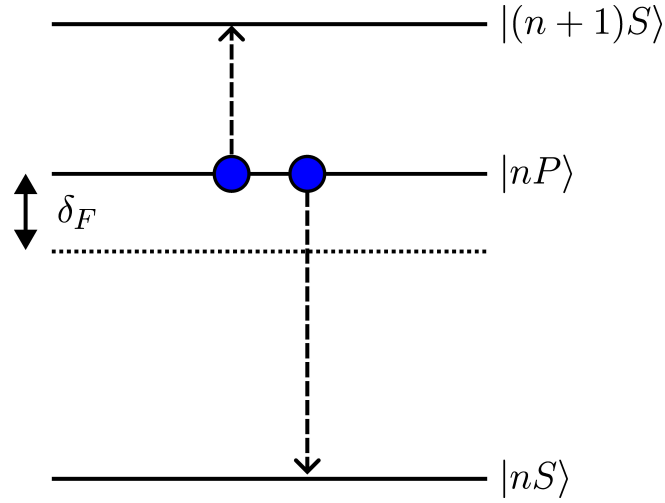
- **S-P resonant exchange**



**Figure 2.7 :** Two-body Förster resonance (2.64) diagram. Atoms pass into the final state by resonant excitation hopping.

$$|nS; nP\rangle \rightarrow |nP; nS\rangle \quad (2.64)$$

This process corresponds to the hopping of excitation between the states of atoms. We assume here that the total momentum and its projection remain unchanged for both atoms. Then the collective states have a zero quantum defect regardless of the applied external field, and therefore this resonance is always present in the system. Resonance is shown on Fig.2.7. Note that experimental demonstration of such resonances requires simultaneous excitation of various Rydberg states in a diatomic ensemble. This requires the use of a complex experimental setup with two independent laser sources.

**•2P - 2S resonant transition**


**Figure 2.8:** Two-body Förster resonance (2.65) diagram. Atoms pass into final  $S$  states by radiation-free transfer. If the Förster defect  $\delta_F = 0$ , the transfer is resonant.

$$|nP; nP\rangle \rightarrow |nS; n'S\rangle \quad (2.65)$$

By exciting atoms into the same initial states, one can also realize a resonant transition between  $nP + nP$  and  $nS + n'S$  collective states, with a concomitant change of the principal quantum number. In this case, compensation of the Förster defect is necessary, which can be obtained with the application of an external electromagnetic field. Figure 2.8 shows an illustration of such a resonance with the change of the main quantum number by one at the  $nP \rightarrow n'S$  transition. Such resonances play a key role in our study, since they are the most energetically advantageous due to the smallness of the Förster defects. In turn, the states  $n' = n \pm i$ , where  $i > 1$ , are significantly remote in the spectrum and do not make a sizable contribution to the dynamics of the atomic ensemble.

Note that the  $2P \rightarrow 2S$  resonance naturally depends also on the value of the total momentum  $j$  as well as its projection. Consider the case of a resonance induced by external DC electric field applied in the direction  $Z$ . In an unstructured atomic ensemble such field creates the quantization axis along  $Z$ , hence removing the degeneracy between the states with different projections of the magnetic moment. So, for a transition  $|nP_{3/2} |m_j\rangle^{\otimes 2} \rightarrow |nS, (n+1)S\rangle$  resonance is possible for both values of  $|m_j| = 1/2, 3/2$ . As a consequence, due to the lift of degeneracy, the resonance values of the external electric field will be different in these cases.

## 2.3. Rydberg quantum computing

We have previously reviewed the physics of Rydberg alkali atoms, as well as the basics of quantum information processing. Synthesizing the previous experience, we describe in this

section the peculiarities of Rydberg atoms application in quantum computing. We focus on the description of ordered atomic setups suitable for digital quantum computing, since these are the systems considered in the framework of this thesis. A substantial amount of information for this section was collected from [28, 60, 156].

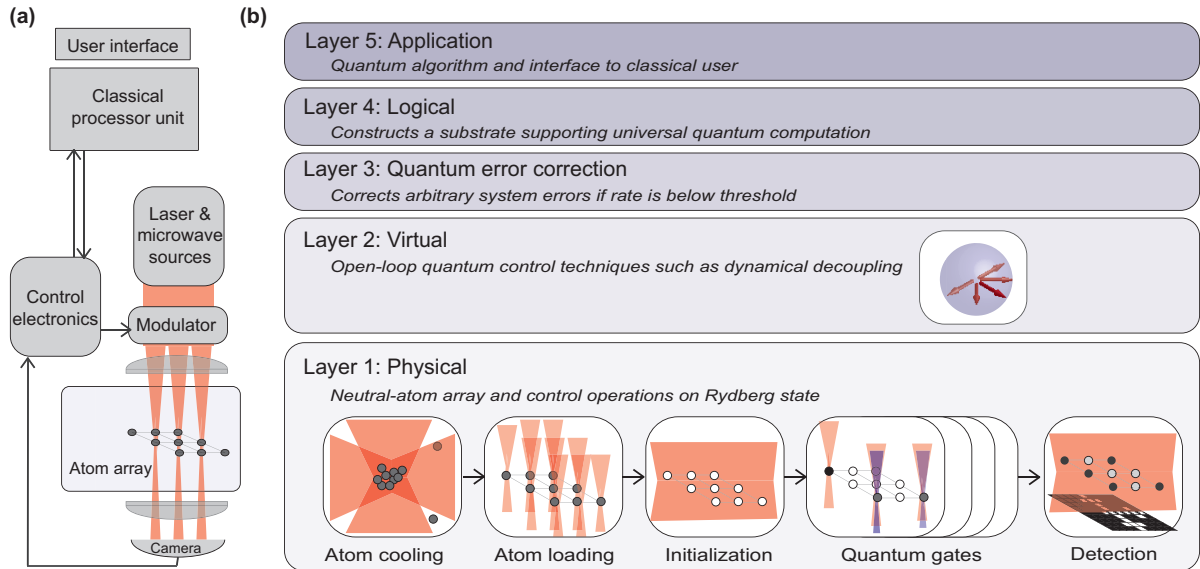


**Figure 2.9 :** Neutral atom quantum computation platform. (a) The platform consists of a classical computer and a neutral atom based quantum processor. (b) A generic outline for neutral atom quantum computation architecture (see [157]). In the physical layer, neutral atoms in the quantum processor are first cooled and captured by a magnetic optical trap (MOT) in ultra-high vacuum chamber. After subsequently loading atoms into an optical tweezer array or an optical lattice, they are initialized with optical pumping, followed by a sequence of quantum gates controlled via laser and microwave fields. In the end, quantum information is read out through fluorescence imaging. The combination of noisy physical qubits and open-loop quantum control techniques such as dynamical decoupling constructs virtual qubits with improved effective coherence time and minimized systematic gate errors, which serve as the basic building blocks for quantum-error-correction-based universal quantum computation or noisy intermediate-scale quantum applications. In the logic and QEC layer, decompositions of quantum algorithm in terms of quantum circuits, together with data processing of detection results, are processed by classical computer. The user interfaces in the application layer are also aided by classical computer. This figure was recollected from [156] along with the provided description.

Figure 2.9(a) shows the general model of the quantum computing platform considered in this study. The platform can be divided into two components - a classical computing interface and a quantum processor based on neutral atoms. The latter comprises arrays of atoms housed within a vacuum chamber, along with the necessary peripheral components for the detection and control of these atoms. These peripherals include resources such as lasers and microwave sources for manipulating the atomic states, optical and microwave modulators for fine-tuning the interactions, cameras for capturing experimental data, and the corresponding control electronics to manage and coordinate these elements.

According to the model formulated in [157], quantum computation processing is divided into 5 layers (see Fig 2.9(b)). The first layer describes the used physical system, thus neutral

atoms. Inside this layer, five important steps could be allocated, including the gas sample cooling, atom loading, register initialization, quantum processing and readout. Since we are interested in the physical implementation of quantum computing, it is the execution of the steps of the first layer that will be discussed in this chapter. Layers 2-5 refer to the process of organization of quantum computing and its practical applications. These issues are beyond the scope of the material discussed in this thesis.

### 2.3.1. Atomic ensemble preparation

The atoms are initially cooled and captured using a magneto-optical trap (MOT) within an ultra-high vacuum chamber. Then, a register of individually trapped atoms is formed. In modern quantum registers, optical tweezers are most commonly used to form atomic arrays [158]. The trap laser isolating individual atoms is divided by the spatial light modulator (SLM) into a set of highly focused spots ( $\sim 1 \mu\text{m}$  in diameter). Strong focusing allows to ensure that each of the beams (individual tweezers) contains no more than one atom in the trapping volume. This technology allows to create atomic ensembles of different architecture and dimensionality: the size of the quantum register is limited only by the trapping laser power and the capabilities of the optical system [60]. However, since the population probability of an individual tweezer is typically  $\sim 50\%$ , additional permutations may be necessary to create a defect-free quantum register. Such permutations can be accomplished using programmable moving optical tweezers controlled by a 2D acousto-optic deflector (AOD) [159]. They are superimposed on the main capturing beam using a polarizing beam splitter (PBS). During these permutations, imaging of the atomic array fluorescence is performed to determine which of the tweezers have been filled. The movement pattern is generated from the data at the external classical processor, which controls the moving tweezers by driving the 2D AOD.

### 2.3.2. Rydberg excitation

The excitation of atoms or atomic ensembles into Rydberg states occurs due to the absorption of external laser radiation. For simplicity, we consider here only the excitation of hyperfine states  $5S_{1/2}$  of Rb atoms, which will be further used as qubit states in quantum gate modeling. In this case, coherent laser radiation is used to induce dipole transitions in the individual atom inside the ensemble. Depending on the number of absorbed photons and the number of intermediate levels involved in the excitation, it can be either single-photon or multi-photon [28].

#### • Single-photon excitation

In single-photon excitation process, the ultraviolet photon induces a transition between the ground state  $|g\rangle = 5S_{1/2}$  and the Rydberg state  $|r\rangle = nP_{1/2}$  or  $|r\rangle = nP_{3/2}$  [160, 161]. Since the induced interaction is dipolar, only  $P$  states can be effectively excited in this process from the initial  $S$  state. The excitation Hamiltonian in the rotating wave approximation is of the form (2.66). The resulting AC Stark shift of the Rydberg levels due to the applied radiation should

be taken into account when setting the excitation frequency. Thus, when a  $\pi$ -pulse is applied, the transition  $|g\rangle \rightarrow e^{-i\pi/2}|r\rangle$  occurs. The same pulse could be applied to de-excite the atom from the Rydberg state back to the original ground state, with additional  $\pi$  phase accumulated during the process [28, 162].

$$H_{ex}^{1\gamma} = \frac{\hbar\Omega}{2}|r\rangle\langle g| + H.c. \quad (2.66)$$

Although the single-photon excitation scheme is simple and very robust, it has a number of significant drawbacks. Firstly, with single-photon excitation, the dipole matrix elements between the ground and excited states are extremely small [163]. This means that when the power of the laser source is limited, it can be difficult to obtain high excitation accuracy. Nevertheless, high-precision single-photon excitation of Rydberg atoms was previously demonstrated for Cs, Sr and Rb [28]. Another serious and, in general, unavoidable disadvantage of single-photon excitation is the emerging Doppler dephasing, which significantly affects the accuracy of the possible quantum gate implementations.

#### • Two-photon excitation

Compensation for the described disadvantages can be achieved by using the excitation schemes with a number of intermediate levels. When using two-photon excitation, two dipole transitions  $|5S_{1/2}\rangle \rightarrow |p\rangle = |5P_{1/2}\rangle \rightarrow |nS_{1/2}\rangle$  allow to excite the high-lying Rydberg levels. With the same approximations as for the one-photon case, the two-photon excitation Hamiltonian can be written as (2.67) [127, 131, 163, 164]:

$$H_{ex}^{2\gamma} = \hbar \left( \frac{\Omega_1}{2}|p\rangle\langle g| + \frac{\Omega_2}{2}|r\rangle\langle p| + H.c. \right) + \hbar\Delta|p\rangle\langle p| + \hbar\Delta_r^{ac}|r\rangle\langle r| + \hbar\Delta_g^{ac}|g\rangle\langle g| \quad (2.67)$$

Here,  $\Omega_{1(2)}$  represent the Rabi frequencies for the  $5S \rightarrow 5P$  and  $5P \rightarrow nS$  transitions, respectively, and  $\Delta$  is the frequency mismatch between the laser fields and the atomic transition.  $\Delta_{r(g)}^{ac}$  are the AC Stark shift caused energy defects for the ground and Rydberg states, respectively. Normally, one chose a  $\Delta$  to be large to avoid possible losses due to the intermediate level decay [165]. When the  $\Delta$  is large compared to the decay rate of the intermediate  $|p\rangle$  state, it can be adiabatically eliminated, thus producing the effective Hamiltonian [28, 166]:

$$H_{ex}^{2\gamma} = \hbar \left( \frac{\Omega_{eff}}{2}|r\rangle\langle g| + H.c. \right) + \hbar\Delta_r|r\rangle\langle r| + \hbar\Delta_g|g\rangle\langle g| \quad (2.68)$$

where

$$\Delta_{r(g)} = -\Omega_{2(1)}^2/4\Delta + \Delta_{r(g)}^{ac} \quad (2.69)$$

$$\Omega_{eff} = -\Omega_1\Omega_2/(2\Delta) \quad (2.70)$$

As shown in [28], resonant conditions with  $\Delta_r = \Delta_g$  can be recovered. Note that due to additional complexity of the level structure in two-photon excitation case, a dephasing of the

ground state after the  $2\pi$  pulse sequence application is possible. Thus, one needs to apply specific conditions to obtain an exact  $\pi$  phase shift [163].

The two-photon excitation scheme is useful because it allows one to highly suppress Doppler dephasing. According to [167, 168], several methods of dephasing suppression exist. For example, by applying a transition between two close Rydberg states  $|r_1\rangle, |r_2\rangle$  through a low-lying intermediate level induced by  $2\eta\pi$  pulses. However, the two-photon scheme does not allow Rydberg  $P$  states to be excited. In alkali atoms, such states exhibit significantly higher lifetimes than the  $S$  and  $D$  states. At room temperature, blackbody radiation is the dominant factor in Rydberg state decay. At the same time, when using a cryostat, spontaneous emission becomes dominant, which strongly depends on the angular momentum value. For Rb atoms, the lifetimes of the Rydberg ( $n = 100$ ) states are 0.33, 0.38 and 0.32 ms for  $S$ ,  $P$  and  $D$  orbitals, respectively, at room temperature. At a temperature of 4 K, these times are 1.2, 2.1 and 0.9 ms [169], respectively. Thus, it is preferable to use Rydberg  $P$  states for quantum gates [28].

### • Three-photon excitation

The three-photon excitation scheme can be used to excite  $P$  Rydberg states by involving two intermediate energy levels of the opposite parity. According to [170], with the correct spatial configuration of the pulses, three-photon excitation allows to compensate for Doppler broadening due to atomic motion, as well as for a possible change in the momentum during excitation [28]. If the total momentum of the three exciting photons turns out to be zero, no atomic movement is observed after excitation. The spatially dependent phase change is also compensated. For the moment, three-photon excitation was effectively implemented in atomic gases, demonstrating the described effect of Doppler dephasing suppression [171].

### 2.3.3. Quantum computations

When the preparation of the register is finished, quantum computations can be performed in it. We briefly consider here some possible strategies of quantum operations implementation in atomic registers.

### • Qubit states

Hyperfine Zeeman sublevels of the atomic ground states can be used as qubit logical levels. This method of storing quantum information is convenient due to the fact that these levels provide extremely long coherence times (typically, of several seconds). Also, the energy gap between hyperfine states is  $\sim h * 10$  GHz, which is suitable for optical control of qubit states. As stated in [63], the energy splittings of the atomic qubit states are significantly larger compared to the typical interactions induced by external fields and the energy scales associated with thermal motion, which are on the order of 1 MHz. Thus, the qubits are very stable when initialized. The initialization of the proper qubit states can be achieved by dissipative optical pumping [156].

During the following theoretical studies of three-body quantum gates we use hyperfine sublevels of  $^{85}\text{Rb}$  or  $^{87}\text{Rb}$  atom ground state  $5S_{1/2}$  as qubit logical states. Thus, the typical energy gap between qubit states is  $\sim h * 6.8$  GHz. Experimental two-qubit entanglement has been

demonstrated previously for  $^{87}\text{Rb}$  in numerous experiments [47, 127, 131, 164, 172].

#### • Single-qubit operations

There are several strategies to realize single-qubit quantum operations in neutral-atom-based quantum registers. First, since qubits are usually encoded in hyperfine sublevels of ground atomic states, radiofrequency or microwave radiation can be used to realize single-qubit rotations [63, 156]. High-precision quantum gates (with errors on the order of  $\sim 10^{-5}$ ) can be realized using this strategy in small atomic ensembles [173]. However, this method is limited in the possibility of creating individually-addressed gates for closely spaced atoms. Therefore, an additional site-dependent Stark shift [174] or magnetic field gradient can be used in combination with global microwave dressing to adapt the method for utilization in large atomic registers. Alternatively, one-qubit gate schemes based on two-photon Raman transitions are used [156]. In particular, a stimulated Raman adiabatic passage can be applied, leaving the qubit in the dark state during evolution. Alternative schemes involving elimination of the intermediate level have been studied in [175, 176].

#### • Two-qubit operations

In registers of neutral atoms, multiqubit quantum operations are realized via dipole-dipole interactions. As was shown in Section 2.2.4, the high-lying Rydberg states of alkali atoms can exhibit extremely strong interactions between collective two-atom states. Thus, the induction of interaction between qubits can be realized by their Rydberg excitation.

During the last two decades, Rydberg quantum computing has developed very rapidly. A large number of quantum schemes for realizing two-qubit gates have been proposed [28, 60, 63, 177]. In particular, gate schemes have been designed based on the effects of dipole blockade [91, 163, 164, 178–180], electromagnetically induced transparency [67, 181], antiblockade [182, 183] and simultaneous Rydberg excitation [184] in weak coupling regime. An alternative approach, based on the use of Stark-tuned Förster resonances, has been proposed for the implementation of fast high-precision two-qubit quantum gates [185–187]. The increasing potential is also demonstrated for Rydberg mediated gate schemes, which exhibit the high fidelity values along with ease of experimental implementation [47, 48].

Since a complete description of the variety of Rydberg two-qubit gate schemes is beyond the scope of this thesis, we encourage the interested reader to refer to the paper [28]. It provides a full description of many different Rydberg gate schemes, and an essential part of this section is based on material collected from this publication. Nevertheless, we find it useful to show an example of a two-body gate scheme based on Förster resonance adiabatic passage.

The schemes of quantum *CNOT* and *CZ* gates proposed in [187] are shown in Figure 2.10. Two neutral atoms isolated at distance  $R$  from each other act as qubits. The logical  $|1\rangle$  states of the qubits are paired with the Rydberg  $|r\rangle$  levels. If both qubits are initialized to  $|1\rangle$  states, the excitation  $|11\rangle \rightarrow |rr\rangle$  occurs. The external electric field is then adiabatically varied, shifting the collective Rydberg levels and leading to a Förster resonance  $|rr\rangle \rightarrow |r'r''\rangle$ . By passing the resonance twice, one can achieve a deterministic phase shift suitable for realizing a *CZ* gate. In turn, the *CNOT* gate can be realized by applying two additional one-qubit rotations to the

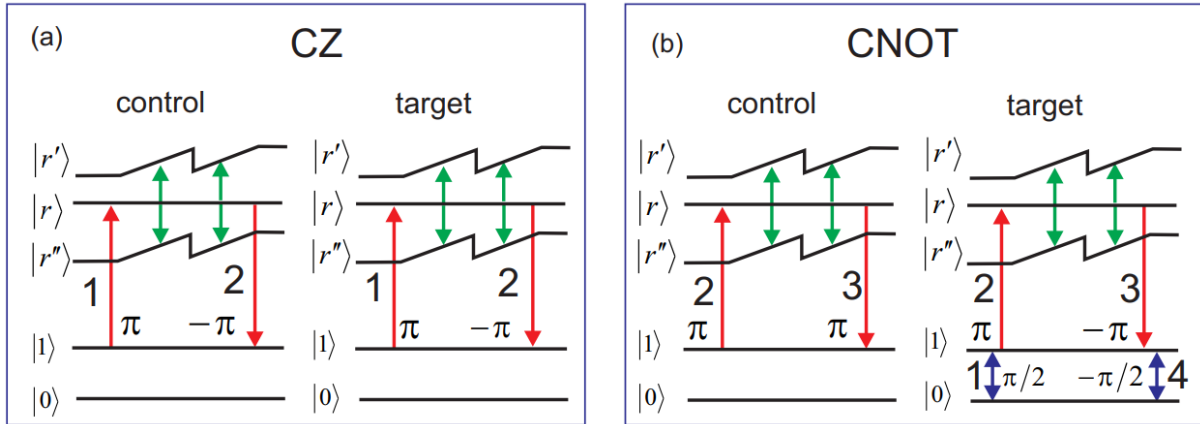


**Figure 2.10 :** (a) Scheme of a  $CZ$  gate using double adiabatic rapid passage across Stark-tuned Förster resonance. Two atoms are excited to Rydberg states. An external electric field shifts the energy levels of the Rydberg atoms so that the Förster resonance is passed adiabatically two times. Then the atoms are de-excited to ground state. The phase shift is deterministically accumulated if both atoms are initially prepared in state  $|1\rangle$ . (b) Scheme of a  $CNOT$  gate. Two additional  $\pi/2$  pulses rotate the target qubit around the y axis in the opposite directions. This figure was recollected from [187] along with the provided description.

target qubit, acting as Hadamar gates. Also, the phase of de-excitation pulse 3 was changed in order to avoid unwanted phase accumulation.

The proposed gate schemes were simulated numerically for  $90S + 96S \rightarrow 90P + 95P$  resonances in Cs Rydberg atoms. The gate fidelity of  $> 99\%$  demonstrated in the paper [187] allowed one to consider Förster resonances as promising utilities for the realization of quantum computations.

### • Three-qubit operations

The implementation of the Toffoli quantum gate in a system of neutral atoms was described by Levine et al. in [47]. The proposed implementation is based on a strong blockade of the nearest neighbors in a trimerized 1D array, accompanied by a discrete excitation phase jump between two laser pulses. The achievable gate fidelity in this case was  $F = 0.87(4)$  (after state preparation and measurement (SPAM) errors correction). Recent studies [49] propose an improvement of the described blockade gates using optimal continuum phase profiles for a single pulse instead of a phase jump [64]. This technique allowed for significant increase of three-qubit gate fidelity, up to 97.9% for parallel  $CCZ$  gates in seven atomic trimers. However, these values are far from the threshold required for the implementation of fault-tolerant quantum computing in atomic registers ( $F \geq 0.99$ ). Equally important is the fact that the quantum gates based on the Rydberg blockade effect require a sufficiently close arrangement of atoms [91]. The use of strong resonant dipole-dipole interactions is one of the promising solutions for working in large-scale registers, where it is required to implement gates between qubits spatially isolated from each other at distances of about 10 microns or more. Thus, few-body Förster resonances appear to be of interest for the implementation of three-qubit quantum gate circuits [98].

### 2.3.4. Ensemble readout

After the quantum computation is completed, the state readout is necessary to obtain information about the result of the computation [63]. Methods of readout of quantum states in atomic registers are based on detection of fluorescence of ground states. Destructive detection methods are based on squeezing atoms in a selected state out of the register and recording fluorescence of the remaining atoms [156]. This class of methods demonstrates high accuracy, but leads to the necessity to restore the register after each measurement. To compensate for this disadvantage, non-destructive methods were proposed based on state-selective fluorescence. Also, a frequently used technique applied to large registers is single-site imaging involving electron-multiplying charge-coupled-device (EMCCD) cameras, which allow successful recording with an accuracy close to 99% [188]. Postprocessing of images in this case is performed using Bayesian inference methods [156].



# Chapter 3

## Few-body Förster resonances: Early-stage studies

This chapter will present the results of early-stage studies of few-body Förster resonances in Rydberg systems conducted prior to this thesis. These results were obtained in Aime Cotton Laboratory (LAC) and in Rzhhanov Institute of Semiconductor Physics (ISP). The author of this thesis has worked in both of these institutions during the last 6 years. To the best of our knowledge, the topic of few-body resonant interactions in Rydberg ensembles had not been studied in any scientific team before. In this regard, this research, which has been going on for more than 11 years, can be considered completely original. Nevertheless, as the author was not involved in the project from the beginning, the studies conducted before 2018 can be considered preliminary to the results of the thesis. Therefore, a separate chapter is dedicated to these results, which form the theoretical basis for the research of three-body Rydberg quantum gates based on Förster resonances.

Note that although the studies of multi-particle Förster resonances conducted at LAC and ISP were pioneering by the time the project began, other groups have also made significant contributions to the study of these effects. For instance, the group led by Michael W. Noel in Bryn Mawr College has conducted a large-scale study of two-, three-, and four-particle resonances in Rb atoms. In particular, the time dynamics of resonance processes [189] and the thermalization of dipole-dipole interactions [190] were deeply investigated. However, we do not describe these studies in detail here because they are not directly related to the subject of this thesis and consider multiparticle resonances in disordered ensembles. The interested reader can refer to the original articles.

This chapter is divided into three sections corresponding to the three main stages of Förster resonances research conducted at LAC and ISP from 2012 to 2018. Specifically, Section 3.1 presents an initial proposal on the structure of the many-body Förster resonance process in Rydberg ensembles, as well as an experiment on the recording of four-body resonances in a low-density gas of Cs atoms. This study was carried out at LAC by the team of P. Pillet in 2012 [191]. Section 3.2 outlines the three-body Borromean resonances in Cs atoms recorded in the same team in 2015 [107]. An experiment on the recording of three-body resonances in small ensembles of Rb atoms [192], performed in 2017 at ISP by the team of I. Beterov and I. Ryabtsev, is described in Section 3.3. The results of numerical studies of the coherence of three-body resonances in small Rydberg ensembles are also described in this section [193].

### 3.1. Four-body Förster resonances in Cs ensembles

Investigating few-body interactions in atomic systems stands as one of the fundamental tasks of modern physics. Such studies allow one to better understand the structure of elementary physical systems, paving the way for the creation of new materials and computational models. Various few-body effects have been demonstrated over the past 20 years in such systems, including trimer photoassociation [194], Efimov physics [195–197], as well as three-body recombination leading to the formation of molecules in a trap [198, 199].

Rydberg atomic ensembles have been successfully used for the investigation of few-body effects [155, 200–202]. Since Rydberg atoms exhibit strong dipole-dipole interactions [137, 203], as well as high lifetimes in a cold sample [169], low-density Rydberg gases represent a convenient playground for studying multiparticle interactions. In this regard, the study of few-body resonance processes in ensembles of ultracold Rydberg atoms presented an important and interesting task, motivating the start of our research project.

The pioneering experiments on the observation of few-body Förster resonances were carried out in the Aime Cotton Laboratory during the last decade. Thus, in 2012, a four-body Stark induced resonance was first demonstrated in a low-density cloud of Rydberg Cs atoms in a magneto-optical trap [191]. In this section we present the results of this study. Note that we do not review all the details of the study, focusing on the parts relevant to this thesis. For a more detailed analysis see the original paper.

#### 3.1.1. Four-body resonance proposal

Before starting the discussion of many-body Förster resonances, it will be useful to briefly recall the theoretical basis for their implementation. By the time this study began, the two-atom Förster resonances described in Subsection 2.2.5 had been extensively investigated [155]. Resonance transitions require efficient compensation of the energy defects between collective states, which leads to quasi-degeneracy of energy levels. Dipole transitions between resonant states must also be allowed, which imposes constraints on their parity. This requirement, however, can be circumvented by realizing a “ladder” of dipole-resolved transitions occurring simultaneously in a multi-atomic system. Thus, the two-atom transition  $|n_1^i l_1^i, n_2^i l_2^i\rangle \rightarrow |n_1^f l_1^f, n_2^f l_2^f\rangle$ , where  $l_m^f = l_m^i \pm k$  for integer  $k$ , is replaced by a sequence of transitions  $|n_1^i l_1^i, n_2^i l_2^i\rangle \rightarrow \dots \rightarrow |n_1^a l_1^a, n_2^a l_2^a\rangle \rightarrow \dots \rightarrow |n_1^f l_1^f, n_2^f l_2^f\rangle$ , given that each of those transitions is dipole-resolved. Here, the indices  $i$  and  $f$  denote the initial and final states, respectively, while the index  $a$  denotes some intermediate state (one of many). To realize such a transit, the final and initial states of the system must also be degenerate. Thus, the sum of energy defects of all the two-body transitions involved in ladder-like transfer should tend to zero, leading to zero energy difference between initial and final states.

For many-body resonances, parallel transitions can involve different atoms, still subject to the requirement of the total energy defect negligibility. So, given a multi-atom Rydberg system with  $N$  atoms, one can describe the following many-body Förster resonant transition (3.1), composed of at least  $N - 1$  dipole-resolved two-body transitions.

### 3.1. Four-body Förster resonances in Cs ensembles

$$|n_1^i l_1^i; n_2^i l_2^i; \dots; n_N^i l_N^i\rangle \rightarrow |n_1^f l_1^f; n_2^f l_2^f; \dots; n_N^f l_N^f\rangle \quad (3.1)$$

Inspired by the idea of resonant population transfer based on parallel two-body resonances, a group of researchers led by Pierre Pillet proposed a possible scheme for the realization of a four-body resonance, and also conducted an experiment on its recording. Four-body Stark induced resonance (3.2) was studied in a low-density cloud of Rydberg caesium atoms in a magneto-optical trap for  $n = 23$ . All the results described below were originally presented in the article [191] and are given here with the permission of the authors. The notations used in the original article have been retained.

$$4 \times 23p_{3/2} \rightarrow 2 \times 23s + 23p_{1/2} + 23d_{5/2} \quad (3.2)$$

$$2 \times 23p_{3/2} \rightarrow 23s + 24s \quad (3.3)$$

$$2 \times 24s \rightarrow 23p_{1/2} + 23d_{5/2} \quad (3.4)$$

In contrast to the previously described two-body resonances, this resonance corresponds to a simultaneous change of states of four atoms. The resonance process can be described as three two-body transitions in a four-atom system occurring simultaneously. During the first stage of the transition, all four atoms pass from the initial  $23p$  state into a collective mixture of  $24s$  and  $23s$  states, as a result of two two-body non-resonant transitions (3.3) in atomic pairs. At the second stage, the atoms in the  $24s$  state undergo a transition (3.4) to the  $23p$  and  $23d$  states. Each of these individual steps does not represent a resonant transition, while the full four-body transition has a resonant character. Note that the transition (3.4) is quasi-forbidden and can occur due to mixing of  $P$  and  $D$  states in the electric field. We will discuss quasi-forbidden resonances in detail in the Subsections 4.2.2 and 4.2.3 of Chapter 4. We assume that  $|m_J| = 1/2$  for all states unless specified otherwise. For simplicity, we further indicate the states  $23s, 23p_{1/2}, 23p_{3/2}, 23d_{5/2}$  and  $24s$  as  $s', p', p, d$  and  $s$ , respectively.

Figure 3.1 shows resonance processes in a four-atom system. The Stark diagram of the atomic collective states was obtained from numerical simulations. The Stark induced collective level crossings here correspond to two-body resonances ( $a_1, a_2$ ) and a four-body resonance ( $b$ ). As can be seen, these resonances occur at slightly different electric fields. Concretely, resonance (3.3) corresponds to the controlling electric field value of 79.94 V/cm, while resonance (3.4) occurs at 80.42 V/cm. Four-body resonance (3.2) arises at its full amplitude at 79.99 V/cm electric field. Thus, if the four-body  $p \rightarrow d$  process is resonant, each of the underlying two-body processes will be characterized by a Förster defect  $\Delta E_1 = E_s + E_{s'} - 2 \times E_p$  and  $\Delta E_2 = E_d + E_{p'} - 2 \times E_{s'}$ , respectively. If  $2\Delta E_1 = -\Delta E_2$ , a resonant four-body process occurs. Note that coefficient 2 arises in the last equation, since the first two-body resonance (3.3) must occur twice in the system.

#### 3.1.2. Experimental results

The resonance recording experiment was carried out in a caesium magneto-optical trap (MOT) at a temperature of  $\sim 100$  microkelvin. Three-photon excitation  $6s \rightarrow 6p \rightarrow 7s \rightarrow nl$  was

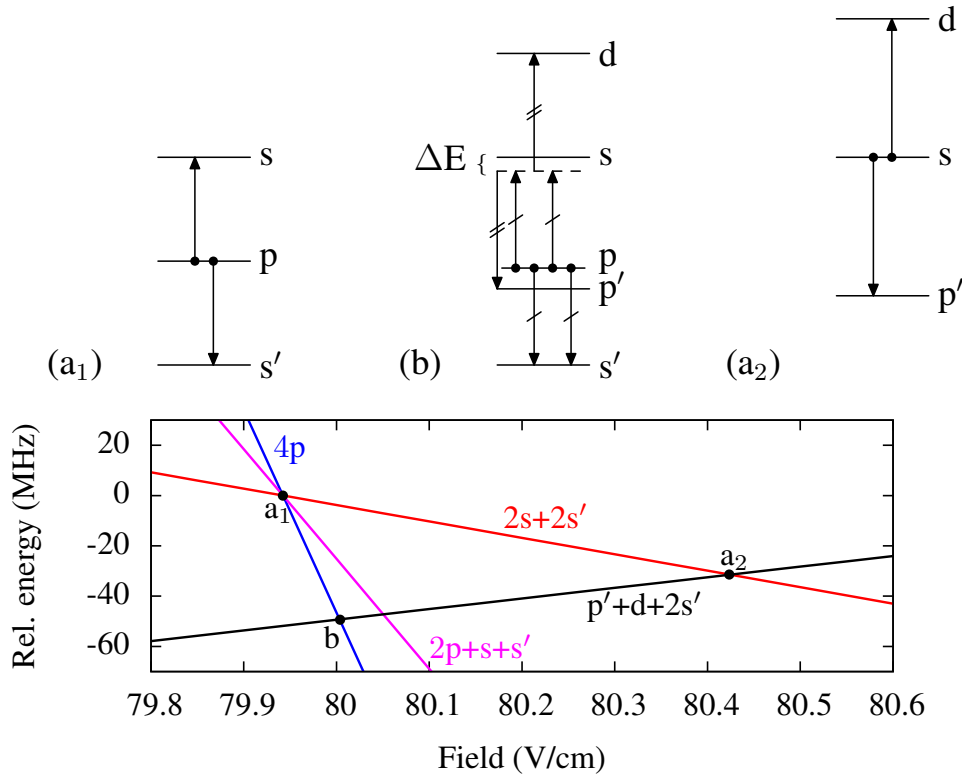


**Figure 3.1 :** Four-atom Stark diagram in the vicinity of four-body resonant transfer. Two-body resonances (3.3) and (3.4) are shown as the intersections ( $a_1$ ) and ( $a_2$ ), respectively. Intersection ( $b$ ) corresponds to four-body resonance (3.2). Transition diagrams are also presented for each case to illustrate the processes.

used to produce a low-density Rydberg gas. As a result of the excitation, a Gaussian cloud of  $\sim 2 \times 10^5$   $^{23}\text{p}$  cold Caesium atoms was produced. The cloud diameter was  $\sim 260 \mu\text{m}$ , with a peak atomic density of  $\sim 9 \times 10^9 \text{ cm}^{-3}$ . The population of Rydberg states was measured using the Selective Field Ionization method (SFI). Please see the article [191] for more detail.

The experimental results on the Förster resonance are shown in Figure 3.2. The two-body  $p \rightarrow s$  resonance (Fig. 3.2(a)) is observed at 79.94 V/cm. The flat top of the resonance suggests that the transition is saturated. Similar behavior is also observed for the  $s \rightarrow d$  resonance at 80.42 V/cm (Fig. 3.2(b)). Note that the observed saturation demonstrate that the interatomic interaction is sufficiently strong even for low-density gaseous sample.

The four-body  $p \rightarrow d$  resonant transition is observed at an electric field value of 79.99 V/cm. The detection of population in the  $d$  state serves as a distinct indicator of an interaction involving a minimum of four atoms. The pronounced evidence that this process is not a mere combination of two sequential 2-body processes, but rather an authentic 4-body phenomenon, is discernible from the relative strengths of the  $d$  transfer at the 4-body resonance field during initial excitation of either the  $p$  or  $s$  state.

In order to compare the obtained data with the theoretical calculation, numerical simulations of the resonances were performed. The  $p \rightarrow d$  resonance was modeled between four

### 3.1. Four-body Förster resonances in Cs ensembles

atoms arranged equidistantly, choosing arbitrarily a tetrahedron shape in three-dimensional space. The numerical model included two-body dipole-dipole interactions between  $|pppp\rangle$ ,  $|ss'pp\rangle$ ,  $|ss'ss'\rangle$ , and  $|ds'p's'\rangle$  states in an external electric field. The ultimate distributions, presented in Figure 3.2 as the blue dashed curves, are derived through calculations utilizing the density matrix in conjunction with the experimental peak density and field inhomogeneity.

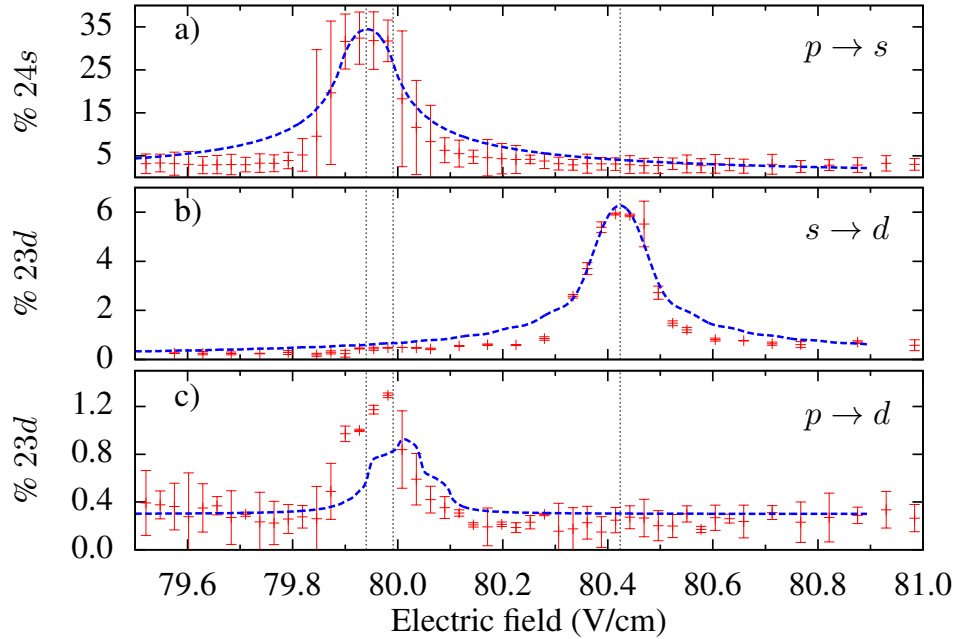


**Figure 3.2:** Number of detected Rydberg atoms as a function of applied electric field. (a) Percentage of detected  $s$  atoms when exciting the  $p$  state. (b) Percentage of  $d$  detected when exciting the  $s$  state. (c) Percentage of  $d$  detected when exciting the  $p$  state. The results of presented calculation for four equidistant atoms are overlaid as dashed blue lines, with the  $p \rightarrow s$  calculation amplified by a factor of two and the  $s \rightarrow d$  divided by a factor of three to coincide with experimental results. The three resonant field values are illustrated by the vertical dotted lines.

#### 3.1.3. Conclusion

This study has experimentally confirmed for the first time the existence of many-body resonant processes in ultracold atomic ensembles. While two-body Förster resonances have been widely known and investigated in various research groups, multi-particle resonance effects have not been studied. At the same time, such effects can have a significant influence on the spectra of Rydberg systems. The theoretical model proposed in this study has offered an explanation for multiparticle resonance transitions, paving the way for further research.

According to the authors conclusion, many-body Förster resonances are of exceptional interest for the implementation of quantum computations in ordered atomic registers, due to wide possibilities of interaction control presented by Stark-induced resonant processes. In particular, multiparticle resonant transitions have a high potential to realize multiqubit quantum

gates and also can be used to create multi-atom entangled states. In this regard, additional work has been carried out to further investigate few-body resonances in Rydberg gases. In the subsequent sections of this chapter, we will describe few-body resonance studies inspired by this pioneering research.

## 3.2. Borromean Förster resonances in Cs ensembles

The successful experimental demonstration of four-atom Förster resonances carried out by the group of P. Pillet in 2012 has aroused great interest from the scientific community due to their potential use for the creation of quantum entanglement in large-scale quantum registers of individual cold atoms. However, such resonances are weakly pronounced, and obtaining high-contrast coherent interactions between individual isolated atoms would be challenging.

Of particular interest to the ultracold atom physics community are the so-called Borromean interactions in three-atom systems [204, 205]. The Borromean character of the interaction consists in the predominance of three-atom effects over two-atom effects, which in the ideal case are negligibly small. Such interactions potentially allow the creation of quantum entanglement between three atoms, and hence can be used to realize three-qubit quantum gates such as Toffoli and  $CNOT^2$  gates [92].

The interaction enhancement provided by the Förster resonance presents an ideal opportunity to realize Borromean interactions. In this regard, an experiment was performed in the Aime Cotton Laboratory to record such resonances in a cold gas of cesium atoms in 2015 [107].

### 3.2.1. Three-body Förster resonance

The three-body resonance scheme presented in this study is based on two consecutive Stark-induced two-body transitions (3.5) and (3.6):

$$2 \times nP_{3/2} \rightarrow nS_{1/2} + (n+1)S_{1/2} \quad (3.5)$$

$$nP_{3/2}(|m| = 3/2) + (n+1)S_{1/2} \rightarrow (n+1)S_{1/2} + nP_{3/2}(|m| = 1/2) \quad (3.6)$$

$$nP_{3/2}(|m| = 1/2) + nP_{3/2}(|m| = 3/2) \rightarrow nS_{1/2} + (n+1)S_{1/2} \quad (3.7)$$

Process (3.5) presents a widely studied two-body transition, shown in detail in the previous section as a part of 4-body resonant transfer. In alkali atoms such resonances are possible for projections  $|m_J| = 1/2, 3/2$  of the initial  $nP_{3/2}$  states. This transition is depicted on Figure 3.3(c). Since the degeneracy of collective levels with different momentum projections is removed in the presence of the external electric field due to the Stark effect, an energy defect  $\delta_{pp'} = E_{p'} - E_p$  of a few tens of MHz arises between the states  $p = nP_{3/2}(|m_J| = 1/2)$  and  $p' = nP_{3/2}(|m_J| = 3/2)$ . Nevertheless, the magnitude of the defect is significantly smaller than the Förster defects of the possible resonances, which thus remain grouped at close resonant fields. To follow the original article descriptions, we denote the energy defect constants as a half of corresponding Förster defect for each two-body resonance:  $\Delta_p = \frac{E_s + E_{s'} - 2E_p}{2}$  and  $\Delta_{p'} = \frac{E_s + E_{s'} - 2E_{p'}}{2}$ , where  $s = nS_{1/2}$ ,



direct two-body Förster resonance energy transfer (FRET) connecting the donor and the acceptor. Thus, the presented arrangement culminates in a Borromean three-body energy transfer process! The Borromean character of the interaction is guaranteed by the resonant behaviour of the three-body transfer, which prevails over all two-body transitions at the resonance value of the electric field  $F_{res}$ .

$$3p \rightarrow s + s' + p \rightarrow s + p' + s' \quad (3.8)$$

$$3p' \rightarrow p' + s + s' \rightarrow s + p + s' \quad (3.9)$$

Figures 3.3(a) and 3.3(b) show schemes of three-body resonances for the cases when the initial states  $3 \times p$  and  $3 \times p'$  are excited, respectively. Such resonances are described by expressions (3.8) and (3.9). For transition (3.8) the first two-body interaction has the detuning  $\Delta_1 = 2\Delta_p = -\delta_{pp'}$ , while the  $S - P$  hopping detuning is  $\Delta_2 = \delta_{pp'}$ . Thus, these detunings completely compensate each other, leading to the resonance condition  $\Delta_p = -\delta_{pp'}/2$ . Similarly, for transition (3.9), the resonance condition  $\Delta_{p'} = \delta_{pp'}/2$  is presented.

### 3.2.2. Experimental results

The same experimental setup was used as for the demonstration of four-atom resonances described in the previous section. Resonances were recorded in a cesium magneto-optical trap. With three-photon excitation, about  $10^5$  Rydberg atoms were generated in an excitation volume with  $\sim 300 \mu\text{m}$  diameter. The typical Rydberg atom density in the MOT was  $\sim 5 \times 10^9$  atoms  $\text{cm}^{-3}$  during the experiment. For more detail on the experimental implementation, please see the original paper [107].

Figure 3.4 shows the results of Förster resonance recording as the dependence of  $ss'$  transfer rate from the applied field. The transfer rate is defined as  $R_{ss'} = \frac{N_s + N_{s'}}{\sum_k N_k}$ , where  $N_s$  is the  $s$ -state population obtained from the experiment. The  $3p \rightarrow s + s' + p'$  resonance (I, Fig. 3.4(a)) is recorded in a field of 3.17 V/cm, on the slope of the two-body resonance  $2p \rightarrow s + s'$  (II), which reaches a maximum at 3.30 V/cm. Good agreement with the theoretical values (3.15 V/cm and 3.28 V/cm) obtained from the numerical calculations [107] is observed. Similar results obtained for resonances  $3p' \rightarrow s + s' + p$  (I') and  $2p' \rightarrow s + s'$  (II') are shown in Figure 3.4(b). The resonances are observed at fields of 3.80 V/cm and 3.60 V/cm, respectively.

The introduction of varying delays in Figure 3.4 allows one to estimate the temporal evolution of the transfer process. Considering the experimental atomic density of approximately  $5 \times 10^9$  atoms per  $\text{cm}^3$ , the anticipated maximum for the two-body FRET coupling, denoted as  $V_{dip}$ , is around 15 MHz for the average interatomic distance of  $3 \mu\text{m}$ . This transfer becomes completely saturated at the shortest delays. However, for the case of  $\delta_{pp'} = 70$  MHz (for FRET I) the three-body interaction coupling is anticipated to be around 3 MHz for the same interatomic distance, much smaller than for two-body case. The same decrease is observed for the resonance I', when  $\delta_{pp'} = 95$  MHz, leaving the corresponding coupling of 2 MHz. Consequently, one observe temporal evolution at the shortest delays. Nevertheless, the pronounced dependence of the three-body interaction on interatomic distances along with the stochastic distribution of

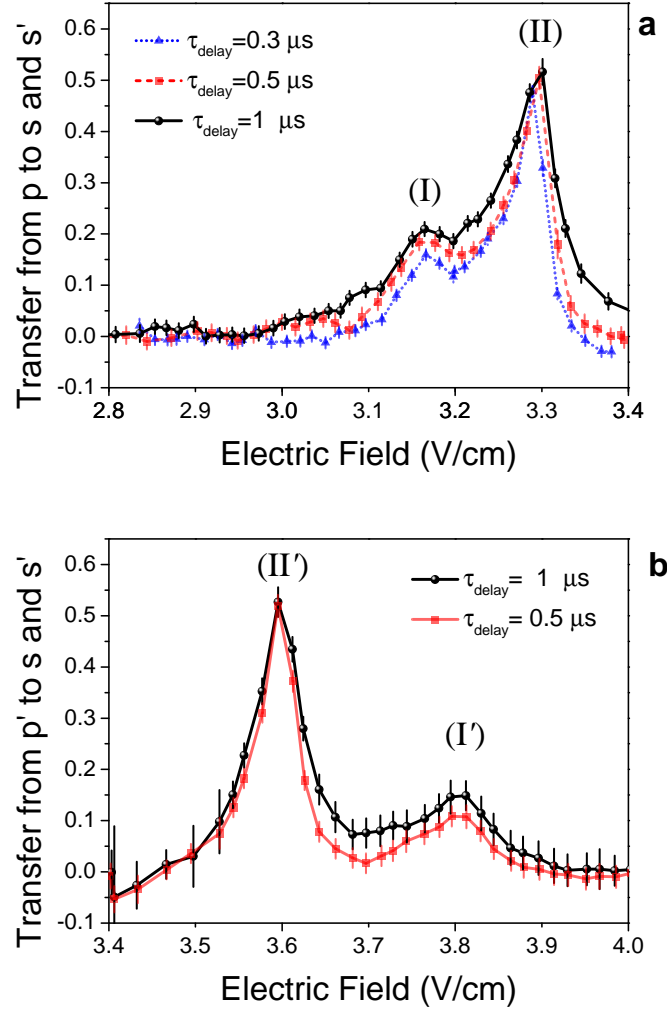


**Figure 3.4 :** Averaged transfer ratio  $R_{ss'}$  from the initial  $p$  state (a) or  $p'$  state (b) to  $s + s'$  states for  $n = 35$  at different  $\tau_{\text{delay}}$  versus the electric field. In (a), the resonance at around 3.3 V/cm is attributed to the two-body FRET (3.5) (denoted as II) while the resonance at around 3.17 V/cm is attributed to the three-body FRET (3.8) (denoted as I). In (b), the resonances are attributed to two-body (3.5) (II') and three-body (3.9) (I') transfers. Each point corresponds to the average of 50 – 150 individual measurements. The error bars correspond to the sum of the s. e. m. and the estimated error in the state discrimination.

Rydberg atoms within the gaseous sample, hinders any coherent oscillatory dynamics in these experiments.

Note that for two-atom resonances the transfer saturation limit is expected to be 50% in an approximate model of independant pairs, due to the random arrangement of Rydberg atoms in the gas sample. The random arrangement leads to a statistical mixture between  $pp$  and  $ss'$  two-atom states. For the same reason, the expected amplitude of three-body resonances is 33% for a statistical mixture of initial and final states. Nevertheless, this threshold is not

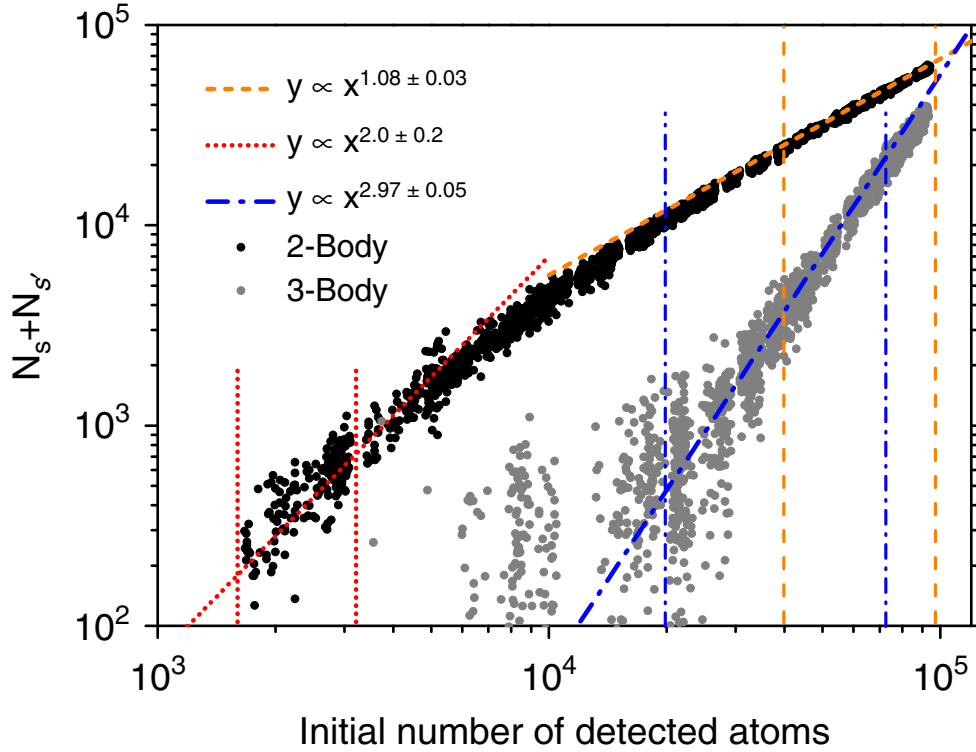


**Figure 3.5 :** Sum of detected atoms in  $s$  and  $s'$  states,  $N_s + N_{s'}$  versus the initial  $35p'$  Rydberg atoms density for a transfer time of  $\tau_{delay} = 0.5 \mu\text{s}$  at a fixed electric field of  $3.60 \text{ V/cm}$  for the two-body FRET (black dots) in bi-logarithmic scale. Two fits check the quadratic behaviour in the low density regime (red dotted line) and the linear saturation in the high-density regime (orange dashed line). A second set of data are taken at  $3.80 \text{ V/cm}$  for the three-body FRET (grey dots) and a fit checks the expected cubic behaviour (blue dotted dashed line). The result and the standard error of each fit is presented in the legend. The data range used for each fit is demarcated by couples of vertical lines with corresponding colour and style.

reached in this experiment, which may be due to both experimental measurement uncertainty and the proximity of the two-atom resonance leading to additional phase dynamics. Thus, the resonance I reaches a maximum amplitude of 21%, while the resonance amplitude of I' is 15%.

Additional confirmation of the correct identification of two- and three-atom peaks was obtained by estimating the dependence of the transfer on the initial density of the Rydberg gas. According to [107, 191], in the low-density limit, the  $N$ -partial process will exhibit dynamics proportional to the  $N^{th}$  power of the initial density. Nevertheless, with an increase in density, the transfer reaches saturation at a certain moment, provided that the maximum peak intensity is reached under experimental conditions.

As shown on Fig.3.4, the peaks I' and II' are highly resolved and the resonance crosstalk is minimized. Thus, for this study the  $p'$  initial state was selected with the transfer time of  $\tau_{delay} = 0.5 \mu\text{s}$ . By varying the Rydberg atom density through adjustments in the duration of the Rydberg excitation pulse, the data depicted on Fig.3.5 was obtained. This figure shows the resulting count of transferred atoms against the initial number of Rydberg atoms, both for the two-body

## 3.2. Borromean Förster resonances in Cs ensembles

FRET at 3.60 V/cm and for the three-body FRET at 3.80 V/cm.

In the case of the two-body FRET, the anticipated quadratic behaviour was observed at the lowest densities, followed by rapid saturation at moderate densities. Once the 50% transfer limit is achieved, a linear dependence emerges. Remarkably, this saturation transpires at a density of about  $5 \times 10^8$  atoms per  $\text{cm}^3$ . This density corresponds to a coupling strength of around 1.5 MHz at a 3  $\mu\text{m}$  distance, which is consistent with the employed delay of  $\tau_{\text{delay}} = 500$  ns.

On the other hand, the cubic relationship between the transferred population and the density for the three-body FRET signals validates the previously described resonant picture. The estimated interaction strength reached approximately 3 MHz at the highest density. Thus, the saturation is observed when the transfer reaches approximately 25%. This value is close to the anticipated maximum of 33% for this particular case.

Note that the proposed resonant scheme also admits generalization to a larger number of atoms. The many-body Borromean Förster resonances in this case require several relay atoms and could be reflected as a sequence of two-body transitions in a many-atom system. The general scheme of such a resonance can be represented as

$$(2N + M)p \rightarrow Ns + Ns' + Mp' \quad (3.10)$$

Here,  $2N$  atoms transfer to the corresponding  $S$  states via two-body non-resonant transfers, while  $M$  relay atoms compensate for the resonance defect. If the condition of energy defect compensation (3.11) is satisfied, the final transfer is resonant. Note that in [107], four- and five-atom resonances of the form (3.10) were also demonstrated. Nevertheless, their description is beyond the scope of this thesis.

$$\Delta_p = \frac{-M}{2N} \delta_{pp'} \quad (3.11)$$

### 3.2.3. Conclusion

In the presented research, new types of many-body resonant Förster transitions have been demonstrated. Such resonances offer a wide range of possibilities for controlling interactions in atomic systems and can potentially serve to realize quantum entanglement in multi-atomic registers. Borromean three-atom transitions, which are the central topic of this study, have been demonstrated for different values of the principal quantum number  $n$ , indirectly confirming the general nature of the resonance transfer. Three-body FRET could thus be used to realize three-body quantum gate schemes (specifically, Toffoli and  $CNOT^2$  gates) through the creation of quantum entangled triplet states. Additionally, controlled SWAP gates producing state transfer between atoms can also be realized by  $sp's' \rightarrow ppp \rightarrow s'p's$  transitions. When the transition is resonant, the exchange between the  $s$  states takes place. Thus, by controlling the external electric field, a controlled exchange operation could be realized. Also, it should be noted that heralded entanglement can be realized using a three-body FRET. In such a case, the relay atom could serve as an indicator, via its detection in the new  $p$  or  $p'$  state, of the states entanglement of the other two atoms.

The high potential of multi-particle Förster resonances for Rydberg quantum informatics has attracted considerable interest from the scientific community. In this regard, the studies of many-body resonance interactions have been continued. The following section describes results on the study of such resonance transitions in ensembles of Rb atoms carried out collaboratively at LAC and ISP.

### 3.3. Three-body Förster resonances in Rb ensembles

Experiments carried out at Aime Cotton Laboratory clearly showed the presence of multi-particle resonant processes in the spectra of low-density Rydberg gases. Demonstrated resonances involved 2 – 5 Cs atoms, thus allowed one to suggest the possibility that multi-qubit quantum gates can be realized based on Förster transitions [191]. Nevertheless, a number of important questions about the nature of resonance transitions in atomic systems required additional investigation.

First, the question was raised whether such resonances exist for arbitrary alkali Rydberg atoms. Previous studies had been carried out using solely Cs gas as an active environment for limited range of  $n$  values. Although the analogy between the physics of different alkali Rydberg systems is obvious, experimental confirmation of the presence of many-body resonances for other atomic species was required. Of particular interest was the search for such resonances in rubidium isotopes  $^{85}\text{Rb}$  and  $^{87}\text{Rb}$ , which are often used for neutral-atom-based quantum computing implementations [22, 59, 67].

Second, it was desirable to develop an analytical model for the three-atom resonances demonstrated in the previous section [107]. Such resonances can be represented as several parallel two-body transitions occurring in a system of three Rydberg atoms. The relative ease of the theoretical analysis of the three-level quantum system problems allowed one to hope that the analytical description of resonances is possible, taking into account certain approximations.

Third, the development of a numerical model for the simulation of multiparticle Förster resonances was of great interest. For the exact calculation of the resonance peaks shapes, as well as the prediction of possible resonant processes, it was necessary to take into account the Zeeman sublevels of each individual atom in the system, together with the losses associated with blackbody radiation and spontaneous decay of Rydberg states. Similar models have been presented earlier for two-body Förster interactions in [185, 206, 207] and [186].

Fourth, the possibility of coherent Förster transitions in atomic ensembles required confirmation. Previously, no coherent resonant dynamics had been demonstrated, due to the Rabi oscillations washout caused by the atomic dynamics randomness in Rydberg gas samples. Nevertheless, coherent transitions are necessary to precisely control the collective states of the atomic quantum register, and hence to realize quantum gates in it. Thus, it was necessary to numerically investigate resonance interactions in a structured Rydberg ensemble to demonstrate coherent interactions. The study of the properties of these interactions also became an important task.

To address these questions, the study of three-body Förster resonances was initiated in

Laboratory №32 of the Institute of Semiconductor Physics in Novosibirsk under the direction of I. Ryabtsev and I. Beterov. The research was conducted in collaboration with the Aime Cotton Laboratory, relying on the vast expertise acquired by P. Cheinet in P. Pillet's group. In this section, we present the results of these studies, which were published in [192] and [193]. It should be noted that although the author of this thesis was an employee at ISP SB RAS at the time of publication, he did not take any participation in the research process. Nevertheless, the numerical model developed in this study was further adapted for the Rydberg quantum gates studies conducted by the author, as will be presented in the next chapter.

#### 3.3.1. Three-body resonance scheme

Multiparticle resonant interactions recording in the Rydberg system was reported at ISP SB RAS in 2017 [192]. Three-body Borromean resonances (3.12) for  $n = 36, 37$  were chosen as the object of study. They are analogous to resonance transitions that were previously experimentally demonstrated in LAC [107], and are of great interest for the implementation of quantum simulations and multiqubit quantum gates in Rydberg registers [19, 59, 177, 202, 208–217].

$$3 \times nP_{3/2}(|M|) \rightarrow nS_{1/2} + (n + 1)S_{1/2} + nP_{3/2}(|M^*|) \quad (3.12)$$

Note that the notations used in this section correspond to those used in the original article. Thus,  $M$  denotes here the momentum projection of an individual atom (unless specified otherwise), while in the main text of this thesis it represents the total momentum projection of the collective state.

Several qualitative differences from previous experiments made the results of this study particularly valuable. First, transitions were demonstrated between cold  $^{85}\text{Rb}$  atoms, thus confirming the universality of the model of multiparticle resonances presented earlier. Second, during the experiment, a small number of atoms ( $N = 1 - 5$ ) were excited into Rydberg states, thereby allowing a clear demonstration of the absence of three-body interactions in systems containing less than three atoms. This fact was an additional confirmation of the conclusions about the three-body nature of demonstrated resonances made in [107].

Figure 3.6 shows the numerically calculated Stark structure of the atomic collective states exhibiting Förster resonant transitions. Note that interatomic interactions have not been taken into account within the numerical model used to calculate the Stark map. In this regard, level crossings are shown in Fig.3.6 instead of anti-crossings. Nevertheless, this model still gives sufficiently accurate predictions of resonant electric fields and can also be used to determine the polarizabilities of collective states by numerical approximation of individual energy levels.

Here, each of the enumerated line crossings corresponds to a Förster resonance. Thus, crossings 2-7 represent the two-body resonant transfers  $2 \times nP_{3/2} \rightarrow nS_{1/2} + (n + 1)S_{1/2}$ , which leave the state of the third  $P$  atom unchanged throughout the process. As shown in the Subsection 3.2.1, such processes are also major components of the three-body resonance transfer. In the following, we will re-discuss the peculiarities of such transitions when describing the analytical and numerical models of resonances developed in the course of this study.

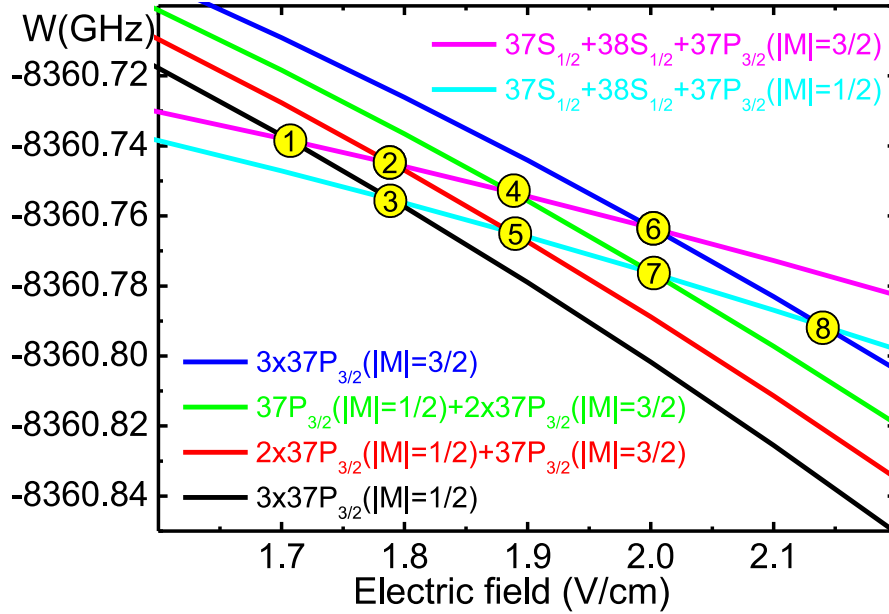


**Figure 3.6 :** Numerically calculated Stark structure of the Förster resonance  $3 \times 37P_{3/2} \rightarrow 37S_{1/2} + 38S_{1/2} + 37P_{3/2}^*$  for three Rb Rydberg atoms. The energies  $W$  of various three-body collective states are shown versus the controlling electric field. Intersections between collective states (labeled by numbers) correspond to the Förster resonances of various kinds. Intersections 2-7 are, in fact, two-body resonances that do not require the third atom. The intersections 1 and 8 are three-body resonances occurring only in the presence of the third atom that carries away an energy excess preventing the two-body resonance.

Intersections 1 and 8 represent three-body Förster resonances (3.12). They are characterized by a simultaneous change of states of all three atoms, which confirms their Borromean nature [107]. The third atom acts as a relay and serves to provide a dipole-dipole population transfer. It also compensates the Förster defect of non-resonant two-body processes, as described in Subsection 3.1.1.

### 3.3.2. Experimental results

The experimental setup used in this study to register Förster resonances had significant similarities to the one used in previous studies [107, 191]. A sparse gas of  $^{85}\text{Rb}$  atoms was confined in a magneto-optical trap discussed in [208, 218]. The magneto-optical trap was placed between two stainless steel plates used to apply external electric field. Note that a non-zero DC electric field was applied during the whole experimental sequence and was switched to the resonant field to activate the Förster resonant transfer. A Stark-switching technique used in this study is described in [207, 219]. Three-photon laser excitation was utilized to put atoms into Rydberg states according to the following scheme:  $5S_{1/2} \rightarrow 5P_{3/2} \rightarrow 6S_{1/2} \rightarrow nP_{3/2}$  [207, 208]. Thus, in a small excitation volume ( $\sim 15 \mu\text{m}$  in size), several Rydberg atoms ( $N = 1 - 5$ ) were obtained at each experimental cycle.

### 3.3. Three-body Förster resonances in Rb ensembles

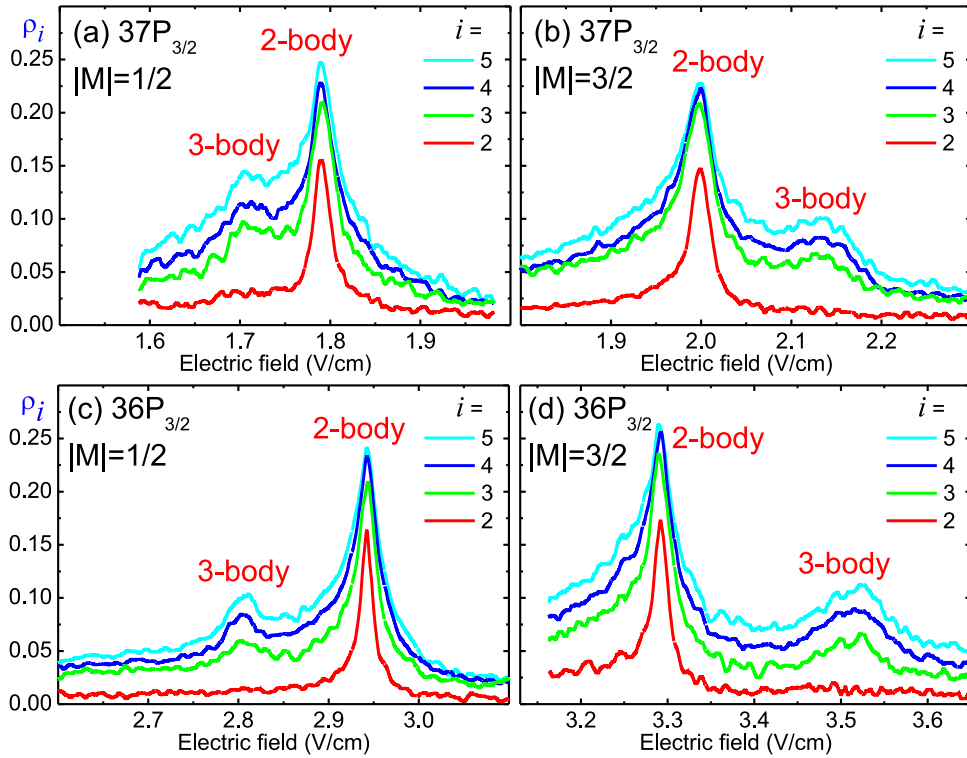


**Figure 3.7 :** Stark-tuned Förster resonances in Rb Rydberg atoms observed for various numbers of atoms  $i = 2 - 5$  and various initial states: (a)  $37P_{3/2}(|M| = 1/2)$ ; (b)  $37P_{3/2}(|M| = 3/2)$ ; (c)  $36P_{3/2}(|M| = 1/2)$ ; (d)  $36P_{3/2}(|M| = 3/2)$ . The main peaks are two-body resonances, and the additional peaks are three-body resonances. The three-body resonance is absent for  $i = 2$  in all records, evidencing its three-body nature.

Rydberg states population was recorded using a selective field ionization (SFI) method, with the help of channel electron multiplier (CEM) [220]. The CEM output pulses are then detected using two independent gates, making it possible to distinguish between signals from  $nS$  states and a mixture of  $nP$  and  $(n + 1)S$  states. The CEM signal is also number resolved, which thus allows to record the exact number of energy transfers as a function of the total number  $N$  of excited atoms. The fraction of atoms transitioned to  $nS$  states  $S_N$  is used to represent the resonance spectra. For more detail on the experimental setup, please see original paper [192].

Figure 3.7 shows the experimental results on the recording of Förster resonances in a small ensemble of  $^{85}\text{Rb}$  atoms. Note that due to the atomic excitation in an external electric field, only one of the states  $37P_{3/2}(|M| = 1/2)$  and  $37P_{3/2}(|M| = 3/2)$  can be excited in each experimental cycle. Because of this, the spectra of resonances 1 and 3, shown in Figure 3.6, are recorded separately from resonances 6 and 8 since they require different initial states. Resonances 2,4,5 and 7 cannot be recorded in the proposed experimental setup since the superposition of different initial states is required.

The spectra around the resonances 1 and 3 is shown in Figure 3.7(a) for different numbers of interacting atoms  $i = 2 - 5$ . When there are two Rydberg atoms in the system, the two-body resonance 3 occurs in an electric field of 1.79 V/cm. However, in this case the three-body

peak 1 is absent. If a third atom is added, this peak appears in a field of 1.71 V/cm, on the slope of the two-body resonance. The amplitudes of the peaks increase with the addition of atoms but do not change their positions, in satisfactory agreement with the precomputation predictions shown in Fig. 3.6. Note that the resonances partially overlap. The overlap increases with increasing number of atoms due to the broadening of the two-body resonance and growing interaction energy.

Figure 3.7(b) shows the spectra of resonances 6 and 8. As can be seen, the three-body peak changes its position relative to the two-body peak. The two-body resonance is observed for  $i = 2 - 5$  atoms at 2.0 V/cm, growing when the number of atoms in the system increases. The three-body peak at 2.14 V/cm is absent for  $i = 2$  and appears only for  $i = 3 - 5$ . Figures 3.7(c) and 3.7(d) show the spectra of similar resonances for the value of the principal quantum number  $n = 36$ . The relative positions of the resonances as well as their amplitudes are in agreement with expectations. However, the separation of three-body and two-body peaks is more pronounced than for the case of  $n = 37$ . This is due to the strong dependence of polarizabilities on the value of the principal quantum number, as well as due to the exact values of quantum defects of the involved states [59].

The obtained results allow us to draw several important conclusions. As it was shown, resonances (3.12) arise only in the presence of three or more Rydberg atoms in the system. Nevertheless, the occurrence of resonances is possible for different values of the principal quantum number. Also, these resonances change their position and amplitude in full agreement with expectations. Thus, we can consider these results as confirmation of the hypothesis about the nature of many-body resonances shown earlier in [107].

### 3.3.3. Analytical model

The experimental results have clearly demonstrated that three-body effects significantly modify the spectra of Rydberg systems, provoking their asymmetry. In previous publications devoted to the description of Förster resonances, only two-body transitions were taken into account, leading to the full symmetry of the resonance spectra in numerical simulations. Experimental observations in [192] show the irrelevance of this description. Therefore, it became necessary to develop a new analytic theory that would increase the understanding of resonance dynamics. Such a model was developed and described in detail in [193].

To facilitate the analytical description, several assumptions were made when constructing the theoretical model. First, without claiming full universality, the authors concentrated on the description of the results of the experiments performed. Since the main channels of interaction in these experiments were two- and three-body resonances, the description was limited to the case of interaction of three atoms. Secondly, an equidistant spatial configuration was chosen. Thus, in the following description it is assumed that the interacting atoms are located in the corners of an equilateral triangle. Third, the minimum number of three collective levels which are necessary to describe the transfer process were considered in this simplified analytical model.

Figure 3.8 shows a simplified scheme of three-body resonances (3.12) for states with  $n = 37$ . Here state 1 is the initial state of the three-atomic system  $3 \times 37P_{3/2}$ , and state 3 is its final state

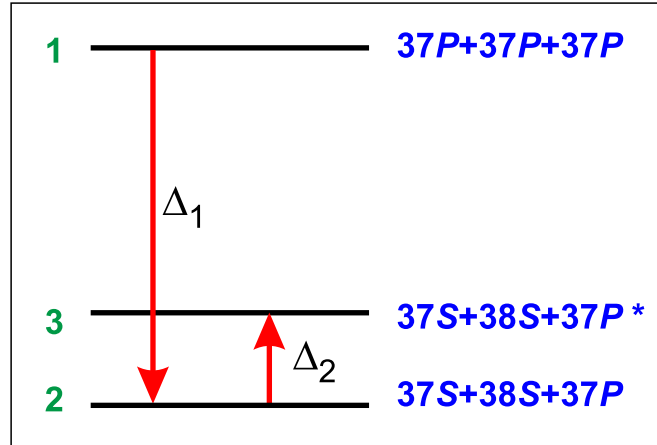


**Figure 3.8 :** Simplified scheme of the three-body Förster resonance  $3 \times 37P_{3/2}(|M| = 1/2) \rightarrow 37S_{1/2} + 38S_{1/2} + 37P_{3/2}(|M^*| = 3/2)$  for three Rydberg atoms. The initially populated collective state 1 is  $3 \times 37P_{3/2}(|M| = 1/2)$ . The final collective state 3 is  $37S_{1/2} + 38S_{1/2} + 37P_{3/2}(|M^*| = 3/2)$  with the changed momentum projection of the  $P$  state. The intermediate collective state 2 is  $37S_{1/2} + 38S_{1/2} + 37P_{3/2}(|M| = 1/2)$  with the initial momentum projection of the  $P$  state. The energy defects  $\Delta_1 = E_1 - E_2$  and  $\Delta_2 = E_3 - E_2$  are controlled by the DC electric field. The three-body resonance occurs at  $\Delta_1 = \Delta_2$ , while the two-body one occurs at  $\Delta_1 = 0$ .

$37S_{1/2} + 38S_{1/2} + 37P_{3/2}^*$  in the case of a successful three-body transfer. The intermediate state 2 serves to ensure the ladder-like transfer character described in the Subsection 3.1.1. Thus, the three-body process can be described as a sequence of two-body transitions  $1 \rightarrow 2 \rightarrow 3$  occurring simultaneously. The detunings  $\Delta_1$  and  $\Delta_2$ , which represent the Förster defects of the respective two-body resonances, control the character of the multiatomic transit. When the condition  $\Delta_1 = \Delta_2$  is satisfied, levels 1 and 3 are degenerate, provoking a three-body resonance (resonance 1 or 8 in Figure 3.6). The two-body resonance, in turn, is induced by the condition  $\Delta_1 = 0$ , which means that levels 1 and 2 are degenerate (resonances 3 and 6 in Figure 3.6).

Note that the  $\Delta_i$  detunings can be controlled by an external electric field due to the Stark effect, as described in [59, 107, 191]. However, the degree of control of each detuning depends on the polarizabilities of the states. While  $\Delta_1$  can be chosen arbitrarily,  $\Delta_2$  is in fact the Stark splitting between  $|M| = 1/2$  and  $|M| = 3/2$  sublevels of the  $37P_{3/2}$  state, and changes only slightly near the Förster resonance.

Authors describe the dynamics of the system using the Schrödinger equation formalism for the probability amplitudes of states 1, 2 and 3. The matrix elements of the dipole-dipole transitions  $1 \rightarrow 2$  and  $2 \rightarrow 3$ , are denoted as variables  $V_1$  and  $V_2$ , respectively. These elements can also be expressed in frequency units as  $\Omega_1 = V_1/\hbar$ ,  $\Omega_2 = V_2/\hbar$ . The methods for calculating such matrix elements were shown in [135, 137, 193] (see Appendix A). Note that this model considers only the energies of the collective levels without specifying the states of each particular atom. This means that levels 2 and 3 are additionally sixfold degenerate due to possible permutations of atoms. Also, these states experience always-resonant hopping interactions between  $S$  and  $P$  states, which leads to the presence of an energy shift. Then, the Schrödinger equation will have the following form:

$$\begin{aligned}
 i\dot{a}_1 &= 6\Omega_1 a_2 e^{-i\Delta_1 t} \\
 i\dot{a}_2 &= 2\Omega_1 a_2 + \Omega_1 a_1 e^{i\Delta_1 t} + 2\Omega_2 a_3 e^{i\Delta_2 t} \\
 i\dot{a}_3 &= 2\Omega_2 a_3 + 2\Omega_2 a_2 e^{-i\Delta_2 t}
 \end{aligned} \tag{3.13}$$

Here, the terms containing no explicit time dependence are produced by always resonant excitation hopping described in Subsection 2.2.5. The terms containing exponential time dependence, in turn, drive dipole transitions between the collective states.

Analytical solution of the system (3.13) is possible for arbitrary values of interaction energies, detunings, and time. Nevertheless, it requires large-scale calculations. For this reason, we leave it in Appendix C, and invite the interested reader to review it.

The form of the three-body resonance spectrum we are interested in can thus be calculated as (3.14). Here,  $\rho_3$  corresponds to the probability to find one of the atoms in the final  $37S_{1/2}$  state, thus representing the signal measured in the experiments described in the previous subsection. The multiplier 6 is related to the sixfold degeneracy of the corresponding states.

$$\rho_3 = \frac{6|a_2|^2 + 6|a_3|^2}{3} \tag{3.14}$$

### 3.3.4. Resonance analysis

The previously obtained expression can be used to analyze the peculiarities of the experimentally recorded spectrum. We analyse this formula in the limit of weak dipole-dipole interaction. “Weakness” in this case means that states 2 and 3 remain almost unpopulated, while the population of the initial state  $a_1 \approx 1$ . Consequently, the angular factors  $\Omega_i t$ , which determine the rate of evolution of the states, remain small throughout the process, giving  $\Omega_1 t, \Omega_2 t \ll 1$ . Given the above assumption, we can describe the shape of the spectrum (using the analytical solutions for  $a_i$  obtained in the Appendix C) as:

$$\begin{aligned}
 \rho_3 &\approx \frac{8\Omega_1^2}{\Delta_1^2} \sin^2 \left[ \frac{\Delta_1 t}{2} \right] \\
 &+ 32\Omega_1^2 \Omega_2^2 \times \left( \frac{1}{\Delta_1 \Delta_2 (\Delta_1 - \Delta_2)^2} \sin^2 \left[ \frac{(\Delta_1 - \Delta_2)t}{2} \right] \right. \\
 &+ \frac{1}{\Delta_1 \Delta_2^2 (\Delta_1 - \Delta_2)} \sin^2 \left[ \frac{\Delta_2 t}{2} \right] \\
 &\left. - \frac{1}{\Delta_1^2 \Delta_2 (\Delta_1 - \Delta_2)} \sin^2 \left[ \frac{\Delta_1 t}{2} \right] \right)
 \end{aligned} \tag{3.15}$$

While analysing the equation, it is useful to remember that two resonance conditions were given earlier. The two-body resonance occurs at  $\Delta_1 = 0$ , while the three-body resonance occurs at  $\Delta_1 = \Delta_2$ . We will analyze these two cases separately.

### 3.3. Three-body Förster resonances in Rb ensembles

At  $\Delta_1 = 0$ , the amplitude of the first term in the eq. (3.15) increases faster compared to the second and third terms, since it contains in the denominator the square of the first energy defect. At the same time, the fourth term, also depending on  $\Delta_1^{-2}$ , turns out to be inversely proportional to  $\Delta_2^2$ , and is therefore much smaller than the first term. The second and third terms in this case become completely identical, and eliminate each other. Thus, the two-body resonance is described predominantly by the first term, while the fourth term causes only a small reduction in the strength of the two-body interaction. The resonance amplitude of the two-body transition grows as  $\rho_3 \rightarrow 2(\Omega_1 t)^2$ , while the peak width is determined by the Fourier width of the interaction pulse.

When  $\Delta_1 = \Delta_2$ , the third and fourth terms of expression (3.15) compensate each other due to the fact that  $\Delta_2$  is always nonzero in the presence of an external electric field. At the same time, the second term of the equation has the most significant growth  $\rho_3 \rightarrow 8(\Omega_1 \Omega_2 t / \Delta_2)^2$ . Thus, we can conclude that this term is responsible for the three-body resonance. At the same time, the two-body dynamics is also observed near the resonance due to the presence of the first term. This explains the incomplete isolation of the peaks from each other.

It is instructive to compare the ratio of peak magnitudes. As can be concluded from the analysis, the amplitudes of the three-body and two-body peaks are related as  $(2\Omega_2 / \Delta_2)^2$ . Thus, the three-body resonance appears to be generally weaker than the two-body resonance in the weak interaction limit. Note that when deriving this relation we have compared the absolute values of the resonance amplitudes in two different limits (at  $\Delta_1 = 0$  for the two-body resonance and at  $\Delta_1 = \Delta_2$  for the three-body resonance). If we compare the relative amplitudes of both resonances in the limit  $\Delta_1 = \Delta_2$ , according to equation (3.15), we obtain that the three-body contribution relates to the two-body contribution as  $2(\Omega_2 t)^2$ . This means that the three-body contribution in this case exceeds the two-body contribution if the interaction time is sufficiently long. Thus, we can expect the coherence time of the three-body resonance to significantly exceed the coherence time for its two-body counterpart. The comparison of the coherence times of these two processes is relevant due to similar phase dynamics. While the frequency of the population oscillations can be significantly different for these processes, the phase of the collective three-body state evolves at a similar rate both for two-body and three-body resonances. Nevertheless, as we have seen earlier, the two-body peak will always be higher than the three-body peak in absolute value.

To analyze the case of three-body resonance in more detail, we consider equation (3.14) under the conditions  $|\Delta_1 - \Delta_2| \ll \Delta_2$  ( $\Delta_1$  is scanned in the vicinity of  $\Delta_2$ ) and  $\Omega_1, \Omega_2 < \Delta_2$ . Since the difference between  $\Delta_1$  and  $\Delta_2$  is small, the three-body resonance will be dominant in this case. Note that in the framework of the previously conducted experiment  $\Delta_2 / 2\pi \simeq 9.5$  MHz for the Stark sublevels of the  $37P_{3/2}$  state of Rb atoms in the electric field corresponding to the three-body resonance. At the same time, the average dipole-dipole interaction energy in the ensemble was  $\sim 1$  MHz. Thus, this approximation is consistent with the experimental conditions used for the observation of the three-body resonance. The equation (3.14) is transformed into the following form:

$$\rho_3 \approx \frac{\Omega_0^2/3}{(\Delta - \Delta_0)^2 + \Omega_0^2} \sin^2 \left[ \frac{t}{2} \sqrt{(\Delta - \Delta_0)^2 + \Omega_0^2} \right] \quad (3.16)$$

Here  $\Delta = \Delta_1 - \Delta_2$  is the detuning from the unperturbed three-body resonance. In turn,  $\Delta_0$  represents an interaction-induced three-body resonance shift. This shift can be denoted as  $\Delta_0 = -2\Omega_2 + (4\Omega_2^2 - 6\Omega_1^2)/(\Delta_2 + 2\Omega_1)$ , where the first term is caused by excitation hopping between  $S$  and  $P$  states, while the second term denotes a dynamical AC Stark shift. Finally,  $\Omega_0 = 4\sqrt{6}\Omega_1\Omega_2/(\Delta_2 + 2\Omega_1)$  is the Rabi-like oscillation frequency.

We now concentrate on analyzing the above equation. As can be seen, the exact resonance with maximum amplitude  $1/3$  is realized at  $\Delta = \Delta_0$ . In this case, the equation is reduced to the standard population oscillation equation given in Subsection 2.2.4. The coherent Rabi frequency of such oscillations is  $\Omega_0 \ll \Omega_1, \Omega_2$  because of the large value of  $\Delta_2$ . Consequently, the coherence time of three-body resonances can be much larger than for two-body resonances, in good agreement with the earlier analysis. Note that the large detuning value and small frequency of the three-body resonant oscillations make this scheme in many ways analogous to the two-photon transition scheme in a three-level system with a strongly detuned intermediate state. This analogy is extremely fortunate because the original scheme of two-body Förster resonances also has an analogy to the transfer in a two-level system. As we described in Subsection 2.2.5, Förster resonances, originally proposed in chromophores, are commonly understood as radiation-free transitions in quantum systems, replacing real photons by virtual ones.

It should be noted that the above equation does not take into account the wide variety of Stark and Zeeman atomic sublevels, which can lead to the appearance of a large number of interaction channels with different matrix elements, and hence to the formation of numerous resonance peaks in the spectrum of the three-atomic system. Nevertheless, the dynamic energy shift  $\Delta_0$  dependent on the ratio of matrix elements  $V_1$  and  $V_2$  can be used to separate different channels in order to preserve coherence.

Summarizing the analysis, it is important to focus on the following facts:

- It is convincingly shown that coherent Rabi-like oscillations can be obtained by implementing three-body Förster resonance transfer in the simplified analytical model.
- The coherence times for three-body resonances are, theoretically, larger than those of two-body resonances.
- Three-body resonances can be demonstrated in both strong and weak interaction limits.

Thus, we can conclude that coherent three-body resonances occur when the interaction strength between the atoms is fixed. As can be seen from equation (3.16), each minimum of resonant Rabi oscillations refers to a  $\pi$  phase shift for the collective wave function of the Rydberg system. Since such oscillations are controllable and reversible, they can be used to realize multiqubit quantum gates.

### 3.3.5. Numerical simulations

The analytical model shown in the previous subsection allows us to characterize the properties of the three-body Förster resonances and qualitatively describes the shape of the experimentally registered peaks. Nevertheless, this model does not allow us to consider the case of large interaction times that result in broadening of the three-body resonance. Also, it does not give an accurate description of the Stark and Zeeman atomic sublevels, which can lead to the formation of different channels of the three-body interaction. Thus, to continue the study of the properties of Förster resonances, the development of a numerical computational model is necessary.

In the paper [193], the authors provide a highly accurate numerical model for the calculation of many-body Förster resonant transitions in Rydberg systems. This model was subsequently widely used in my studies of three-body resonances and was also adapted for the calculation of many-body quantum gate schemes. Therefore, this model is described here in detail to give the reader a baseline for understanding the results of further research. However, in order to avoid overcomplicating the text, a portion of the material is presented in the Appendix A.

The model is based on solving the Schrödinger equation numerically, taking into account interatomic interactions in the quasi-classical approximation. Many-body transitions are represented as sequences of two-body transitions occurring in a system of  $N$  atoms. In this case the basis of collective atomic states is formed as  $\bigotimes_{i=1}^N |\gamma_i\rangle$ , where  $|\gamma\rangle = |nLJM_J\rangle$  represents the individual state of each atom. For  $N = 3$ , transitions are considered in a system of 3 atoms in the basis of collective states  $|\gamma_1\gamma_2\gamma_3\rangle = |n_1L_1J_1M_1; n_2L_2J_2M_2; n_3L_3J_3M_3\rangle$ . Thus, for the atoms initially excited to high  $37P_{3/2}$  states, the basis was formed from the eight states  $|37P_{3/2}(M = \pm 1/2, \pm 3/2)\rangle$ ,  $|37S_{1/2}(M = \pm 1/2)\rangle$ ,  $|38S_{1/2}(M = \pm 1/2)\rangle$ . Similarly, for the  $36P_{3/2}$  states, the basis was composed of  $|36P_{3/2}(M = \pm 1/2, \pm 3/2)\rangle$ ,  $|36S_{1/2}(M = \pm 1/2)\rangle$ ,  $|37S_{1/2}(M = \pm 1/2)\rangle$  states. The initial state of the three-atom system was taken as the defined or random superposition of the eight degenerate collective states where all three atoms were in the  $|37P_{3/2}(M = \pm 1/2)\rangle$  states (or in the  $|37P_{3/2}(M = \pm 3/2)\rangle$  states, if the exciting laser was tuned to the excitation of the  $37P_{3/2}$  atoms with  $|M| = 3/2$ ), with the defined or equal statistical weights. For the random superposition, it was assumed that after laser excitation the sign of the total momentum  $M = \sum_i M_i$  for the initial state is undetermined. To reduce the computational complexity, the basis was further restricted by discarding strongly detuned states. Specifically, states whose zero-field Förster defect is more than 2 GHz relative to the initial state were not included in the calculation. Thus, a basis of  $\sim 160$  states was formed.

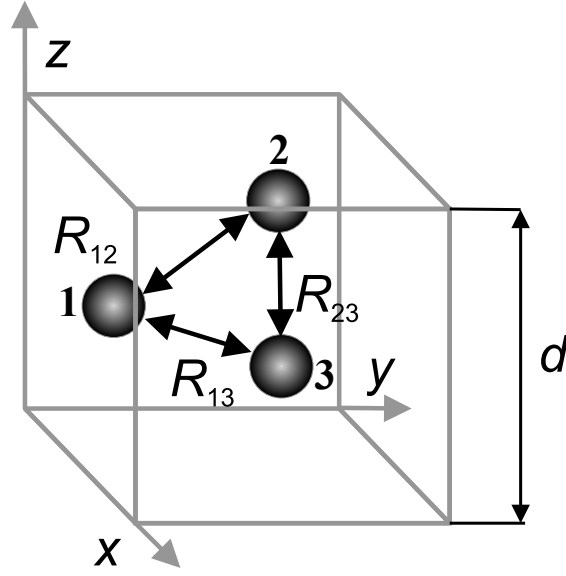


**Figure 3.9:** Geometry of the interaction of the three Rydberg atoms. The atoms are positioned either randomly in a cubic volume to perform numerical simulations with Monte Carlo averaging over the atom positions, or are spatially fixed to provide Rabi-like population oscillations.

Note that although the basis is formed from three-body collective states, the two-body transitions are considered as the basic element of the interaction, and hence all transitions in a three-atom system involve only two atoms. Such transitions have the form  $|\gamma_a, \gamma_b\rangle \rightarrow |\gamma_s, \gamma_t\rangle$ , with initial states of atoms  $\gamma_a, \gamma_b$  and their final states  $\gamma_s, \gamma_t$ . Suppose the atoms are arbitrarily arranged in space as depicted in Figure 3.9. The dipole-dipole interaction operator between atoms 1 and 2 is

$$\hat{V}_{dd} = \frac{1}{4\pi\epsilon_0 R_{12}^3} \left[ \hat{d}_1 \hat{d}_2 - 3(\hat{d}_1 \vec{n}_{12})(\hat{d}_2 \vec{n}_{12}) \right] \quad (3.17)$$

Here  $R_{12}$  denotes the distance between the first and the second atoms, the unit vector  $\vec{n}$  indicates the direction of interatomic axis, and  $\hat{d}_{1(2)}$  are the dipole moment operators of atoms 1 and 2, respectively. To simplify the representation of matrix elements, it is convenient to use spherical coordinates. Then,  $\vec{n}_{12} = (\cos \phi \sin \theta, \sin \phi \sin \theta, \cos \theta)$ , and  $\hat{d}_{k,\pm} = \mp(\hat{d}_{k,x} \pm i\hat{d}_{k,y})/\sqrt{2}$  for the  $k$ -th atom. In the spherical basis, the operator  $\hat{V}_{dd}$  can be written as

$$\begin{aligned} \hat{V}_{dd} = & \frac{1}{4\pi\epsilon_0 R_{12}^3} \times \left[ A_1(\theta)(\hat{d}_{1+}\hat{d}_{2-} + \hat{d}_{1-}\hat{d}_{2+} + 2\hat{d}_{1z}\hat{d}_{2z}) \right. \\ & + A_2(\theta, \phi)(\hat{d}_{1+}\hat{d}_{2z} - \hat{d}_{1-}\hat{d}_{2z} + \hat{d}_{1z}\hat{d}_{2+} - \hat{d}_{1z}\hat{d}_{2-}) \\ & + A_3(\theta, \phi)(\hat{d}_{1+}\hat{d}_{2z} + \hat{d}_{1-}\hat{d}_{2z} + \hat{d}_{1z}\hat{d}_{2+} + \hat{d}_{1z}\hat{d}_{2-}) \\ & \left. + A_4(\theta, \phi)(\hat{d}_{1+}\hat{d}_{2+} + \hat{d}_{1-}\hat{d}_{2-}) + A_5(\theta, \phi)(\hat{d}_{1+}\hat{d}_{2+} - \hat{d}_{1-}\hat{d}_{2-}) \right] \end{aligned} \quad (3.18)$$

### 3.3. Three-body Förster resonances in Rb ensembles

The angular prefactors  $A_i$  are

$$\begin{aligned}
A_1(\theta) &= \frac{1 - 3 \cos^2(\theta)}{2} \\
A_2(\theta, \phi) &= \frac{3 \sin(2\theta) \cos(\phi)}{2\sqrt{2}} \\
A_3(\theta, \phi) &= -i \frac{3 \sin(2\theta) \sin(\phi)}{2\sqrt{2}} \\
A_4(\theta, \phi) &= -\frac{3 \sin^2(\theta) \cos(2\phi)}{2} \\
A_5(\theta, \phi) &= \frac{3 \sin^2(\theta) \sin(2\phi)}{2}
\end{aligned} \tag{3.19}$$

The spherical representation of the operator  $\hat{V}_{dd}$  gives easy selection rules for two-body dipole-dipole transitions. Thus, the operator couples states with  $\Delta M = 0, \pm 1, \pm 2$ , where  $M = M_1 + M_2$  is the total momentum projection of the system. Finally, the matrix element of the operator between the collective two-atom states  $|\gamma_a, \gamma_b\rangle \rightarrow |\gamma_s, \gamma_t\rangle$  can be represented as [146]:

$$\begin{aligned}
&\langle n_s M_s L_s J_s; n_t M_t L_t J_t | \hat{V}_{dd} | n_a M_a L_a J_a; n_b M_b L_b J_b \rangle = \\
&= \frac{e^2}{4\pi\epsilon_0 R_{12}^3} \left\{ A_1(\theta) \left[ C_{J_a M_a 11}^{J_s M_s} C_{J_b M_b 1-1}^{J_t M_t} + C_{J_a M_a 1-1}^{J_s M_s} C_{J_b M_b 11}^{J_t M_t} + 2 C_{J_a M_a 10}^{J_s M_s} C_{J_b M_b 10}^{J_t M_t} \right] \right. \\
&+ A_2(\theta, \phi) \left[ \left( C_{J_a M_a 11}^{J_s M_s} - C_{J_a M_a 1-1}^{J_s M_s} \right) C_{J_b M_b 10}^{J_t M_t} + C_{J_a M_a 10}^{J_s M_s} \left( C_{J_b M_b 11}^{J_t M_t} - C_{J_b M_b 1-1}^{J_t M_t} \right) \right] \\
&+ A_3(\theta, \phi) \left[ \left( C_{J_a M_a 11}^{J_s M_s} + C_{J_a M_a 1-1}^{J_s M_s} \right) C_{J_b M_b 10}^{J_t M_t} + C_{J_a M_a 10}^{J_s M_s} \left( C_{J_b M_b 11}^{J_t M_t} + C_{J_b M_b 1-1}^{J_t M_t} \right) \right] \\
&+ A_4(\theta, \phi) \left[ C_{J_a M_a 11}^{J_s M_s} C_{J_b M_b 11}^{J_t M_t} + C_{J_a M_a 1-1}^{J_s M_s} C_{J_b M_b 1-1}^{J_t M_t} \right] \\
&+ A_5(\theta, \phi) \left[ C_{J_a M_a 11}^{J_s M_s} C_{J_b M_b 11}^{J_t M_t} - C_{J_a M_a 1-1}^{J_s M_s} C_{J_b M_b 1-1}^{J_t M_t} \right] \left. \right\} \\
&\times \sqrt{\max(L_a, L_s)} \sqrt{\max(L_b, L_t)} \sqrt{(2J_a + 1)(2J_b + 1)} \\
&\times \begin{pmatrix} L_a & 1/2 & J_a \\ J_s & 1 & L_s \end{pmatrix} \begin{pmatrix} L_b & 1/2 & J_b \\ J_t & 1 & L_t \end{pmatrix} \\
&\times (-1)^{L_s + \frac{L_a + L_s + 1}{2}} (-1)^{L_t + \frac{L_b + L_t + 1}{2}} (-1)^{J_a + J_b} R_{n_a L_a}^{n_s L_s} R_{n_b L_b}^{n_t L_t}
\end{aligned} \tag{3.20}$$

To avoid overcomplication, we do not provide the derivation of the formula (3.20) in the text of this thesis. Yet, its derivation can be found in a textbook by M. Saffman [135]. Although it is still unpublished, we recommend that the interested reader refer to it, because it presents a perfect material on the advanced atomic physics. The derivation can also be found in much less detail in [146]. In our computations, the radial matrix elements were calculated in the quasi-classical approximation, according to the method described in [221]. This method forms the basis of our model, therefore we present it in the Appendix A.

It is important to note that the finite lifetimes of atomic levels are not considered at this stage of the numerical model. Although these lifetimes are scaled as  $\sim n^3$  for Rydberg atoms, the presence of level decay can lead to observable consequences in simulations, including the collapse of the expected coherence in structured ensembles.

### 3.3.6. Disordered ensemble simulation

The constructed model enables the simulation of multiparticle resonance interactions obtained from the experiment. For this purpose, the numerical calculation was first performed for  $i = 3$  atoms in a disordered ensemble. The atoms were assumed to be arbitrarily arranged in the volume  $15 \times 15 \times 15 \mu\text{m}^3$  (see Fig. 3.9). According to the described method, the Schrödinger equation was solved followed by Monte Carlo averaging over 1000 arbitrary atomic configurations. The spatial coefficients of the Hamiltonian  $A_i$  (see Eq. 3.19) were calculated for each iteration. Note that during this simulation, finite Rydberg lifetimes were not taken into account.

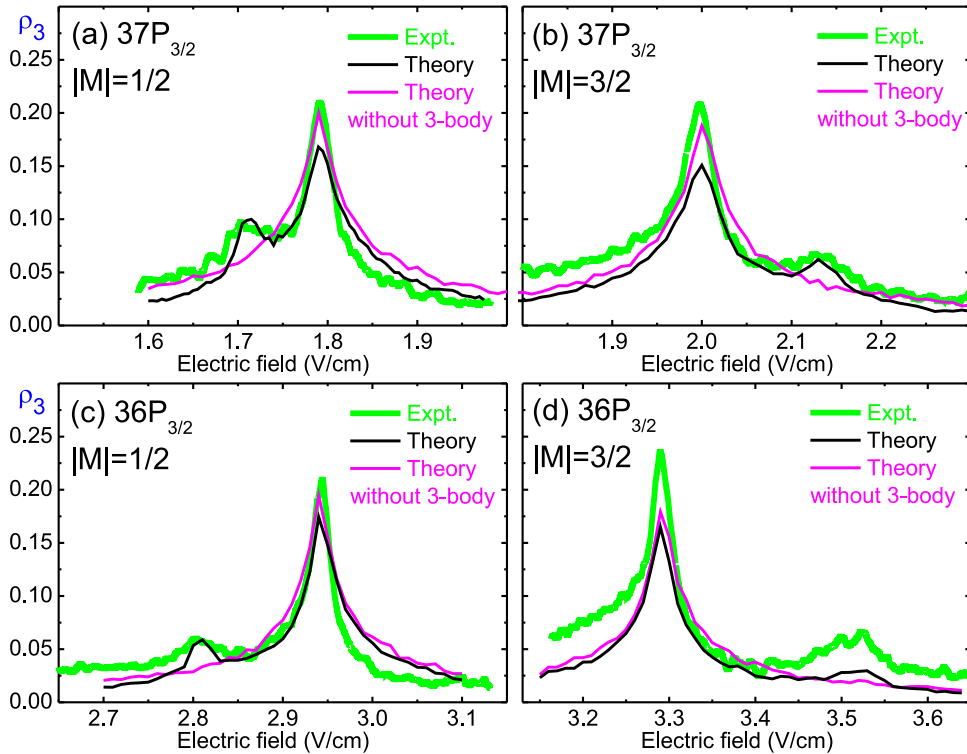


**Figure 3.10:** Comparison between the theory and experiment for the three-atom Stark-tuned Förster resonances  $3 \times nP_{3/2}(|M|) \rightarrow nS_{1/2} + (n+1)S_{1/2} + nP_{3/2}(|M^*|)$  in Rb Rydberg atoms for the initial states: (a)  $37P_{3/2}(|M| = 1/2)$ ; (b)  $37P_{3/2}(|M| = 3/2)$ ; (c)  $36P_{3/2}(|M| = 1/2)$ ; (d)  $36P_{3/2}(|M| = 3/2)$ . The theoretical spectra have been calculated for the cubic interaction volume of  $15 \times 15 \times 15 \mu\text{m}^3$ ,  $3 \mu\text{s}$  interaction time, and Monte Carlo averaging over 1000 random atom positions. The thick green lines are the experimental data, the thin black lines are the full theory, and the thin magenta lines are the theory without accounting for the three-body resonances [192].

Figure 3.10 shows the results of theoretical modeling of experimentally obtained peaks. Here, the green line represents the experimental results, while the black line shows the numerically obtained results. The magenta line is also presented, which refers to the theoretical model that does not take into account the presence of the three-body resonance. The general agreement between experimental and theoretical data is demonstrated. The three-body resonances are accurately reproduced in their height and width, proving the validity of the presented numerical model. However, a significant discrepancy is observed in Fig. 3.10(d), where the proposed model underestimates the height of the resonances. The authors attribute this to the high value of the energy defect  $\Delta$  for the transition at the initial state  $36P_{3/2}$ , and conclude that the proposed model works qualitatively at small values of  $\Delta$ , while for larger values the model might give incorrect predictions. We also suggest that this discrepancy may be caused by the involuntary enhancement of the atomic density that occurred in the experiment. As can be seen, the experimental two-body peak in the Figure 3.10(d) has a significantly larger amplitude than its counterparts from other images, which confirms our hypothesis.

#### 3.3.7. Coherent oscillations in various spatial configurations

As it was shown in Subsection 3.3.4, coherent time dynamics can be demonstrated for a three-body resonant transfer process in Rb atoms. To achieve coherence, the condition of interaction strength constancy must be satisfied. The matrix elements of the dipole-dipole interaction are distance dependent. Thus, spatial fixation of atoms is required to obtain coherent resonant dynamics.

In [193], the results of coherence analysis of two- and three-body Förster resonances in a system of three spatially fixed Rydberg atoms were presented. Numerical simulations of the multi-atomic transitions were performed using the methods described in the Subsection 3.3.5. Specifically, three-body Stark-induced Förster resonances  $3 \times 37P_{3/2}(M = 1/2) \rightarrow 37S_{1/2} + 38S_{1/2} + 37P_{3/2}(M = \pm 3/2)$  were investigated. Three spatial configurations were studied; equilateral triangle in the  $X - Y$  plane (which provides fully symmetric interaction and was considered in the analytical calculations); one-dimensional chain along  $X$  axis; one-dimensional chain along  $Z$  axis. Note that an external controlling electric field is applied along the  $Z$  axis, thus instigating an additional symmetry of the system. The interatomic distances in all three configurations were  $R = 10 \mu\text{m}$ , with the assumption of atoms to be completely immobile during the whole interaction process. The possible consequences of the presence of spatial deviations in atomic register will be discussed below. All spectra were calculated for an interaction time of  $7 \mu\text{s}$ , which corresponds to the maximum of the three-body transfer for the chosen interatomic distance.

Figure 3.11 displays the results of the numerical simulations. The left column shows the selected atomic configuration. The second column from the left shows the recorded resonance spectrum for the corresponding configuration. The spectrum of the three-body interactions is also additionally shown in a magnified view in the third column. The fourth column shows the coherent Rabi-like two-body (green line) and three-body (blue line) oscillations of the final state population obtained by choosing the respective resonance value of the external electric field.

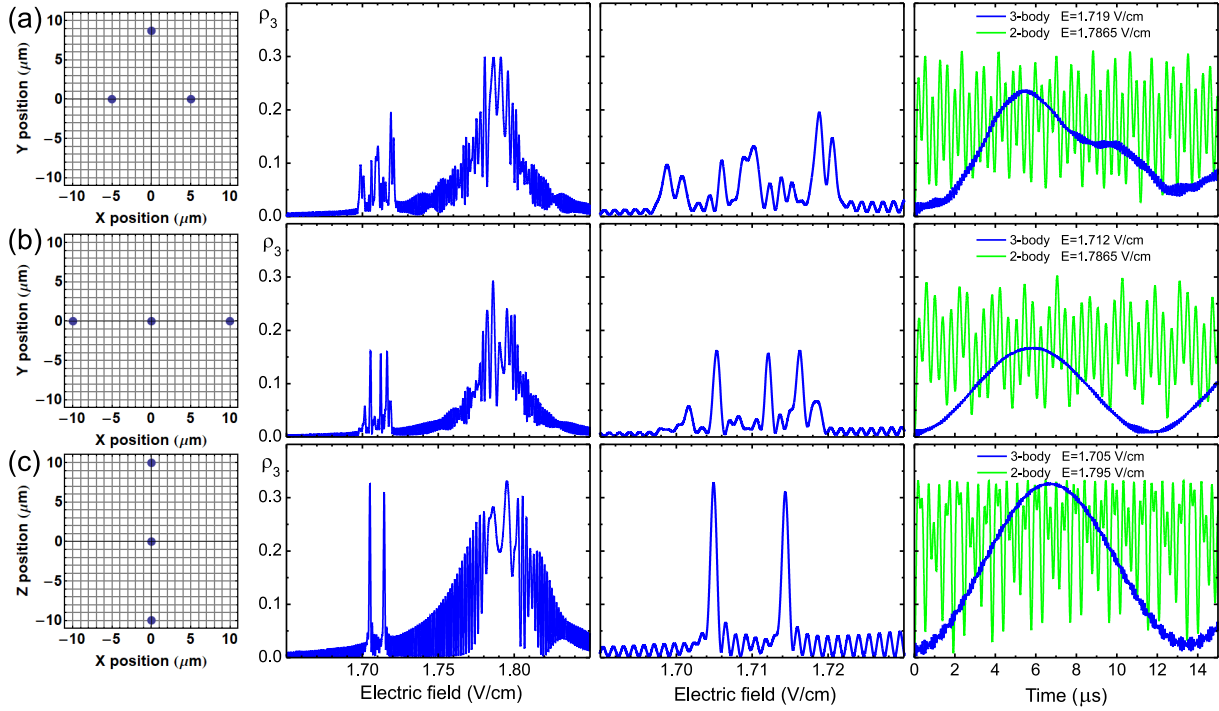


**Figure 3.11:** Numerically calculated three-atom Stark-tuned Förster resonances  $3 \times 37P_{3/2}(M = 1/2) \rightarrow 37S_{1/2} + 38S_{1/2} + 37P_{3/2}(M = \pm 3/2)$  in Rb Rydberg atoms for the three spatial configurations: (a) equilateral triangle in the  $X - Y$  plane; (b) one-dimensional chain along the  $X$  axis; (c) one-dimensional chain along the  $Z$  axis. The  $Z$  axis is directed along the controlling electric field. The three atoms are supposed to be completely immobile. The left panels show the corresponding spatial configurations with the micron-sized grids. The second from the left panels are the spectra of three-atom Förster resonances calculated for the interaction time of  $7 \mu\text{s}$ . The broad saturated two-body resonance is centered near  $1.79 \text{ V/cm}$ , while there are several narrow three-body resonances near  $1.71 \text{ V/cm}$ . The third from the left panels show the same three-body resonances zoomed in to demonstrate the number of three-body channels and their possible interplay. The right panels show the Rabi-like population oscillations for the centers of the two-body resonance [the green curves] and of the most intense three-body resonance [the blue curves].

Note that the narrow three-body resonances require precise setting of the resonant electric field that depends on the spatial configuration and interaction channel.

#### • Triangular configuration

Figure 3.11(a) presents the simulation results for the triangular configuration. As can be seen, a broad two-body peak is observed at near  $1.79 \text{ V/cm}$ , in good agreement with expectations. At the same time, the three-body resonance expected around  $1.71 \text{ V/cm}$  shows a complex structure and splits into a family of at least 6 partially overlapping peaks. These peaks correspond to different three-body interaction channels, which appear in the simulation due to the complex Stark structure of the Rydberg levels as described above. Different matrix elements  $\Omega_1$  and  $\Omega_2$  (explained earlier in the analytical approach) and different values of the dynamical shift  $\Delta_0$  correspond to different interaction channels. The dipole-dipole interaction in this case activates all allowed transitions with  $\Delta M = 0, \pm 1, \pm 2$ , and the resonant peaks do not reach the

maximum value of  $1/3$  due to the population leakage through different channels. In this regard, the three-body Rabi oscillations do not exhibit full coherence. The two-body resonances also have several possible interaction channels leading to partial dephasing and irregular behavior, as can be seen from the right graph in Fig. 3.11(a).

#### • X-oriented linear configuration

Reduction in the number of interaction channels can be facilitated by weakening the dipole-dipole interaction between one of the atomic pairs. Such weakening is achieved by using a linear atomic configuration. Figure 3.11(b) shows the results for this configuration when the atoms are arranged along the  $X$ -axis. The outermost atoms are essentially isolated from each other, which leads to reduction of some interaction channels due to the fact that at the beginning of the three-body interaction, the configurations in which the central atom appears in the  $S$  state are strongly suppressed. The central atom is most likely to end up in the  $37P_{3/2}$  state, while the outermost atoms switch to the  $37S$  and  $38S$  states. As a result, although all transitions with  $\Delta M = 0, \pm 1, \pm 2$  are allowed, half of them are strongly suppressed, and only 3 peaks prevail, as shown in the figure. However, for long interaction times,  $S - P$  excitation hopping, which is always resonant, will lead to complete channel mixing. Therefore, peak amplitude of  $1/3$  is not achieved. A slight defasing of the two-body oscillations is also present, which is caused by the same hopping interactions.

#### • Z-oriented linear configuration

A reduction in the number of interaction channels can also be implemented by fixing the projection of the total momentum of the atomic system. To achieve this, one can arrange the atoms along the  $Z$ -axis coinciding with the external electric field direction. Thus, the natural quantization axis coincides with the interatomic axis, and only transitions with  $\Delta M = 0$  are allowed. The results for this configuration are shown in Figure 3.11(c). Only two three-body peaks are present in the spectrum, which correspond to two allowed interaction channels. The peak amplitudes reach the maximum allowed value of  $1/3$ . The resonance width is extremely small ( $\sim 1$  mV/cm or  $\sim 0.13$  MHz), and is limited by the Fourier width of the interaction pulses, in full agreement with the analytical model constructed earlier. At the same time, a broad and saturated two-body resonance is preserved, whose width ( $\sim 40$  mV/cm or  $\sim 5$  MHz) corresponds to the two-body interaction energy, as shown in [192, 193]. The left wing of this resonance weakly overlaps with the narrow three-body peaks, providing in this case a minimal ( $\sim 5\%$ ) contribution to their amplitude. This contribution can be made even smaller by increasing the interaction time or the interatomic distance.

Thus, high degree of coherence has been demonstrated for the three-body resonances in the linear  $Z$ -oriented configuration. The period of the three-body population oscillations is  $\sim 13.7$   $\mu$ s, which demonstrates a significant increase in the coherence time of the resonance compared to the two-body transition. However, the two-body resonance also becomes more coherent in the linear configuration, as can be seen from the Figure 3.11(c).

### 3.3.8. Coherence dependence on atomic position variations

In the previous subsection, structured ensembles of spatially fixed atoms were investigated for coherence of three-body resonance interactions. Nevertheless, fluctuations of atomic positions in a real experiment, accompanied by changes in the dipole-dipole interaction strength, can lead to coherence disruption of Rabi-like population oscillations. To evaluate the influence of such fluctuations, a numerical experiment was carried out, described in [193]. Resonances  $3 \times 37P_{3/2}(M = 1/2) \rightarrow 37S_{1/2} + 38S_{1/2} + 37P_{3/2}(M = \pm 3/2)$  were modeled in an ensemble of Rb atoms. The atoms were arranged linearly along the  $Z$ -axis, co-directed with an external controlling electric field. The difference between this experiment and the one presented previously laid in the uncertainty of the atomic positions fluctuating with a maximum allowed deviation  $\Delta R$  from their equilibrium value. In the absence of fluctuations, the interatomic distance was 10 microns. The interaction time was  $7 \mu\text{s}$ , similar to the simulations described in the previous subsection. To record the change in the resonance character, the numerical simulations were realized 100 times, and then the obtained values were averaged over the number of realizations.

Figure 3.12 shows numerical simulation results for different values of  $\Delta R$ . Obviously, even small fluctuations of 100 nm (Fig. 3.12(b)) significantly reduce the coherence of the two-body resonance, causing dephasing and a decrease in the Rabi oscillation amplitude already  $\sim 5$  microseconds after the interaction starts. Nevertheless, the three-body resonances show greater stability. Thus, the amplitude of the first maximum of the Rabi oscillations at a time of  $7 \mu\text{s}$  in Figure 3.12(b) is almost identical to that in Figure 3.12(a). The decoherence of the three-body interaction appears clearly for the first oscillation minimum at  $13 \mu\text{s}$ . It can be seen that the oscillation amplitude is reduced compared to Figure 3.12(a). Nevertheless, the dephasing is periodic in nature, as the population transfer amplitude recovers thereafter, resulting in a greater depth of the second oscillation minimum compared to the first one. Thus, the coherence times of three-body resonances appear to be significantly longer than for two-body resonances.

Nevertheless, when the uncertainty in the atomic positions increases, the coherence is significantly disturbed. As can be seen from Figures 3.12(c) and 3.12(d), the resonances in this case become lower and broader due to fluctuations of the dynamical shift. Population bounces are observed instead of full-fledged Rabi-like oscillations, making the ensemble unsuitable for demonstrating coherent dynamics. Thus, a high degree of control of atomic positions must be realized in order to maintain high values of coherence times and realize multiqubit quantum gates. Note that the experimental feasibility of realizing interatomic distance control on sub-50 nm scale [222] has been recently demonstrated.

Within the [193], the influence of atomic drift on the coherence of oscillations has been studied in terms of changes in the interaction strength. Nevertheless, it should be mentioned that such drift may entail other undesirable effects, which also lead to decoherence of the resonant dynamics. First, the influence of the Doppler shift is present in a real experiment, which was not taken into account in the presented calculations. Also, the atomic drift can lead to differences in the laser excitation phases of the hyperfine ground states. Although the described effects can be compensated in the experiment by three-photon excitation (see Subsection 2.3.2), additional modification of the computational model is required to account for them.

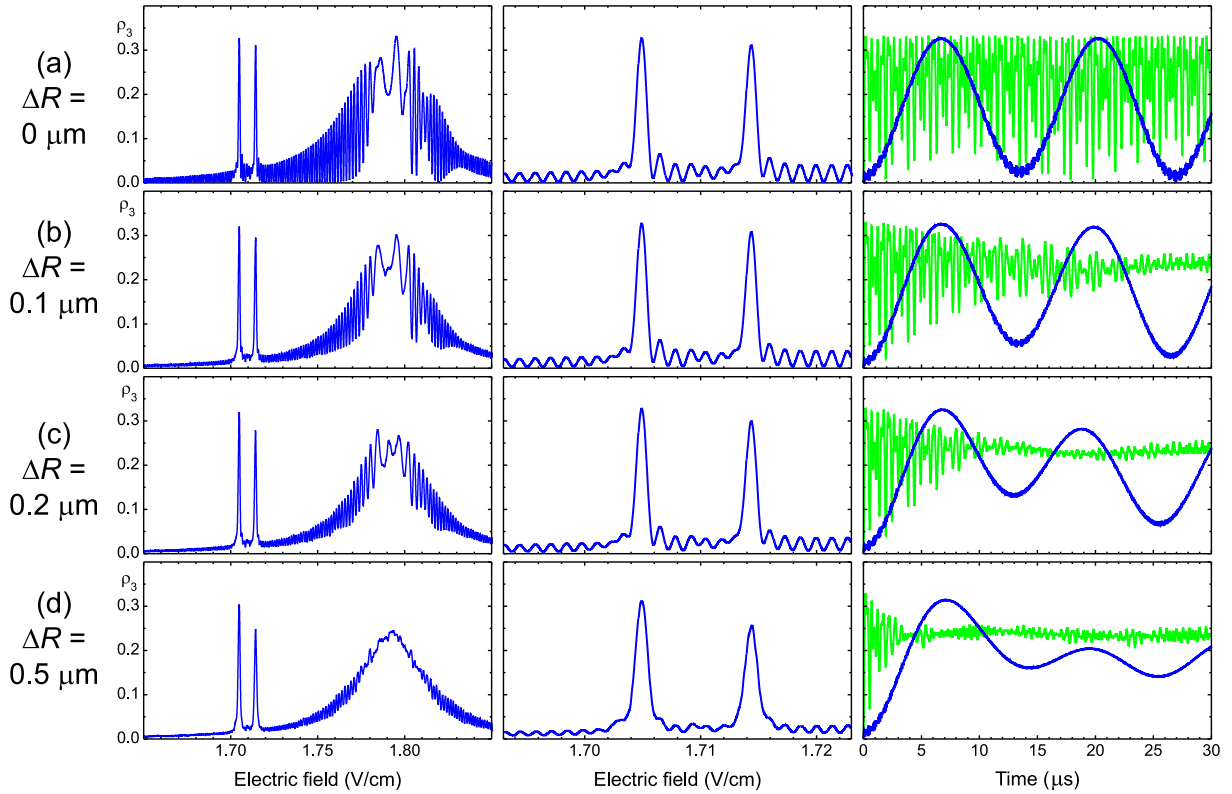


**Figure 3.12 :** Numerically calculated three-atom Stark-tuned Förster resonances  $3 \times 37P_{3/2}(M = 1/2) \rightarrow 37S_{1/2} + 38S_{1/2} + 37P_{3/2}(M = \pm 3/2)$  in Rb Rydberg atoms for the spatial configuration of one-dimensional chain along  $Z$  axis with the atom spacing  $R = 10 \mu\text{m}$  and uncertainty in the position of each atom: (a)  $\Delta R = 0 \mu\text{m}$ ; (b)  $\Delta R = 0.1 \mu\text{m}$ ; (c)  $\Delta R = 0.2 \mu\text{m}$ ; (d)  $\Delta R = 0.5 \mu\text{m}$ . The left panels show the spectra of three-atom Förster resonances calculated for the interaction time of  $7 \mu\text{s}$ . The middle panels show the three-body resonance zoomed in to demonstrate the relevant interaction channels. The right panels show the Rabi-like population oscillations for the centers of the two-body resonance at  $1.795 \text{ V/cm}$  [the green curves] and of the three-body resonance at  $1.705 \text{ V/cm}$  [the blue curves].

### 3.3.9. Conclusion

The studies shown in the articles [192, 193] have demonstrated several important results. It was experimentally shown that three-body Förster resonances can be observed in small Rb atomic ensembles. Numerical simulation of many-body interactions in an atomic system allowed to confirm the possibility of realizing coherent Borromean resonances for three atoms. The main condition for coherence is the fixation of the interaction force provoked by the spatial fixation of atoms. As for two-body transitions, Rabi oscillations arise for three-body resonances in the case of degeneracy of initial and final collective levels. Such oscillations are accompanied by a phase change of the collective states, which makes the described resonance interactions potential candidates for the realization of three-body quantum gates. Nevertheless, it is important to take into account that deviations of atomic positions which can lead to coherence violation, and negatively affect the accuracy of quantum gates.



# Chapter 4

## Results

In this chapter, research results on Förster three-body resonances and their application to the implementation of three-qubit quantum gates are presented. Each of the sections in this chapter describes a different scientific result obtained between 2018 and 2023. Thus, Section 4.1 describes the specific Förster resonance scheme chosen in our first proposal for the implementation of a three-qubit Toffoli gate [98], as well as the proposed gate protocol. Section 4.2 discusses an alternative scheme of fine-structure-state-changing (FSSC) three-body Förster resonances that simplifies the experimental realisation of quantum gates, described in [223, 224]. A Toffoli quantum gate based on this alternative resonance scheme is described in Section 4.3 [225]. Finally, Section 4.4 presents the research results on few-body radio-frequency-induced Förster resonances and *CCPHASE* gate scheme proposals based on such resonances [226].

The author of this thesis was directly involved in the research process described in this chapter. However, not all of the results presented here were obtained by him personally. Therefore, in each section of this chapter, the author's contribution will be indicated separately.

Note that the material presented in this chapter is based on articles written by the author of this thesis. In this regard, the text of this chapter contains significant borrowings from the articles, up to direct citations. Most of the images in this chapter were also taken from our previously published papers. Nevertheless, due to the need for an expanded presentation of the research material, a substantial adaptation of the text was made compared to the original articles.

### 4.1. Toffoli gate: First proposal

The three-body Förster resonances studied in the paper [193] (see Section 3.3) provide an opportunity to realize coherent population transfer between collective states of a three-atomic system. This transfer is controlled by an external electric field, which enables tuning of the interaction strength along with the resonance activation. While in unstructured atomic ensembles such resonances are significantly broadened due to the arbitrary atomic motion, resonances in structured ensembles provide highly coherent and contrasted population oscillations. Note that the phase dynamics of a multiatomic system is also strongly dependent on the external control field. Thus, a precise coherent interaction control tool is provided that can be used to implement multiqubit quantum gates.

Nevertheless, the implementation of quantum gates via the Förster resonances described in the Section 3.3 is practically impossible due to the presence of natural limitations. First, such resonances exist only for principal quantum number values  $n < 38$  in Rb atoms, and  $n < 42$  in Cs atoms. This is due to the specific values of polarisabilities and quantum defects of the Rydberg

levels of alkali atoms. Due to the higher polarisability of  $P$ -states, the Förster resonance is possible only under the condition that the energy defect of the initial and final collective states is positive in zero electric field. However, this condition is fulfilled only for Rydberg states with relatively low values of principal quantum number. When passing to higher  $n$ , the two-body transition  $2 \times nP \rightarrow nS + (n+1)S$  acquires negative energy defect in zero field. The application of an external electric field in this case leads to an increase in the collective level energy defect, thus prohibiting Stark-induced resonance. Since this two-body transition is an essential element of the three-body resonance transfer described in Section 3.3, it also appears to be essentially suppressed.

The relatively short lifetimes of the Rydberg states with  $n \sim 40$  then present an important disadvantage for the quantum gates implementation. As it was shown earlier, the coherence time of three-body resonances is much longer than that of two-body resonances. In turn, the Rabi oscillation frequencies of the three-body resonances turns out to be much smaller. During the gate execution time, comparable with the oscillation period, the Rydberg level decay can cause a complete collapse of the gate. To compensate for this drawback, the advance to higher Rydberg levels is preferred due to their longer lifetimes. Also, the high-lying Rydberg levels exhibit enhanced dipole-dipole interactions, which means that acceleration of the coherent dynamics is possible with decreasing gate realisation time. Note that the finite lifetimes of the atomic states were not taken into account in the simulations carried out in [193].

A new scheme of Förster resonances has been proposed in [98] for high-lying Rydberg levels  $n = 80$ . The strong dipole-dipole interactions arising in the Rydberg system, coupled with long Rydberg lifetimes, lead to highly coherent dynamics of populations and phases in atomic register. A protocol implementing a Toffoli gate controlled by the electric field was also proposed based on the discovered resonances. In this section, we first describe novel three-body energy transfer scheme, and then analyze in detail the proposed Toffoli gate protocol. Note that most of the material presented is adapted from the original article [98].

The analysis of many-body Förster interactions was the direct responsibility of the author of this thesis during the research. All data presented in this section were obtained with his direct involvement. The author also developed an algorithm to optimize the quantum register parameters, which resulted in a high Toffoli gate fidelity. Nevertheless, the original scheme of three-body resonances as well as the Toffoli gate protocol were proposed by the author's colleagues. The software used during this study to perform numerical simulations of many-body interactions is a modification of the previously developed software, and utilizes the computational model described previously in the Subsection 3.3.5.

### 4.1.1. New Förster resonance scheme

Before starting the description of the novel type of resonance transitions, it is useful to analyze the experience of previous studies. In Chapter 3, many-body resonant transitions in disordered ensembles of Rb [192, 193] and Cs [107, 191] were described. According to the theoretical model presented in these studies, such transitions were always characterized as the result of several simultaneous two-body transitions. Thus, the three-body Förster resonance

was represented as a nonresonant two-body  $2P \rightarrow 2S$  transition in a three-atom ensemble, complemented by  $P \rightarrow S$  nonresonant excitation hopping. However, as discussed in the introduction to this section, the two-body  $2 \times nP \rightarrow nS + (n+1)S$  transition, which is the basis of the three-body Borromean process, is suppressed for states with high values of the principal quantum number. In this regard, in order to realize the three-body transfer according to the familiar scheme, it is necessary to find a new two-body transition, which will replace the absent one.

$$nP_{3/2} + (n+1)P_{3/2} \rightarrow nS_{1/2} + (n+2)S_{1/2} \quad (4.1)$$

Removing the constraint of using a single Rydberg level for the initial collective state, many Förster resonant interactions can be easily found. The new type of two-body transitions proposed and investigated in [98] has the form (4.1). As can be seen, the realization of transitions of this type requires simultaneous excitation of atoms into initial states with different values of the principal quantum number. As a result, the energy of the initial state is essentially increased and Förster defect is positive for the presented transition in zero electric field.

$$\begin{aligned} nP_{3/2}(m=3/2) + (n+1)P_{3/2}(m=3/2) + (n+1)P_{3/2}(m=-3/2) \rightarrow \\ \rightarrow nS_{1/2}(m=1/2) + (n+2)S_{1/2}(m=1/2) + (n+1)P_{3/2}(m=1/2) \end{aligned} \quad (4.2)$$

Using the two-body transition (4.1) as an auxiliary element, we have developed a scheme of three-body transition (4.2) similar to the one presented earlier in [192]. During the three-body transfer process, all three atoms change their quantum states, which confirms its Borromean nature. While two atoms change from  $P$  states to  $S$  states, the third atom changes its momentum projection  $m_j$ .

As before, the three-body transition is realized through several parallel non-resonant two-body transitions. The resonant condition for the three-body transition is the mutual compensation of Förster defects of two-body interactions, leading to the degeneracy of collective three-atom states. Thus, if the transition (4.1) is characterized by a Förster defect  $\Delta_1$ , while the excitation hopping  $(n+2)S_{1/2} + (n+1)P_{3/2}(|m|) \rightarrow (n+2)S_{1/2} + (n+1)P_{3/2}(|m^*|)$  has a quantum defect  $\Delta_2$ , the three-body resonance in the system occurs under the condition  $\Delta_1 = \Delta_2$ . The two-body resonance, in turn, can occur at  $\Delta_1 = 0$ .

In this study, the transitions (4.1) and (4.2) have been examined for a wide range of values of  $n$ . However, in this thesis we only present results for  $n = 80$ . The choice of this value of  $n$  is motivated by several factors. First, in order to realize highly coherent population and phase dynamics in a three-atom ensemble, high lifetimes of Rydberg levels are required, as was shown in [193]. In this regard, we considered quantum states with the highest possible values of  $n$ . Moreover, the dipole moment of the Rydberg atom also increases significantly with  $n$ , thus leading to a stronger dependence of the interaction force on the external electric field, and hence to a narrowing of the resonance peaks (see Subsection 2.2.2.2). To implement resonance transitions at  $n = 80$ , the required electric field of  $\sim 10^{-1}$  V/cm must be controlled with the relative accuracy of  $\sim 10^{-6}$  V/cm. The realization of such a high-precision control is a difficult experimental task. Thus, while choosing the value of the principal quantum number, we tried

to find a satisfactory compromise between the desire to increase the atomic lifetimes and the need to set realistic conditions for a possible experimental implementation.

### 4.1.2. Numerical simulations

When implementing numerical simulations of multiatomic transitions, we used the computational model proposed earlier in [193] and described in detail in Subsection 3.3.5. Nevertheless, this model has been substantially refined to meet the goals of the current study. This subsection will describe novel computational model in detail.

#### 4.1.2.1. Configuration and basis

The main goal of this study was to realize a multiqubit quantum gate in an atomic register. In this regard, we focus on the study of highly coherent resonant processes. In the paper [193] it was shown that for the fixed atomic positions it is possible to observe coherent three-body Förster interactions and Rabi-like population oscillations (see Subsection 3.3.7). The highest degree of resonance coherence is achievable in a linear spatial configuration. For this reason, we chose this configuration for the Toffoli gate implementation. In our numerical simulations, we assume that atoms are arranged linearly along the  $Z$  axis, which coincides with the direction of the external controlling electric field (see Fig.4.1). This spatial configuration imposes the selection rule  $\Delta M = 0$  (here  $M$  is the total momentum projection of the collective state) on all two-body and three-body transitions, significantly reducing the number of interaction channels and simplifying the dynamics of collective states. Thus, at least 6 interaction channels are observed when atoms are arranged in the corners of the equilateral triangle. In turn, only two interaction channels are observed for the  $Z$ -oriented linear configuration.

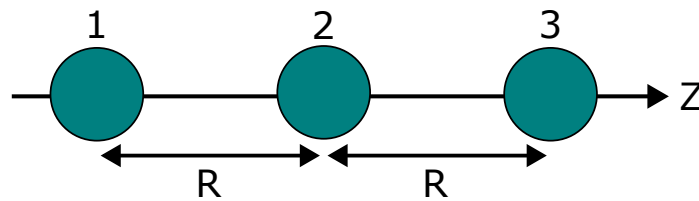


**Figure 4.1:** Atomic register configuration. Three Rb Rydberg atoms are arranged linearly at a distance  $R$  from each other along the  $Z$  axis. The  $Z$  axis is aligned with the direction of external electric field.

The description of the interatomic interaction used within this study is based on the physical model given earlier in Subsection 3.3.5. The operator of the dipole-dipole interaction between two neighboring atoms located along the  $Z$  axis can be written as [227]:

$$\begin{aligned} \hat{V}_{dd} &= \frac{e^2}{4\pi\epsilon_0 R^3} (\hat{a} \cdot \hat{b} - 3\hat{a}_z \hat{b}_z) = \\ &= -\frac{\sqrt{6}e^2}{4\pi\epsilon_0 R^3} \sum_{q=-1}^1 C_{1q1-q}^{20} \hat{a}_q \hat{b}_{-q}. \end{aligned} \quad (4.3)$$

Here  $\varepsilon_0$  is the dielectric constant,  $e$  is the electron charge, while  $\vec{a}$  and  $\vec{b}$  are the vectorial positions of the two Rydberg electrons. This operator couples only two-atom collective states with  $\Delta M = 0$ . The radial matrix elements of the dipole moment are calculated using a quasiclassical approximation [221]. For more information on the radial matrix elements calculation, see the Appendix A.

We consider collective Rydberg states  $|n_1 l_1 j_1 m_{j1}; n_2 l_2 j_2 m_{j2}; n_3 l_3 j_3 m_{j3}\rangle$  of the three rubidium atoms. The Förster energy defect is the difference between the energy of an arbitrary final collective state and of the initial collective state. In this subsection, we focus on the description of resonances for  $n = 80$ . Thus, in our simulations, we have taken into account all magnetic sublevels of the  $|80S_{1/2}\rangle$ ,  $|81S_{1/2}\rangle$ ,  $|82S_{1/2}\rangle$ ,  $|80P_{1/2}\rangle$ ,  $|80P_{3/2}\rangle$ ,  $|81P_{1/2}\rangle$  and  $|81P_{3/2}\rangle$  Rb Rydberg states. We assumed that  $M = 3/2$  for the initial collective state, and only considered collective three-atom states with  $M = 3/2$ , since the total moment projection is conserved for the spatial configuration which we have chosen. To reduce the complexity of the calculations, we neglected far-detuned collective states with the Förster energy defect larger than 1 GHz. The influence of neighboring  $D$  states is negligible due to large Förster defects on the order of 10 GHz.

#### 4.1.2.2. Stark effect

In order to take into account the Stark shifts of energy levels when an electric field is applied, the values of polarizabilities of the Rydberg states of Rb atoms were calculated by polynomial approximation of the Rydberg level energy trends. The energy trends were obtained by constructing single-atom Stark diagrams. The Hamiltonian of the system had the form (4.4). The diagonal elements of the Hamiltonian were calculated by formula (4.5), where  $\delta_i$  is the quantum defect of the corresponding level. The interaction with the electric field  $F$  was taken into account in the second order of perturbation theory by adding the interaction operator  $\hat{U} = -\hat{d}\vec{F}$  to the Hamiltonian of the unperturbed atomic system  $\hat{H}_1$ . The calculated Stark diagrams are shown in Figure 4.2. In order to increase the visibility of all relevant atomic levels, we present two different pictures for different values of magnetic quantum number. Polarizability values of atomic states obtained from the approximation are given in Table 4.1.

$$\hat{H} = \hat{H}_1 + \hat{U} = \begin{pmatrix} E_1 & \dots & E_2 & \dots \\ \dots & \dots & \dots & \dots \\ \dots & E_2 & \dots & \dots \\ \dots & \dots & \dots & E_1 \end{pmatrix} \quad (4.4)$$

$$E_1^{ii} = \frac{-Ry}{(n_{ii} - \delta_i)^2} \quad (4.5)$$

$$E_2^{ij} = \langle \Psi_j | \hat{U} | \Psi_i \rangle = \langle \Psi_j | -\hat{d}\vec{F} | \Psi_i \rangle \quad (4.6)$$

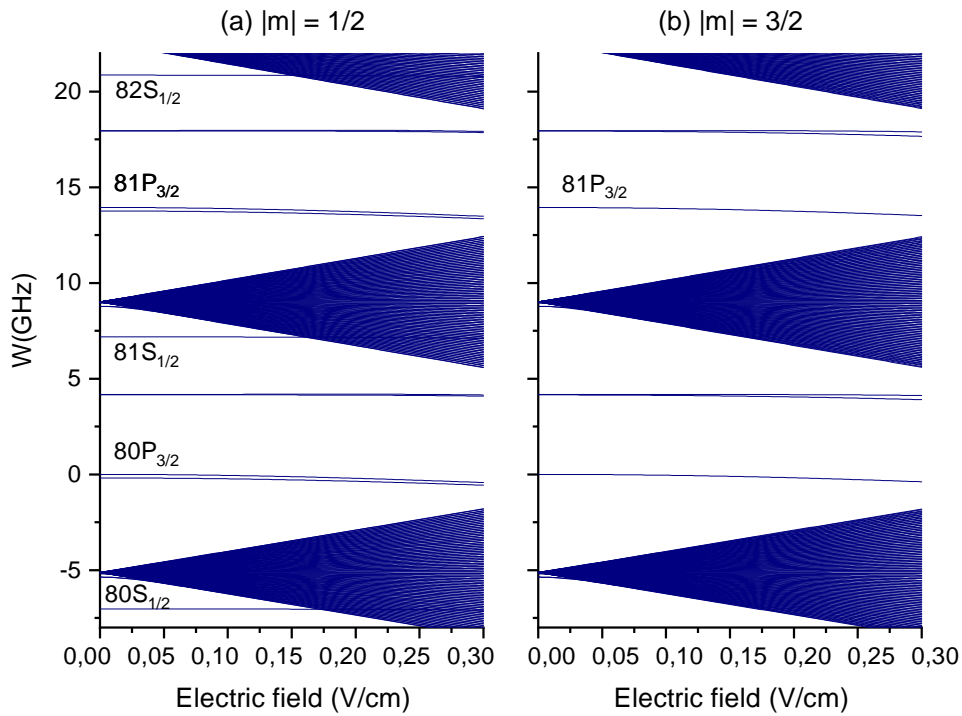


**Figure 4.2:** Numerically calculated Stark diagrams for high-lying ( $n \sim 80$ ) Rydberg levels. The energy of  $|80P_{3/2}\rangle$  state was taken as a reference in zero electric field. The diagrams for the value of momentum projection  $|m_j| = 1/2$  and  $|m_j| = 3/2$  are shown in Figures (a) and (b), respectively.

**Table 4.1:** Numerically estimated polarizabilities  $\alpha$  for relevant atomic levels. Polarizabilities are measured in  $GHz/[V/cm]^2$  units.

Atomic state	$\alpha$	Atomic state	$\alpha$
$ 80S_{1/2}(1/2)\rangle$	-670.9	$ 80P_{3/2}(3/2)\rangle$	-4513.1
$ 81S_{1/2}(1/2)\rangle$	-730.95	$ 81P_{1/2}(1/2)\rangle$	-4821.9
$ 82S_{1/2}(1/2)\rangle$	-757.5	$ 81P_{3/2}(1/2)\rangle$	-5713.9
$ 80P_{1/2}(1/2)\rangle$	-4427.4	$ 81P_{3/2}(3/2)\rangle$	-4927.4
$ 80P_{3/2}(1/2)\rangle$	-5259.95		

### 4.1.2.3. Rydberg lifetimes

In order to correctly calculate the population dynamics in atomic ensembles, one must take into account the finite lifetimes of Rydberg states. To account for them, we calculated the natural linewidths  $\gamma_{eff}$  of  $nL$  Rydberg states taking into account their interaction with thermal radiation. The  $\gamma_{eff}$  is known to be inversely proportional to the total lifetime of the Rydberg state  $nL$ . Taking into account the natural linewidth dependence on the blackbody radiation (4.7) and the spontaneous decay rate (4.8), we can express the  $\gamma_{eff}$  as (4.9) [169]. Note that in the given expressions  $A(nL \rightarrow n'L')$  denotes the Einstein coefficient for the transition between the states  $nl$  and  $n'l'$ ,  $\omega_{nn'}$  is the frequency of this transition, while  $\tau_0$  and  $\tau_{BBR}$  are the lifetimes of the states in view of spontaneous decay and blackbody radiation, respectively. The relevant values

**Table 4.2:** Numerically calculated  $\gamma_{eff}$ -factors for relevant atomic levels at room temperature (300 K). Substantial part of presented data was recollected from [169].

Atomic state	$\gamma, s^{-1}$	Atomic state	$\gamma, s^{-1}$
$ 80S_{1/2}\rangle$	0.0047	$ 80P_{3/2}\rangle$	0.00397
$ 81S_{1/2}\rangle$	0.0046	$ 81P_{1/2}\rangle$	0.0038
$ 82S_{1/2}\rangle$	0.0045	$ 81P_{3/2}\rangle$	0.00386
$ 80P_{1/2}\rangle$	0.0039		

for the gamma-factors are presented in Table 4.2. Numerical calculation of gamma-factors was performed using software produced by the authors of original article [169]. This software has been adapted for relevant Rydberg levels.

$$\gamma_{BBR} = \frac{1}{\tau_{BBR}} = \sum_{n'} A(nL \rightarrow n'L') \frac{1}{\exp(\omega_{nn'}/kT) - 1} \quad (4.7)$$

$$\gamma_0 = \frac{1}{\tau_0} = \sum_{E_{nL} > E_{n'L'}} A(nL \rightarrow n'L') \quad (4.8)$$

$$\gamma_{eff} = \frac{1}{\tau_{eff}} = \gamma_0 + \gamma_{BBR} \quad (4.9)$$

#### 4.1.2.4. General Hamiltonian

Now, having defined all necessary constants, we can give the general form of the proposed physical model of the many-body interactions. Below you can see the interaction Hamiltonian in the collective states basis represented by formula (4.10). The elements of the Hamiltonian are defined by formulas (4.11-4.14). Note that the electric and magnetic fields presented in the system are directed along the axis  $Z$ , which is allocated as an axis of quantization. As can be seen from the equation (4.13), the diagonal elements include the terms related to the account of the Stark level shift, the energy of atomic levels, and the Zeeman effect.

$$\hat{H} = \begin{pmatrix} E_{pol} & \dots & E_{dd} & \dots \\ \dots & \dots & \dots & \dots \\ \dots & E_{dd} & \dots & \dots \\ \dots & \dots & \dots & E_{pol} \end{pmatrix} \quad (4.10)$$

$$E_{pol}^{ii} = \langle \Psi_i | \hat{V}_{pol}^{ii} | \Psi_i \rangle \quad (4.11)$$

$$E_{dd}^{ij} = \langle \Psi_j | \hat{V}_{dd} | \Psi_i \rangle \quad (4.12)$$

$$E_{pol}^{ii} = \sum_{j=1}^3 2\pi \left( -\frac{Ry}{(n_j^{ii} - \delta_j^{ii})^2} + \alpha_j^{ii} F^2 + \mu_B B(m_j^{ii} g_j^{ii}) \right) \quad (4.13)$$

$$\hat{V}_{dd} = \frac{e^2}{4\pi\epsilon_0 R^3} (\hat{a} \cdot \hat{b} - 3\hat{a}_z \hat{b}_z) = -\frac{\sqrt{6}e^2}{4\pi\epsilon_0 R^3} \sum_{q=-1}^1 C_{1q1-q}^{20} \hat{a}_q \hat{b}_{-q} \quad (4.14)$$

In the framework of the given physical model we have compiled a system of Schrödinger equations (4.16) in the collective states basis, which was described above. To take into account the finiteness of the Rydberg states lifetimes, an additional operator  $\hat{\Gamma}$  was introduced. This operator is diagonal, and its elements are represented by the total  $\gamma$ -factors of the collective states.

$$\Psi = \sum_j C_j \psi_j e^{-iE_j t/\hbar} \quad (4.15)$$

$$i\hbar \frac{d\Psi}{dt} = \left( \hat{H} - \frac{i}{2} \hat{\Gamma} \right) \Psi \quad (4.16)$$

$$\hat{\Gamma} = \begin{pmatrix} \Gamma_{11} & 0 & \dots \\ 0 & \dots & 0 \\ \dots & 0 & \Gamma_{nn} \end{pmatrix} \quad (4.17)$$

$$\Gamma_{ii} = \sum_{j=1}^3 \gamma_i \quad (4.18)$$

### 4.1.3. Resonance simulation results

The two-body and three-body transitions (described earlier by equations (4.1) and (4.2), respectively) were numerically modeled in an ensemble of three Rb atoms for  $n = 80$ . Figure 4.3 shows Förster resonances as the intersections of collective energy levels in external electric field. Note that this image is based on the previously obtained single atom Stark diagrams, thus, does not take into account dipole-dipole interactions. Nevertheless, it provides a preliminary estimate of the mutual location of the resonances. We see that the two-body resonance (crossing 1) corresponds to an electric field of  $F = 0.1172$  V/cm, while the three-body resonance (crossing 2) is expected at a field of  $F = 0.123$  V/cm.

We now proceed to a full-fledged simulation of multiparticle resonances in a system of three linearly arranged Rydberg atoms, in accordance with the physical model described in the previous subsection. We solved the Schrödinger equation for the probability amplitudes of the 165 collective states taking into account Rydberg lifetimes [169]. For simplicity, we consider an open system and neglect the return of the population from Rydberg to the ground

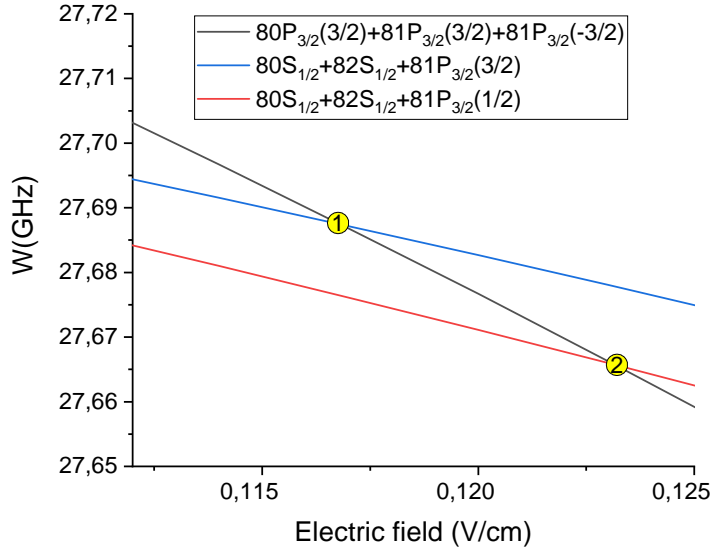


**Figure 4.3 :** Numerically calculated Stark diagram for collective Rydberg levels. The black line represents the initial state of the atomic register  $|80P_{3/2}(3/2); 81P_{3/2}(3/2); 81P_{3/2}(-3/2)\rangle$ , while the blue and red lines represent the  $|80S_{1/2}; 82S_{1/2}; 81P_{3/2}(3/2)\rangle$  and  $|80S_{1/2}; 82S_{1/2}; 81P_{3/2}(1/2)\rangle$  final states, respectively. The intersections 1 and 2 correspond to the two- and three-body Förster resonances (4.1) and (4.2), respectively.

state due to spontaneous decay. We have numerically calculated the dependence of the fraction  $f$  of atoms in the final state  $|80S_{1/2}\rangle$  on the DC electric field for the ensembles of two and three Rydberg atoms, initially prepared in the collective states  $|80P_{3/2}(3/2) 81P_{3/2}(-3/2)\rangle$  or  $|80P_{3/2}(3/2) 81P_{3/2}(3/2) 81P_{3/2}(-3/2)\rangle$ , respectively. For both resonances, we considered the interaction time of  $1.8 \mu\text{s}$ . The Stark shift of the Rydberg states in an external electric field was taken into account using polarizabilities of the Rydberg states, numerically calculated for a single atom in an external DC electric field [228]. We also introduced a Zeeman splitting of the Rydberg states in an external magnetic field in order to lift the degeneracy of magnetic sublevels and shift the three-body resonance peaks. Finite Rydberg lifetimes were taken into account by considering decay rates  $\gamma_i$  of each individual Rydberg state. For more detail on the model, please see the previous subsection.

Figure 4.4 shows the results of the numerical simulation of the Förster resonances. The two-body Förster resonance is observed as an increase of the fraction  $f$  of atoms in the final state  $|80S_{1/2}\rangle$  if two atoms are initially prepared in a collective state  $|80P_{3/2}(3/2) 81P_{3/2}(-3/2)\rangle$ . The numerically calculated dependence of  $f$  on the DC electric field for two atoms at interatomic distance  $25 \mu\text{m}$  and interaction time  $1.8 \mu\text{s}$  is shown in Fig. 4.4(a). The resonance is observed in the electric field of  $0.117 \text{ V/cm}$ , which corresponds to the position of the two-body Förster resonance 1 in Fig. 4.3. This resonance is insensitive to the magnetic field due to the compensation of the Zeeman shifts for two-atom  $|PP\rangle$  and  $|SS\rangle$  collective states with the total momentum projection  $M = 0$ .

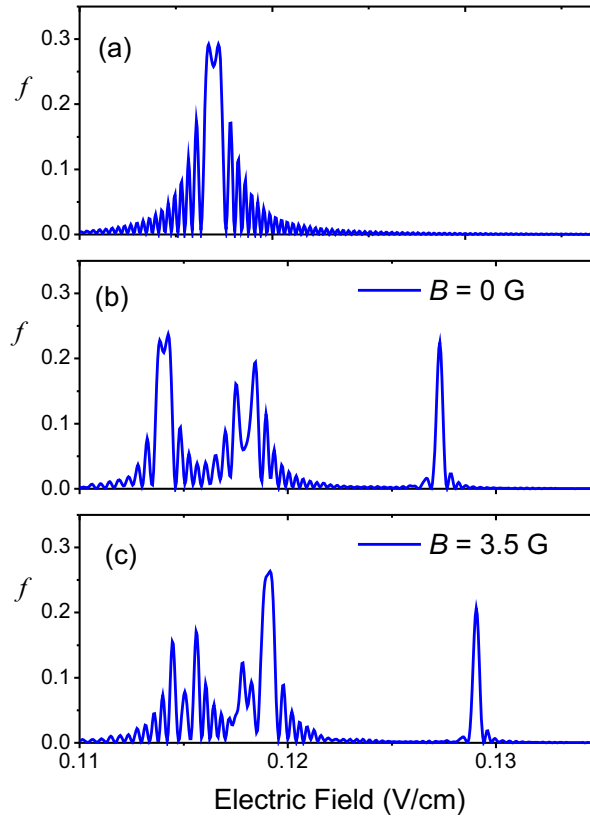


**Figure 4.4 :** Numerically calculated dependence of the fraction  $f$  of atoms in the final  $|80S_{1/2}\rangle$  state on the DC electric field for the interaction time of  $\tau = 1.8 \mu\text{s}$ : (a) for two atoms initially prepared in the collective state  $|80P_{3/2}(3/2)81P_{3/2}(-3/2)\rangle$  at the interatomic distance  $R = 25 \mu\text{m}$ ; (b) for the three-atom ensemble initially prepared in the state  $|80P_{3/2}(3/2)81P_{3/2}(3/2)81P_{3/2}(-3/2)\rangle$  at the interatomic distance  $R = 12.5 \mu\text{m}$  in the external magnetic field  $B = 0 \text{ G}$ ; (c) for the three-atom ensemble initially prepared in the state  $|80P_{3/2}(3/2)81P_{3/2}(3/2)81P_{3/2}(-3/2)\rangle$  at the interatomic distance  $R = 12.5 \mu\text{m}$  in the external magnetic field  $B = 3.5 \text{ G}$ .

$$\begin{aligned}
 & |80P_{3/2}(3/2)81P_{3/2}(3/2)81P_{3/2}(-3/2)\rangle \\
 & \rightarrow |80S_{1/2}(1/2)82S_{1/2}(1/2)81P_{3/2}(1/2)\rangle
 \end{aligned} \tag{4.19}$$

If we place a third atom in the state  $|81P_{3/2}(3/2)\rangle$  between the two atoms, which are prepared in states  $|80P_{3/2}(3/2)\rangle$  and  $|81P_{3/2}(-3/2)\rangle$ , respectively, additional three-body resonances arise. The three-body transition (4.19) couples initial and final collective three-atom states through the intermediate state  $|80S_{1/2}(1/2)81P_{3/2}(3/2)82S_{1/2}(-1/2)\rangle$ . We note that other three-body interaction channels through different intermediate states also exist and may contribute to the population transfer and phase shifts [193].

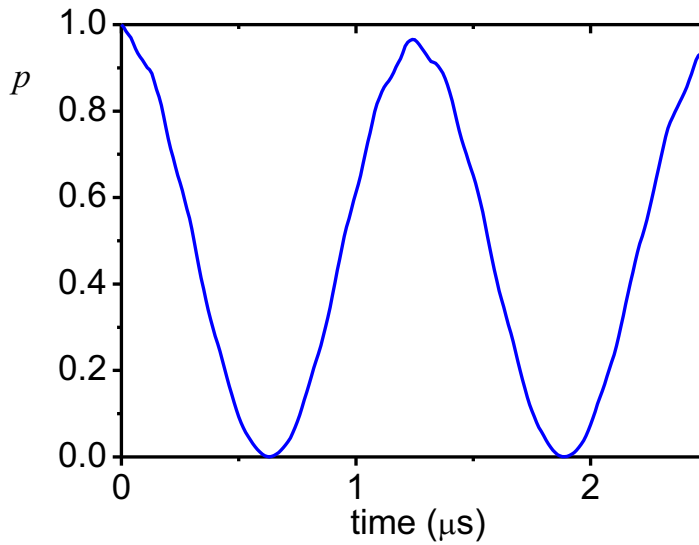
The calculated dependence of the fraction  $f$  of atoms in the final state  $|80S_{1/2}(1/2)\rangle$  on the controlling DC electric field for three interacting atoms in the magnetic field is shown in

Fig. 4.4(b) for  $B = 0$  G and in Fig. 4.4(c) for  $B = 3.5$  G. The atoms are arranged linearly at a distance  $R = 12.5$   $\mu\text{m}$  from each other. The direction of the magnetic field is opposite to the direction of the electric field in order to shift the three-body resonances to the right-hand side. Narrow three-body peaks are clearly observed in Figs. 4.4(b) and 4.4(c). The coherent three-body resonance is split due to always-resonant exchange interactions [193]. Therefore the positions of the three-body resonances are different from 0.123 V/cm if the interaction energy is sufficiently large [193]. The shape of the two-body resonance is modified due to the three-body incoherent population transfer to state  $|80S_{1/2}\rangle$ . The incoherent transfer occurs when the intermediate state (for example,  $|80S_{1/2}(1/2) 81P_{3/2}(3/2) 82S_{1/2}(-1/2)\rangle$ ) is populated. In contrast to Fig. 4.4(a), the positions of the resonances in Figs. 4.4(b) and 4.4(c) are sensitive to the external magnetic field.

The spatial configuration which we selected is advantageous for the observation of three-body interactions due to suppression of the resonant two-body interaction between pairs of atoms despite the large interaction energies used. Due to the selection rule  $\Delta M = 0$ , collective state of atoms 1 and 2  $|80P_{3/2}(3/2) 81P_{3/2}(3/2)\rangle$  is not dipole coupled to two-atom state  $|80S_{1/2}(1/2) 82S_{1/2}(1/2)\rangle$ . Therefore, the two-body interaction between atoms 1 and 2 is forbidden for these particular states. The two-body interaction between atoms 2 and 3, which are both excited into  $|81P_{3/2}\rangle$  state, is suppressed due to the large (157 MHz) Förster energy defect for the interaction channel  $|81P_{3/2}(3/2) 81P_{3/2}(-3/2)\rangle \rightarrow |81S_{1/2}(1/2) 82S_{1/2}(-1/2)\rangle$  in zero electric field, which increases further to 283 MHz when resonant electric field of 0.123 V/cm is applied. However, we should additionally take into account the always-resonant exchange interaction appearing due to excitation hopping between  $S$  and  $P$  Rydberg atoms [107]. It drives the unwanted transition  $|81P_{3/2}(3/2) 81P_{3/2}(-3/2)\rangle \rightarrow |81P_{3/2}(-3/2) 81P_{3/2}(3/2)\rangle$  through several off-resonant intermediate states.

Finally, the interaction between atoms 1 and 3, which are prepared in states  $|80P_{3/2}\rangle$  and  $|81P_{3/2}\rangle$  is enhanced by the two-body Förster resonance  $|80P_{3/2}(3/2) 81P_{3/2}(-3/2)\rangle \rightarrow |80S_{1/2}(1/2) 82S_{1/2}(-1/2)\rangle$ . At the same time, it is reduced due to the twice larger distance between these atoms compared to the distance between the neighboring atoms.

If we tune the electric field to the resonant value  $F = 0.11905$  V/cm in magnetic field  $B = 3.5$  G, coherent Rabi-like population oscillations are observed for the probability  $p$  to find the ensemble back in the initially prepared state, as shown in Fig. 4.5. This is a remarkable feature of the three-body Förster resonance, which has not been demonstrated experimentally yet [193]. The decrease in the contrast of the oscillations as time increases is mostly caused by finite lifetimes of the Rydberg states, although the leakage of the population to other collective three-atom Rydberg states can also be important.



**Figure 4.5 :** Time dependence of the population  $p$  of the initial state  $|80P_{3/2}(3/2)81P_{3/2}(3/2)81P_{3/2}(-3/2)\rangle$  for the interatomic distance  $R = 12.5 \mu\text{m}$ , the external magnetic field  $B = 3.5 \text{ G}$  and the electric field  $F = 0.11905 \text{ V/cm}$ .

#### 4.1.4. Toffoli gate proposal

In this subsection, we describe the proposed original scheme for the Toffoli gate implementation based on the three-atom resonant transition (4.2) in an ordered ensemble of three Rb atoms for  $n = 80$ . Toffoli gate (or *CCNOT* gate) is a basic example of a three-qubit quantum gate. It represents a generalization of the well-known *CNOT* gate for the three-qubit case, and performs the operation of doubly-controlled negation. The state of the target qubit is reversed if both controlling qubits are in logical state  $|1\rangle$  when the Toffoli gate is applied [229]. As shown in Subsection 2.1.2.2, this gate can be implemented using a controlled-controlled-*Z* (*CCZ*) gate, which shifts the phase of the target qubit by  $\pi$  if both controlling qubits are in state  $|1\rangle$ , and two Hadamard gates applied to the target qubit before and after the *CCZ* gate (see Fig 4.6(a)). Thus, the task of Toffoli gate implementation can be reduced to the *CCZ*-gate implementation task.

Förster resonances provide a way to induce a fast phase dynamics on the collective states of a multi-atomic system. In principle, a doubly-controlled phase gate can be based on coherent Rabi-like oscillations at exact resonance, which should lead to a  $\pi$  phase shift of the collective state after the end of the  $2\pi$  pulse. This is similar to two-qubit controlled phase gates, considered in previous works [59, 154, 230]. However, off-resonant two-body Förster interactions result in a complex behavior of the collective states phases. Consequently, it is necessary to develop an alternative approach to the quantum gate implementation that takes into account the presence of two- and three-body interactions.

The proposed scheme of the Toffoli gate is shown in Fig. 4.6(b). Three Rb atoms are isolated in individual optical dipole traps which are evenly located along the  $Z$  axis with distance  $R$

between neighboring traps. The  $Z$  axis is still chosen along the controlling DC electric field. In [193] we revealed that this configuration provides maximum coherence of the population oscillations due to specific selection rules, which close some unwanted interaction channels (see Subsection 3.3.7), and this result was indeed verified in Figure 4.5. The logical states  $|0\rangle$  and  $|1\rangle$  are hyperfine sublevels of the ground state  $5S_{1/2}$  (see Subsection 2.3.3). To couple the logical states, two-photon Raman laser pulses, which do not populate the intermediate excited state  $5P$  [231], can be used. As an alternative, they can be replaced by microwave pulses with individual addressing. This can be achieved using an intense off-resonant laser acting on a selected qubit to AC Stark shift its energy levels into resonance with the microwave radiation [232–234]. Note that in our studies we focus on possible limits linked to the Rydberg interactions and assume both Rydberg excitation and individual qubit gates to be perfect.

The Toffoli gate can be implemented using 8 laser pulses. The first Hadamard gate of Fig. 4.6(a) is replaced in Fig. 4.6(b) by the  $\pi/2$  rotation around the  $Y$  axis, which is implemented by a laser pulse numbered 1. Then, the three laser pulses 2-4 are simultaneously applied to all three qubits. They drive the transitions  $|1\rangle \rightarrow |r\rangle$  for the left control qubit,  $|0\rangle \rightarrow |r'\rangle$  for the target qubit and  $|1\rangle \rightarrow |r''\rangle$  for the right control qubit, respectively. Here  $|r\rangle = |80P_{3/2}(3/2)\rangle$ ,  $|r'\rangle = |81P_{3/2}(3/2)\rangle$  and  $|r''\rangle = |81P_{3/2}(-3/2)\rangle$ . The numbers in the parentheses are the projections of the momentum  $m_j$  on the  $Z$  axis. Note that we consider a single-photon excitation scheme to facilitate numerical calculations. Nevertheless, in a real experiment, the three-photon excitation scheme will be preferable to compensate for Doppler shifts.

Similarly to the proposal [235], we consider Rydberg excitation in different Rydberg states. Our analysis has shown that with the selected states it is possible to obtain high fidelity due to long radiative lifetimes, large dipole moments and specific three-body interaction channels.

We assume that for a selected distance between the atoms, Rydberg interaction is sufficiently weak to avoid Rydberg blockade. Depending on the initial state of the atoms, after laser pulses 2-4, the number of the excited Rydberg atoms varies from zero to three. When two or three Rydberg atoms are excited, the interaction shifts the phases of the collective three-body atomic states. These phases can be controlled by external electric and magnetic fields if the interactions are tuned to a three-body Förster resonance.

At the final stage, Rydberg atoms are de-excited by laser pulses 5-7. Raman laser or microwave pulse 8 drives the additional  $-\pi/2$  rotation of the target qubit around the  $Y$  axis, which is equivalent to the second Hadamard gate in Fig. 4.6(a).

The timing diagram of all controlling pulses is shown in Fig. 4.6(c). In our numerical model, pulses 1-8 have the duration of 10 ns and are applied in a zero electric field. After the laser excitation ends, the electric field is switched on. The magnetic field is always present, since it cannot be rapidly switched in experiments. Short laser pulses with high intensity are required to reduce the effect of Rydberg blockade by increasing the Rabi frequencies, which leads to a blockade breakdown. The phase shift of the Rydberg energy levels due to the non-zero electric field is compensated for by adjusting the phases of laser pulses 5-7.

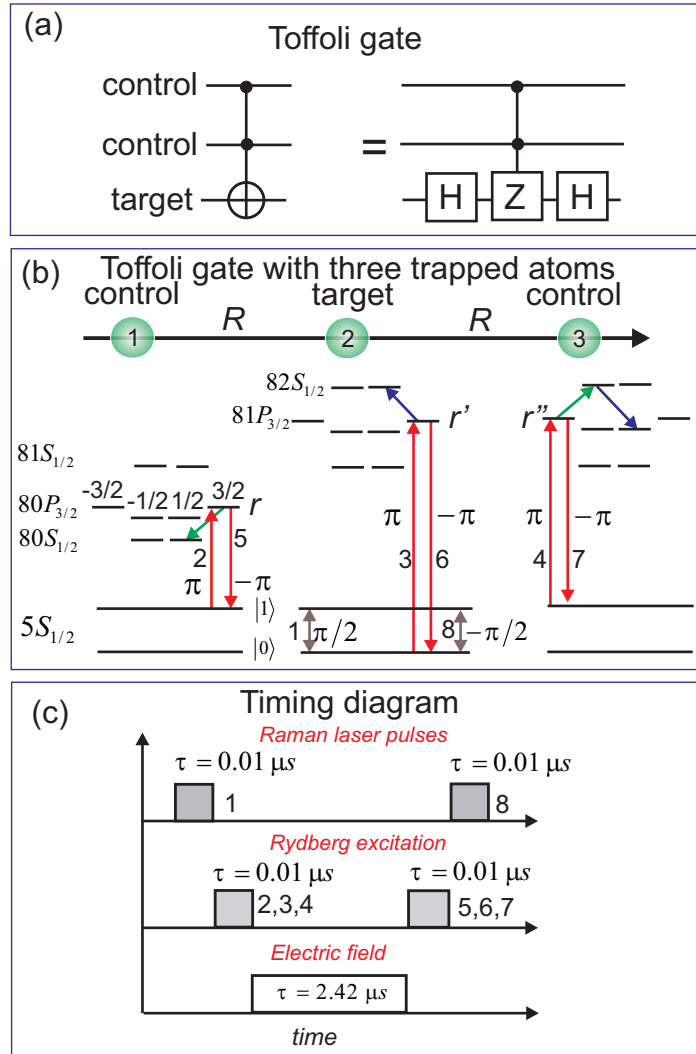


**Figure 4.6 :** (a) General scheme of a three-qubit Toffoli gate. (b) Scheme of the Toffoli gate based on three-body Rydberg interactions. Three atoms are located in individual optical dipole traps along the  $Z$  axis directed along the controlling DC electric field. Laser Raman (or microwave) pulses 1 and 8 drive transitions between the logical states  $|0\rangle$  and  $|1\rangle$  of the target qubit. Laser pulses 2-7 excite and de-excite the chosen Rydberg states of the three atoms. The phase shift due to the two-body interaction of atoms 1 and 3 is  $\pi$  if they are both excited into Rydberg states and atom 2 remains in the ground state. Otherwise, all phase shifts are zeroed by the three-body interaction. (c) Timing diagram of the pulses in the proposed three-qubit Toffoli gate.

For the implementation of the Toffoli gate it is necessary to find the conditions for which the three-body and two-body interactions result in the correct phase shifts of all possible initially excited collective states. Specifically, in the case of excitation of atoms 1 and 3, the two-body resonance should lead to a  $\pi$  phase shift of the collective state, while in the other cases the phase shift should be fully compensated. The necessary phase and population dynamics obtained from the gate simulations is shown in Fig. 4.7. We numerically calculated the time dependences

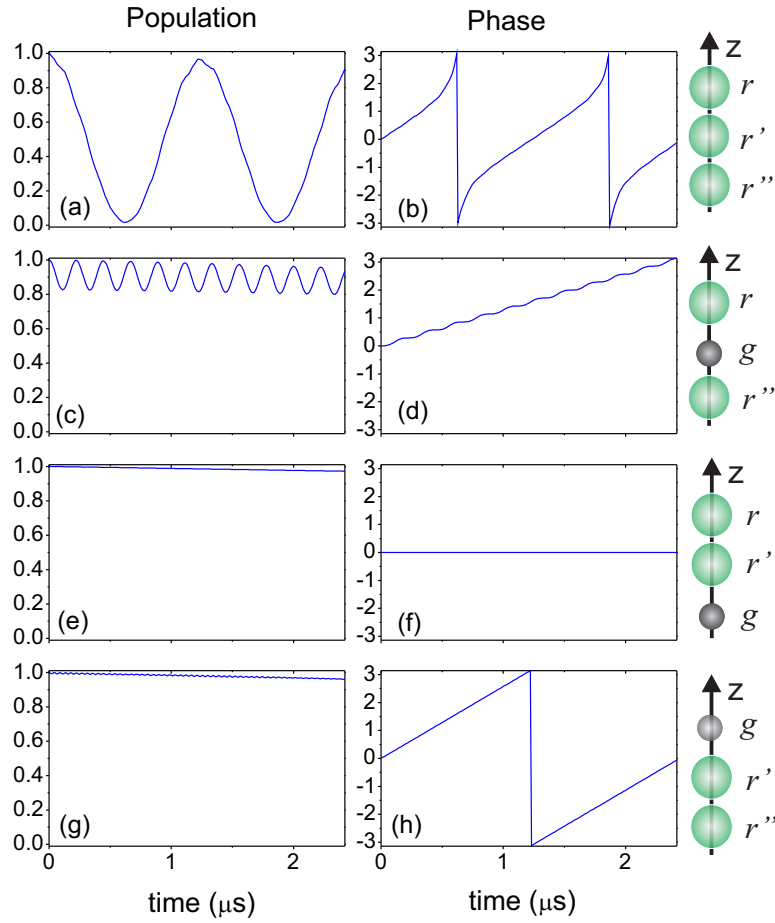


**Figure 4.7 :** Numerically calculated time dependences of the population and phase of the collective states of three interacting atoms  $|rr'r''\rangle$  [(a),(b)];  $|rg'r''\rangle$  [(c),(d)];  $|rr'r'g\rangle$  [(e),(f)];  $|gr'r''\rangle$  [(g),(h)]. The interatomic distance is  $R = 12.5 \mu\text{m}$ , the electric field is  $F = 0.11912 \text{ V/cm}$  and the magnetic field is  $B = 3.5 \text{ G}$ .

of the population and phase of the initially excited collective two-atom or three-atom Rydberg states in the electric field  $F = 0.11912 \text{ V/cm}$  and magnetic field  $B = 3.5 \text{ G}$  for the interatomic distance  $R = 12.5 \mu\text{m}$ . The electric field is very close to exact resonance value of  $0.11905 \text{ V/cm}$ , and it is supposed to be set with high precision, as the three-body resonances are extremely narrow. A small variation of the electric field from the exact resonance does not significantly affect the amplitude of the Rabi oscillations, but modifies the phase of the state, allowing to reduce phase errors. If collective three-atom Rydberg state  $|rr'r''\rangle$  is initially excited, we observe almost-resonant Rabi-like oscillations. After time  $\tau = 2.42 \mu\text{s}$  the system returns to the initial state with almost zero phase shift, as shown in Figs. 4.7(a) and 4.7(b), respectively.

If the ensemble is initially excited into state  $|rg'r''\rangle$  (here  $g$  is the ground state which can be either  $|0\rangle$  or  $|1\rangle$  logic state, depending on the location of the atom in Fig. 4.5(b)), the off-resonant two-body Förster interaction  $|80P_{3/2}81P_{3/2}\rangle \rightarrow |80S_{1/2}82S_{1/2}\rangle$  shifts the phase of the initially excited state by  $\pi$ , as shown in Figs. 4.7(c) and 4.7(d). This phase shift is sensitive to the electric field which acts directly on the Förster defect. It corresponds to the controlled phase shift when

all three atoms are in state  $|1\rangle$  prior to the Rydberg excitation in Fig. 4.6(b). The population of the initial state is reduced by approximately 10% due to finite Rydberg lifetimes and leakage of the population to other collective states by Rydberg interaction. These are found to be the major sources of the gate error.

If the ensemble is initially excited into state  $|rr'g\rangle$  (Figs. 4.7(e) and 4.7(f)), there is no interaction due to the selection rule  $\Delta M = 0$ , and the probability to find the ensemble in the initial state reduces only due to finite Rydberg lifetimes.

If the ensemble is initially excited into state  $|gr'r''\rangle$  [Figs. 4.7(g) and 4.7(h)], the always-resonant two-body exchange interaction  $|81P_{3/2}(3/2)81P_{3/2}(-3/2)\rangle \rightarrow |81P_{3/2}(-3/2)81P_{3/2}(3/2)\rangle$  occurs in a multi-step manner via intermediate  $S$  states, including  $|81S82S\rangle$  collective state. This leads to the phase shift of the initially excited state, which is compensated for to zero in Fig. 4.7(h). This phase shift is found to be weakly sensitive to the electric field.

Finally, when only one atom in the ensemble is temporarily excited into the Rydberg state  $|r\rangle$ ,  $|r'\rangle$  or  $|r''\rangle$ , the  $\pi$  and  $-\pi$  pulses, shown in Fig. 4.6(b), will return the system into the initial state with zero phase shift. However, temporary Rydberg excitation will result in population loss due to the finite lifetimes of Rydberg states. The trivial case is when no Rydberg atoms are excited. No population or phase dynamics are observed in this case.

#### 4.1.5. Numerical optimization

We applied the following optimization procedure to find the experimental conditions used in Fig. 4.7:

1. For the selected interatomic distance we find the value of the magnetic field when the two-body and three-body Förster resonances weakly overlap, as shown in Figs. 4.4(b) and 4.4(c). This overlapping should be weak enough to avoid distortion of coherent Rabi-like oscillations, shown in Fig. 4.7(a). At the same time, two-body interactions must be sufficiently large to produce the  $\pi$  phase shift in Fig. 4.7(d) during the interaction time, which is substantially smaller than Rydberg lifetime.
2. We select the value of the electric field near the three-body resonance and find the time interval that compensates for the phase shift due to exchange interaction, as shown in Fig. 4.7(h).
3. We adjust the value of the electric field to obtain the phase shift close to  $\pi$  for the off-resonant two-body Förster interaction (Fig. 4.7(d)).
4. We adjust the value of the magnetic field to tune the frequency of three-body Rabi-like oscillations and to find the conditions when the system returns back to the initial state with zero phase shift, as shown in Figs. 4.7(a) and 4.7(b).

If the last step is not successful, a different interatomic distance should be selected. A compromise has to be found as at larger interatomic distances longer time intervals are required for phase accumulation. Therefore, the fidelity decreases due to finite Rydberg lifetimes. At the same time, at smaller interatomic distances both overlapping of the three-body and two-body resonances and exchange interactions become larger, and it is difficult to find suitable experimental conditions.

To automatize the described optimization procedure, specialized software was developed.

The optimization was performed using numerical nonlinear global optimization methods. The parameters of the algorithm were the interatomic distance  $R$ , the gate time  $T$ , and the values of external electric and magnetic fields. In the preparatory step of the algorithm, the resonant electric field was determined for the current distance value by numerical simulation within the physical model described above. For the purpose of the gate implementation, values near the left three-body peak from Figure 4.4(b) were scanned at a resolution of  $10^{-6}$  V/cm. The scanning range was  $\pm 0.01$  V/cm from the peak value to prepare for the application of the algorithm. Next, steps 1-4 were implemented to determine the required parameter values. Based on this initial estimation, a Nelder-Mead optimization [236] was further carried out using an iterative method. The parameters were varied within predetermined ranges in the first iteration, but narrowed for subsequent iterations. Thus, the interatomic distance  $R$  was varied at the first iteration within  $\pm 0.1$   $\mu\text{m}$  relative to a predetermined value, the interaction time  $T$  within  $\pm 0.1$   $\mu\text{s}$ , the electric field within  $\pm 0.001$  V/cm, and the magnetic field within  $\pm 0.1$  G. Each iteration of the algorithm involved  $10^2$  steps within the specified limits for each parameter, calculating the gate fidelity at each step. As a result, the optimization algorithm produced a new estimate for the parameter values. After that, the iteration was terminated and the parameter variation bounds were narrowed by a factor of 3. The next iteration repeated all the described steps, excluding the preparatory stage. Thus, successively maximizing the quantum gate fidelity, we obtained values for the experimental parameters. Note that this optimization did not take into account the durations of Hadamard gates and excitation pulses (which were considered perfect) when calculating the fidelity value. Nevertheless, we implemented an additional simulation to take them into account. According to the analysis performed, the obtained fidelity values had a direct correlation in both simulations. Thus, the preferred parameter values for the full gate scheme were not significantly different from the values obtained as a result of the optimization. The final adaptation of the parameters was carried out using a direct search algorithm.

#### 4.1.6. Gate fidelity

We have numerically calculated the truth table for our Toffoli gate protocol (Fig. 4.8). To estimate the gate fidelity, we have used the method proposed in [237]. This method was also described in detail in Subsection 2.1.5. We considered 6 single-qubit configuration states  $|0\rangle$ ,  $|1\rangle$ ,  $(|0\rangle + |1\rangle)/\sqrt{2}$ ,  $(|0\rangle - |1\rangle)/\sqrt{2}$ ,  $(|0\rangle + i|1\rangle)/\sqrt{2}$  and  $(|0\rangle - i|1\rangle)/\sqrt{2}$ . We formed a set of three-qubit states as all  $6^3 = 216$  combinations of three single-qubit basis states. We simulated the density matrices  $\rho_{sim}$  of all final states after Toffoli gate was applied to each initial state. Then we calculated the fidelity of each final state comparing to the etalon state  $\rho_{et}$ , which is the final state of the ensemble after the ideal Toffoli gate is performed, as follows [1]:

$$F = \text{Tr} \sqrt{\sqrt{\rho_{et}} \rho_{sim} \sqrt{\rho_{et}}} \quad (4.20)$$

After averaging over all 216 states the simulated gate fidelity reaches 98.3%. It is limited mainly by decay of Rydberg states, undesirable population transfer to different Rydberg states

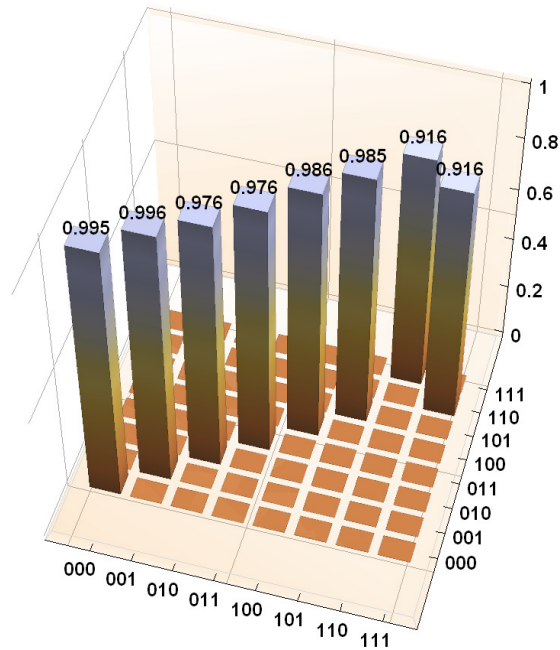


**Figure 4.8:** Numerically simulated truth table for the Toffoli gate protocol.

due to off-resonant Rydberg interactions and finite efficiency of phase compensation at three-body Förster resonance. Although this value is below the threshold for fault-tolerant quantum computation, it was substantially better than the values reported for other protocols [177] at the time of the first publication. We still believe that presented scheme can be useful for many-body quantum simulations with Rydberg atoms in optical lattices [238–242]. Additional decrease of gate fidelity can result from dephasing between the laser pulses due to atomic motion. Coherent Rydberg excitation by short laser pulses with large Rabi frequencies which are necessary to avoid Rydberg blockade is also a challenging task. However, such technical difficulties were present for most of the schemes of quantum computing based on Rydberg atoms in 2018 [177].

#### 4.1.7. Conclusion

In this study, we proposed and numerically investigated new schemes of two-body and three-body Förster transitions. We also proposed a protocol to implement a three-qubit Toffoli gate based on resonant Borromean three-body interactions in the ensemble of Rb Rydberg atoms trapped in three individual optical dipole traps. The described protocol represents the first proposal for the realization of multiqubit gates based on Stark-induced Förster resonance. The collective phase shifts induced by Rydberg interactions are controlled by external electric and magnetic fields. We have shown that it is possible to reach a fidelity exceeding 98% for a short gate duration of less than 3  $\mu\text{s}$ , thus significantly exceeding the performance of other Toffoli gates available at the time of publication. The scheme we proposed relies on the resonant long-range Rydberg interactions. This reduces the effect of the complex structure of Rydberg energy levels on gate fidelity, which appears to be the major source of gate error if the Rydberg

interactions are strong [243]. The proposed protocol also allows gates for larger interatomic distances compared to standard blockade gates based on van der Waals interactions.

It is also important to acknowledge the organisations that provided financial resources to support the implementation of the research presented in this section. This work was supported by Russian Science Foundation Grant № 16-12-0083 in the part of simulation of the Toffoli gate and Grant № 18-12-00313 in the part of the simulation of three-body interactions, RFBR Grant № 17-02-00987 in the part of simulation of the off-resonant Rydberg interactions and Grant № 16-02-00383 in part of simulation of coherent three-body Förster resonances, and Novosibirsk State University, the public Grant CYRAQS from Labex PALM (ANR-10-LABX-0039) and the EU H2020 FET Proactive project RySQ (Grant №. 640378). M.S. was supported by the ARL-CDQI program through Cooperative Agreement № W911NF-15-2-0061 and NSF award № 1720220.

## 4.2. FSSC three-body Förster resonances

In the previous section the concept of quantum Toffoli gate implementation based on three-body Förster resonances in ordered ensembles of Rb atoms was outlined. The high accuracy of the gate was ensured by the resonance interactions coherence for the chosen spatial geometry of the atomic register, combined with long lifetimes of the Rydberg atomic states. The quantum gate was controlled by an external DC electric field providing accurate Stark shifts of the collective atomic states. An external magnetic field was also used to provide isolation of resonances to increase the coherence of the three-atom interaction. The demonstrated scheme meets modern standards of quantum computing, and, according to the conclusion of the paper [98], can be extremely useful for the realization of various quantum algorithms.

Nevertheless, certain drawbacks inherent in the proposed gate protocol have been revealed. First, the shown three-body resonances  $nP_{3/2} + (n + 1)P_{3/2}(m_1) + (n + 1)P_{3/2}(m_2) \rightarrow nS_{1/2} + (n + 2)S_{1/2} + (n + 1)P_{3/2}(m_3)$  require simultaneous excitation of different Rydberg states. This significantly complicates the experimental realization of the quantum gate, since the use of several sources of laser radiation is required. The sources must be mutually coherent, since phase noise can negatively affect the final accuracy of the gate. An additional obstacle is presented by the need to pair different ground states with the Rydberg states. As shown in Fig. 4.6(b), the laser excitation of the first and third atoms occurs from the  $|1\rangle$  state, while the target atom is excited from the  $|0\rangle$  state.

Second, the strong influence of two-body processes significantly complicates the population and phase dynamics in the three-atom system. As shown in Subsection 4.1.3, two-body and three-body resonances occur for close values of the external controlling electric field, since the energy defect between the states with different momentum projections, determining the nature of resonance, is relatively small. When the external field is fine-tuned to the three-body resonance, two-body interactions are still observed, which, being non-resonant, still lead to significant population and phase dynamics. In this regard, additional tricks, such as the use of an external magnetic field for peak isolation, were required to realize the Toffoli gate. Note that the need to apply an external homogeneous magnetic field also significantly complicates

a potential experimental realization.

The approach applied to gate implementation in article [98], although showing high accuracy, appears to be counterintuitive. As shown in Subsections 3.3.4 and 4.1.4, coherent Rabi-like population oscillations in a three-body process are accompanied by a phase change of the system states. Each oscillation period corresponds to a  $\pi$  phase shift of the collective state. It would be logical to use this property to realize the  $CCZ$  gate, which requires exactly the  $\pi$  phase change, as was shown in Subsection 2.1.2.2. Then, during the first oscillation of the population, the phase of the system would reach the required value, and the only difficulty would be to compensate for the additional phases accumulated as a result of two-body processes. Unfortunately, the complex behavior of multiparticle Rydberg transitions did not allow us to achieve the necessary phase and population dynamics in the proposed scheme, and we had to invent a different, less rational approach.

Although the proposed protocol has demonstrated an accuracy significantly superior to all analogs available at the time of publication, further improvements in the gate fidelity were necessary for its compatibility with quantum error correction. Additional efforts were also needed to improve the robustness of the gate to variations in experimental parameters.

The described drawbacks motivated us to search for new possibilities to implement three-qubit quantum gates using Förster resonances. The primary task in this regard was to search for new three-body interaction schemes suitable for the realization of quantum gates and investigate them. In this section, we describe fine-structure-state-changing (FSSC) three-body Förster transitions in ensembles of ultracold Rydberg atoms that we proposed in 2020 [223]. This study, like the previous ones, was carried out jointly at Aime Cotton Laboratory and at Rzhanov Institute. The scheme of resonances studied in it was proposed by Dr. Patrick Cheinet, who is the scientific director of this thesis. The author of this thesis, in turn, performed the numerical study of resonances in structured and unstructured ensembles of Rb and Cs Rydberg atoms.

### 4.2.1. Resonant scheme description

As described in Sections 3.2, 3.3 and 4.1, Borromean three-body transitions are based on two simultaneous two-body non-resonant processes. Thus, the three-body population transfer can be represented as a ladder-like transit between the initial state 1 and the final state 3 through the strongly detuned level 2 (see Fig. 4.9). The condition for the emergence of the three-body resonance is the degeneracy of the initial and final collective states of the atomic system. Such degeneracy arises under when the energy defects of the transitions  $1 \rightarrow 2$  and  $2 \rightarrow 3$  compensate each other ( $\Delta_1 = \Delta_2$ ). In turn, the two-body transfer between levels 1 and 2 (or levels 2 and 3) arises under the condition  $\Delta_{1(2)} = 0$ .

While searching for the scheme of three-body transitions used in the previous section to implement the Toffoli gate, we proposed a new kind of two-body transit  $1 \rightarrow 2$ , which appears for high values of the principal quantum number  $n$ . Although this transition is indeed realizable and allows for highly coherent dynamics in the atomic register, it requires excitation of atoms to different initial states. As described in the introduction to this section, the need for such excitation carries significant experimental difficulties, limiting the applicability of this scheme

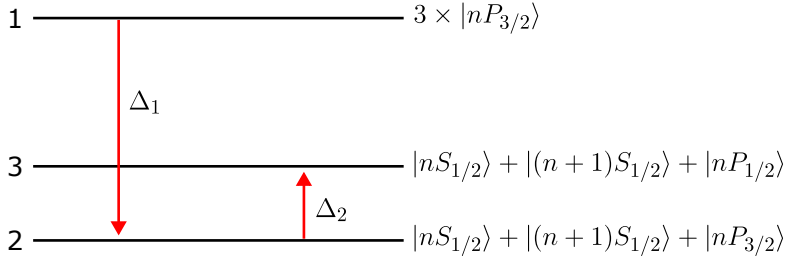


**Figure 4.9 :** Simplified scheme of the three-body Förster resonance for three Rydberg atoms. The initially populated collective state is 1. The final collective state is 3. The intermediate collective state is 2. The energy defects  $\Delta_1 = E_1 - E_2$  and  $\Delta_2 = E_3 - E_2$  are controlled by the DC electric field. The three-body resonance occurs at  $\Delta_1 = \Delta_2$ , while the two-body one occurs at  $\Delta_1 = 0$ .

in modern quantum registers. Therefore, we have taken a different approach when developing a new three-body resonance scheme. We did not try to reduce the energy defect of the first two-body transfer to match the small defect of the second transition. Instead, we have decided to increase the defect of the second transition to coincide with the large defect of the first transition.

Among the two transitions necessary to realize the three-body transfer, we thus tried to replace the  $2 \rightarrow 3$  transition, which was earlier represented by the  $S - P$  excitation hopping  $(n+1)S_{1/2} + nP_{3/2}(|m|) \rightarrow nP_{3/2}(|m^*|) + (n+1)S_{1/2}$  accompanied by a change of the projection of the  $P$ -state momentum. In turn, the  $1 \rightarrow 2$  transition was chosen as (4.21) again: this two-body transition was introduced earlier in Subsections 2.2.5, 3.1.1, 3.2.1, 3.3.1, and was the basic element of the originally proposed three-body resonances  $3 \times nP_{3/2}(|m|) \rightarrow nS_{1/2} + (n+1)S_{1/2} + nP_{3/2}(|m^*|)$  [192, 193].

$$2 \times nP_{3/2} \rightarrow nS_{1/2} + (n+1)S_{1/2} \quad (4.21)$$

$$(n+1)S_{1/2} + nP_{3/2} \rightarrow nP_{1/2} + (n+1)S_{1/2} \quad (4.22)$$

As a replacement for the two-body excitation hopping transfer used in paper [98] (see previous section) we propose to use transition (4.22). Due to this transition the total momentum of the  $P$ -state changes its value from  $J = 3/2$  to  $1/2$ . Thus, the excitation transfer is non-resonant for any electric field value. Also, the energy defect of this transition is large enough to compensate the energy defect of the two-body transition (4.21), provoking the three-body resonance.

$$3 \times nP_{3/2} \rightarrow nS_{1/2} + (n+1)S_{1/2} + nP_{1/2} \quad (4.23)$$

The new three-body transition proposed in paper [223] has the form (4.23). It is the result of two transitions (4.21) and (4.22) occurring parallelly in a three-atomic system. Note that the initial atomic states are identical, which greatly facilitates the experimental realization of such a transition. The presented resonance turned out to be realizable for arbitrary initial Rydberg states  $nP_{3/2}$  both for Rb and Cs. A distinctive feature of this resonance is that the third atom transits to a state with different total angular momentum  $J = 1/2$  and we name this process Fine-Structure-State-Changing (FSSC) transition. It is important to note that the state

with  $J = 1/2$  has no Stark structure, thus an isolated single three-body resonance occurs for a single initial state. Therefore, the experimental study of such a three-body resonance should be much simpler, since two-body interaction does not induce resonant transitions (4.21) when scanning the electric field.

As indicated earlier, we aim at application of the described scheme for the high-lying Rydberg states. As shown in Subsection 4.1.4, the long lifetimes of high-lying Rydberg states contribute to the coherence of Rabi oscillations, which is critical for the realization of high-precision quantum gates. At the same time, FSSC resonance may be noticeably weaker for high  $n$  due to significantly larger detunings of intermediate levels (about 200 MHz for  $n = 70$ ) than in the case of the three-body resonance  $3 \times 37P_{3/2}(|m|) \rightarrow 37S_{1/2} + 38S_{1/2} + 37P_{3/2}(|m^*|)$  (about 10 MHz). On the other hand, for high Rydberg states, the dipole moments of transitions are much larger than for the initial interaction scheme that was blocked in principal quantum number. Thus, we assume that the dipole moment enhancement could help to compensate for the possible weakening of the three-body interaction.

### 4.2.2. FSSC resonance study

When presented, three-body transitions of the type (4.23) were considered as perspective candidates for the realization of multiqubit quantum gates. Nevertheless, to evaluate the applicability of the transitions to quantum computing problems, an extended study of their properties was needed. In this study, two main issues were investigated. First, it was useful to analyze the various interaction channels contributing to the system dynamics for different alkali atoms in order to find the best suited atomic species for quantum gate implementation. Second, we needed to show that the resonance interactions (4.23) can exhibit coherent dynamics, and to choose a suitable atomic configuration to realize the quantum gate. In this section, we present the research conducted to address these issues by numerical simulations of many-body resonance interactions.

We begin with the question of the applicability of the resonance scheme in various atomic species. Previously the many-body resonances in ensembles of Cs [107, 191] and Rb [192, 193] atoms were studied in detail. As was shown in Section 3.3, two-body non-resonant processes make a significant contribution to the dynamics of a multi-atomic system, leading to a possible overlap of two-body and three-body peaks. The existence of additional higher order two-body effects can also influence the behavior of the three-body system [244]. Previously, we considered only fully resolved two-body transitions satisfying the selection rule for dipole-dipole transitions  $l' = l \pm 1$ . In turn, an external electric field can lead to mixing of atomic states of different parity. In the classical field, each pair of states  $|a\rangle$  and  $|b\rangle$  satisfying the selection rule  $\Delta l = \pm 1$  is coupled by the Stark effect. Then the eigenstates of the atomic Hamiltonian are no longer states with a fixed momentum  $l$ , but combinations of states with different  $l$ . For example, when  $P$  and  $D$  levels cross in the external field, the state can no longer be described as a pure state, but only as a combined  $P + D$  state. Such a state, in turn, is coupled to both even and odd parity states, relaxing the requirements for selection rules. We call such transitions quasi-forbidden, due to the fact that the initial and final states of the system are in principle not

dipole-coupled in zero electric field, but can couple in its presence. Nevertheless, the mixing of states depends essentially on the energy defect between them. For example, the  $nP_{3/2}$  states are strongly isolated from the rest of the spectrum, as shown in the Stark diagrams presented earlier (see Subsection 4.1.2). In this regard, we can consider that their mixing with the rest of the spectrum is small and the states possess a certain momentum  $l$ , at least in weak fields.

Previously, quasi-forbidden resonance transitions have been investigated in detail in sodium and potassium [245, 246]. Note that the two-body quasi-forbidden  $2 \times S \rightarrow P + D$  resonance has also been used as an essential element of the resonant four-atom transfer demonstrated in [191] (see Section 3.1). Also quasi-forbidden resonances have been experimentally investigated in Cs for low-lying Rydberg levels with  $n = 28$  and  $n = 32$  [244]. It has been shown that such resonances can contribute significantly to the dynamics of a multi-atomic system. However, according to the results presented in [244], such processes have modest effect on the resonances between  $S$  and  $P$  states in unstructured samples at low values of the electric field; therefore, they were not taken into account in the articles [107, 192]. Nevertheless, an additional study is needed to describe the effect of quasi-forbidden resonance interactions in ordered Rydberg ensembles for high values of the principal quantum number to ensure the possibility of high-fidelity quantum gates based on FSSC scheme.

A study of quasi-forbidden resonance processes for high values of  $n$  was carried out in the paper [224]. In this study, we described in detail various quasi-forbidden resonances in Rb and Cs atoms for  $n = 50, 70$ . The primary objective of the conducted research was to investigate the relative strength between the new class of three-body resonances and quasi-forbidden resonances nearby in rubidium or cesium Rydberg atoms. We assumed that strong quasi-forbidden resonances could indeed perturb possible gate protocols and might reduce significantly the resulting gate fidelity. This study allowed us to conclude on optimum scenario to perform a quantum gate from FSSC resonant interaction scheme. Note that these results were also presented in Ku-Luc Pham's PhD thesis, which he defended in Aime Cotton Laboratory in 2021. The author of this thesis, in turn, participated in the discussions while conducting the research presented in the article [224]. However, the results presented in the article are not the fruit of his direct labor.

### 4.2.3. Quasi-forbidden resonances

For this study, we follow the methodology developed in [244] that we present briefly. We start by computing the Stark energies of all states around the considered  $|nP_{3/2}\rangle$  starting state of a given three-body resonance of type (4.23). In this study, we restricted our calculations to states  $|m| = 1/2$  to avoid searching through too numerous resonances. It was demonstrated in [244] that resonances involving higher  $|m|$  display similar strengths. We then obtain a resonance map, as displayed from  $|50P_{3/2}\rangle$  of cesium in Figure 4.10: we plot in black the Stark energies  $E_{nlj}$  of all states in a given energy interval above the starting state and in red we plot the symmetric energy  $2E_{50P_{3/2}} - E_{nlj}$ . Any crossing between a black line and a red line then corresponds to a possible interaction resonance. The strongest are the ones for which at least one state follows the zero field selection rule  $\delta_l = \pm 1$  [244]. We have marked in Figure 4.10 the first resonances

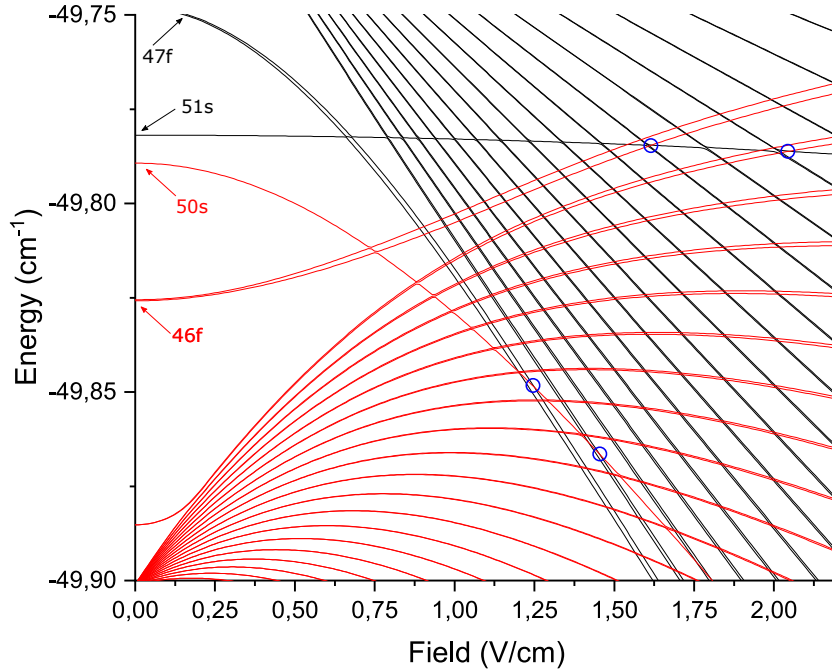


**Figure 4.10 :** Stark Förster resonance diagram for cesium atoms in  $|50P_{3/2}\rangle$  starting state (energy of around  $-50.9 \text{ cm}^{-1}$ ), limited to  $|m| = 1/2$  states. (black) Stark energies  $E_{nlj}$ . (red) Symmetric energy  $2E_{50P_{3/2}} - E_{nlj}$ . The crossings between these curves are possible Förster resonances. The blue circles show the resonances which follow the condition  $\delta_l = \pm 1$  for at least one state at zero field and for which we calculate interaction strength.

implying states  $|50S_{1/2}\rangle$  or  $|51S_{1/2}\rangle$ . For the electric field range, we arbitrarily choose to search up to around twice the 3-body resonance field.

In our search through different energy ranges in cesium, we find the following resonances:

$$2 \times |nP_{3/2}\rangle \rightarrow |nS_{1/2}\rangle + |(n-3)l_j\rangle \quad (4.24)$$

$$2 \times |nP_{3/2}\rangle \rightarrow |(n+1)S_{1/2}\rangle + |(n-4)l_j\rangle \quad (4.25)$$

$$2 \times |nP_{3/2}\rangle \rightarrow |(n+1)P_{1/2}\rangle + |(n-2)D_j\rangle \quad (4.26)$$

$$2 \times |nP_{3/2}\rangle \rightarrow |(n-1)P_{1/2}\rangle + |nD_j\rangle \quad (4.27)$$

$$2 \times |nP_{3/2}\rangle \rightarrow |(n+1)D_j\rangle + |(n-3)D_{j'}\rangle \quad (4.28)$$

When the resonances have been identified, we compute the corresponding dipole-dipole interaction energy using the transition dipole moments between the two starting  $|nP_{3/2}\rangle$  states and the two ending Stark states [244]. They will depend, among other things, on the overlap integral between the radial wavefunctions which is large for states close in energy to the starting state.

The closest states leading to resonances and fulfilling the  $\delta_l = \pm 1$  selection rule are the two states  $|nS_{1/2}\rangle$  and  $|(n+1)S_{1/2}\rangle$ . The first two resonances (4.24) and (4.25) are thus the strongest as found previously [244]. We also note that the resonance (4.28) is fully allowed regarding the selection rules but the involved states are separated from the initial state by about 2 multiplicities leading to small overlap integrals.

Due to significantly different quantum defects in rubidium Rydberg atoms, the resonances found for this atom are of different type:

$$2 \times |nP_{3/2}\rangle \rightarrow |(n-1)S_{1/2}\rangle + |(n-1)l_j\rangle \quad (4.29)$$

$$2 \times |nP_{3/2}\rangle \rightarrow |(n+2)S_{1/2}\rangle + |(n-4)l_j\rangle \quad (4.30)$$

$$2 \times |nP_{3/2}\rangle \rightarrow |(n-2)D_{5/2}\rangle + |(n-2)l_j\rangle \quad (4.31)$$

$$2 \times |nP_{3/2}\rangle \rightarrow |(n-1)D_{5/2}\rangle + |(n-3)l_j\rangle \quad (4.32)$$

We note that in rubidium, the strong quasi-forbidden resonances of type (4.24) and (4.25) do not appear anymore. They occur for fields of typically more than twice the 3-body resonance field. The resonances involved are all of quasi-forbidden type with large energy difference with the initial state, implying small overlap integrals in the dipole-dipole interaction.

In the resonances (4.24-4.32) listed above, the generic label  $l$  indicates that the resonance occurs with states of the Stark multiplicity leading to a large set of consecutive resonances. We do not compute the whole set but the first ones in order to grasp their general behavior. The generic label  $j$  is used when the two possible values  $j = l - 1/2$  and  $j = l + 1/2$  lead to resonances. For the sets of resonances with a multiplicity, we compute one out of the two as they were found of similar strength [244].

Two-body Förster resonances have already been studied in cesium [200, 247, 248] and rubidium [185, 249, 250] atoms below  $n \simeq 40$ , together with the old-type 3-body resonance scheme presented in Sections 3.2 and 3.3. Here we concentrate on high principal quantum numbers and choose  $n = 50$  and  $n = 70$  to test the evolution with increasing  $n$ . We present the results of the different resonances in cesium and rubidium atoms in Figures 4.11 and 4.12 which display their interaction strength and compare to the corresponding FSSC 3-body resonance (4.23). As we consider a potential application to quantum computation and the interaction strength is highly dependent on distance, we compute the interaction strength for a relatively large interatomic distance of 10  $\mu\text{m}$  which is likely to be well controlled experimentally. All interaction strengths displayed in Figures 4.11 and 4.12 are also gathered in Tables 4.3 and 4.4.

In cesium atoms, in Figure 4.11, we can see that at  $n = 50$  the 3-body resonance is embedded within numerous quasi-forbidden resonances which are up to a hundred times stronger. It is therefore unlikely to achieve any reliable quantum computation with this interaction scheme at this principal quantum number. Increasing  $n$  will increase all interaction strengths but the 3-body one, which scales as  $n^{11}$  will increase faster than the 2-body ones which scale as  $n^4$ . We thus check at  $n = 70$  and see that the 3-body interaction strength has indeed significantly increased comparatively to the 2-body ones. It also stands almost alone at its resonance field of 0.19 V/cm. Nevertheless, it is still almost an order of magnitude weaker than the next quasi-forbidden resonances of types (4.24) and (4.25). Increasing  $n$  further will keep strengthening

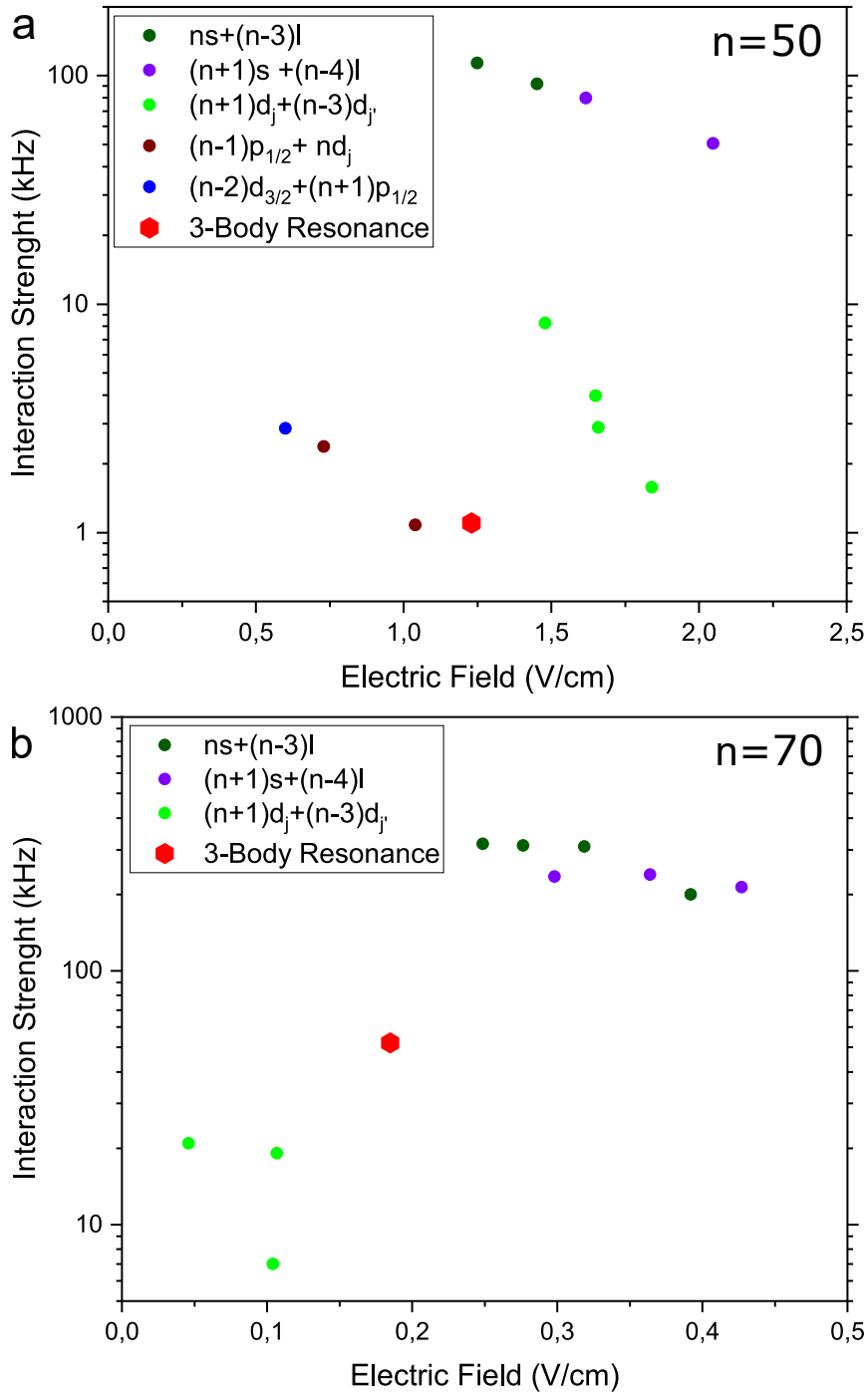


**Figure 4.11 :** Interaction strength at 10  $\mu\text{m}$  interatomic distance versus electric field for various resonances in cesium Rydberg atoms from initial state  $|nP_{3/2}\rangle$ . (a) Resonances at  $n = 50$ . The 3-body resonance is close to much stronger 2-body resonances. (b) Resonances at  $n = 70$ . The 3-body resonance is still weaker than many close 2-body resonances.

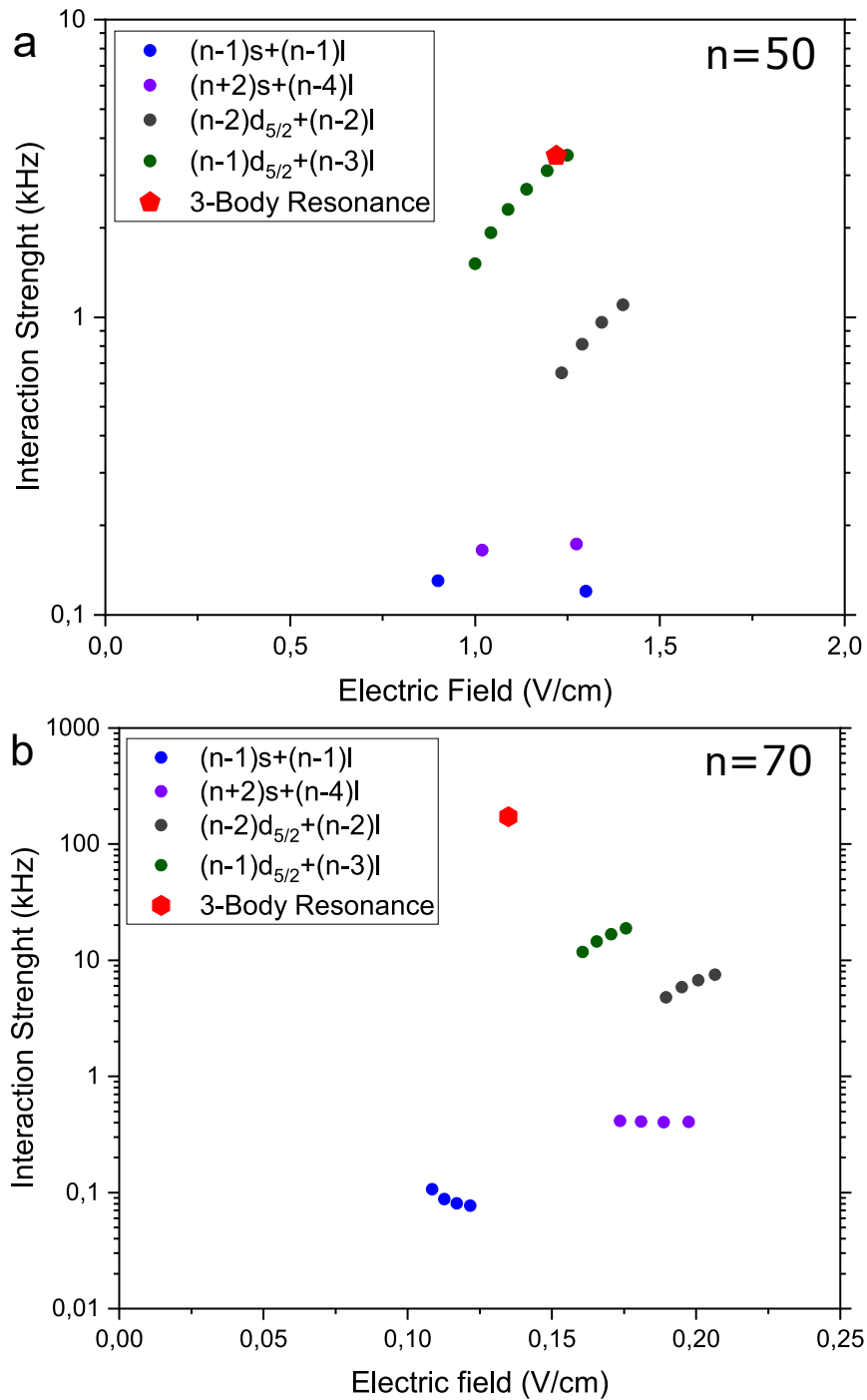


**Figure 4.12 :** Interaction strength at  $10 \mu\text{m}$  interatomic distance versus electric field for various resonances in rubidium Rydberg atoms from initial state  $|nP_{3/2}\rangle$ . (a) Resonances at  $n = 50$ . The 3-body resonance is embedded with numerous 2-body resonances of similar strengths. (b) Resonances at  $n = 70$ . The 3-body resonance is now stronger and well separated from all surrounding 2-body resonances.

the 3-body interaction compared to the quasi-forbidden resonances. However the sensitivity to electric field increases as well, as  $n^7$ , and will eventually become an issue. Another option is to use a smaller interatomic distance. Indeed the 3-body interaction scales as  $1/R^6$  while the 2-body interactions scale as  $1/R^3$  but the sensitivity to the exact distance will then increase and might as well become an issue for a gate protocol fidelity. It is thus interesting to check whether rubidium atoms present better characteristics.

In rubidium Rydberg atoms, the energy difference between  $|nP_{3/2}\rangle$  and  $|nP_{1/2}\rangle$  is smaller than in cesium. This implies that the consecutive 3-body resonance is stronger. We also explained that the resonances (4.24) and (4.25) occur for significantly higher fields than the 3-body resonance. Thus they should not impair a gate protocol. Instead, we found resonances (4.29-4.32) surrounding the 3-body resonance with significant strength. In Figure 4.12, we present the strengths of these resonances together with the 3-body resonance, at  $n = 50$  and  $n = 70$ . We can see that resonances of type (4.32) are the strongest and are, at  $n = 50$ , of similar strength and resonant field as the 3-body resonance. Therefore it seems again unlikely to find suitable experimental parameters at this principal quantum number to perform a high-fidelity 3-body quantum gate. Instead, at  $n = 70$ , the 3-body resonance has become the strongest interaction by almost an order of magnitude while, like in cesium atoms, its resonance field becomes separate from the resonance field of the quasi-forbidden processes.

**Table 4.3:** Cesium computed resonance strengths. For each quasi-forbidden resonance of types (4.24 - 4.28), the resonance electric field  $F$  and expected interaction strength (I.S.) is reported. It is compared at the end of the table with the 3-body resonance.

	$n = 50$		$n = 70$	
	$F(\text{V/cm})$	I.S.(kHz)	$F(\text{V/cm})$	I.S.(kHz)
$nS + (n - 3)l$	1.25	113.568	0.25	316.617
	1.45	91.953	0.28	311.760
			0.32	308.427
			0.39	199.902
$(n + 1)S + (n - 4)l$	1.62	79.728	0.30	234.933
	2.05	50.453	0.36	239.299
			0.43	213.391
$(n + 1)D_{5/2} + (n - 3)D_{5/2}$	1.48	8.250		
$(n + 1)D_{3/2} + (n - 3)D_{5/2}$	1.65	3.970	0.05	20.874
$(n + 1)D_{5/2} + (n - 3)D_{3/2}$	1.66	2.890	0.11	19.118
$(n + 1)D_{3/2} + (n - 3)D_{3/2}$	1.84	1.580	0.10	6.990
$(n - 1)P_{1/2} + nD_{5/2}$	0.73	2.380		
$(n - 1)P_{1/2} + nD_{3/2}$	1.04	1.080		
$(n - 2)D_{3/2} + (n + 1)P_{1/2}$	0.60	2.860		
$nS + (n + 1)S + nP_{1/2}$	1.23	1.100	0.19	52.0

## 4.2. FSSC three-body Förster resonances

**Table 4.4:** Rubidium computed resonance strengths. For each quasi-forbidden resonance of types (4.29 - 4.32), the resonance electric field  $F$  and expected interaction strength (I.S.) is reported. It is compared at the end of the table with the 3-body resonance.

	$n = 50$		$n = 70$	
	$F(\text{V/cm})$	I.S.(KHz)	$F(\text{V/cm})$	I.S.(kHz)
$(n-1)S + (n-1)l$	0.90	0.130	0.109	0.106
	1.30	0.120	0.113	0.088
			0.117	0.081
			0.122	0.077
$(n+2)S + (n-4)l$	1.02	0.165	0.17	0.413
	1.28	0.173	0.18	0.406
			0.19	0.403
			0.20	0.404
$(n-2)D_{5/2} + (n-2)l$	1.24	0.650	0.190	4.794
	1.29	0.810	0.195	5.856
	1.34	0.960	0.201	6.721
	1.4	1.100	0.207	7.513
$(n-1)D_{5/2} + (n-3)l$	1.00	1.510	0.161	11.766
	1.04	1.920	0.166	14.459
	1.09	2.300	0.171	16.710
	1.14	2.690	0.176	18.821
	1.20	3.100		
	1.25	3.500		
$nS + (n+1)S + nP_{1/2}$	1.22	3.493	0.14	172

For increasing  $n$ , the relative strength of the 3-body resonance will keep increasing compared to the spurious quasi-forbidden resonances and will completely dominate them even at interatomic distances of up to 10 microns. We thus conclude that rubidium atoms are indeed suited to implement 3-body quantum gates based on this interaction resonance.

In summary, we have investigated the quasi-forbidden resonances surrounding the 3-body interaction resonance scheme (4.23) presented in [223] and evaluated their relative strengths both in cesium and rubidium Rydberg atoms. The presented study allows us to draw several important conclusions. First, this study points out that rubidium is better suited for implementing strong 3-body interactions than cesium. Second, highly isolated three-body Förster resonances are achievable for high values of the principal quantum number  $n = 70$  in Rb. We conclude that the high-lying Rydberg states of Rb atoms are potentially suitable for the implementation of quantum gate schemes. It is thus clear that the following studies should concentrate on  $n = 70$  levels in rubidium atoms or above.

#### 4.2.4. Numerical simulations

In this subsection, the results of numerical simulations of three-body FSSC resonances (4.23) are presented. Within the framework of this study, we have investigated resonances in ordered and disordered ensembles of Rb and Cs for a wide range of values of the principal quantum number  $n \in [50, 90]$ . Nevertheless, we present here results only for  $n = 70$  levels in Rb atoms. As it was shown earlier, such levels should exhibit highly coherent dynamics due to the presence of strong three-body interactions, which are also essentially isolated from quasi-forbidden two-body resonances.

We performed numerical calculations in the same way as it was done in [193] for three-body resonances  $3 \times 37P_{3/2}(|m|) \rightarrow 37S_{1/2} + 38S_{1/2} + 37P_{3/2}(|m^*|)$  (see Subsection 3.3.5). However, in Ref. [193], all magnetic sublevels of Rydberg states were taken into account, which for the three-body Förster resonance in atoms in the  $37P_{3/2}$  states required 160 collective states with all possible values of the angular momentum projections to be taken into account. For the  $70P_{3/2}$  state, such calculations would require taking into account a much larger number of collective states. Therefore, to reduce the number of basis states and save computing time, we used a simplified model in which the signs of the angular momentum projections were not taken into account (i.e., a simplified model was constructed for Stark Rydberg sublevels rather than Zeeman ones). Its operability was checked earlier in calculations for the  $37P_{3/2}$  state, which showed satisfactory agreement with the experimental results regarding the positions and amplitudes of three-body resonances. We thus formed a basis of collective states combining the  $|nS_{1/2}\rangle$ ,  $|(n+1)S_{1/2}\rangle$ ,  $|nP_{3/2}(|m|=1/2)\rangle$ ,  $|nP_{3/2}(|m|=3/2)\rangle$ ,  $|nP_{1/2}\rangle$  states (see Subsection 4.1.2). To additionally reduce the computational complexity, we excluded collective states whose zero-field Förster defect from the initial state exceeded 2 GHz. Note that during the calculations, finite Rydberg lifetimes were not taken into account in this study. While calculating the matrix elements of the dipole-dipole interaction, the quasi-classical approach was used (see Appendix A).

We considered the interaction of an ensemble of three Rydberg atoms of Rb in a linear spatial configuration as well as in a disordered ensemble. As already discussed in Section 3.3, due to the presence of several interaction channels, a set of several resonances corresponding to different channels should be observed instead of a single three-body Förster resonance. In [193], we showed that in order to reduce the number of such channels, the optimal geometry of the three atoms is their uniform location along the quantization axis  $Z$ , which is chosen along the direction of the control electric field. In this case, only two well-separated three-body Förster resonances corresponding to two interaction channels remain (see Subsection 3.3.7).

To take into account the interaction of atoms with the external electric field, the values of polarizabilities were calculated (presented in Table 4.5). Note that in small fields the quadratic character of such interaction is preserved for the  $70P$  and  $70S$  states of Rb atoms. Nevertheless, at the intersection of these levels with multiplet state sets, the quadratic character of the interaction is broken, and a new method for calculating the polarizability is needed.

Fig. 4.13 shows the calculated Stark map of Rydberg states of Rb atoms near the  $70P$  state and the calculated Stark structure of the FSSC Förster resonance for three Rydberg Rb atoms. For this resonance, the crossings of collective states (indicated by numbers) correspond only

## 4.2. FSSC three-body Förster resonances

**Table 4.5:** Numerically estimated polarizabilities  $\alpha$  for relevant atomic levels. Polarizabilities are measured in  $\text{GHz}/[\text{V}/\text{cm}]^2$  units.

Atomic state	$\alpha$	Atomic state	$\alpha$
$ 70S_{1/2}(1/2)\rangle$	-263.7	$ 70P_{3/2}(1/2)\rangle$	-2006.7
$ 71S_{1/2}(1/2)\rangle$	-290.6	$ 70P_{3/2}(3/2)\rangle$	-1729.7
$ 70P_{1/2}(1/2)\rangle$	-1700		

to three-body Förster resonances, when all three atoms change their states, and there are no two-body resonances at all. Three-body resonances occur at relatively small fields (0.13 – 0.16 V/cm). Thus, for a collective initial state with a single momentum projection, only one three-body resonance arises. As can be seen from the Stark diagram (Fig. 4.13(a)), at such low values of the electric field the individual atomic  $S$  and  $P$  states do not experience essential mixing with neighboring states. Also, as it was shown in the previous subsection, the influence of quasi-forbidden resonances is relatively weak for  $n = 70$ . Thus, we can state that the use of the numerical model from Subsection 3.3.5 remains relevant.

Figure 4.14 shows the results of numerical simulations of the FSSC three-body Förster resonance,  $3 \times 70P_{3/2} \rightarrow 70S_{1/2} + 71S_{1/2} + 70P_{1/2}$ , for three Rydberg Rb atoms in several spatial configurations. Figure 4.14(a) corresponds to the case when three atoms are uniformly located along the  $Z$ -axis spaced by  $R = 10 \mu\text{m}$ , the interaction time being  $0.35 \mu\text{s}$ . At such a distance, the interaction of neighboring Rydberg atoms is relatively weak, and the three-body resonances do not broaden. As expected, only two resonances arise in this configuration, which correspond to two interaction channels. Their resonance electric fields of 0.1247 and 0.140 V/cm are close

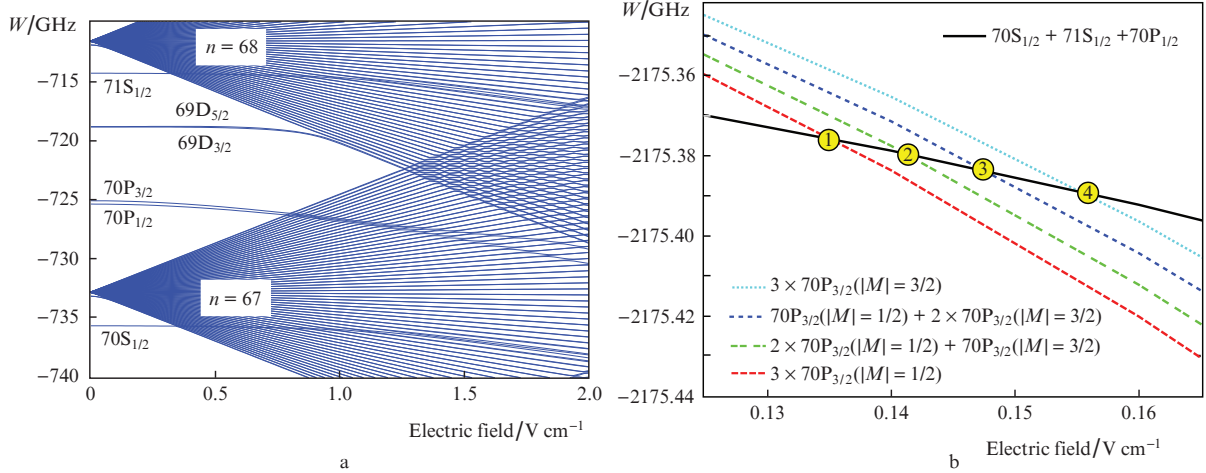


**Figure 4.13:** (a) Calculated Stark map of Rydberg states of Rb atoms near the  $70P$  state and (b) calculated Stark structure of the FSSC Förster resonance  $3 \times 70P_{3/2} \rightarrow 70S_{1/2} + 71S_{1/2} + 70P_{1/2}$  for three Rydberg Rb atoms. Crossings of collective states (indicated by numbers) correspond only to three-body Förster resonances, when all three atoms change their states, while two-body resonances are absent. Note that on this picture  $M$  is used to define the individual momentum projections, while in the main text  $m$  is used for this purpose.

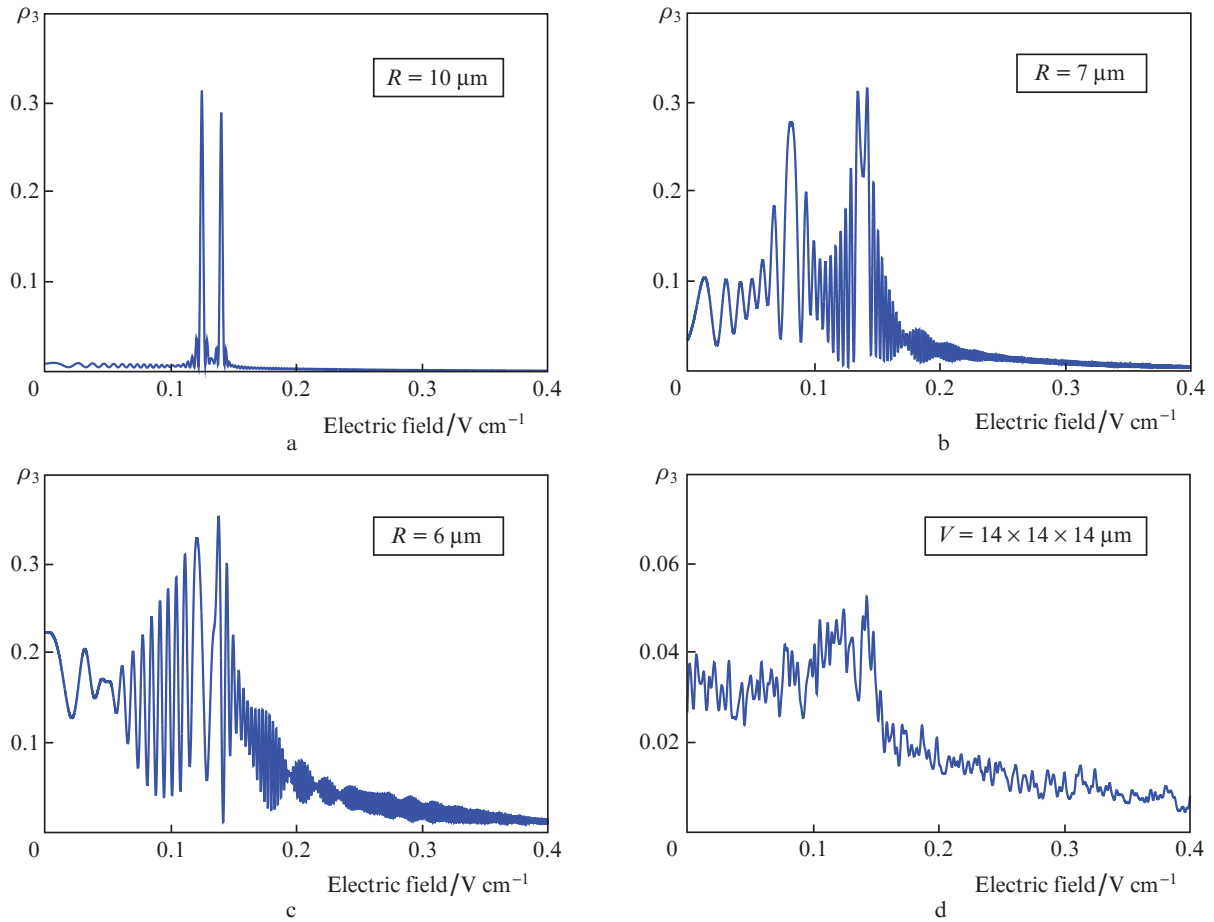


**Figure 4.14 :** Results of numerical calculations of the three-body FSSC Förster resonance spectra  $3 \times 70P_{3/2} \rightarrow 70S_{1/2} + 71S_{1/2} + 70P_{1/2}$ , for three Rydberg Rb atoms in several spatial configurations: (a) three atoms are uniformly located along the  $Z$  axis with the interatomic spacing of  $R = 10 \mu\text{m}$  at an interaction time of  $0.35 \mu\text{s}$ ; (b, c) the same for  $R = 7 \mu\text{m}$  (b) and  $R = 6 \mu\text{m}$  (c); (d) for three atoms randomly arranged in a cubic interaction volume  $V = 14 \times 14 \times 14 \mu\text{m}^3$ , averaged over 100 realizations at an interaction time of  $2 \mu\text{s}$ .

to the calculated value of  $0.135 \text{ V/cm}$  for the crossing of collective levels in Fig. 4.13(b) in the absence of interaction, taking into account additional dynamic shifts. The resonance amplitudes tend to the maximum possible value  $1/3$ , and their width when converted to the frequency scale corresponds to the Fourier width of the interaction pulse (about  $3 \text{ MHz}$ ). The resonances are well resolved, and by tuning the electric field, one can select a specific three-body interaction channel.

With a decrease in the interatomic distance to  $R = 7 \mu\text{m}$  (Fig. 4.14(b)), the effective three-body interaction energy  $\Omega_0$ , which depends on the distance as  $R^{-6}$ , increases by 8.5 times. As a result, the calculated spectra begin to noticeably broaden, shift, and partially overlap in the presence of population oscillations. In this case, one of the resonances shifts toward a smaller electric field, and its wing has a high value even in a zero field. A further decrease

in the distance to  $R = 6 \mu\text{m}$  (Fig. 4.14(c)) increases the energy of three-body interaction by another 2.5 times, which is accompanied by a complete overlap of the two resonances and their considerable broadening. The observed oscillations of the populations at the wings of a three-body resonance have a period that increases with decreasing electric field, which is explained by the quadratic nature of the Stark effect in these states.

We also calculated the case when three atoms were randomly located in a cubic interaction volume  $V = 14 \times 14 \times 14 \mu\text{m}^3$  averaged over 100 realizations at an interaction time of  $2 \mu\text{s}$  (see Fig. 4.14(d)), which approximately corresponded to the conditions of our experiment in Ref. [192] during recording three-body Förster resonances (see Section 3.3). In this case, due to the uncertainty of the distance between the atoms and their mutual orientations, all the interaction channels are involved, the population oscillations are completely washed out, and the spectrum of the resonance approximately corresponds to the resonance envelope in Fig. 4.14(c). The resonance amplitude also decreases noticeably, which is associated with the presence of zeros in the interaction energy for certain spatial configurations of atoms [251]. In this case, the three-body interaction is also present in the zero electric field, which can be explained by those random configurations of atoms, in which they are located close to each other and have large interaction energies comparable with the energy in Fig. 4.14(c). This signal can also be explained by the presence of a non-resonant two-body signal for close pairs.

Based on the results of calculating the spectra of the three-body FSSC Förster resonances (Fig. 4.14), we can draw several conclusions. First, the spectra are highly sensitive to interatomic distances, and when a certain threshold value is reached, they begin to broaden, making individual interaction channels indistinguishable. This should lead to a loss of coherence and the absence of full population oscillations at high interaction energies. Second, with a random arrangement of three atoms in a single volume of laser excitation, coherence is completely lost, and the interaction takes place even in a zero electric field, which complicates its observation under the conditions of previous experiment [192] for old-type resonances. Therefore,

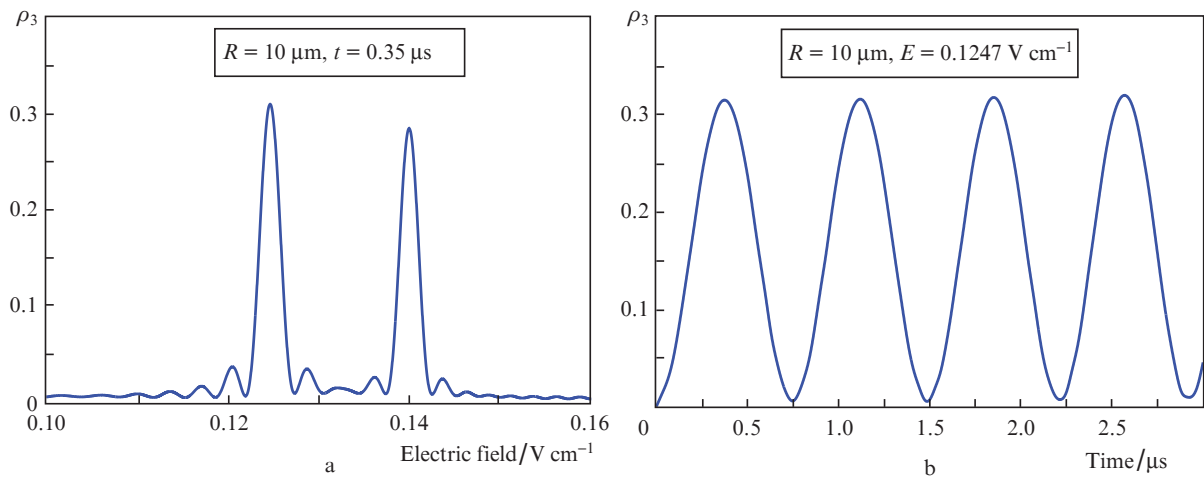


**Figure 4.15 :** (a) Magnified image of the spectrum shown in Fig.4.14(a) and (b) population oscillations when the electric field is tuned to a three-body resonance in an electric field of 0.1247 V/cm.

experiments must be performed with single atoms in separate optical dipole traps with minimal fluctuations in their spatial position, as was done, e.g., in Ref. [155]. Third, for high Rydberg states, the values of the resonant electric field are rather small, therefore, to observe narrow three-body resonances, a high-stability source of the electric field is required, and all possible spurious fields must be carefully compensated to less than 1 mV/cm.

Our calculations also showed that, under the conditions of good spatial localization of atoms and minimization of the electric field noise, experimental realization of coherent population oscillations at the three-body Förster resonance is possible. Figure 4.15(a) shows a magnified image of the spectrum from Fig.4.14(a). There are two well-resolved peaks of three-body resonance at electric fields of 0.1247 V/cm and 0.140 V/cm. Fine tuning to one of the peaks (the required accuracy is  $\sim 0.1$  mV/cm) allows switching on the coherent three-body interaction, accompanied by population oscillations. The calculated population oscillations when tuning to a three-body resonance in an electric field of 0.1247 V/cm are presented in Fig.4.15(b). The contrast of oscillations exceeds 95%, which allows considering them as the basis for three-qubit quantum gates, by analogy with the three-body resonances that we examined in Refs. [98, 193] (see Sections 3.3, 4.1).

#### 4.2.5. Conclusion

Based on the results of the conducted research, the following conclusions can be drawn. We have developed and numerically investigated a new scheme of three-body FSSC Förster resonances. For quantum computing purposes, the scheme has several advantages over the previously proposed ones. First, identical initial Rydberg states are used to realize the three-body resonances, which facilitates the experimental implementation of quantum gates. The absence of closely located two-body resonances, in turn, significantly simplifies the resonance dynamics, thus facilitating the algorithm for controlling a possible quantum gate. Also, the quasi-forbidden resonances observed in the system in the presence of an external controlling electric field can have a significant effect on the FSSC resonance processes. Nevertheless, the relative strength of quasi-forbidden transitions can be significantly reduced when switching to higher Rydberg levels. In particular, for the high-lying Rydberg  $n = 70$  levels of rubidium, the strength of the three-body interaction exceeds that of the nearby quasi-forbidden two-body transitions by at least an order of magnitude.

Second, our numerical calculations using the example of the three-body Förster resonance  $3 \times 70P_{3/2} \rightarrow 70S_{1/2} + 71S_{1/2} + 70P_{1/2}$  for three Rydberg Rb atoms in several spatial configurations showed that for not too strong interaction, when various interaction channels are well resolved in the spectra, it is possible to observe high-contrast population oscillations. Since such oscillations are accompanied by oscillations of the phase of the collective wave function of three atoms, it is possible to develop new schemes of three-qubit quantum gates controlled by an electric field based on them.

This work was supported by the Russian Foundation for Basic Research (Grant No. 19-52-15010) and Novosibirsk State University.

### 4.3. FSSC-based Toffoli gate

In the previous section, we considered a new scheme of three-body FSSC Förster resonances proposed in [223]. This scheme assumes the use of the same initial states for three Rydberg atoms, and is suitable for different atomic species, as well as for arbitrary values of the principal quantum number  $n$ . An additional advantage of the scheme was the absence of strong dipole-resolved two-body interactions in proximity of the three-body resonance. In turn, the nearby quasi-forbidden resonances turn out to be weak as compared to the three-body interaction for high-lying Rydberg levels. We have convincingly demonstrated coherent population oscillations of the atomic register collective states for the initial  $70P$  states of Rb atoms in a linear spatial configuration. Thus, according to the results of our study, we conclude that the implementation of three-qubit quantum gates is possible based on the presented resonances.

In this section we report our results on the realisation of three-qubit quantum gates based on three-particle FSSC resonances. We have successfully developed and numerically investigated a quantum Toffoli gate protocol based on  $3 \times 70P_{3/2} \rightarrow 70S_{1/2} + 71S_{1/2} + 70P_{1/2}$  resonances in an ensemble of individually isolated Rb atoms. The high coherence of the resonant population dynamics, coupled with the long lifetimes of the high-lying Rydberg states, allows for a high accuracy of the gate implementation for realistic experimental parameters. Also, the dependence of the resonant peak width on the external controlling electric field has been investigated, and methods to improve the stability of the gate have been proposed.

This work was carried out mostly by the author of this thesis. All the results obtained within the framework of this study and presented in the paper [225] were obtained by him. The original Toffoli gate protocol is also the result of the author's contribution. However, it is important to emphasize that the resonances that underlie this scheme were proposed by the author's colleagues (see Section 4.2). The Toffoli gate protocol, although original, is based on a previous scheme presented in [98], developed by the author's colleagues (see Section 4.1).

#### 4.3.1. Numerical model

A new scheme of three-body resonances, also called "fine-structure-state-changing (FSSC) resonances", was studied in detail in [223]. However, as mentioned in the Subsection 4.2.4, such resonances were simulated in a truncated basis. Since the consideration of the full set of Zeeman sublevels of the Rydberg collective states significantly complicates the calculations and leads to an increase in the time required for the simulation, we had restricted ourselves in [223] to the consideration of the Stark sublevels of these states. Nevertheless, the consideration of the Zeeman sublevels is necessary to obtain fully relevant results for the subsequent quantum gate modeling. Therefore, as part of this study, additional simulations of the resonances have been performed in the extended basis. We briefly describe here the simulations performed and the theoretical model used.

The computational model developed in this study is based on a previously developed model detailed in Subsection 4.1.2. We consider the three-body FSSC Förster resonance of the form (4.33) described in the previous section. Note that  $|nP_{3/2}\rangle^{\otimes 3}$  here denotes the product of three

**Table 4.6 :** Numerically calculated  $\gamma$ -factors for relevant atomic levels. Substantial part of presented data was recollected from [169].

Atomic state	$\gamma_{eff}, s^{-1}$	Atomic state	$\gamma_{eff}, s^{-1}$
$ 70S_{1/2}\rangle$	0.0066	$ 70P_{1/2}\rangle$	0.0053
$ 71S_{1/2}\rangle$	0.0064	$ 70P_{3/2}\rangle$	0.0052

identical ket vectors. Since Rb states with  $n = 70$  have demonstrated high coherence of the three-body FSSC interaction (see Section 4.2), we focus on the study of these states. As before, quasi-classical approximation is used to compute matrix elements. The interaction of levels with the external electric field is taken into account by adding the quadratic Stark shift. The values of polarizabilities of the relevant states are given in Subsection 4.2.4. To account for the finiteness of the lifetimes of the Rydberg states, the  $\gamma$ -factors were calculated given in Table 4.6. The method described in [169] was used to calculate these  $\gamma$ -factors.

To compute the population and phase dynamics in the atomic system, we solved the non-Hermitian Hamiltonian based Schrödinger equation for the probability amplitudes of the system collective states taking into account Rydberg lifetimes [169]. For simplicity, we considered an open system and neglected the return of the population from Rydberg states to the ground states due to spontaneous decay.

$$|nP_{3/2}\rangle^{\otimes 3} \rightarrow |nS_{1/2}; (n+1)S_{1/2}; nP_{1/2}\rangle \quad (4.33)$$

As described in our article [223] (see Subsection 4.2.4), sets of three-body resonances are observed in Rydberg atoms instead of a single resonance, due to the large number of interaction channels in Rydberg systems. To reduce the number of observed resonances, it is necessary to choose the optimal geometry of the atomic register. We have proved in Subsection 3.3.7 that the linear arrangement of atoms at the same distances from each other along the quantization axis coinciding in the direction with the external control DC electric field ( $Z$  axis) is optimal [193]. Note that in this case the dipole-dipole interaction operator couples only two-atom collective states with  $\Delta M = 0$ , where  $M$  is the total momentum projection of the collective state.

Throughout the section, we describe the behavior of the collective states of three Rb Rydberg atoms in the spatial configuration described above, as well as the interactions between them. These states have the form  $|n_1 l_1 j_1 (m_{j1}); n_2 l_2 j_2 (m_{j2}); n_3 l_3 j_3 (m_{j3})\rangle$  in Dirac notation. The Förster energy defect is the difference between the energies of the final and initial collective states.

As shown in Subsection 4.2.1, the two-body  $2 \times nP \rightarrow nS + (n+1)S$  Förster resonance is known to be absent in rubidium for principal quantum numbers above  $n = 38$  due to the specific values of quantum defects and polarizabilities of Rydberg states  $nP$  and  $nS$  [223, 227]. Therefore, off-resonant two-body interactions induce small phase shifts but no sizable population transfer, in contrast to the scheme, previously considered in Section 4.1 [98]. This substantially simplifies the population and phase dynamics of the collective three-body states, as will be shown below.

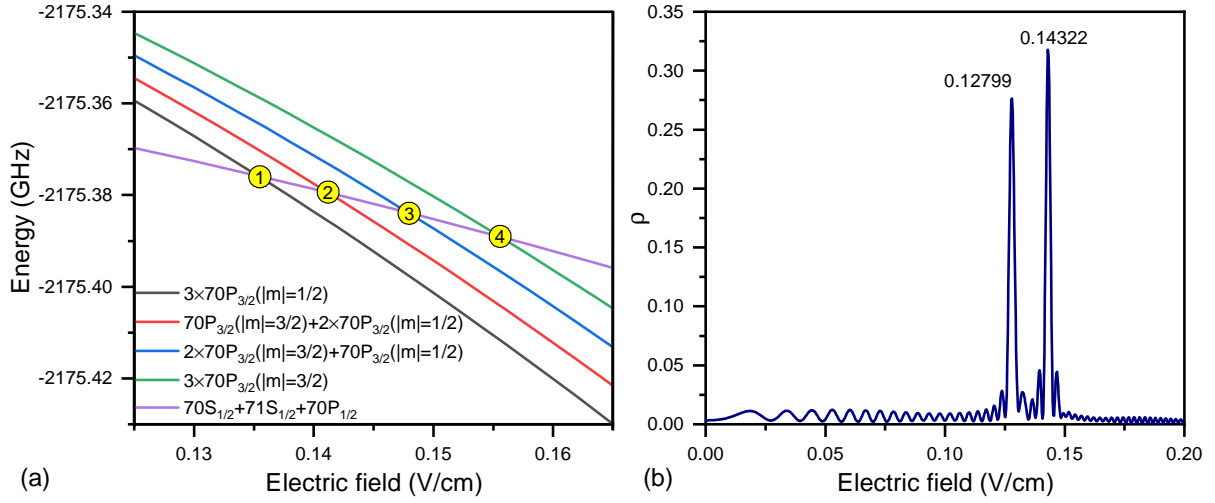


**Figure 4.16 :** (a) Numerically calculated Stark structure of the collective energy levels, involved in three-body Förster resonance  $|70P_{3/2}\rangle^{\otimes 3} \rightarrow |70S_{1/2}; 71S_{1/2}; 70P_{1/2}\rangle$ . The intersections 1-4 mark the positions of three-body resonances. (b) Numerically calculated dependence of the fraction  $\rho$  of atoms in the final  $|71S_{1/2}\rangle$  state after three-body interaction on the external DC electric field for the initial state  $|70P_{3/2}(m=1/2)\rangle^{\otimes 3}$  (marked as 1 in Fig. 1(a)). The atoms are located along the  $Z$  axis at interatomic distance  $R = 10$  microns.

In Figure 4.16(a), the energies of the collective Rydberg states involved in three-body Förster resonance (4.33) are depicted as functions of the external electric field. These dependencies of energy levels are calculated for different fine structure components of Rb  $70P$  state. The intersections with the final quantum state, indicated as 1-4, mark the positions of possible three-body resonances. Note that this picture is analogous to the Figure 4.13(b) and is given here for ease of reading only.

Figure 4.16(b) shows the dependence of the calculated probabilities of the Förster resonant energy transfer on the external electric field when all atoms are initially excited into the state  $|70P_{3/2}(m=1/2)\rangle$ . This corresponds to resonance 1 in Fig. 4.16(a). Two resonant features are clearly seen. The splitting and shift of the resonances are caused by multiple channels of three-body Förster interaction through different intermediate quantum states.

Note that Figure 4.16(b) represents the results of simulations performed in the extended basis. We considered all Zeeman sublevels of the states  $70S_{1/2}$ ,  $71S_{1/2}$ ,  $70P_{3/2}$ ,  $70P_{1/2}$  and formed the collective states from all possible combinations of these levels. To facilitate the calculations, we did not consider collective states with Förster defect larger than 2 GHz in zero electric field. Thus, a basis of  $\sim 360$  collective states was formed. Comparing the obtained peaks with those presented earlier in Subsection 4.2.4 (see Figures 4.14(a) and 4.15(a)), we see a good agreement of the results. Nevertheless, a basis expansion is also necessary for a more accurate account of the resonant phase dynamics.

### 4.3.2. Toffoli gate proposal

The Toffoli quantum gate (or *CCNOT* gate) is a universal three-qubit quantum gate. As discussed before, it is very important for the effective implementation of many quantum algorithms, in particular, for quantum error correction. This gate can also be represented as a *CCZ* gate wrapped with Hadamard gates, as shown in Fig. 4.17(a). For more information on the Toffoli gate, please see Subsection 2.1.2.2 or Subsection 4.1.4.

The proposed scheme for the implementation of the Toffoli gate is shown in Fig. 4.17(b). As before, three Rb atoms are confined in three optical dipole traps located along the direction of the external electric field ( $Z$  axis) with interatomic distance  $R$ . We consider Förster resonances (4.33) for  $n = 70$  described in the previous subsection. In particular, the resonance 1 from Fig. 4.16(a) is used to produce the gate action.

To couple the logical states of qubits (namely,  $|0\rangle$  and  $|1\rangle$ ), we propose to use two-photon Raman laser pulses that do not populate the intermediate excited state  $5P$ . A three-photon excitation scheme can be used to pair the logical states of qubits with Rydberg levels [170]. The effects associated with the phase and intensity noise of the laser were considered in detail in [252]. Note that during the simulations presented in this section, the logical states of qubits were not taken into account. Thus, all the pulses presented on Fig. 4.17(b) are assumed to be perfect and cause no additional losses.

Eight laser pulses are used to implement the gate. As the first step, the pulse 1 is used, which is a  $Y$ -rotation by  $\pi/2$ , carrying out the action of the first Hadamard gate in Fig. 4.17(a) (we consider it to be perfect during our calculations). Then, the pulses 2-4 required for the  $|1\rangle \rightarrow |70P_{3/2}(1/2)\rangle$  transitions are applied simultaneously to all three qubits.

Depending on the initial state of the system, after laser pulses 2-4 have been applied, the number of the excited Rydberg atoms varies from zero to three. When all three atoms are excited, the phase of the collective atomic state is shifted by  $\pi$ , due to the three-body Förster resonance, tuned by an external electric field.

At the final stage, Rydberg atoms are de-excited by laser pulses 5-7. Raman laser or microwave pulse 8 drives the additional  $-\pi/2$  rotation of the target qubit around the  $Y$  axis, which is equivalent to the second Hadamard gate in Fig. 4.17(a). The timing diagram of all controlling pulses is shown in Fig. 4.17(c).

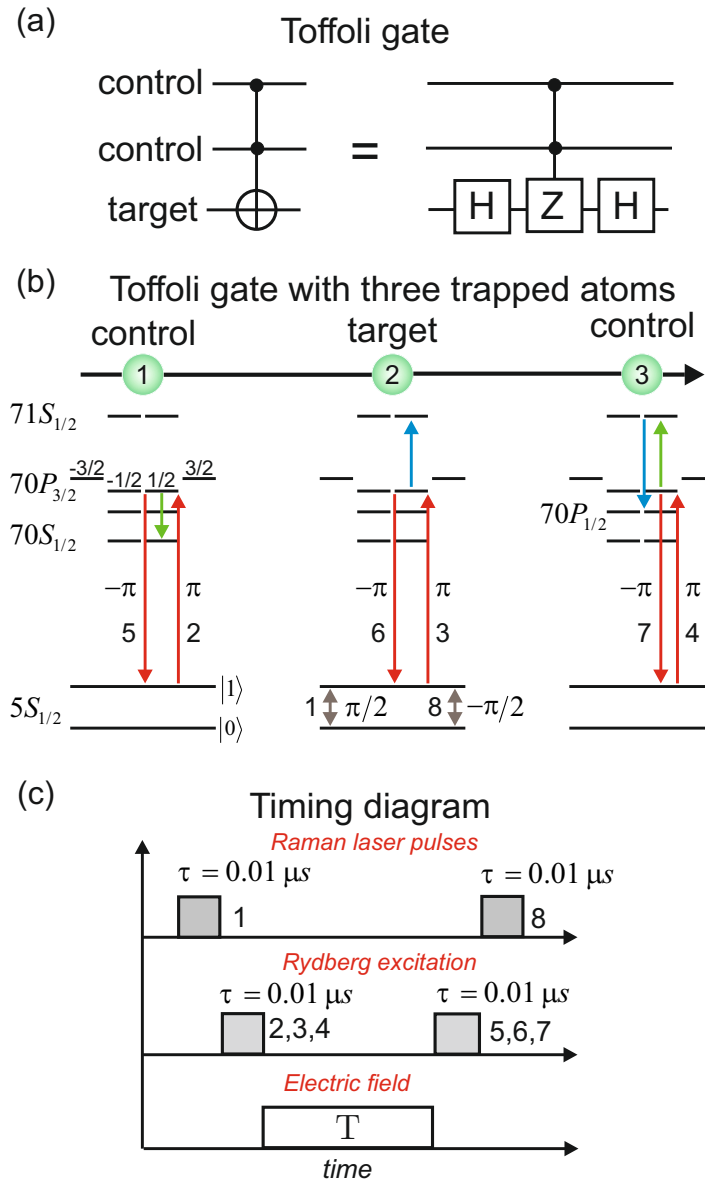


**Figure 4.17:** (a) General scheme of the three-qubit Toffoli gate. (b) Scheme of the Toffoli gate based on three-body FSSC resonance. Three atoms are located in the individual optical dipole traps aligned along the  $Z$  axis, which is co-directed with the controlling DC electric field. Laser Raman (or microwave) pulses 1 and 8 drive transitions between the logical states  $|0\rangle$  and  $|1\rangle$  of the target qubit. Laser pulses 2-7 excite and de-excite the chosen Rydberg states of the three atoms. The  $\pi$  phase shift due to the three-body interaction appears only if all three atoms are excited into Rydberg states. The green and blue arrows here indicate  $|70P_{3/2}\rangle^{\otimes 3} \rightarrow |70S_{1/2}; 70P_{3/2}; 71S_{1/2}\rangle$  and  $|70S_{1/2}; 70P_{3/2}; 71S_{1/2}\rangle \rightarrow |70S_{1/2}; 71S_{1/2}; 70P_{1/2}\rangle$  intermediate two-body transitions, respectively. (c) Timing diagram of the pulses in the proposed gate scheme. The whole gate scheme includes the following 5 steps: application of pulse 1, simultaneous application of pulses 2-4, application of a constant external electric field, simultaneous application of pulses 5-7, application of pulse 8.

## 4.3.3. Phase and population dynamics

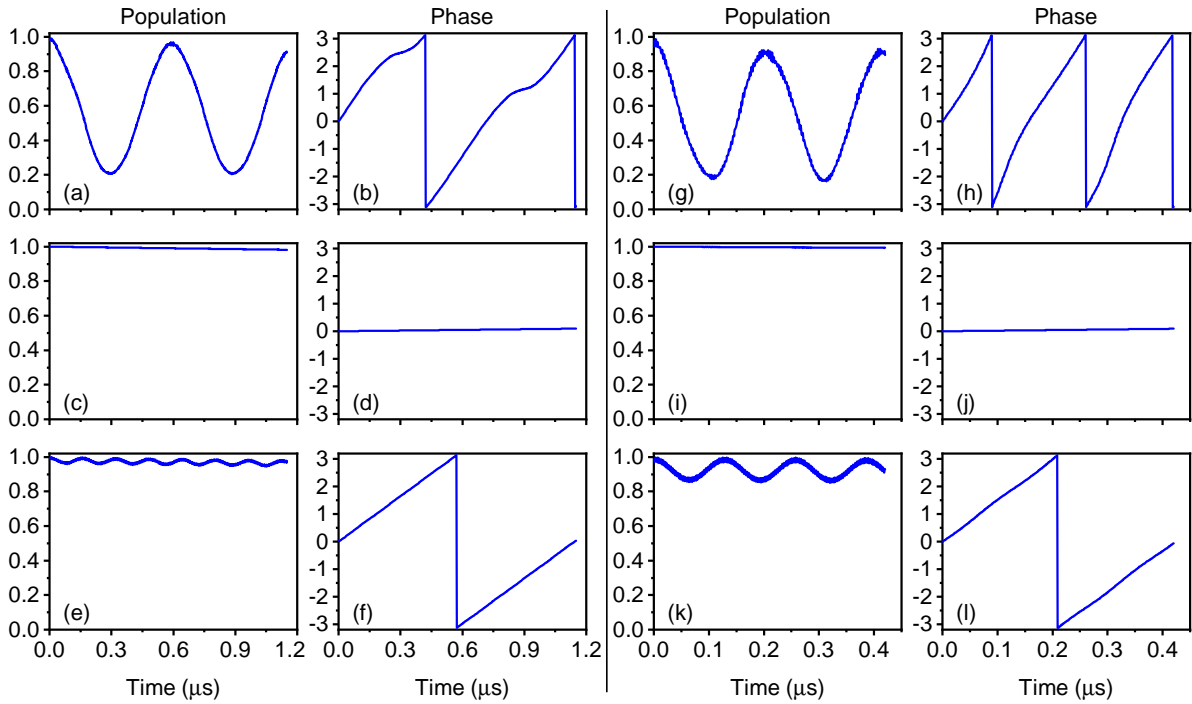


**Figure 4.18:** Numerically calculated time dependences of the populations and phases of the initially excited collective states of three interacting atoms. The upper row (a, b, g, h) depicts the multiparticle state population and phase evolution when all three atoms are excited into Rydberg states ( $|rrr\rangle$ ). The middle (c, d, i, j) and lower (e, f, k, l) rows belong to configurations  $|rgr\rangle$  and  $|grr\rangle$  ( $|rrg\rangle$ ), respectively. Here  $|g\rangle$  is the  $|0\rangle$  ground state,  $|r\rangle$  is the Rydberg state  $|70P_{3/2}(m = 1/2)\rangle$ . The phase values are presented in ordinary units in the range  $(-\pi, \pi)$ . System parameters: (a - f)  $R = 10 \mu\text{m}$ ;  $F = 0.14235 \text{ V/cm}$ ;  $T = 1.15 \mu\text{s}$ ; (g - l)  $R = 8.5 \mu\text{m}$ ;  $F = 0.1469 \text{ V/cm}$ ;  $T = 0.42 \mu\text{s}$ .

To implement the Toffoli gate, it is necessary to find the conditions under which different interatomic interactions lead to the required phase shifts of the initially excited collective states. Therefore, it is necessary to optimize the parameters of the atomic system: the interatomic distance  $R$ , the interaction time  $T$  and the value of the external DC electric field. Taking into account the technical limitations of experimental implementations, it is necessary to pay attention to the required accuracy of the parameter values. In particular, we found the following requirements for accuracy thresholds: the interatomic distance must be controlled with an accuracy of  $0.1 \mu\text{m}$ ; the interaction time -  $0.01 \mu\text{s}$ ; the external electric field -  $10^{-4} \text{ V/cm}$ . Here we assume that the maximum allowable deviation of the gate fidelity cannot exceed one percent.

Figure 4.18 shows the numerically calculated phase and population dynamics of the initially excited collective two- and three-body Rydberg atomic states for optimized system parameters. Left-hand and right-hand panels of Fig. 4.18 show the time dependencies of the populations and phases of initial collective states for interatomic distances  $R = 10 \mu\text{m}$  and  $R = 8.5 \mu\text{m}$ , respectively. When calculating the gate scheme, both two-body and three-body interactions in

the atomic system were taken into account. Note that for the successful execution of the gate, it is extremely important that the populations of the initial states are close to unity after the end of the interaction.

#### • Three Rydberg atoms

If all three atoms are excited into Rydberg states, we observe almost resonant Rabi-like population oscillations (Figs. 4.18(a, g)). In this case, the phase of the state changes by  $\pi$  after the interaction time due to the three-body resonance  $|70P_{3/2}(m=1/2)\rangle^{\otimes 3} \rightarrow |70S_{1/2}; 71S_{1/2}; 70P_{1/2}\rangle$  (Fig. 4.18(b, h)). This phase shift is sensitive to the electric field which acts directly on the Förster energy defect. It corresponds to the controlled phase shift when all three atoms are in state  $|1\rangle$  prior to the Rydberg excitation in Fig. 4.17(b). Note that Fig. 4.17(b) shows only one of the possible transition schemes. In the resonant process, we cannot attribute  $|70P_{3/2}\rangle \rightarrow |70S_{1/2}\rangle$ ,  $|70P_{3/2}\rangle \rightarrow |71S_{1/2}\rangle$  and  $|70P_{3/2}\rangle \rightarrow |70P_{1/2}\rangle$  transitions to a specific atom 1, 2 or 3. The population of initial state after the completion of the interaction is 91.5% due to the finite Rydberg lifetimes and the leakage of population to other collective levels by Rydberg interactions. These are found to be the major sources of the gate error.

#### • Two Rydberg atoms

Consider the case when only two of the three atoms are in Rydberg states. Then, due to the selection rule  $\Delta M = 0$  only off-resonant two-body interactions  $|70P_{3/2}(m=1/2)\rangle^{\otimes 2} \rightarrow |70S_{1/2}(m=1/2); 71S_{1/2}(m=1/2)\rangle$  are possible. The state  $|70S_{1/2}; 71S_{1/2}\rangle$  can also interact off-resonantly with  $|70P_{1/2}\rangle^{\otimes 2}$  and  $|70P_{3/2}; 70P_{1/2}\rangle$  states. A detailed analysis of two-body interactions in three-body systems of Rydberg atoms is given in article [224] (see Subsection 4.2.3).

If the atomic ensemble is initially excited to state  $|rgr\rangle$  (here  $|g\rangle$  is the ground state  $|0\rangle$ ,  $|r\rangle$  is the Rydberg state  $|70P_{3/2}(m=1/2)\rangle$ ), we can consider the influence of the interactions described above on the population and the phase of the final state as negligible (Figs. 4.18(c, d, i, j)). This is due to the fact that the two Rydberg atoms are too far apart from each other. Since the dipole-dipole interaction is proportional to  $R^{-3}$ , an increase in the distance between atoms by a factor of two causes an eightfold decrease in the strength of the dipole-dipole interaction even for resonant processes. But, since the two-particle process described here is not resonant, the interaction exhibits van der Waals character (see Subsection 2.2.4). Thus, the interaction is proportional to  $R^{-6}$ , and hence it will be 64 times smaller than for closely spaced atoms discussed below.

Alternatively, when the ensemble is initially excited into one of the states  $|grr\rangle$  or  $|rrg\rangle$ , we can observe a significant influence of the off-resonant two-body interactions on the phase of the collective state (Figs. 4.18(f, l)). This leads to the phase shift of the initially excited state, which can be compensated to zero during the interaction time  $T$  (see Fig. 4.17(c)). This phase shift is found to be sensitive to the external electric field. Two-body interactions also have a significant impact on the population of the initial state, leading to weak (with an amplitude of 5 – 10%) Rabi-like oscillations (Figs. 4.18(e, k)).

Finally, when only one atom in the ensemble is temporarily excited into the Rydberg state, the  $\pi$  and  $-\pi$  pulses, shown in Fig. 4.17(b), will return the system into the initial state with zero

phase shift. However, temporary Rydberg excitation will result in population loss due to the finite lifetimes of Rydberg states. The trivial case is when no Rydberg atoms are excited. The pulses 2-7 will have no effect in this instance.

In contrast to our previous proposal [98], we obtained the required phase dynamics without the need to use an external magnetic field for fine tuning of the position of three-body Förster resonance in the electric field scale. Moreover, the absence of the two-body Förster resonance in the vicinity of the three-body Förster resonance substantially simplifies the phase dynamics of the collective three-atom states. In this regard, we base the new gate scheme on the phase shift induced by three-body rather than two-body interaction, which makes it much more intuitive. We also obviate the need to excite atoms from different ground states.

#### 4.3.4. Optimization of gate parameters

The optimal values of the system parameters (interatomic distance  $R$ , interaction time  $T$ , electric field value  $F$ ) were calculated by performing multi-objective optimization using the Nelder-Mead method in order to increase the gate fidelity [253]. As mentioned above, for experimental implementation, these parameters must be controlled with high accuracy. Thus, when developing a gate scheme, it is necessary to take into account all possible sources of the gate fidelity losses arising from insufficient control of parameters and suggest ways to minimize their total effect.

The greatest control accuracy is necessary for the DC electric field: as can be seen from Fig. 4.16(b), the resonance peaks are extremely narrow, and even a field variation of  $10^{-4}$  V/cm can critically affect the gate fidelity. To mitigate this disadvantage, we propose to reduce the interatomic distances.

Figure 4.19 shows the dependence of the gate fidelity on the external electric field for two different interatomic distances. It can be seen that with a decrease in distance the requirements for the accuracy of field value control are significantly reduced. At a distance of  $R = 10 \mu\text{m}$ , a fidelity of  $\sim 98\%$  (with a maximum fidelity of 99.05%) is obtained for a field mismatch of  $10^{-4}$  V/cm. Thus, we can attribute this variation of field to the fidelity loss of  $\sim 1\%$ . At  $R = 8.5 \mu\text{m}$ , the same fidelity loss is obtained only at a field mismatch of about  $4 \cdot 10^{-4}$  V/cm (note that the maximum achievable fidelity is the same for both distances).

It should also be noted that the distance reduction has a positive effect on the gate implementation time. Specifically, the time required for gate implementation is  $0.42 \mu\text{s}$  when the distance between atoms is  $8.5 \mu\text{m}$ . In the case when the interatomic distance is 10 microns, the required time is about 3 times higher. Nevertheless, due to the enhanced interatomic interactions, the precise setting of the quantum gate is significantly complicated, and the improvement in accuracy does not arise for shorter distances. In principle, additional controlling parameters could allow fine-tuning of the gate, as will be discussed in the next section.

To estimate the gate fidelity, the method proposed in [237] was used (see Subsection 2.1.5 or Subsection 4.1.6). We considered a set of 216 different initial quantum register configurations and simulated the application of the developed quantum gate to each of these configurations. We calculated the density matrices  $\rho_{sim}$  of all final states after Toffoli gate was applied to each

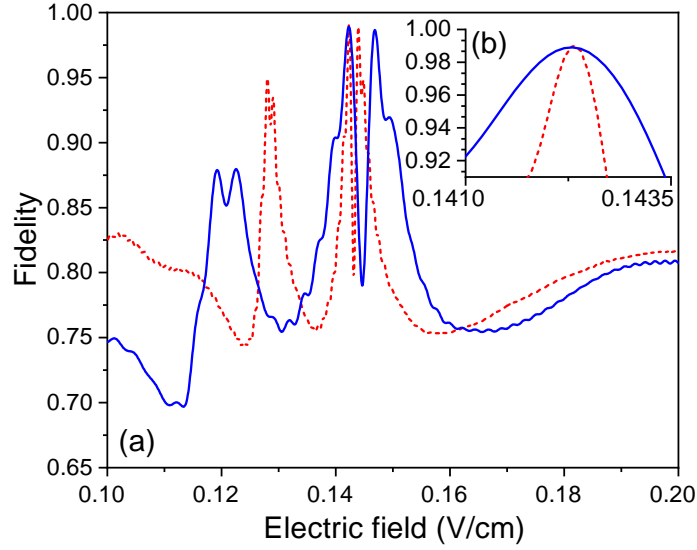


**Figure 4.19 :** Dependence of the fidelity of the Toffoli gate on the DC electric field for two different interatomic distances:  $R = 10 \mu\text{m}$  (red curve) and  $R = 8.5 \mu\text{m}$  (blue curve). The maximum fidelity of 99.05% is achieved with an electric field of 0.14232 V/cm. The interaction times coincide with those indicated in the description of Fig. 4.18 for both cases. (a) For a wide range of electric field values (0.1 – 0.2 V/cm). (b) Near the fidelity maxima.

initial state. Then we calculated the fidelity comparing  $\rho_{sim}$  to the etalon density matrix  $\rho_{et}$ , which represent the final state of the ensemble after the use of the perfect Toffoli gate [1]. Averaging over all 216 initial states, we calculated the gate fidelity.

$$F = Tr \sqrt{\sqrt{\rho_{et}} \rho_{sim} \sqrt{\rho_{et}}} \quad (4.34)$$

Note that the losses of the gate fidelity occurring at the stages of excitation and de-excitation of the Rydberg levels were not taken into account in presented calculations. If excitation takes place in a zero electric field, the different Zeeman sublevels of the initial  $70P$  state are populated during the excitation process. This, in turn, can lead to undesirable two- and three-particle interactions in the Rydberg system, violating the coherence of the resonance. According to our estimate, the maximum fidelity leakage caused by these processes does not exceed 0.88%.

We have conducted an additional study, assuming the Rydberg excitation to be performed at a non-resonant but non-zero electric field. It was found that by applying the external DC electric field of 0.2 V/cm during excitation, one can reduce the fidelity loss to 0.23%. Additional multi-parametric optimization allows us to adjust the fidelity values to compensate for the described effect and make it almost negligible. Thus, an additional fidelity loss of only 0.03% during the Rydberg excitation was obtained for the Toffoli gate model with the following parameter values:  $R = 10 \mu\text{m}$ ;  $F = 0.14225 \text{ V/cm}$ ;  $T = 1.12 \mu\text{s}$ ,  $F_0 = 0.2 \text{ V/cm}$ ,  $\tau = 0.01 \mu\text{s}$ . Here  $F_0$  is the described external excitation field, and  $\tau$  is the duration of the excitation pulse. In this study,

these two parameters were chosen for analytical reasons and were not included in the optimization process. Finally, we can summarize that the theoretical fidelity of the proposed gate is  $F > 99\%$ .

Since the excitation electric field value and the durations of the exciting and de-exciting pulses are variable parameters, they provide an additional opportunity to control the interaction in a three-body system. While providing the described research, we were already confident that by performing multiparametric optimization taking into account these parameters, the gate fidelity could be significantly increased. A similar approach to boost the fidelity of quantum operations was demonstrated in article [254]. However, this issue required additional research. We detail the implications of accounting for excitation effects in the external field in the next section, and show that by involving new controlling parameters, achieving significant accuracy improvements is possible.

As mentioned above, the limited lifetimes of Rydberg states are major sources of the gate error in the proposed gate scheme. A possible solution to this problem may be the use of a cryogenic environment [255], that can greatly improve the Rydberg static lifetimes. For example, Rydberg  $70S$  state lifetime is  $\sim 150 \mu\text{s}$  for 300 K temperature, while for  $\sim 0$  K it improves to  $\sim 410 \mu\text{s}$ . The lifetime extension effect is even more pronounced for Rydberg  $P$  states. Thus, for Rydberg  $70P_{1/2}$  states the lifetime increases from  $\sim 188 \mu\text{s}$  for 300 K environmental temperature to  $\sim 740 \mu\text{s}$  for  $\sim 0$  K environment.

### 4.3.5. Conclusion

We proposed a protocol to implement a three-qubit Toffoli gate based on FSSC three-body resonant Förster energy transfer in the ensemble of Rb Rydberg atoms isolated in three individual optical dipole traps. This new type of resonance is based on a change of fine structure state of one of the atoms involved in the interaction. The collective phase shifts induced by Rydberg interactions are controlled by an external electric field. We have shown that it is possible to reach a fidelity exceeding 99% for a short gate duration from  $0.4 \mu\text{s}$  to  $1.2 \mu\text{s}$ . Gate implementation has been numerically demonstrated for large interatomic distances ( $\sim 10 \mu\text{m}$ ). In order to minimize the decrease in gate fidelity, we found a compromise between the control accuracies of various experimental parameters (interaction time, interatomic distance and DC electric field). We managed to achieve a significant reduction in the sensitivity of the circuit to electric field deviations by applying a slight interatomic distance variation, avoiding a decrease in the gate fidelity.

It is important to emphasize the advantages of the proposed quantum gate protocol with respect to the protocol considered earlier in Section 4.1. First, the FSSC three-body resonances are realized for identical initial atomic states  $nP_{3/2}$ , so the new gate protocol does not require simultaneous excitation of atoms into different Rydberg states. This fact greatly facilitates the potential gate implementation, since the use of the same laser source for the Rydberg excitation is allowed. Facilitation of the experimental implementation is also guaranteed by the simpler Rydberg excitation scheme. To realize the previous protocol from Section 4.1, we needed to guarantee that both logic states  $|0\rangle$  and  $|1\rangle$  are coupled to the high-lying Rydberg levels. In the

current protocol, in contrast, we only need to ensure the connectivity of  $|1\rangle \rightarrow |r\rangle$ , where  $|r\rangle$  is the initial Rydberg state of each atom.

Note that in the proposed protocol, off-resonant two-body interactions lead to relatively weak phase dynamics. This reduces the effect of the complex structure of Rydberg energy levels on gate fidelity, which appears to be the major source of gate error if the Rydberg interactions are strong [243]. Also, it eliminates the need for additional tools to increase peak isolation, such as the magnetic field used earlier in Section 4.1. Finally, due to the absence of strong two-body interactions, we can realize the gate using a three-body phase shift, while fully compensating the two-body phase dynamics. This approach to the implementation of *CCZ*-gate is intuitive, since every oscillation of the population in a multiparticle system is accompanied by a  $\pi$  phase shift.

This work was supported by the Russia-France cooperation grant ECOMBI (CNRS grant №. PRC2312 and RFBR grant №. 19-52-15010). The Russian team was also supported by the Novosibirsk State University and by the Foundation for the Advancement of Theoretical Physics and Mathematics "BASIS". The French team was also supported by the EU H2020 FET Proactive project RySQ (grant №. 640378).

## 4.4. *CCPHASE* gate based on RF-induced FSSC resonances

The scheme of the three-qubit quantum gate presented in the Section 4.3 provides a direct proof of applicability of three-body FSSC Förster resonances for quantum computing purposes. The high quantum gate fidelity, supplemented by simplicity of its implementation, makes it a useful tool for the realization of complex quantum algorithms. In order to build on this success, we have continued to investigate the possibilities of many-body quantum gates implementation in structured Rydberg ensembles.

The purpose of further studies was to search for ways to compensate for the few disadvantages left with the developed gate scheme. First, as it was shown in previous works [98, 225], a high quality of experimental parameters control is required for successful gate implementation. In particular, accurate resonant tuning of the external DC electric field is necessary, down to  $10^{-4}$  V/cm. The implementation of such a degree of field control is in itself a challenging task, especially when considering the necessary change in electric field during the gate implementation which could lead to significant deviations in gate fidelity, linked to the risk of unwanted transitions. Note that in previous gate schemes, atomic excitation was considered in either zero electric field (Section 4.1), or in a strongly non-resonant field (Section 4.3). Thus, the field switching can critically affect the stability of these schemes.

Second, within the numerical computations shown in Section 4.3, the gate behaviour was simulated directly for atoms in the relevant Rydberg states, thus disregarding possible accuracy losses at the stages of excitation and de-excitation of atomic Rydberg states. In the paper [225], we assumed that the time of radiation pulses required at these stages is small compared to the implementation time of the Toffoli gate, and therefore, possible population leakage and addi-

tional phase dynamics will not lead to significant deviations in the gate fidelity. Nevertheless, for absolute confidence in the reliability of the obtained results, it is necessary to extend the numerical model, taking into account all the transitions occurring in the system, including also the stages of Rydberg excitation and de-excitation, during which Rydberg interactions could affect the system dynamics.

Finally, the search for new possibilities to control multiparticle interactions in three-atomic systems is necessary. So far, we have considered only resonances controlled by an external DC electric field. Also, an external magnetic field has been applied in Section 4.1 to isolate two- and three-body resonance peaks. Nevertheless, in order to realize an accurate quantum gate, it is necessary to achieve certain phase and population dynamics in the quantum system, controlling a huge amount of involved quantum states at once. Additional controlling experimental parameters, in turn, can help fine-tune the phases and amplitudes of the resonant oscillations, achieving the desired behavior and improving the gate fidelity. Thus, in this study, we have also focused on searching for new possibilities to implement multi-particle system control. Note that desirable control utilities should provide the opportunity for precise experimental tuning, which is difficult to realize using magnetic and electric DC fields.

To extend the control possibilities in a multiparticle system, we propose to use Förster transitions induced by external radiofrequency radiation. Previously, two-body RF-induced Förster resonances were studied in detail in [153, 207, 256–258]. It was shown that in addition to resonances existing in DC electric fields, RF radiation also allows one to induce inaccessible Förster resonances whose energy defect is negative in zero electric field and increases along with DC field. For example, in [257], two-body RF-induced resonances  $2 \times 39P_{3/2} \rightarrow 39S_{1/2} + 40S_{1/2}$  were demonstrated in Rb atoms. As repeatedly emphasized in the previous sections, the resonance  $2 \times nP_{3/2} \rightarrow nS_{1/2} + (n + 1)S_{1/2}$  cannot be realized in ensembles of Rb atoms for  $n > 38$  in the DC electric field due to the specific values of the polarizabilities and quantum defects of the involved collective states (for example, see Section 4.1). Nevertheless, as the results of [257] show, such resonances can be induced by RF radiation.

The application of RF-induced two-body resonances in Rydberg quantum computing has also been investigated previously [154, 259]. For example, in [154], a two-body quantum *CZ*-gate scheme based on the adiabatic passage of a radiofrequency-induced two-body Förster resonance  $60P_{3/2}(3/2) + 80P_{3/2}(3/2) \rightarrow 59D_{5/2}(5/2) + 78D_{5/2}(5/2)$  was proposed. The generation of Bell states has also been demonstrated in this study.

In [226], we describe for the first time RF-induced three-body Förster resonant transitions in ordered arrays of three Rb atoms. We show that under RF radiation, few-body resonances acquire replicas for parameters that can be chosen with the RF frequency and that even two-body or three-body processes displaying no resonance in DC field can be accessed through one of these replicas. Many-body RF-induced Förster resonances have not been investigated previously, making the results of this study unique. We have also shown that coherent population dynamics resulting from RF-induced resonance can be obtained in three-atom ordered Rydberg arrays. We conclude that RF radiation provides new opportunities to facilitate the experimental realization of many-body Rydberg gates, as well as gives new degrees of freedom in interaction control, allowing to significantly increase the accuracy of the gate implementation.

The use of radiofrequency-induced Förster resonances allowed us to achieve a high degree of control in the three-qubit system. We have proposed new protocols of three-body quantum gates *CCPHASE*, which are based on either accessible three-body or inaccessible two-body Förster resonances. While the gate scheme based on three-body resonance [192] is a significant development of our previous *CCZ* gate proposals [98, 225] (shown as elements of Toffoli gates in Sections 4.1 and 4.3), the scheme based on the two-body resonance replica demonstrates a fundamentally new approach to the three-body operator construction. Both of these schemes demonstrate high gate fidelity ( $\sim 99.7\%$  assuming cryogenic environment and  $\sim 99.3\%$  for room temperature) and are limited mainly by the Rydberg lifetimes. The developed *CCPHASE* gates allow for arbitrary transformations of collective state phases of the three-qubit register by varying the RF parameters. The advantage of this technique is that it can be applied at large interatomic distances ( $\sim 10 \mu\text{m}$ ), paving a way to create full interconnectivity in large atomic arrays [59, 260, 261]. Also, the shown scheme provides a great facilitation for the experimental implementation and Rydberg excitation control due to the fact that the value of external DC electric field is kept constant during the experiment.

The results presented within this section and those presented in the paper [226] were obtained by the author of this thesis. Nevertheless, the idea of investigating RF-induced resonances was proposed by the author's colleagues. The author gratefully thanks his co-authors for their assistance with the simulations as well as fruitful scientific discussions.

##### 4.4.1. Introduction to *CCPHASE* gates

Previously, we have described the possibilities of application of multi-qubit quantum gates to realize complex quantum computational schemes (see Sections 1.7, 2.1.3.2). Thus, it was mentioned that multi-qubit gates allow to achieve a significant reduction in the total number of gates for various quantum algorithms, including QAOA [262], quantum error correction [88, 263, 264], Grover's search [265], Shor's algorithm [11], fault-tolerant quantum computation implementation [266] and many others. A particularly challenging task is the implementation of multi-qubit controlled quantum operations, such as  $C^k\text{NOT}$  and  $C\text{NOT}^k$  gates [100, 267–270], Fredkin gates [271],  $C^k\text{PHASE}$  gates [48]. We also demonstrated in the previous sections of this chapter, that Förster resonances can be applied to implement doubly-controlled three-qubit quantum gates.

The *CCPHASE* gate is a generalization of the well-known *CCZ*-gate for an arbitrary phase  $\phi$  of a final multiqubit state. If both controlling qubits are in the state  $|1\rangle$ , a transformation is applied to the target qubit that changes the phase difference between its logic states by  $\phi$ . The gate action can thus be represented by an operator (4.35).

*CCPHASE* gates are not widely researched, thus the area of their potential application is not completely clear. Nevertheless, since the combination of *CCPHASE* gates with sequences of single-qubit gates and global phase gates allows, in principle, to implement arbitrary doubly-controlled unitary operations [1], we can argue that a successful implementation of such a gate will be useful in all the previously listed algorithms, and can also be applied in a number of quantum simulation algorithms (e.g., in the quantum phase estimation algorithm [19]). Note

that the possibility of realizing arbitrary unitary gate is based on the analysis for  $CU$ -gate  $ABC$  decomposition, shown in Subsection 2.1.2.2. According to [272], arbitrary doubly-controlled phase gates (similar to the  $CCPHASE$  gate proposed in this section) have been successfully applied to solve the MAX-3-SAT problem using QAOA. The experiment realized on a 32-qubit superconducting quantum processor “Aspen-9” demonstrated a qualitative and quantitative improvement in the generated QAOA landscape when using the custom  $CCPHASE$  gate over the full two-qubit decomposition of the circuit.

$$CCPHASE = \begin{pmatrix} 1 & 0 & 0 & 0 & 0 & 0 & 0 & 0 \\ 0 & 1 & 0 & 0 & 0 & 0 & 0 & 0 \\ 0 & 0 & 1 & 0 & 0 & 0 & 0 & 0 \\ 0 & 0 & 0 & 1 & 0 & 0 & 0 & 0 \\ 0 & 0 & 0 & 0 & 1 & 0 & 0 & 0 \\ 0 & 0 & 0 & 0 & 0 & 1 & 0 & 0 \\ 0 & 0 & 0 & 0 & 0 & 0 & 1 & 0 \\ 0 & 0 & 0 & 0 & 0 & 0 & 0 & e^{i\phi} \end{pmatrix} \quad (4.35)$$

To the best of our knowledge, doubly-controlled phase gate protocols have not been explicitly proposed for Rydberg registers before. Nevertheless, according to our analysis, the  $CCZ$  quantum gate protocol implemented in [47] can be adapted to realize arbitrary phase gates. This protocol is based on the use of a controlled excitation phase shift in the presence of a strong dipole blockade. Thus, its application is limited to registers in which the atoms are isolated at a small distance  $\sim 5 \mu\text{m}$  from each other. In turn, our proposed protocol based on three-atom Förster resonances can be applied to much further separated qubits (with interatomic distances up to several tens of  $\mu\text{m}$ ). Thus, we can state that the new  $CCPHASE$  gate protocol is of great interest for modern Rydberg quantum computing.

#### 4.4.2. RF-induced Förster resonances

Resonant interactions induced by a time-dependent periodic electric field were analyzed in detail in [153]. Following the course of this work, we distinguish two approaches to the simulation of RF-induced resonances: the numerical solution of the Schrödinger equation, or the application of an analytical approach using the description of Floquet sidebands. While the Floquet sideband approach provides convenient insights into the understanding of resonant processes in two-level systems, numerical methods are better suited for describing complex multilevel dynamics. Thus, in this section we concentrate on the numerical description, using the elements of the Floquet sideband approach only to provide the reader with some analytical analogies. Note that we introduce the theory of RF-induced resonances only briefly here. For a more detailed description, the reader can refer to the Appendix B, or the original paper [153].

We consider Förster resonances in an ordered ensemble of three Rb atoms. This means that all the operators given in this section are described in the basis of collective states  $\Psi_i = |n_i^1 l_i^1 j_i^1 (m_{ji}^1); n_i^2 l_i^2 j_i^2 (m_{ji}^2); n_i^3 l_i^3 j_i^3 (m_{ji}^3)\rangle$ , unless specified otherwise. Here, the upper indices denote the number of the atom in the ensemble, while the lower indices relate to the

#### 4.4. CCPHASE gate based on RF-induced FSSC resonances

different configurations of the individual quantum numbers of each atomic state.

To describe the dynamics of the interatomic interaction, we solve the Schrödinger equation for the following Hamiltonian:

$$\hat{H} = \hat{H}_0 + \hat{H}_{F_S} + \hat{H}_{F_{RF}} + \hat{V} \quad (4.36)$$

Here  $\hat{H}_0$  denotes the Hamiltonian of the atomic system without taking into account any interactions,  $\hat{H}_{F_S}$  is the Hamiltonian of the interaction with the DC part of the electric field,  $\hat{H}_{F_{RF}}$  stands for the interaction with the RF radiation, that is, the time-dependent component of the field. We define the total field in the system as (4.37), where  $F_S$  and  $F_{RF}$  indicate the amplitudes of the stationary and oscillatory parts of electric field, respectively.

$$F = F_S + F_{RF} \cos(\omega t) \quad (4.37)$$

The operator  $\hat{V}$  describes a set of dipole-dipole interatomic interactions in a system of three Rydberg atoms. According to the previous sections (see Subsections 2.2.4, 3.3.5 and 4.1.2), it can be described as a composition of individual diatomic dipole-dipole interactions, which can be expressed as [227]:

$$\hat{V}_{dd} = -\frac{\sqrt{6}e^2}{4\pi\epsilon_0 R^3} \sum_{q=-1}^1 C_{1q}^{20} \hat{a}_q \hat{b}_{-q}. \quad (4.38)$$

The radial matrix elements of the dipole moment are calculated using a quasiclassical approximation [221] (see Appendix A). Note that in the case of linear arrangement of atoms (which is described in this study) the  $\hat{V}_{dd}$  operator couples only two-atom collective states with  $\Delta M = 0$ , where  $M$  is the total momentum projection of the collective state.

In this work we focus on FSSC three-body Förster resonances (4.39), which were described in detail in the previous sections (see Sections 4.2 and 4.3) [223, 225]. Assuming that at the beginning of the interaction the system is in state  $|nP_{3/2}\rangle^{\otimes 3}$ , we consider transitions of the form (4.40), where, due to the resonant interaction, the amplitude  $C_{fin}$  of the final state  $|nS_{1/2}; (n+1)S_{1/2}; nP_{1/2}\rangle$  is much larger than all other complex amplitudes in the system. Thus, the main part of the population dynamics of the atomic system will be described by equation (4.39).

$$|nP_{3/2}\rangle^{\otimes 3} \rightarrow |nS_{1/2}; (n+1)S_{1/2}; nP_{1/2}\rangle \quad (4.39)$$

$$|nP_{3/2}\rangle^{\otimes 3} \rightarrow \sum_i C_i \Psi_i \quad (4.40)$$

To facilitate an intuitive description, one could consider transitions (4.39) in a two-level system with  $\Psi_{in} = |nP_{3/2}\rangle^{\otimes 3}$  and  $\Psi_{fin} = |nS_{1/2}; (n+1)S_{1/2}; nP_{1/2}\rangle$ . We assume that these are the eigenstates of the Hamiltonian  $\hat{H}_0 + \hat{H}_{F_S}$ , which does not include the interaction of atoms with each other or with radiation. Then the state of the system has the form (4.41).

$$\Psi = a\Psi_{in}(r)e^{-iE_1t/\hbar} + b\Psi_{fin}(r)e^{-iE_2t/\hbar} \quad (4.41)$$

Here, the energy levels depend on the external electric field. We consider the case of the quadratic Stark effect (4.42). If the energy levels become degenerate ( $E_1 = E_2$ ), this intersection denotes a three-body Förster resonance.

$$E_{1(2)} = E_{1(2)}^0 - \frac{1}{2}\alpha_{1(2)}F_S^2 \quad (4.42)$$

We take into account the other interactions in the system by adding the corresponding parts of the Hamiltonian  $\hat{V}$  and  $\hat{H}_{RRF}$ . The interatomic interaction leads to the removal of the energy levels degeneracy in the resonant field, and induces an avoided crossing. This avoided crossing has a width of Rabi frequency  $\Omega_0 = 2\langle\Psi_{fin}(r)|\hat{V}|\Psi_{in}(r)\rangle$ .

Interaction with the AC electric field leads to the fact that the energy levels of the system also become time-dependent (4.43). Then, we can conclude that the anti-crossings which lead to a resonant interaction of the form (4.39) will multiply in this case and that they will be repeated with the periodicity determined by the frequency of RF radiation.

$$E_{1(2)} = E_{1(2)}^0 - \frac{1}{2}\alpha_{1(2)}(F_S + F_{RRF} \cos(\omega t))^2 \quad (4.43)$$

Note that the given two-level model is incomplete and serves only for the purposes of demonstration of the RF-induction principle for many-body resonances. To obtain an informative result, the interaction with external radiation should be taken into account in the numerical simulation including a wide range of Rydberg states.

### 4.4.3. Numerical simulations

This subsection provides a detailed description of our numerical simulations of Förster resonances induced by RF radiation in a three-atom system. We model the interaction between atoms isolated in individual optical dipole traps arranged linearly and equidistantly along the direction of the external control electric field ( $Z$  axis). As described previously in Subsection 3.3.7, the choice of such an atomic configuration reduces the number of interaction channels (due to the presence of axial symmetry), and makes it easier to describe polyatomic resonances.

We consider level  $|RRR\rangle = |70P_{3/2}(m = 1/2)\rangle^{\otimes 3}$  as the initial Rydberg level for resonances (4.39). Thus, the three-body resonance under study has the form (4.44). Note that arbitrary value for the principal quantum number  $n$  can be chosen, according to the experimental requirements. For the demonstration purposes, we consider  $n = 70$ , since a good compromise between robustness to small fluctuations of DC electric field and individual Rydberg lifetimes was shown for this value in previous sections (see Sections 4.2 and 4.3) [223, 225]. To reduce the number of basis states, we limit the collective state spectra by  $\pm 2$  GHz relative to the energy of  $|70P_{3/2}\rangle^{\otimes 3}$  state, thus considering only atomic states with a momentum value  $l \leq 1$ .

#### 4.4. CCPHASE gate based on RF-induced FSSC resonances

Also, due to the linear configuration of the atomic ensemble, a selection rule  $\Delta M = 0$  arises [98, 193], which allows us to exclude collective states whose total moment projection differs from  $M$  of the initial state. Thus, we significantly reduce the basis of states under consideration, down to  $\sim 360$  collective states, presented by combinations of all the magnetic sublevels of  $|70S_{1/2}\rangle, |71S_{1/2}\rangle, |70P_{1/2}\rangle, |70P_{3/2}\rangle$  individual Rydberg states.

$$|70P_{3/2}\rangle^{\otimes 3} \rightarrow |70S_{1/2}; 71S_{1/2}; 70P_{1/2}\rangle \quad (4.44)$$

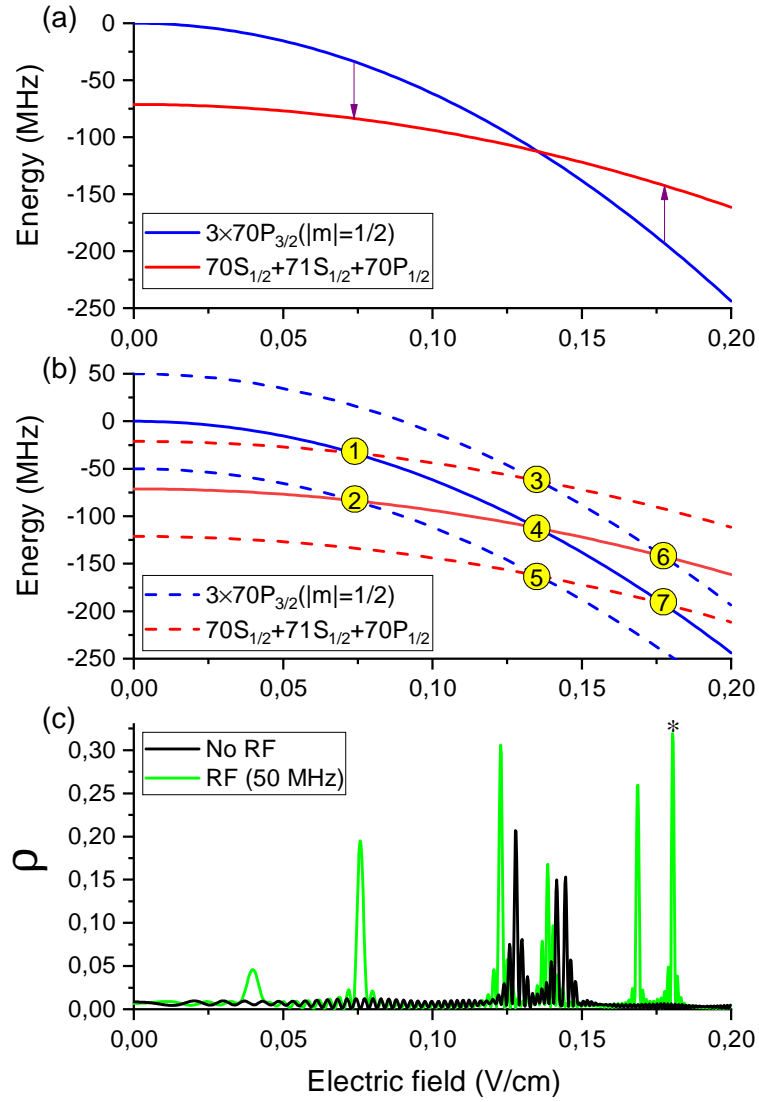
Numerical approach to the simulation of resonant interactions induced by a time-dependent periodic electric field was analysed in detail in [153]. We incorporate this approach into the numerical model presented earlier in Sections 4.1 and 4.3. To model the time dynamics of the three-body system, we solve numerically the non-Hermitian Hamiltonian based Schrödinger equations for the complex amplitudes of the collective basis states taking into account Rydberg lifetimes [169]. During the simulation, we take into account the dipole-dipole interatomic interactions (DDI) [227], as well as the interaction of atoms with an external cumulative electric field  $F = F_S + F_{RF} \cos(2\pi\omega t)$  [153]. Here  $F_S$  denotes the static part of electric field (DC field), while  $F_{RF}$  is the amplitude of RF field (AC field).

Figure 4.20 depicts the three-body Förster resonances (4.44) obtained from the simulation. This effect has several physical interpretations. On the one hand, the energy barrier  $\delta$  between the collective states of the multiatomic system is compensated by radiofrequency radiation. Thus, by absorbing or emitting one or several photons of frequency  $\omega$ , atoms experience the Förster resonance in the case if  $\delta = k\omega$ , where  $k$  is an integer. This process is represented in the Stark diagram Fig. 4.20(a). Here the arrows show the transfer from the initial (blue line) to the final (red line) state of the triatomic system as a result of emission (left arrow) or absorption (right arrow) of a single photon. The electric field differences between the original three-body resonance  $|70P_{3/2}\rangle^{\otimes 3} \rightarrow |70S_{1/2}; 71S_{1/2}; 70P_{1/2}\rangle$ , depicted by the intersection of the solid blue and red lines, and the RF-induced resonances shown by arrows, are only determined by the frequency of the external radiation. Thus, we gain the possibility to control the position of the induced resonances in the scale of the DC electric field by changing only the frequency of RF-radiation.

An alternative description is based on the Floquet approach. The energies (4.43) depend on time periodically, which leads to the formation of an infinite number of sidebands in the spectrum, separated by  $\omega$  (Fig. 4.20(b)). The eigenfunctions of the Hamiltonian, in turn, also have relative amplitudes  $a_{nL,m}$ , described by generalized Bessel functions (see Appendix B).

$$a_{nL,m} = \sum_{k=-\infty}^{\infty} J_{m-2k} \left( \frac{\alpha_{nL} F_S F_{RF}}{\omega} \right) J_k \left( \frac{\alpha_{nL} F_{RF}^2}{8\omega} \right) \quad (4.45)$$

Figure 4.20(b) depicts the three-body Förster resonances in a form of Stark diagram, including both the collective atomic states and their Floquet sidebands. It shows the initial and final states of the system (solid lines), accompanied by sidebands (dashed lines). Each intersection



**Figure 4.20:** (a) Numerically calculated Stark structure of the collective energy levels, involved in three-body Förster resonance  $|70P_{3/2}\rangle^{\otimes 3} \rightarrow |70S_{1/2}; 71S_{1/2}; 70P_{1/2}\rangle$ . The energy of the initial state  $|70P_{3/2}\rangle^{\otimes 3}$  is taken as a reference. The intersection of solid blue (initial state) and red (final state) lines mark the position of the original three-body resonance, while the arrows indicate the corresponding RF-induced resonances. (b) Floquet representation of the Stark structure of collective energy levels. Solid lines correspond to the initial (blue) and final (red) states of the system. Dashed lines denote the corresponding first-order Floquet sidebands. Each intersection corresponds to a three-body resonance. (c) Numerically calculated dependence of the fraction  $\rho$  of atoms in the final  $|71S_{1/2}\rangle$  state after three-body interaction on the external DC electric field for the initial state  $|70P_{3/2}(m=1/2)\rangle^{\otimes 3}$ . The atoms are located along the  $Z$  axis at interatomic distance  $R = 10$  microns. Different groups of peaks represent original or RF-induced resonances. Two cases are presented: three-body resonance in the absence of RF induction (black line); three-body RF-induced resonant peaks along with the original resonance (green line).

of the lines corresponds to a resonance. The original three-body resonance (4.44) is still represented by the intersection of solid blue (initial state) and red (final state) lines, and is indicated by the number 4. This resonance naturally exists in the corresponding DC electric field even in absence of RF radiation. The intersections of the sidebands with the original levels correspond to first-order resonances and are located in the same DC electric field as the “arrows” in Figure 4.20(a). Two RF-induced first-order resonances were found near the original three-body resonance, depicted by the intersections 1, 2 and 6, 7 between the original energy levels and corresponding Floquet sidebands. Also, resonances 3 and 5 appear in the same DC electric field as original resonance due to the Floquet sidebands intersection. These resonances are completely analogous to the original resonance 4 and do not create additional interaction channels. Note that during the calculation of the presented Stark diagrams, no interatomic interactions were taken into account.

In Figure 4.20(c), numerically simulated three-body Förster resonances (4.44) are shown. When RF radiation is turned off, only original resonance 4 remains (black line). Note that in the resonant process, we cannot attribute  $|70P_{3/2}\rangle \rightarrow |70S_{1/2}\rangle$ ,  $|70P_{3/2}\rangle \rightarrow |71S_{1/2}\rangle$  and  $|70P_{3/2}\rangle \rightarrow |70P_{1/2}\rangle$  transitions to a specific atom in an ensemble. In this regard, several resonant interaction channels are formed, from which only two are allowed due to symmetry reasons [193]. This process is similar to the Autler–Townes effect, and leads to the splitting of resonant peaks into 2 satellites due to always resonant excitation hopping, as it is shown in the Figure 4.20(c). Presence of the RF radiation induces additional first-order peaks (green line). The relative distances between the resonances correspond to the applied radiation frequency of 50 MHz. The displacement of the doublet centers relative to the expected resonant positions provided in Figures 4.20(a, b), is due to the presence of the interatomic dipole-dipole interaction  $\hat{V}$  in the Hamiltonian  $\hat{H}$  for the complete simulation, while it was not taken into account during Stark maps calculation. The expected DC field of the resonance peak is also displaced due to the AC Stark shift produced by the RF field applied. This effect is clearly noticeable for the original three-body resonance peak (black line on Fig.4.20(c)), which shifts when the RF part of the field is switched on (central doublet, green line in Fig.4.20(c)).

A great decrease of intensity can be seen for the left Floquet sideband (which is represented by two leftmost peaks in Fig.4.20(c), green line), when comparing with the right sideband (two rightmost peaks in Fig.4.20(c)). This decrease is associated with two effects. First, the amplitude is influenced by two-body exchange interactions between  $S$  and  $P$  states, accompanied by exchange of momentum projection  $m$ . These interactions are resonant in the zero field due to the spectra degeneracy, thus provoking a significant leakage of the initial state population. The influence of such processes decreases quadratically when the DC field increases and becomes negligibly small for the original resonance [223]. Second, the modulation depth (or equivalently the amplitude of the Floquet sideband) depends on the DC electric field. Since the Stark effect is quadratic, the modulation depth increases fast with the DC field component, which is demonstrated by Eq. (4.45). Thus, a significant decrease in peak amplitudes can be expected for small values of  $F_S$  compared to larger values. To avoid the unwanted influence of these two effects, we further concentrate on the rightmost peak from Fig.4.20(b) (signed with asterisk) when considering any resonant dynamics.

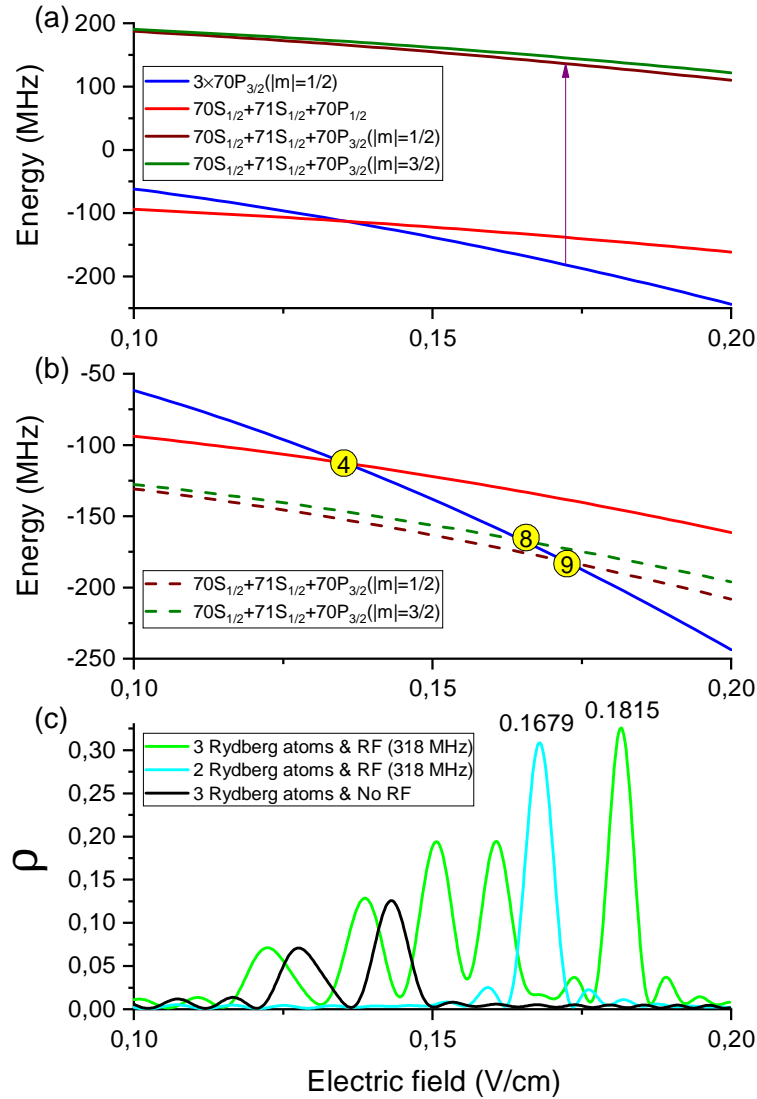


**Figure 4.21 :** (a) Numerically calculated Stark structure of the collective energy levels, involved in resonant Förster interactions. The energy of the initial state  $|70P_{3/2}\rangle^{\otimes 3}$  is taken as a reference in zero field. The intersection of solid blue and red lines mark the positions of the original three-body resonance  $|70P_{3/2}\rangle^{\otimes 3} \rightarrow |70S_{1/2}; 71S_{1/2}; 70P_{1/2}\rangle$ , while the arrow indicates the RF-induced two-body resonance  $|70P_{3/2}\rangle^{\otimes 3} \rightarrow |70S_{1/2}; 71S_{1/2}; 70P_{3/2}\rangle$ . (b) Floquet representation of the Stark structure of collective energy levels. Solid lines correspond to the initial state  $|70P_{3/2}\rangle^{\otimes 3}$  (blue) and the final state  $|70S_{1/2}; 71S_{1/2}; 70P_{1/2}\rangle$  (red). Dashed lines denote the first-order Floquet sidebands of the final states  $|70S_{1/2}; 71S_{1/2}; 70P_{3/2}(|m|=1/2)\rangle$  (brown) and  $|70S_{1/2}; 71S_{1/2}; 70P_{3/2}(|m|=3/2)\rangle$  (green). Each intersection corresponds to a resonant process. (c) Numerically calculated dependence of the fraction  $\rho$  of atoms in the final  $|71S_{1/2}\rangle$  state after the many-body interaction on the external DC electric field for the initial state  $|70P_{3/2}(m=1/2)\rangle^{\otimes 3}$ . The atoms are located along the  $Z$  axis at  $R = 10 \mu\text{m}$  distance. Three cases are presented: three-body resonance in the absence of RF induction (black line); two-body resonance enabled by RF radiation when only two atoms are excited (cyan line); two- and three-body peaks when three Rydberg atoms are exposed to RF radiation (green line).

#### 4.4. CCPHASE gate based on RF-induced FSSC resonances

The use of RF radiation also makes it possible to induce transitions that are energetically forbidden under the conditions of the DC Stark effect. Figure 4.21 demonstrates an example of a two-body transition between states  $|70P_{3/2}\rangle^{\otimes 3}$  and  $|70S_{1/2}; 71S_{1/2}; 70P_{3/2}\rangle$ . As it was explained in previous sections (for example, see Section 4.1), such transitions are forbidden under the ordinary conditions of resonance (4.44) provoked by DC electric field, since the Stark effect in this case leads to an increase of the energy gap of initial and final states (Fig. 4.21(a)). Nevertheless, by applying RF radiation, we can induce new two-body resonances for arbitrary values of DC electric field. For example, choosing the RF frequency to be 318 MHz we obtain this resonance for almost the same DC field as for the previous scheme with 50 MHz. This is demonstrated in Figure 4.21(a), where the arrow shows the RF-induced two-body transition (at 0.1815 V/cm) appearing close to the DC electric field, for which RF-induced three-body resonance was observed in Figure 4.20(c) (0.1805 V/cm). In principle, we can induce resonances in an exactly matching electric field by slightly changing the radiation frequency. Thus, by changing only the frequency of the field, we can activate different strong interactions in the system.

Turning to the Floquet approach (Figure 4.21(b)), we can see several intersections between the collective energy levels. Thus, the intersection 4 of the solid red and blue lines here, as in the previous picture, refers to the three-body resonance. This resonance is shown in Figure 4.21(c) as the two leftmost peaks (green line and black line). Note that the signal evolution time was chosen to maximise the two-body resonance peak. Therefore, the three-body resonance has a smaller amplitude than in Fig. 4.20. The intersections of first-order Floquet sidebands of levels  $|70S_{1/2}; 71S_{1/2}; 70P_{3/2}(|m| = 3/2)\rangle$  and  $|70S_{1/2}; 71S_{1/2}; 70P_{3/2}(|m| = 1/2)\rangle$  (dashed green and brown lines, respectively), with the initial state (solid blue line), reflect resonances (4.46) and (4.47), respectively. The peaks corresponding to these resonances only appear when the external RF radiation is applied. Note that Figure 4.21(b) shows only the intersections of the end-state sidebands with the initial state, and does not show a complementary picture (which, nevertheless, is present at higher energy values).

$$|70P_{3/2}(|m| = 1/2)\rangle^{\otimes 3} \rightarrow |70S_{1/2}; 71S_{1/2}; 70P_{3/2}(|m| = 3/2)\rangle \quad (4.46)$$

$$|70P_{3/2}(|m| = 1/2)\rangle^{\otimes 3} \rightarrow |70S_{1/2}; 71S_{1/2}; 70P_{3/2}(|m| = 1/2)\rangle \quad (4.47)$$

It is important to point out that the nature of resonances (4.46) and (4.47) is fundamentally different. The resonance (4.46) is a three-body resonance, since the states of all three atoms change in the process. It is shown by the central pair of peaks on the green line (Fig. 4.21(c)). In turn, the resonance (4.47) is two-body, shown by the rightmost peak on the green line in Fig. 4.21(c). Note that for two-body interactions the peak doubling effect we described earlier is not observed, thus a single peak represents a Floquet sideband. To demonstrate the two-body nature of this effect, we conducted a simulation taking into account the presence of only two atoms in the ensemble (cyan line in Fig. 4.21(c)), separated by a distance  $R$ . It can be seen that in this case the peak is present and retains its amplitude, which proves its fundamental two-body nature. The significant peak shift in this case is explained by the absence of interaction with the third atom.

The data presented in this subsection demonstrate a wide range of possibilities provided

by external RF radiation for controlling a triatomic system. Let's assume that an experimental setup has been prepared, consisting of a register of Rydberg atoms isolated in individual optical dipole traps, and an external electric field co-directed with the interatomic axis. Then, we have the opportunity to switch between various polyatomic interactions and adjust their strength only by controlling the parameters of external RF radiation (frequency and amplitude, as well as the shape of the pulses). This control mechanism is extremely convenient for implementing complex multiqubit gates. In the next chapter, we will demonstrate exactly how the described interactions can be used to implement a three-qubit *CCPHASE* quantum gate.

#### 4.4.4. *CCPHASE* gate proposal

RF-induced resonant interactions shown in the previous subsection allows the direct control of phase and population dynamics of many-body Rydberg states in atomic ensemble. Thus, we state that presented interactions are promising candidates for the implementation of many-body quantum gate protocols. To prove this, we demonstrate here two examples of *CCPHASE* gate protocol for arbitrary value of  $\phi$ , based either on three-body, or on two-body resonant interaction.

The universal gate scheme we present is a substantial modification of our previous proposal [225], shown in Section 4.3. The same linear arrangement of atomic qubits is kept, which was described above. We use the central atom as a target qubit, and two outer atoms as control ones. We utilize RF field to induce the Förster resonance for a chosen value of  $F_S$  and thus implement a quantum doubly-controlled phase gate *CCPHASE*. Note that the DC part of the electric field is being kept constant during the whole process, thus facilitating the experimental implementation of the scheme.

The significant improvement lies in the application of non-resonant DC electric field, which allows us to limit unwanted interactions during laser excitation, as well as avoid the influence of always-resonant zero-field interactions of the form  $|nP_{3/2}(m_1)\rangle^{\otimes 3} \rightarrow |nP_{3/2}(m_2); nP_{3/2}(m_3); nP_{3/2}(m_4)\rangle$ . Such interactions can arise due to the degeneracy of states with different projections of the magnetic moment in the zero field. Nevertheless, when the DC field is present, these interactions are no longer resonant and do not lead to any unwanted dynamics.

##### • Gate protocol

The implementation of the desired *CCPHASE* gate can be divided into a sequence of three steps (see Fig.4.22).

Step 1: The laser excitation  $\pi$  pulses 1-3 are applied simultaneously to all three atomic qubits. We assume that prior to the excitation, the atoms were in their logical states (namely,  $|0\rangle$  and  $|1\rangle$ ). These states are represented by two pre-selected hyperfine sublevels of rubidium ground states  $|5S_{1/2}\rangle$  (see Subsection 2.3.2) [59, 273]. We consider fully resonant single-photon laser excitation in rotating wave approximation, assuming that only transitions of the form  $|1\rangle \rightarrow |R\rangle = |70P_{3/2}(m = 1/2)\rangle$  are allowed. We thus account for interactions during laser excitation, in contrast with the previously used models. For practical applications, a three-photon

#### 4.4. CCPHASE gate based on RF-induced FSSC resonances

excitation scheme can be used to pair the logical states of qubits with Rydberg levels [170], as discussed in Subsection 2.3.2. The effects associated with the phase and intensity noise of the laser were considered in [252] and were not taken into account in this study, which focuses on the influence of Rydberg interactions.

Step 2: RF pulse of the duration  $T$  is applied to the system, inducing resonance for a chosen value of the DC electric field. Note that the DC field, which is non-resonant in the absence of RF, appears to be resonant for a certain Floquet sideband, which arises as a result of the radiofrequency radiation application. The RF pulse is accompanied by two waiting times  $T_{wait}^1$  and  $T_{wait}^2$ , which are additional configurable system parameters. The DC and AC parts of the electric field are co-directed, thus keeping the symmetry of the atomic system unchanged. The resonant interaction causes the phase of the collective state  $|RRR\rangle$  to change by  $\phi$  during the

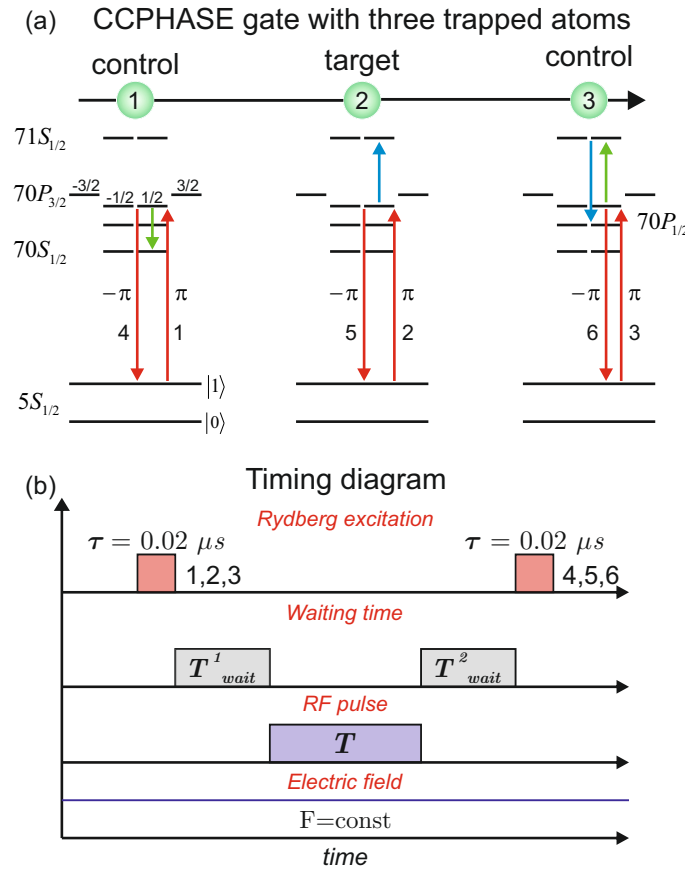


**Figure 4.22 :** (a) Scheme of general *CCPHASE* gate based on three-body Rydberg interactions. Three Rb atoms are located in the individual optical dipole traps aligned along the  $Z$  axis, which is co-directed with the external control electric field. Laser pulses 1-6 excite and de-excite the chosen Rydberg atomic states. The  $\phi$  phase shift due to the three-body interaction appears only if all three atoms are excited into Rydberg states. The green and blue arrows here indicate  $|70P_{3/2}\rangle^{\otimes 3} \rightarrow |70S_{1/2}; 70P_{3/2}; 71S_{1/2}\rangle$  and  $|70S_{1/2}; 70P_{3/2}; 71S_{1/2}\rangle \rightarrow |70S_{1/2}; 71S_{1/2}; 70P_{1/2}\rangle$  two-body transitions, respectively. Thus, the full scheme corresponds to a collective resonant transition  $|70P_{3/2}\rangle^{\otimes 3} \rightarrow |70S_{1/2}; 71S_{1/2}; 70P_{1/2}\rangle$ . (b) Timing diagram of the pulses in the proposed gate scheme.

interaction time. This corresponds to a *CCPHASE* gate implementation, provided that all other states of the system remain unchanged after the application of RF radiation terminated.

Step 3: The de-excitation  $-\pi$  pulses 4-6 are applied simultaneously to all three atomic qubits.

We performed numerous simulations of the operation of *CCPHASE* gate scheme for a wide range of  $\phi$ . The simulations were performed in an extended basis of states, which also included the logical states of qubits, in contrast with previously considered scheme in Section 4.3. For the first demonstration of the gate operation, we consider the implementation of the Toffoli gate (see Fig. 4.23), based on a three-body RF-induced Förster resonance (4.44). We use the  $CCPHASE(\pi) \equiv CCZ$  gate, supplementing it with two Hadamard gates on target qubit. These Hadamard gates are performed by two-photon Raman  $Y_{\pi/2}$  pulses [274].

### • Three-body resonance-based protocol

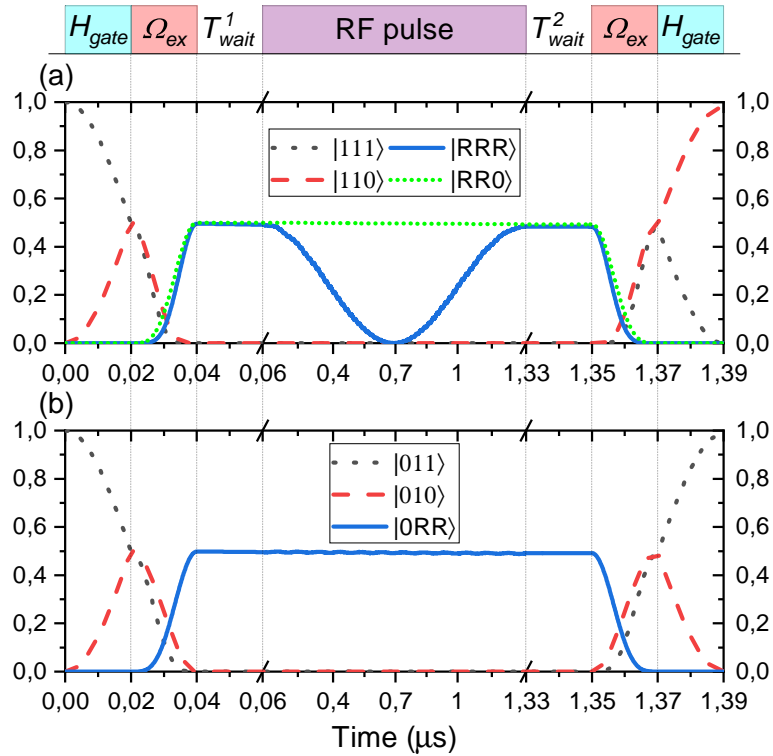


**Figure 4.23:** Population dynamics of collective states of a triatomic register in the process of implementing a Toffoli gate based on a three-body resonance (Eq. 4.44) for the initial states  $|111\rangle$  (a) and  $|011\rangle$  (b). The applied pulses are indicated at the top of the figure. The initial state of the quantum register is represented by a black dotted line, and the final state is represented by a red dashed line. The blue line in each case represents the corresponding collective Rydberg state, and green line corresponds to its counterpart associated with a partial Rydberg state. System parameters:  $R = 10 \mu\text{m}$ ,  $F_S = 0.1805 \text{ V/cm}$ ,  $F_{RF} = 0.05 \text{ V/cm}$ ,  $\omega = 50 \text{ MHz}$ ,  $T = 300 \text{ K}$ ,  $t = 1.27 \mu\text{s}$ . The estimated gate fidelity is 99.31% for non-cryogenic environment.

Figure 4.23(a) shows the behavior of the relevant collective states of the system in the case when the initial state of the register is  $|111\rangle$ . Note that we use standard qubit state notation  $|Control\rangle \otimes |Control\rangle \otimes |Target\rangle$  for the register states, although in the proposed gate, target qubit is the central one. Due to the application of the Hadamard gate, the population is first evenly distributed between states  $|111\rangle$  and  $|110\rangle$ . Then the atoms are excited into the Rydberg state  $(|RRR\rangle - |RR0\rangle) / \sqrt{2}$ . The subsequent RF pulse, which in this case has a duration of  $1.27 \mu\text{s}$ , induces a three-body resonance (4.44), shown in Figure 4.20(c) by the rightmost peak (signed with asterisk). As a result of the resonant interaction, the phase evolution accelerates, and the phase of the  $|RRR\rangle$  state changes by  $\pi$ . Additional waiting times  $T_{wait}^1$  and  $T_{wait}^2$  allow to adapt the phases of different collective states and compensate for unwanted phase shifts. The stages of de-excitation of atoms and the second application of the Hadamard gate complete the scheme. As demonstrated in Fig. 4.23(a), the accumulated phase shift leads to the final population interchange between  $|111\rangle$  and  $|110\rangle$  states.

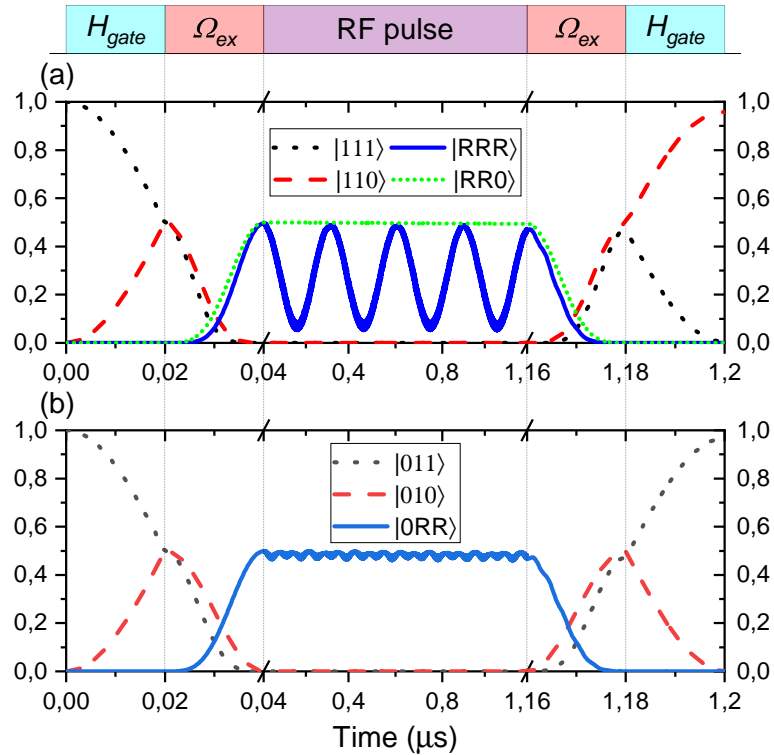
Although two-body interactions are present in the system, they do not add any sizeable effect on the Rydberg states presented on Fig.4.23(a). For the  $|RRR\rangle$  state, the three-body resonance has a dominant influence. The  $|RR0\rangle$  state, in turn, is characterized by a doubled distance between atoms excited into Rydberg states, and the absence of resonant dynamics. In this case, the effect of two-body interactions is sufficiently weakened [227].

Figure 4.23(b) depicts the simulated dynamics of populations in the case when only one of the controlling qubits was initialized into state  $|1\rangle$  along with the target qubit. Insignificant population dynamics, expressed in small population oscillations of the  $|0RR\rangle$  state, is associated here with the presence of non-resonant two-body interactions  $|70P_{3/2}\rangle^{\otimes 2} \rightarrow |70S_{1/2}; 71S_{1/2}\rangle$ . The two-body state  $|70S_{1/2}; 71S_{1/2}\rangle$  can also interact off-resonantly with the states  $|70P_{1/2}\rangle^{\otimes 2}$  and  $|70P_{3/2}; 70P_{1/2}\rangle$ . These interactions also lead to the accumulation of the phase shift of the collective Rydberg state. Nevertheless, by choosing precise values of experimental parameters (interatomic distance, gate execution time, delay times, and external field parameters), this shift can be fully compensated. As a result, the majority of population of the initial state  $|011\rangle$  returns back to unity, while the population of the opposite state  $|010\rangle$  effectively returns to zero after applying the pulse sequence. A detailed analysis of two-body interactions in three-body systems of Rydberg atoms is given in our previous articles [154, 193, 223, 225] as well as in previous Sections 4.2 and 4.3.

For initial states  $|100\rangle$ ,  $|010\rangle$ ,  $|001\rangle$ , only one atom is excited to the Rydberg state (or partially excited due to a Hadamard key application for the  $|001\rangle$  state). Thus, the dynamics of the system is limited by the decay of the Rydberg state associated with finite lifetimes. Finally, for initial state  $|000\rangle$ , we assume the absence of any dynamics.

##### • Two-body resonance-based protocol

A similar *CCPHASE*-gate scheme can also be realized through the use of the inaccessible two-body resonance (4.47). This seems counterintuitive since a two-body operator cannot lead to entanglement of the states of the three atoms under ordinary circumstances. To describe the nature of the proposed gate implementation technique, let us refer to Figure 4.21(c). As can be seen from this figure, in the case of excitation of only two closely spaced atoms (e.g., atoms 1



**Figure 4.24 :** Population dynamics of collective states of a triatomic register in the process of implementing a Toffoli gate based on a two-body resonance (4.47) for the initial states  $|111\rangle$  (a) and  $|011\rangle$  (b). The applied pulses are indicated at the top of the image. The initial state of the quantum register is represented by a black dotted line, and the final state is represented by a red dashed line. The blue line in each case represents the corresponding collective Rydberg state, and green line corresponds to its counterpart associated with a partial Rydberg state. System parameters:  $R = 10 \mu\text{m}$ ,  $F_S = 0.1805 \text{ V/cm}$ ,  $F_{RF} = 0.052 \text{ V/cm}$ ,  $\omega = 318 \text{ MHz}$ ,  $T = 300 \text{ K}$ ,  $t = 1.27 \mu\text{s}$ . The estimated gate fidelity is 99.29% for non-cryogenic environment.

and 2 or atoms 2 and 3) into Rydberg states, the two-body resonance arises at  $F_S = 0.1679 \text{ V/cm}$ . However, if all three atoms have been excited into Rydberg states, the two-body peak is strongly shifted, and is found at  $F_S = 0.1815 \text{ V/cm}$ . At the same time, an external DC electric field is kept constant throughout the gate implementation time. By tuning the field to a value close to the position of the two-body peak in the three-atomic excitation case, we can thus induce strong resonant phase and population dynamics for the  $|RRR\rangle$  state. In turn, the phase dynamics will be highly suppressed at the same electric field in the case of two-atom excitation. Thus, adjusting the position and strength of the resonance by tuning the parameters of the inducing RF radiation, we can regulate the phase and population dynamics of the three-body system and implement the quantum *CCPHASE* gate according to steps 1-3 described above. Note that three-body interaction process (4.46) would also present a small off-resonant contribution into the system dynamics and should be taken into account.

We again demonstrate here the gate performance on the example of the Toffoli gate. As can be seen from Figure 4.24(a), the population of  $|RRR\rangle$  state demonstrates rapid Rabi oscillations (in full accordance with the analyses presented in Subsection 3.3.7). These oscillations correspond to a two-body transition (4.47), and are accompanied by a  $\pi$  phase shift. However, such oscillations are absent for  $|RR0\rangle$  state, when only two atoms are excited into Rydberg states. This is due to the return of the two-body resonance to its original value in the absence of the third Rydberg atom (see the cyan and green curves in Figure 4.21(c)). An increase in the interatomic distance also plays a significant role, as we discussed above. Combined, these two effects suppress population oscillations to negligible values. Yet, if only the resonance displacement effect is active, small population oscillations remain noticeable, as shown for the  $|ORR\rangle$  state in Figure 4.24(b). As in the previous scheme, such interactions lead to a significant phase shift, compensation of which is achieved by optimising the system parameters. Note that in this case the delay times were not used as control parameters, since the correct phase dynamics was obtained with RF frequency and amplitude control only.

It is also important to emphasize that in the described two-body-based protocol, the used values of the parameters of the quantum register ( $R$ ,  $T$  and  $F_S$ ) are completely similar to the values for previously described three-body-based protocol. This may be surprising, since, according to the analysis of Figures 4.20(c) and 4.21(c), the three-body and two-body resonances (4.44) and (4.47) occur at slightly different values of the external electric field for  $R = 10 \mu\text{m}$ . Nevertheless, the proposed protocol is implemented for  $F_S = 0.1805 \text{ V/cm}$ , in a slight deviation from the exact peak of the two-body resonance. This can be noticed from the incomplete amplitude of the Rabi oscillations in Figure 4.24(a). In turn, this value of the electric field exactly corresponds to the value used in the three-body gate protocol described earlier.

#### 4.4.5. Gate fidelity

Using the method proposed earlier in Subsections 2.1.5, 4.1.6 and 4.3.4, we measured the accuracy of *CCPHASE* gates for a wide range of  $\phi$  values. Several exemplar results are shown in Table 4.7 for the gate protocol based on three-body resonance (4.44). The second two-body resonance-based gate protocol demonstrates similar fidelity results (with variations on the order of 0.05%). Note that the characteristics of the applied RF radiation are the only controlling parameters of the gate. To perform different phase gates, we only change  $F_{RF}$  and  $\omega$ , and keep all the other parameters fixed.

For the described experimental conditions of resonance (Eq. 4.44), the average accuracy of gate implementation is 99.27% for a room-temperature environment. The main source of fidelity losses ( $\sim 0.51\%$ ) is the finiteness of the lifetimes of Rydberg states. Compensation for these losses down to 0.13% can be achieved using a cryostat at 4 K [58, 275] temperature for the proposed parameter values, increasing the average fidelity to 99.65%. Additional compensation for Rydberg lifetime losses can be achieved by using higher Rydberg levels [59, 156]. The losses associated with the non-optimal choice of parameter values are estimated as  $\sim 0.22\%$  after the application of multiparametric optimization routines based on simulated annealing technique [276]. However, this optimization is preliminary and does not allow us to obtain fully optimal

**Table 4.7:** Estimated  $CCPHASE(\phi)$  gate fidelities for different values of  $\phi$ . The three-body resonance based implementation was considered. Results for room temperature (300 K) and cryogenic setup (4 K) are presented. System parameters:  $R = 10 \mu\text{m}$ ,  $F_S = 0.1805 \text{ V/cm}$ ,  $T = 1.27 \mu\text{s}$ ,  $T_{wait}^1 = T_{wait}^2 = 0.2 \mu\text{s}$ . RF parameters are shown in the table for each gate.

$T, \text{K}$	$CCPHASE(\frac{\pi}{4})$	$CCPHASE(\frac{\pi}{2})$	$CCPHASE(\frac{3\pi}{4})$	$CCPHASE(\pi)$
300	99.27	99.26	99.22	99.31
4	99.64	99.63	99.6	99.69
$F_{RF}, \text{V/cm}$	0.0389	0.0388	0.0416	0.05
$\omega, \text{MHz}$	46.75	48.5	48.35	50

parameter values in an atomic system due to the complexity of the task. Remaining losses could be compensated by applying additional multi-parametric optimization routines along with appropriate composite pulse sequences [277, 278] or coherent control techniques [279, 280]. For practical applications, we propose to use simulated annealing method in conjunction with Nelder-Mead pre-processing [281]. QAOA optimization techniques may also be applicable [84, 262].

To implement correct phase gates experimentally, it is necessary to pay attention to the required accuracy of the parameter values control. Assuming that the allowable fidelity deviation from the maximum value cannot exceed 0.1% we found the following requirements for parameter accuracy thresholds: the interatomic distance must be controlled with an accuracy of 20 nm; the interaction time - 0.025  $\mu\text{s}$ ; DC electric field amplitude -  $7 \cdot 10^{-5} \text{ V/cm}$ , AC electric field amplitude -  $9 \cdot 10^{-5} \text{ V/cm}$ , RF frequency - 20 KHz. While the control of the interaction time, as well as of the RF frequency, does not present any experimental challenges [282], the limiting factors are the complexity of the DC and AC field amplitudes control, along with the interatomic distance control. A method to reduce possible gate errors due to electric field variations was proposed in Section 4.3, based on the interatomic distance reduction for the chosen value of  $n$  [225]. Thus, if necessary, one can find a compromise between the sensitivities to these two parameters suitable for a particular experimental realization. A complete analysis on electric field calibration was proposed both for DC [283, 284] and AC [285–287] fields in Rydberg systems. A proper level of interatomic distance control has been demonstrated with modern holographic and AOD-based tweezer techniques [179, 222, 288, 289].

#### 4.4.6. Conclusion

In this section, we have proposed and numerically investigated RF-induced many-body Förster resonances for  $70P$  states of Rb atoms. In particular, we have considered RF-induced three-body FSSC resonances in a system of ordered Rb atoms. The performed numerical simulations allowed us to reliably demonstrate that coherent population oscillations are exhibited by tuning the DC electric field on the Floquet sideband of the FSSC resonance. Thus, by controlling the parameters of the external RF radiation, one can control the phase and population dynamics in the Rydberg system.

We proposed a protocol of three-body quantum  $CCPHASE$  gate based on the described

#### 4.4. *CCPHASE* gate based on RF-induced FSSC resonances

---

resonances. The high accuracy of the gate for arbitrary values of  $\phi$  was demonstrated in simulations. The main advantage of this protocol over possible analogues is its applicability at large interatomic distances ( $\sim 10 \mu\text{m}$ ). Thus, we can conclude that proposed gate protocol is promising for realisation of quantum computations in large-scale Rydberg registers.

Comparing the quantum gate protocol proposed in this section with the schemes proposed earlier in Sections 4.1 and 4.3, it is important to note several key advantages. First, the external DC electric field is kept constant throughout the gate implementation, avoiding possible interaction deviations at the moment of field switching. Also, since the excitation and de-excitation of atoms are performed in the external field, the undesirable effects associated with population leakage due to two-body exchange interactions, which are resonant in the zero field, become negligible. Second, the interaction control is performed predominantly by external RF radiation parameters. Tuning the delay times, as well as the frequency and amplitude of the external radiation, allows one to realise gates for different values of  $\phi$ , keeping all other parameters of the system unchanged. Thus, the experimental realisation of the gate is greatly facilitated. Additional variation of the RF pulse shape can also be used to reduce the gate implementation time. Third, since RF radiation allows inducing resonances for arbitrary values of the external DC field, a compromise can be chosen to reduce the influence of quasi-forbidden resonances.

In addition to the three-body FSSC resonances, the controlling RF radiation also allows one to realise inaccessible two-body resonances for high-lying Rydberg states. We demonstrated an example of such a resonance, and shown that coherent population and phase dynamics can be obtained for it. Note that this resonance can be induced for the same system parameters used for three-body resonance induction previously. The only control parameters needed to switch between the interactions are the frequency and amplitude of the RF radiation.

We have also proposed a protocol to realise the *CCPHASE* gate based on two-body inaccessible resonances. This protocol is based on the effect of the resonance peak shift upon variation in the number of excited Rydberg atoms. To the best of our knowledge, this technology of many-body gate production has not been used before, which makes this gate protocol an interesting object for further studies.

This work was supported by French government, under the “Vernadski” scholarship program grant, and by National Research Agency (ANR), under grant ANR-22-CE47-0005 (QIPRYA project). The Russian team was supported by Russian Science Foundation grant №. 23-12-00067.



# Chapter 5

## Summary and Outlook

### 5.1. Summary

Many-body Förster resonances in Rydberg systems were first discovered in Aime Cotton Laboratory (LAC) in 2012. Four-body resonance transitions in a low-density Rydberg gas of Cs atoms demonstrated the potential for enhancing dipole-dipole interactions in Rydberg ensembles. Further studies carried out in LAC and Rzhanov Institute of Semiconductor Physics (ISP) allowed both teams to experimentally register three-body Borromean resonances in ensembles of Cs and Rb atoms. The numerically demonstrated possibility of realising coherent resonance dynamics in structured atomic ensembles allowed one to consider Borromean resonances as potential candidates for the implementation of three-qubit quantum gates. The main advantage of Förster resonances is their long-range nature, which allows quantum gates between distant qubits. This is important for creating full interconnectivity in a quantum register.

Within the framework of this thesis, a comprehensive study of the applicability of Förster resonances for the quantum computation implementation in neutral-atom-based quantum registers has been carried out. The research cycle consisted of four stages. At each stage, different variants of resonance schemes were proposed, as well as approaches to their use for creating quantum gates.

#### 5.1.1. First stage

During the first stage of investigations, new three-body resonances of the type (5.1) were proposed and numerically modelled. The main advantage of such resonances over the previously investigated transitions (5.2) was the possibility of their realisation for high-lying Rydberg atomic states with  $n > 38$  in Rb. This became possible due to the fact that the first two-body transition  $2 \times nP \rightarrow nS + (n + 1)S$ , necessary for the realisation of the parallel Borromean transfer, was replaced by the  $nP + (n + 1)P \rightarrow nS + (n + 1)S$  transition, thus relaxing the constraint of using a single initial Rydberg level for all atoms. Such transitions have a positive quantum defect in the zero electric field, and can be used in conjunction with non-resonant  $SP$  excitation hopping to realise a three-body population transfer. Coherent population oscillations were demonstrated for this new resonant interaction scheme in a structured ensemble, accompanied by a phase change of the collective register states. Thus, it was shown that these resonances are promising for the realisation of three-qubit quantum gates.

$$\begin{aligned} nP_{3/2}(m = 3/2) + (n + 1)P_{3/2}(m = 3/2) + (n + 1)P_{3/2}(m = -3/2) \rightarrow \\ \rightarrow nS_{1/2}(m = 1/2) + (n + 2)S_{1/2}(m = 1/2) + (n + 1)P_{3/2}(m = 1/2) \end{aligned} \quad (5.1)$$

$$3 \times nP_{3/2}(|m\rangle) \rightarrow nS_{1/2} + (n + 1)S_{1/2} + nP_{3/2}(|m^*\rangle) \quad (5.2)$$

The scheme of the Toffoli quantum gate was proposed based on the resonance (5.3) in Rb atoms. The use of high-lying  $n = 80$  states allowed us to significantly increase the lifetimes of the collective Rydberg states and reduce the influence of decay on the coherence of population oscillations. In the framework of the numerical simulations, the atoms were arranged linearly at a distance  $R = 10 \mu\text{m}$  from each other along the quantisation axis  $Z$  coinciding with the direction of the external DC electric field. This configuration allows to reduce essentially the number of multiparticle interaction channels due to the presence of the selection rule on the total projection of the system momentum  $\Delta M = 0$ . To further isolate the two- and three-body resonant peaks, an external magnetic field was utilised. High gate fidelity of  $\sim 98.3\%$  was demonstrated in numerical simulations, obtained due to the multi-parametric optimisation based on the Nelder-Mead method. The implementation time of the gate was 2.42 microseconds.

$$\begin{aligned} &|80P_{3/2}(3/2); 81P_{3/2}(3/2); 81P_{3/2}(-3/2)\rangle \rightarrow \\ &\rightarrow |80S_{1/2}(1/2); 82S_{1/2}(1/2); 81P_{3/2}(1/2)\rangle \end{aligned} \quad (5.3)$$

Among the significant drawbacks of the developed scheme, the complexity of its potential experimental realisation should be noted. In particular, the excitation of atoms into different Rydberg states requires the use of several mutually coherent laser sources. Also, the necessity to use an external magnetic field to isolate the relevant three-body interaction channel complicates the experimental setup. The high sensitivity of the gate to deviations of the controlling DC electric field places demands on the setup isolation from the environment. Additional research was also needed to improve the fidelity of the quantum gate up to values of  $> 99\%$  to make it compatible with quantum error correction techniques. We concluded that although the proposed gate could potentially be applied to the implementation of complex quantum algorithms, additional efforts were required to compensate for the described drawbacks.

### 5.1.2. Second stage

As shown before, relaxing the constraint for using a single Rydberg level leads to experimental drawbacks. Therefore, a different Förster resonance scheme was required. We proposed and numerically investigated fine-structure-state-changing (FSSC) three-body Förster resonances (5.4). Their main difference from the previously presented transitions (5.1) is that during the three-body FSSC process the total momentum of the third atom changes to a lower value. Since the  $SP$ -hopping process with momentum change  $J = 3/2 \rightarrow J = 1/2$  has a significant energy defect, the condition of mutual defect compensation  $\Delta_1 = \Delta_2$  can be fulfilled using the standard two-body transition  $2 \times nP \rightarrow nS + (n + 1)S$ . At the same time, due to the negative energy defect, the two-body transition cannot be resonant in an external field, as already discussed. Thus, only three-body resonances are realised in a three-atomic system, in the absence of two-body peaks. This greatly simplifies the phase and population dynamics in the quantum register.

$$3 \times nP_{3/2} \rightarrow nS_{1/2} + (n+1)S_{1/2} + nP_{1/2} \quad (5.4)$$

The resonances (5.4) were numerically investigated for ensembles of Rb and Cs atoms. We also investigated many-body quasi-forbidden Förster resonances located near the (5.4) scheme resonant DC electric field. Determination of the strength of such resonances was necessary to assess their potential influence on the coherence of Rabi oscillations in atomic ensembles, and to determine the most suitable atomic elements and Rydberg states for the realisation of multiqubit quantum gates. Based on the results of this study, we concluded that three-atom rubidium ensembles exhibit highly isolated three-body resonances whose strength is an order of magnitude greater than that of nearby quasi-forbidden transitions for high-lying Rydberg states with  $n = 70$  or above.

An extended numerical study of many-body resonances (5.4) was then carried out in structured and unstructured ensembles of Rb atoms. In the linear spatial configuration of the register, only two three-body channels were observed for large interatomic distances  $R = 10 \mu\text{m}$ , in the complete absence of two-body resonance interactions. Highly coherent population oscillations were also demonstrated, accompanied by phase changes of the system states. Thus, we concluded that the FSSC resonances shown are promising for implementation of multiqubit quantum gate protocols and proceed to the development of the corresponding gates.

### 5.1.3. Third stage

During the third stage of research, the Toffoli quantum gate protocol based on FSSC resonances (5.4) for  $n = 70$  was proposed and numerically modeled. The linear spatial configuration of the three-atom register was chosen similarly to the previous case. The main difference of the new quantum gate protocol from the previously considered protocol was the lack of necessity to excite atoms into different Rydberg states. Also, the absence of two-body resonance processes near three-body peaks significantly simplified the phase dynamics of the system.

Through a series of numerical experiments, we convincingly demonstrated that the fidelity of our proposed Toffoli quantum gate is  $> 99\%$ . Thus, a significant improvement in fidelity was achieved compared to the previous protocol described in Subsection 5.1.1.

We achieved a significant reduction of the quantum gate time compared to the previously proposed scheme (up to  $1.15 \mu\text{s}$  at interatomic distance  $R = 10 \mu\text{m}$  and up to  $0.42 \mu\text{s}$  at  $R = 8.5 \mu\text{m}$ ). This seems counterintuitive, since the strength of the three-body interaction certainly decreases with decreasing  $n$ . Nevertheless, due to the essential simplification of the phase dynamics of the system in absence of two-body resonance processes, we managed to implement the gate during the first period of Rabi oscillations, which had been impossible for the previous scheme.

We also investigated the influence of variations of atomic register parameters on the fidelity of the quantum gate. As was shown, the main limiting factor preventing an increase in fidelity is the strong sensitivity of the gate to variations in the electric field and interatomic distance. Nevertheless, a compromise can be reached that allows relaxing the requirements for controlling one of the parameters. In particular, strong dependence of the gate fidelity on the DC field

variations can be reduced when the interatomic distance  $R$  is decreased due to the enhancement of the interatomic interaction and broadening of the resonance peaks. It was shown that when the interatomic distance is reduced from  $R = 10 \mu\text{m}$  to  $R = 8.5 \mu\text{m}$ , the sensitivity to field fluctuations decreases by about a factor of 4. Although the reduction of the interatomic distance does not meet the goals of realizing quantum gates between distant atoms, the presented study provides an opportunity to evaluate different variants of the quantum register balancing necessary to achieve the maximum experimental fidelity of the gate.

Despite the significant improvement of the fidelity of the quantum gate compared to the previous proposal, a number of drawbacks of the scheme required additional efforts. First of all, the necessity to change the external controlling field by means of the Stark-switching technique remained, which imposed significant limitations on the possible accuracy of experimental realizations. Also, the insufficient number of controllable system parameters significantly limited the possibility of compensating for undesired phase and population dynamics. Thus, further studies were required to compensate for the described shortcomings.

### 5.1.4. Fourth stage

At this stage, we concentrated on the search for additional mechanisms to control multiparticle resonance interactions in Rydberg systems. In particular, we studied in detail the use of external radio frequency radiation to induce Förster resonances. Previously, radio-frequency (RF) induced resonances had been studied in detail in two-atom systems. However, studies of many-body RF-induced Förster resonances were not presented prior to this work, to the best of our knowledge.

We proposed and numerically investigated three-body RF-induced FSSC resonances in systems of spatially isolated Rydberg atoms of Rb. Such resonances are based on the application of a composite inducing field, which includes both DC electric field and radio frequency radiation. The RF photons allow to compensate the Förster defect of the collective Rydberg states for an arbitrarily chosen value of the external inducing DC field. Also, external RF radiation allows to achieve the induction of inaccessible two-body Förster resonances  $2 \times nP \rightarrow nS + (n + 1)S$  for high-lying Rydberg states. Such resonances cannot be realized for collective Rydberg states of Rb with  $n > 38$  due to specific values of polarizabilities and quantum defects of these states. Nevertheless, the compensation of the two-body energy defect is possible due to the RF emission or absorption. Thus, external RF radiation provides a flexible tool for manipulating the dipole-dipole interaction.

We numerically simulated two-body (5.5) and three-body (5.6) RF-induced resonance interactions in the ordered ensemble of Rb atoms for  $n = 70$ . It was shown that for both types of resonances, the position of the first Floquet sideband is effectively controlled by external radiation. Thus, the resonance can be induced for an arbitrary value of the DC electric field. This fact makes it possible to achieve a significant isolation of the three-body peaks from the surrounding quasi-forbidden resonances, and to reduce their influence on the dynamics of the quantum system. According to the conclusions of this study, multiparticle resonances demonstrate coherent population dynamics in a linear spatial configuration, and are well suited for

the realization of quantum gates.

$$|70P_{3/2}\rangle^{\otimes 3} \rightarrow |70S_{1/2}; 71S_{1/2}; 70P_{3/2}(|m| = 1/2)\rangle \quad (5.5)$$

$$|70P_{3/2}\rangle^{\otimes 3} \rightarrow |70S_{1/2}; 71S_{1/2}; 70P_{1/2}\rangle \quad (5.6)$$

We also proposed and numerically investigated protocols of three-qubit *CCPHASE* gates based on the proposed two-body and three-body RF-induced resonances. The use of inducing radiation allows us to effectively control the population and phase dynamics of the system, giving ample opportunities to manipulate quantum states. Thus, we can use the frequency and amplitude of the external radiation as exclusive control parameters to control the phase of the gate. It was shown that by keeping all system parameters (interatomic distance, external DC electric field and time of the gate realization) unchanged, we can realize the *CCPHASE* gate for arbitrary value of  $\phi$  with high fidelity by varying only the frequency and amplitude of the RF field. Also, the activation of two-body or three-body resonances can be implemented by varying the RF field parameters, while fully preserving all the other experimental parameters. In this regard, different variations of the proposed gates can be realized in the same experimental setup. Note that the ability to implement arbitrary gates without changing the register geometry is crucial for performing algorithms in large-scale quantum computing devices.

The proposed protocols of quantum gates demonstrate high fidelity. In particular, the average fidelity of gates based on three-body resonances was  $\sim 99.3\%$  at room temperature. The main source of losses, as in the previously proposed protocols, was represented by the finite lifetimes of Rydberg states. Thus, when modeling the realization of the gate in a cryogenic setup (with a temperature of 4 K), we managed to achieve a fidelity of  $\sim 99.7\%$ , which significantly exceeds the fidelity of all currently available experimental realizations of three-body gates.

### 5.1.5. Results

Summarizing the above information, we can highlight the following important results we achieved as an outcome of our research:

- Förster resonances (5.1) in Rb atoms were numerically investigated. Coherent resonance dynamics was numerically demonstrated in a linear spatial configuration of the quantum register.
- A Toffoli quantum gate based on (5.1) resonances for  $n = 80$  in Rb atoms was proposed and numerically simulated. The quantum gate demonstrated high speed ( $T = 2.42 \mu\text{s}$ ), high fidelity (98.3%), and long-range performance ( $R = 12.5 \mu\text{m}$ ).
- FSSC three-body Förster resonances (5.4) were proposed and numerically investigated in ensembles of Rb and Cs. Coherent resonance dynamics was demonstrated in a structured ensemble. The absence of additional resonance peaks was demonstrated.
- A Toffoli quantum gate based on three-body FSSC resonances (5.4) for  $n = 70$  in Rb atoms was proposed and numerically studied. The improved fidelity of the quantum gate

(> 99%) as well as the acceleration of its implementation time ( $T = 0.42 - 1.15 \mu\text{s}$ ) while preserving the long-range action ( $R = 8.5 - 12.5 \mu\text{m}$ ) favorably distinguished it from the previously demonstrated gate. The potential experimental realization of the gate was considerably simplified in comparison with the previous proposal by reducing the complexity of the resonance dynamics and due to the utilization of identical initial Rydberg states.

- Three-body radio-frequency induced FSSC Förster resonances in Rb atoms were proposed and numerically investigated. Coherent dynamics was demonstrated for resonances in a structured ensemble. It was shown that RF radiation could be used to induce inaccessible two-particle resonances.
- The protocols of *CCPHASE* quantum gates for arbitrary phase  $\phi$  were proposed and numerically analyzed based on many-body RF-induced Förster resonances. The theoretically achievable fidelity of the gates was  $\sim 99.3\%$  ( $\sim 99.7\%$  for a cryogenic setup), while maintaining fast ( $T \sim 1.4 \mu\text{s}$ ) and long-range performance ( $R = 10 \mu\text{m}$ ). The use of RF parameters as exclusive interaction controls significantly facilitated the potential experimental realization of the gate.

## 5.2. Outlook

The presented study offers various options for realization of multiqubit quantum gates based on many-body Förster resonances. The proposed protocols demonstrate high theoretical fidelity values, as well as a high rate of performance. The main advantage of the proposed approach is the possibility of realizing gates between distant qubits, which can be useful for creating interconnectivity of large-scale quantum registers. Inspired by the potential of Förster quantum gates for quantum computer science problems, we intend to continue our research in this area. In this subsection, we describe a number of possible research directions, in which the further investigation would be required for the development of the presented technology.

### 5.2.1. Fidelity improvement

High fidelity values in the range  $F \in [98.3\% - 99.7\%]$  have been theoretically demonstrated for three-qubit quantum gates in this thesis. Nevertheless, the efficient implementation of complex quantum algorithms requires further improvements in fidelity. For example, solving the problem of computing a 256-bit elliptic private key based on the Shor algorithm requires  $\sim 5 \times 10^7$  three-qubit Toffoli gates [290, 291]. Thus, the fidelity losses of  $\sim 3 \times 10^{-3}$  are unacceptable. At the same time, proposals of three-qubit gates based on dipole blockade and pulse shaping currently available demonstrate theoretical error values of  $\sim 10^{-6}$  [28, 64].

As it was noted repeatedly in Chapter 4 (for example, see the Subsection 4.4.5), the main sources of accuracy losses are finite lifetimes of Rydberg atoms, as well as suboptimal choice of parameters of the quantum system. We are actively working on developing possible solutions

to both of these difficulties.

Several approaches exist to overcome the accuracy limit imposed by finite lifetimes. First, a transition to higher Rydberg levels is possible, which allows one to significantly extend the lifetimes, as well as to increase the interaction strength, thereby speeding up the gate performance. However, enhanced coupling also leads to a significant narrowing of the resonance peaks, and imposes additional constraints on the level of electric field control. An alternative solution is to use two-body RF-induced resonances to realize three-qubit quantum operations, as was shown in Section 4.4. Since the strength of two-body resonances is significantly superior to that of three-body resonances, the execution of the gate can be faster if the phase dynamics is accelerated. At the moment, we are investigating the inaccessible two-body resonances and their application to the realization of fast multiqubit quantum operations.

The non-optimal choice of parameters of the quantum system is related to the complexity of solving the multi-parameter optimization problem. When determining the quantum gate parameters, we need to achieve the desired phase and population dynamics for all  $N$  collective quantum states of the considered register ( $2N - 1$  parameters in total). Note that the number of controlling parameters (interaction time, interatomic distance, etc.) is most often much smaller than the number of involved quantum states. Thus, an absolutely exact solution of this problem is not possible. In principle, the solution of such a problem for a three-atom system can be efficiently approximated using simulated annealing or Nelder-Mead algorithms. Nevertheless, the available software solutions showed low efficiency in solving this problem. Thus, the used internal optimization tools of "Wolfram Mathematica" software gave substantially non-optimal results and also required long implementation time on the processors available to us (approximately 3 days for the optimization of a system with  $\sim 360$  collective states on a 16-core Intel Core i7 processor).

To overcome this obstacle, we develop an optimization algorithm focused on optimizing the parameters of multi-atom quantum registers in order to maximize the fidelity of quantum gates. This algorithm is based on truncation and linearization of the optimization problem. We briefly describe here the main ideas of this algorithm.

According to the previous considerations, in order to obtain an absolutely optimized quantum gate scheme, certain phase and population dynamics must be achieved for  $N$  collective states of the quantum system. Nevertheless, since we focus on excitations of a single initial state (e.g.,  $3 \times nP_{3/2}$ ), it can be argued that for a large number of spectrum states not paired with the ground state, the population dynamics will be negligible. Thus, we can reduce the problem to considering eight different initial ground states of the quantum register, their corresponding initial Rydberg states, and the collective final Rydberg states paired with them. On average, after truncation, the problem typically contains 5 – 10% of the original number of quantum states. Nevertheless, with a rough approximation, one can dispense with optimizing only the Rydberg states, and hence the problem can be reduced to several states exhibiting the largest dynamics. Specifically, for the quantum gate protocols we described earlier, the most significant dynamics is demonstrated for states with three Rydberg atoms, as well as for states with two closely spaced Rydberg atoms. In turn, if two excited atoms are located at a long distance from each other (outermost atoms in the linear register), insignificant phase dynamics is

observed, which can be taken into account in the more precise calculations. Thus, we reduce the problem from  $\sim 360$  states to three states  $|rrr\rangle$ ,  $|grr\rangle$ ,  $|rrg\rangle$ , leaving only five parameters needed to be optimized.

The linearization of the problem is achieved by looking at the collective state amplitude oscillations and extracting their phase which evolves linearly with time. In principle, in the absence of essential deviations related to strong non-resonant interactions, the population dynamics of any quantum state can be described in the form of Rabi oscillations with a certain detuning from resonance. Approximating the population oscillations by periodic dependences, we introduce the concept of “population phase” - a linear parameter depending on the effective Rabi frequency and time. Thanks to this concept, we can represent the desired result of the whole optimization problem as a vector consisting of the values of the “population phase” and the real phases of the collective states.

Finally, the linearized constrained problem can be efficiently solved using standard optimization algorithms. Currently, we are trying out the solution of such a problem using a composition of the Nelder-Mead algorithm (for global optimization) and simulated annealing (for exact optimization near a local minimum). Although the algorithm is not yet fully ready, we are already getting the first results. For example, multiparametric optimization allowed us to obtain 0.3% improvement in fidelity for the *CCPHASE* gates described in Section 4.4, increasing the fidelity from  $\sim 99.4\%$  to  $\sim 99.7\%$ . We're hoping to achieve further fidelity improvement once the described algorithm is refined.

### 5.2.2. Sensitivity to atomic positions

Within the framework of this thesis, we have only slightly touched upon the issue of dependence of quantum gates accuracy on atomic positions. Nevertheless, careful study of this issue is necessary for successful realization of multiqubit quantum gates.

High position sensitivity of the demonstrated gate protocols arises for two reasons: the interaction strength depends on the interatomic distance and laser excitation of the atoms to the Rydberg levels adds a position dependent phase. The position dependent phase sensitivity is in principle solved if using a multi-photon excitation with the right angles and should not represent more than a technical detail. On the other hand, the interaction strength dependence on the interatomic distance is a fundamental consequence of the few-body interaction and cannot be removed. Different strategies can be pursued to minimize this effect, including the use of “echo” technique that could allow to time reverse the effect of the position dependence, or finding the composite-pulse sequences [277] of the interaction removing the sensitivity to the interatomic distance. We intend to study these methods and investigate their possible application in modern quantum registers.

### 5.2.3. Förster blockade gates

Previously, we have referred several times to the possibility of quantum gates implementation based on the dipole blockade effect. Such gates are extremely convenient for complex

quantum computations, and show the highest accuracy results among all proposals for Rydberg quantum computing. In a recent publication, the group of M. Lukin reported a parallel realization of high-precision ( $\sim 99.5\%$ ) two-qubit quantum gates on up to 60 atoms [49]. This amazing result allows to declare reaching the gate fidelity sufficient for effective quantum error correction.

The high fidelity of gates based on dipole blockade compared to technologies based on simultaneous Rydberg excitation is caused by several factors. First, such gates are much more robust to interatomic distance fluctuations if the atoms are deep inside the blockade radius. Second, since fewer atoms are excited into Rydberg states, the influence of the finite lifetimes of these states is also significantly reduced. This effect is further enhanced by the short realization times of the gates (on the order of a few hundred nanoseconds). Nevertheless, as described earlier, a significant disadvantage of such gates is their small-range effect. Due to the fact that the dipole blockade is based on the van der Waals interaction, one can expect the formation of such gates only between atoms located at a distance of several microns from each other.

One possible way to compensate for this effect could be to use blockade in the Förster regime. As mentioned in Subsection 2.2.4, when compensating for the Förster defect, dipole-dipole interactions are observed that depend on distance as  $\sim 1/R^3$ . Thus, by exciting the atoms near the Förster resonance, one can achieve an enhancement of the dipole blockade effect, which leads to a significant increase in the blockade radius. Previously, the blockade effect upon excitation at the Förster resonance has been studied in Aime Cotton Laboratory [200]. However, no gates based on this effect have been proposed so far, to the best of author's knowledge. We plan to conduct theoretical research aimed at finding algorithms for realizing multi-qubit gates using the Förster blockade effect. We believe that such gates will be able to exhibit the high accuracy of blockade gates and the long-range performance of Förster gates, benefiting from the advantages of both approaches.

#### 5.2.4. Experiment proposal

The results of the theoretical study shown in the framework of this thesis reflect the high prospectivity of Förster resonances for Rydberg quantum computing problems. As part of a project on the study of complex Rydberg interactions conducted at the Institute of Semiconductor Physics (ISP), an experiment is planned to observe three-body FSSC Förster resonances in an ensemble of three rubidium atoms.

The experimental procedure is based on the approaches proposed in [155]. Three Rb atoms are assumed to be isolated in microscopic optical tweezers arranged linearly at a distance  $R$  from each other. Three-photon laser excitation of the atoms will be used to compensate for the Doppler shifts [292]. It is assumed that the high-lying  $70P_{3/2}$  state will be chosen as the initial Rydberg state, in accordance with the numerical calculation results given in Section 4.2. Independent external electrodes will be used to apply an external electric field for the induction of multiparticle resonances.

The first stage of the experiment is expected to demonstrate many-body coherent Förster interactions (5.4), and compare the results with the numerical demonstration shown in Sec-

tion 4.2 of this thesis. In the second stage, it is intended to demonstrate a three-qubit quantum Toffoli gate based on FSSC resonances as shown in Section 4.3.

The experiment is planned to be carried out within the next two years. We are convinced that the experimental study will confirm the previously obtained theoretical results and further demonstrate the high potential of Förster resonance interactions for Rydberg quantum computing.

### 5.3. Afterword

Rydberg quantum computing is an actively developing area of applied research. During the last 20 years, it has attracted increasing interest of the scientific community due to the prospect of atomic registers for realization of quantum computations. The most important recent discoveries in this field are related to the construction of large-scale quantum registers based on individual Rydberg atoms [44], demonstration of high lifetimes of individual atoms in optical traps [58], and realization of high-precision parallel two-qubit quantum gates [49].

Solving the problem of interconnectivity of quantum registers by realizing multiqubit quantum gates between distant atoms is highly demanded due to the prospect of QC devices scaling up to several thousands of atoms within the next few years. The research results described in this thesis present one possible approach to this problem, based on the use of few-body resonant Förster transitions for three-qubit gate protocols. We are convinced that this method will in the long run enable great progress in the efficiency of quantum computing in atomic registers. Intending to continue both theoretical and experimental studies of multiparticle Förster resonances, we believe in the soon and indispensable success of our chosen approach.

The main goal of this text was to familiarize the reader with the results of our research in the field of resonant Förster interactions in Rydberg ensembles. We hope that this text will be relevant to both young researchers and specialists, and will allow all interested to understand the unique features of Rydberg physics that we are so passionate about. Thank you for reading! Good luck!

# Appendix

## A. Alkali wave functions and radial matrix elements

### A.1. Wave functions

The description of alkali-atom spectra provided by the quantum defect model gives a good agreement with the experimental results. Nevertheless, to model the interatomic interaction, we need to formalize the description of the system wavefunctions. Unfortunately, the exact solution of the Schrödinger equation with an effective potential of the form (A.1) cannot be obtained analytically for good predictive  $Z_{eff}$  models. In turn, the use of numerical methods for multilevel atomic systems significantly slows down the calculation. An alternative approach is to solve the Schrödinger equation for non-integer values of the principal quantum number, called the Coulomb approximation. Although this approach leads to divergence of wave functions, it can be successfully applied for some interaction models. We present here the summary of this approach, based on the description given in [135]. Note that the wave functions described here are not used for the quasi-classical matrix element calculations described in the subsequent paragraph.

$$\hat{V}_{eff} = -\frac{Z_{eff}(r)q^2}{r} \quad (\text{A.1})$$

As for the case of a hydrogen-like atom, we concentrate on finding wave functions in the form  $\psi = R_{\gamma l}(r)Y_{lm}(\theta, \phi)$ . A significant correction here is the factor  $\gamma = n - \delta_{nlj}$ , which replaces the principal quantum number  $n$ . The Schrodinger equation for bound states thus reduces to

$$\frac{d^2\phi}{dz^2} - \frac{l(l+1)}{z^2}\phi + \frac{2\gamma}{z}\phi - \phi = 0 \quad (\text{A.2})$$

Here  $z = \kappa r$  with  $\kappa = \sqrt{-2\mu E/\hbar^2}$  and  $\phi(z) = zR(z/\kappa)$ .

According to [135], the solutions to equation (A.2) can be described as Whittaker functions  $M_{\gamma, l+1/2}(2z)$  and  $W_{\gamma, l+1/2}(2z)$ . Since the function  $M_{\gamma, l+1/2}$  does not exist for integer values of  $2l+1$ , it is not suitable for description. We thus can express two linearly independent solutions in terms of  $W_{\gamma, l+1/2}$  function as (A.3). These solutions can be represented in terms of confluent second-kind hypergeometric function  $U$ .

$$\begin{aligned} \phi_+(z) &= W_{\gamma, l+1/2}(2z) = e^{-z}(2z)^{l+1}U(1+l-\gamma, 2+2l, 2z) \\ \phi_-(z) &= W_{-\gamma, l+1/2}(-2z) = e^z(-2z)^{l+1}U(1+l+\gamma, 2+2l, -2z) \end{aligned} \quad (\text{A.3})$$

Finally, taking into account the boundary conditions and normalisation conditions we can express the wave functions as (A.4).

$$P_{\gamma l} = rR_{\gamma l} = \frac{1}{\sqrt{a_0}} \frac{1}{\gamma [\Gamma(\gamma + l + 1)\Gamma(\gamma - l)]^{1/2}} \times \quad (\text{A.4})$$

$$\times e^{-r/(a_0\gamma)} (2r/(a_0\gamma))^{l+1} U(1 + l - \gamma, 2 + 2l, 2r/(a_0\gamma))$$

For the integer values of  $\gamma$  this formula can be transformed to the previous description of Hydrogen-like wavefunctions by introducing the additional phase factor  $(-1)^{n+l-\langle\gamma\rangle}$ , where  $\langle\gamma\rangle$  is the nearest integer to  $\gamma$ . However, for non-integer  $\gamma$  the function may diverge in the origin. It is thus instructive to pick a cutoff radius  $r_{min} = a_0 l(l + 1)/2$  when calculating matrix elements. For more detailed description, please see [135].

## A.2. Matrix elements

Calculation of matrix elements of the alkali-atom wavefunctions is an extremely complex process. As stated in [137, 138], wave functions can be calculated numerically using Runge-Kutta [293] or Numerov [294] methods. However, in this case, the calculation of matrix elements takes considerable time for a system including large number of atoms in the presence of complex interactions with additional external fields.

Within the framework of this study, we calculate the radial matrix elements of wave functions in a quasi-classical approximation. The method of such calculation was presented by Kaulakus in 1995 [221]. The quasi-classical approximation shows good agreement with numerical methods when calculating the interactions of Rydberg alkali atoms.

In order to maintain the uniformity of the designations presented in the original article [221], we will use atomic units for further calculations. We perform calculations in momentum representation. Thus, the quasiclassical form of the radial wave function  $P_{nl} = rR_{nl}(r)$  can be represented in the classically allowed region as

$$P_{nl} = \frac{2}{\sqrt{Tv_r(r)}} \cos \Phi_{nl}(r) \quad (\text{A.5})$$

Here  $T$  represents the classical rotation period,  $v_r$  is the electron radial velocity and  $\Phi_{nl}$  is radial-dependent phase.

$$v_r(r) = \sqrt{2E_{nl} - 2U(r) - \frac{\left(l + \frac{1}{2}\right)^2}{r^2}} \quad (\text{A.6})$$

$$\Phi_{nl} = \int_{r_1}^r v_r(r) dr - \frac{\pi}{4} \quad (\text{A.7})$$

Here  $U(r)$  represents an effective potential which defines the motion of the valence electron,  $r_{1(2)}$  are the classical turning points. We thus can represent the dipole matrix element as

$$D_{nl}^{n'l\pm 1} = \frac{1}{\omega} \int P_{nl}(r) \left( \frac{dP_{n'l\pm 1}(r)}{dr} \pm l_{max} \frac{P_{n'l\pm 1}(r)}{r} \right) dr \quad (\text{A.8})$$

where  $l_{max} = \max(l, l \pm 1)$ ,  $\omega = E_{n'l'} - E_{nl}$ .

While integrating, we neglect the rapidly oscillating terms containing the sum of frequencies. We also take into account that, according to expressions (A.6) and (A.7) the phase difference  $\Delta\Phi = \Phi_{n'l'} - \Phi_{nl} \simeq \omega t - \Delta l\phi + \dots$ , where  $\phi$  is the polar angle. Thus, integration of the Eq.(A.8) yields to the  $r$ -form of the radial dipole matrix element:

$$R_{nl}^{n'l\pm 1} = \langle nl|r|n'l \pm 1 \rangle = \frac{2}{\sqrt{TT'}} \int_0^{T_c/2} r(t) \cos \Delta\Phi(t) dt \quad (\text{A.9})$$

Here  $T_c$  is a mean period to be defined later. It is also convenient to express the matrix element in Cartesian coordinates:

$$R_{nl}^{n'l\pm 1} = \langle nl|r|n'l \pm 1 \rangle = \frac{2}{\sqrt{TT'}} \int_0^{T_c/2} (x(t) \cos \omega t \pm y(t) \sin \omega t) dt \quad (\text{A.10})$$

In the previous expressions, we did not specify the interaction potential  $U$ . We do not dwell in detail on the case of a hydrogen-like atom, and immediately proceed to the description of the case when the atom has a quantum defect, as it was described in Subection 2.2.2.1. A convenient model of interaction in this case will be the sum of the Coulomb potential and the perturbation potential  $\Delta U(r)$  arising due to the deviation from the Coulomb approximation:

$$U(r) = -\frac{Z}{r} + \Delta U(r) \quad (\text{A.11})$$

The addition to the potential acts only at small values of  $r$  when the electron is near the nucleus and the inner core is not shielded. At the same time, the main contribution to radial matrix elements occurs at large distances, where the interaction is precisely approximated by the Coulomb potential. The influence of  $\Delta U$  can thus be taken into account in the form of a non-Coulomb scattering phase  $\phi_\delta = \pi\delta_{nlj}$ . Thus, in the high- $r$  region, the phase and phase difference may be represented as

$$\Phi_{nl}(r) = \int_{r_1^c}^r v_r^c(r) dr + \phi_\delta - \frac{\pi}{4} \quad (\text{A.12})$$

$$\Delta\Phi \simeq \omega t - \Delta l\phi \simeq \Delta + \omega t_c - \Delta l\phi_c \quad (\text{A.13})$$

$$\begin{aligned} r &= (\nu_c^2/Z)(1 - e \cos \xi), \quad t_c = (\nu_c^3/Z^2)(\xi - e \sin \xi) \\ \phi_c &= \arccos \left( \frac{\cos \xi - e}{1 - e \cos \xi} \right), \quad e = \left[ 1 - \left( \frac{l + l' + 1}{2\nu_c} \right)^2 \right]^{1/2} \end{aligned} \quad (\text{A.14})$$

Here  $v_r^c$  is the radial velocity for the Coulomb potential, and  $e$  is eccentricity. For the further simplicity, we also denote the classical orbit period  $T_c = 2\pi\nu_c^3/Z^2$  and turning points  $r_{1,2}^c = (\nu_c^2)/Z(1 \mp e)$ . Here  $\nu_c$  denotes the centered effective principal quantum number, which is assigned as (A.15) due to the quasiclassical quantization conditions.

$$\nu_c^3 = \frac{2(\nu\nu')^2}{\nu + \nu'} \quad (\text{A.15})$$

Note that for non-hydrogenic atoms the phase difference  $\Delta(r) = \phi_{\delta'} - \phi_{\delta}$  mostly increases in the region  $r \simeq r_1^c$ , while the main contribution to the matrix elements is acquired on much larger distances  $r \sim \nu^2$ . Thus, we can replace in expression (A.10)  $\omega t \rightarrow \Delta + \omega t_c$  for the further calculations, while  $\phi \simeq \phi_c$ . Finally, we can substitute all the new parameters into original integral, which gives the following result:

$$R_{nl}^{n'l\pm 1} = (-1)^{\Delta n} \frac{\nu_c^5}{Z(\nu\nu')^{3/2}} D_r^{\pm}(e, s) \quad (\text{A.16})$$

$$D_r^{\pm} = \frac{1}{s} \left( J'_{-s}(es) \pm \sqrt{e^{-2} - 1} \left( J_{-s}(es) - \frac{\sin \pi s}{\pi s} \right) \right) + \frac{1 - e}{\pi s} \sin \pi s \quad (\text{A.17})$$

Here  $s = \nu' - \nu$ , and  $J$  are the Anger functions. Due to the Anger function symmetry properties we can express  $J_s(-z) = J_{-s}(z)$  and  $J'_s(z) = -J'_s(-z)$ . Then, the resulting matrix elements are perfectly symmetric.

Although the above representation of matrix elements is extremely accurate, it can be improved by switching to momentum representation. The difference between the representations is that when we switch to the coordinate representation, we replace the potential  $U$  with an additional phase, and therefore the second term of the formula (A.17) arises. However, this difference is a small correction  $\sim \alpha^2$ , where  $\alpha = \sqrt{1 - e^2}$ . Thus, the above quasi-classical approximation of matrix elements represents a highly accurate result, and allows calculating the dynamics of large quantum systems in a reasonable time with limited processor power.

In the framework of this study, we use the Eq.(A.16) given here to calculate the matrix elements when computing the interaction Hamiltonians for numerical simulations. We note that all the results in this paragraph have been presented more extensively in [221]. We encourage the interested reader to refer to the original paper for further details.

## B. RF-induced resonance model

In this appendix, we describe the interactions of alkali Rydberg ensembles with external radiation. Providing this description presents a rather hard issue due to the complex structure of the collective energy levels of atoms in an external electric field. Thus, we will demonstrate a simplified model that takes into account only 2 collective states. The following description is based on the results presented in [153]. Note that in the numerical simulations carried out in Section 4.4, we solved the Schrödinger equation for the full Hamiltonian of the system. Therefore, the description given here only provides a simplified picture of the observed processes.

We consider a system of logical levels  $|1\rangle$  and  $|2\rangle$  interacting with each other through the previously described dipole-dipole interaction  $\hat{V}$ , in the presence of a composite electric field  $F(t) = F_S + F_{RF} \cos(\omega t)$ . The Hamiltonian of this system can be described as  $\hat{H} = \hat{H}_0 + \hat{H}_{F_S} + \hat{H}_{F_{RF}} + \hat{V}$ . Here  $\hat{H}_0$  represents the Hamiltonian of a non-interacting two level system. To simplify the problem, we consistently consider the perturbation of the Hamiltonian  $\hat{H}_0$  by the other three terms.

We firstly describe the interaction of the two-level system with a static field. Let the Hamiltonian include only the first two terms  $\hat{H} = \hat{H}_0 + \hat{H}_{FS}$ . Thus, the system can be described by the wavefunction

$$\psi(r, t) = a\psi_1(r, t) + b\psi_2(r, t) \quad (\text{B.1})$$

$$\psi_{1(2)}(r, t) = \psi_{1(2)}(r)e^{-iW_{1(2)}t} \quad (\text{B.2})$$

Here  $\psi_{1(2)}$  are the system eigenstates, and  $W_{1(2)}$  are the corresponding eigenenergies. As shown in Subsection 2.2.2.2, these energies can be described by the sum of the atomic level energy and the quadratic Stark shift. For simplicity, the level  $|1\rangle$  energy can be kept referent, providing  $W_1 = 0$ ,  $W_2 = W_0 - \frac{1}{2}\alpha F_S^2$ , where  $W_0 = W_2 - W_1$  is the energy difference between the system eigenstates.

As a second step we add the perturbations provided by dipole-dipole interaction and the external radiation. Depending on the order in which the corresponding operators are added to the Hamiltonian, two kinds of solution representations arise, both of which are useful for understanding the dynamics of the system. We consider them both, starting with the case when we add the operator  $\hat{V}$  first. This operator provides a quantum beat oscillation frequency  $\Omega = 2\langle\psi_2|\hat{V}|\psi_1\rangle$ , as it was described earlier. Note that in case of a Förster resonance this additional interaction also lifts the collective level degeneracy.

To add the time-dependent radiation field component, we further separate the wavefunction into time- and distance - dependent parts as

$$\psi(r, t) = T_1(t)\psi_1(r) + T_2(t)\psi_2(r) \quad (\text{B.3})$$

Here  $\psi_{1(2)}$  are the original eigenstates of the system in DC field. This separation remains valid for long interatomic distances, when both spatial states remain approximately unchanged during the interaction. Hence, according to the Schrodinger equation

$$i\dot{T}_{1(2)}(t) = W_{1(2)}T_{1(2)}(t) + \frac{\Omega}{2}T_{2(1)}(t) \quad (\text{B.4})$$

The energies  $W_{1(2)}$  are time dependent because they are determined by the Stark effect in an alternating field:

$$W_2 = W_0 - \frac{1}{2}\alpha(F_S + F_{RF}\cos(\omega t))^2 \quad (\text{B.5})$$

Equation (B.4) could be solved numerically to provide the corresponding eigenfunctions of the system. Nevertheless, the insights gained from this approach are limited. In this regard, we present below the Floquet sideband approach, which is considered to be more informative for describing the interaction of a field with an atomic ensemble. While both methods yield equivalent results, obtaining an answer through a coherent superposition of stationary states proves to be more informative than understanding the time evolution of a wavefunction. It's important to note that the numerical approach remains applicable to all types of time-dependent fields, whereas the Floquet approach is specifically tailored to periodic functions.

In Floquet approach, we describe the dipole-dipole interactions for a system which includes external radiation. So we first add the perturbation  $\hat{H}_{F_{RF}}$  and then the dipole operator  $\hat{V}$  to the Hamiltonian. Thus, using the time-dependent Schrödinger equation for basis states  $\psi_{1(2)}(r, t) = T_{1(2)}(t)\psi_{1(2)}(r)$ , we obtain:

$$i\dot{T}_{1(2)}(t) = W_{1(2)}(t)T_{1(2)}(t) \quad (\text{B.6})$$

The time dependence of the energies  $W_{1(2)}$  was represented earlier by the formula (B.5). Integrating the resulting equation, we obtain:

$$T_2(t) = \exp\left(-i\left(W_0 - \frac{1}{2}\alpha\left(F_S^2 + \frac{F_{RF}^2}{2}\right)\right)t\right) \times \exp\left(i\frac{\alpha F_{RF} F_S}{\omega}\sin(\omega t)\right) \times \exp\left(i\frac{\alpha F_{RF}^2}{8\omega}\sin(2\omega t)\right) \quad (\text{B.7})$$

The last two exponential terms of this expression can be represented as generalized Bessel functions. We thus have for the resulting wavefunction:

$$\psi_2(r, t) = \psi_2(r) e^{-i\left(W_0 - \frac{1}{2}\alpha\left(F_S^2 + \frac{F_{RF}^2}{2}\right)\right)t} \times \sum_{n=-\infty}^{\infty} e^{in\omega t} J_n\left(\frac{\alpha F_{RF} F_S}{\omega}, \frac{\alpha F_{RF}^2}{8\omega}\right) \quad (\text{B.8})$$

This expression reveals that the wavefunction comprises the initial spatial wavefunction, but with a modified time dependence characterized by an infinite number of sidebands. Thus, we have potentially an infinite number of possible level intercrossings which correspond to Förster resonances. It is also instructive to reveal sideband energies:

$$W_{2,n} = W_0 - \frac{1}{2}\alpha\left(F_S^2 + \frac{F_{RF}^2}{2}\right) - n\omega \quad (\text{B.9})$$

Thus, each sideband of the wave function can be considered as a state containing  $n$  additional photons. The sideband amplitude, in turn, depends on both DC and AC electric field amplitudes, as well as on the frequency of the applied radiation. For a more detailed description, please refer to [153].

## C. Analytical model of three-body Förster resonances

In this appendix, we describe the analytic model of three-body Förster resonance interactions given in [193]. Figure C.1 shows a simplified scheme of three-body resonances (3.12) for states with  $n = 37$ . Here state 1 is the initial state of the three-atomic system  $3 \times 37P_{3/2}$ , and state 3 is its final state  $37S_{1/2} + 38S_{1/2} + 37P_{3/2}^*$  in the case of a successful three-body transfer. The intermediate state 2 serves to ensure the ladder-like transfer character described in the Subsection 3.1.1. Thus, the three-body process can be described as a sequence of two-body transitions

### C. Analytical model of three-body Förster resonances

$1 \rightarrow 2 \rightarrow 3$  occurring simultaneously. The detunings  $\Delta_1$  and  $\Delta_2$ , which represent the Förster defects of the respective two-body resonances, control the character of the multiatomic transit. When the condition  $\Delta_1 = \Delta_2$  is satisfied, levels 1 and 3 are degenerate, provoking a three-body resonance (resonance 1 or 8 in Figure 3.6). The two-body resonance, in turn, is induced by the condition  $\Delta_1 = 0$ , which means that levels 1 and 2 are degenerate (resonances 3 and 6 in Figure 3.6).

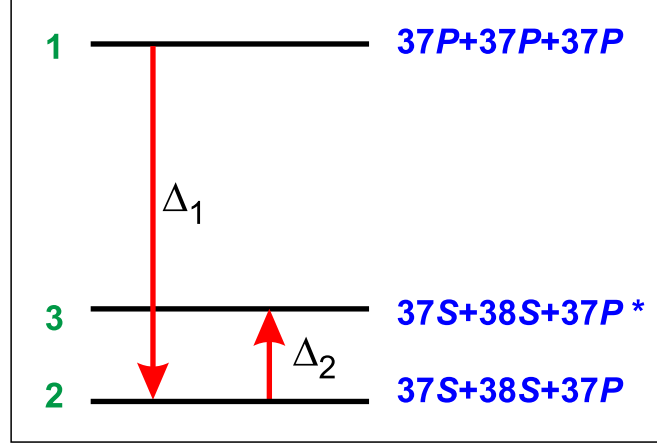


**Figure C.1:** Simplified scheme of the three-body Förster resonance  $3 \times 37P_{3/2}(|M|) \rightarrow 37S_{1/2} + 38S_{1/2} + 37P_{3/2}(|M^*|)$  for three Rydberg atoms. The initially populated collective state 1 is  $3 \times 37P_{3/2}(|M|)$ . The final collective state 3 is  $37S_{1/2} + 38S_{1/2} + 37P_{3/2}(|M^*|)$  with the changed momentum projection of the  $P$  state. The intermediate collective state 2 is  $37S_{1/2} + 38S_{1/2} + 37P_{3/2}(|M|)$  with the initial moment projection of the  $P$  state. The energy defects  $\Delta_1 = E_1 - E_2$  and  $\Delta_2 = E_3 - E_2$  are controlled by the DC electric field. The three-body resonance occurs at  $\Delta_1 = \Delta_2$ , while the two-body one occurs at  $\Delta_1 = 0$ .

Authors describe the dynamics of the system using the Schrödinger equation formalism for the probability amplitudes of states 1, 2 and 3. The matrix elements of the dipole-dipole transitions  $1 \rightarrow 2$  and  $2 \rightarrow 3$ , are denoted as variables  $V_1$  and  $V_2$ , respectively. These elements can also be expressed in frequency units as  $\Omega_1 = V_1/\hbar$ ,  $\Omega_2 = V_2/\hbar$ . The methods for calculating such matrix elements were shown in [135, 137, 193], as well as in Appendix A. Note that this model considers only the energies of the collective levels without specifying the states of each particular atom. This means that levels 2 and 3 are additionally sixfold degenerate due to possible permutations of atoms. Also, these states experience always-resonant hopping interactions between  $S$  and  $P$  states, which leads to the presence of an energy shift. Then, the Schrödinger equation will have the following form:

$$\begin{aligned}
 i\dot{a}_1 &= 6\Omega_1 a_2 e^{-i\Delta_1 t} \\
 i\dot{a}_2 &= 2\Omega_1 a_2 + \Omega_1 a_1 e^{i\Delta_1 t} + 2\Omega_2 a_3 e^{i\Delta_2 t} \\
 i\dot{a}_3 &= 2\Omega_2 a_3 + 2\Omega_2 a_2 e^{-i\Delta_2 t}
 \end{aligned} \tag{C.1}$$

Here, the terms containing no explicit time dependence are produced by excitation hopping described in Subsection 2.2.5. The terms containing exponential time dependence, in turn, are

representations of dipole-dipole transitions and were described in the same subsection.

To simplify the system of equations, we introduce substitutions  $a_2 = \alpha_2 e^{-2i\Omega_1 t}$ ,  $a_3 = \alpha_3 e^{-2i\Omega_2 t}$ . These substitutions exclude the time-independent terms, leading to the following form of the expressions:

$$\begin{aligned} i\dot{a}_1 &= 6\Omega_1\alpha_2 e^{-i(\Delta_1+2\Omega_1)t} \\ i\dot{a}_2 &= \Omega_1 a_1 e^{i(\Delta_1+2\Omega_1)t} + 2\Omega_2\alpha_3 e^{i(\Delta_2+2\Omega_1-2\Omega_2)t} \\ i\dot{a}_3 &= 2\Omega_2\alpha_2 e^{-i(\Delta_2+2\Omega_1-2\Omega_2)t} \end{aligned} \quad (\text{C.2})$$

The complex amplitudes  $a_1$ ,  $\alpha_2$  and  $\alpha_3$  can be found analytically in this system of equations. Let us demonstrate this for  $\alpha_3$ . Differentiating the last expression twice and substituting the values of the derivatives into the previous equations, we can reformulate the system exclusively in terms of  $\alpha_3$ . After several substitutions, a single differential equation can be found:

$$\begin{aligned} \ddot{\alpha}_3 + i(2\Delta_2 - \Delta_1 + 2\Omega_1 - 4\Omega_2) \dot{\alpha}_3 \\ + \left[ (\Delta_2 + 2\Omega_1 - 2\Omega_2) (\Delta_1 - \Delta_2 + 2\Omega_2) + 6\Omega_1^2 + 4\Omega_2^2 \right] \alpha_3 \\ - 4i(\Delta_1 - \Delta_2 + 2\Omega_2) \Omega_2^2 = 0 \end{aligned} \quad (\text{C.3})$$

It is convenient to search for solutions of this expression as  $\alpha \sim e^{i\mu t}$ . Then, for equation (C.3) we obtain

$$\begin{aligned} \mu^3 + (2\Delta_2 - \Delta_1 + 2\Omega_1 - 4\Omega_2) \mu^2 \\ - \left[ (\Delta_2 + 2\Omega_1 - 2\Omega_2) (\Delta_1 - \Delta_2 + 2\Omega_2) + 6\Omega_1^2 + 4\Omega_2^2 \right] \mu \\ + 4(\Delta_1 - \Delta_2 + 2\Omega_2) \Omega_2^2 = 0 \end{aligned} \quad (\text{C.4})$$

The resulting expression is a standard cubic equation that can be solved analytically. We omit the exact calculations, giving here only the expressions necessary to write down the equation roots.

$$\begin{aligned} S &= - \left[ (\Delta_2 + 2\Omega_1 - 2\Omega_2) (\Delta_1 - \Delta_2 + 2\Omega_2) + 6\Omega_1^2 + 4\Omega_2^2 \right] \\ T &= 4(\Delta_1 - \Delta_2 + 2\Omega_2) \Omega_2^2 \\ A &= S - (2\Delta_2 - \Delta_1 + 2\Omega_1 - 4\Omega_2)^2 / 3 \\ B &= 2(2\Delta_2 - \Delta_1 + 2\Omega_1 - 4\Omega_2)^3 / 27 \\ &\quad - (2\Delta_2 - \Delta_1 + 2\Omega_1 - 4\Omega_2) S / 3 + T \\ D &= (A/3)^3 + (B/2)^2 \\ U &= (-B/2 + \sqrt{D})^{1/3} \\ U^* &= -(B/2 + \sqrt{D})^{1/3} \end{aligned} \quad (\text{C.5})$$

## C. Analytical model of three-body Förster resonances

---

The equation roots can be denoted as

$$\begin{aligned}\mu_1 &= U + U^* - (2\Delta_2 - \Delta_1 + 2\Omega_1 - 4\Omega_2)/3 \\ \mu_2 &= -(U + U^*)/2 + i\sqrt{3}(U - U^*)/2\end{aligned}\tag{C.6}$$

$$\mu_3 = -(U + U^*)/2 - i\sqrt{3}(U - U^*)/2\tag{C.7}$$

Solutions  $\alpha_3$  for the original equation (C.3) could thus be found as

$$\alpha_3 = \sum_{i=1}^3 c_i e^{i\mu_i t}\tag{C.8}$$

To find the probability amplitudes, initial conditions should be applied. We assume that only the state 1 was populated prior to the interaction, giving the following conditions:  $\alpha_3(0) = 0$ ,  $\dot{\alpha}_3(0) = 0$ ,  $\ddot{\alpha}_3(0) = -2\Omega_1\Omega_2$ . Thus, for the coefficients  $c_i$  we can find

$$\begin{aligned}c_1 &= \frac{2\Omega_1\Omega_2}{(\mu_2 - \mu_1)(\mu_1 - \mu_3)} \\ c_2 &= \frac{2\Omega_1\Omega_2}{(\mu_2 - \mu_1)(\mu_3 - \mu_2)}\end{aligned}\tag{C.9}$$

$$c_3 = \frac{2\Omega_1\Omega_2}{(\mu_1 - \mu_3)(\mu_3 - \mu_2)}\tag{C.10}$$

We then can use the Eq. (C.2) to find  $\alpha_2$  from  $\alpha_3$

$$\alpha_2 = i\dot{\alpha}_3 e^{i(\Delta_2 + 2\Omega_1 - 2\Omega_2)t} / (2\Omega_2)\tag{C.11}$$

The exact analytical solutions for the equations (C.1) could be expressed using  $\alpha_2$  and  $\alpha_3$  for arbitrary values of interaction energies, detunings and time. Nevertheless, these solutions are rather complex and cannot be presented in a comprehensible form. In this regard, the authors limit themselves to describing the form of the obtained resonance spectra within weak dipole-dipole interaction limit, as well as near the exact three-body resonance, where the interactions turns into strong. The analysis of the resonance spectra based on the presented model is given in Subsection 3.3.4. For a more detailed description, please refer to the original article [193].



# List of Publications

## • Articles

1. Ashkarin, I. N., et al. "Toffoli gate based on a three-body fine-structure-state-changing Förster resonance in Rydberg atoms." *Physical Review A* 106.3 (2022): 032601.
2. Cheinet, P., et al. "Three-body Förster resonance of a new type in Rydberg atoms." *Quantum Electronics* 50.3 (2020): 213.
3. Ashkarin, I. N., et al. "Scheme of a hydrogen-molecule quantum simulator based on two ultracold rubidium atoms." *Quantum Electronics* 49.5 (2019): 449.
4. Beterov, I. I., et al. "Fast three-qubit Toffoli quantum gate based on three-body Förster resonances in Rydberg atoms." *Physical Review A* 98.4 (2018): 042704.

## • Pre-prints

1. Ashkarin, I. N., et al. "High-fidelity  $CCR_Z(\phi)$  gates via RF-induced Förster resonances." arXiv preprint arXiv:2307.12789 (2023).
2. Pham, K-L., et al. "Searching optimal conditions for quantum gates application with the new 3-body Förster resonances in Rb and Cs Rydberg atoms." arXiv preprint arXiv:2012.12845 (2020).

## • Conference proceedings

1. Ashkarin, I. N., Beterov, I. I. (2020). Investigation of three-body FRET in ensembles of ultracold Rb atoms. In ISSC-2020: Photonics and quantum optical technologies (pp. 7-7).
2. Ashkarin, I. N., Beterov, I. I. (2019). Development of a digital quantum simulator based on ultracold atoms in arrays of optical dipole traps. In ISSC-2019: Physical methods in natural sciences (pp. 49-49).
3. Ashkarin, I. N., Beterov, I. I. (2018). Three-qubit TOFFOLI gate based on three-body FRET in Rb atoms. In ISSC-2018: Physical methods in natural sciences (pp. 69-69).
4. Ashkarin, I. N., Yanshole, V. V. (2017). Optimization of the MALDI-TOF mass spectrometer for the registration of fragment ions of peptides. In ISSC-2017: Physical methods in natural sciences (pp. 41-41).



# Resume

Les réseaux d'atomes neutres refroidis et isolés dans des pinces optiques individuelles présentent un grand intérêt pour la réalisation de calculs quantiques. Les durées de vie élevées des atomes dans des pièges individuels ( $\sim 6000$  s), complétées par les vastes possibilités de contrôle cohérent des états quantiques par radiofréquence externe ou rayonnement micro-ondes, garantissent une grande précision des opérations quantiques à qubit unique pour les qubits atomiques. Les registres multiqubits actuellement disponibles contiennent jusqu'à plusieurs centaines d'atomes reliés par des portes à deux qubits très précises ( $\sim 99.5\%$ ). La mise à l'échelle des registres jusqu'à quelques dizaines de milliers d'atomes devrait se poursuivre dans les années à venir.

L'un des principaux obstacles à l'application des registres quantiques atomiques à la résolution de problèmes pratiques est l'impossibilité de réaliser des portes multiqubits à longue portée et de haute précision. Ces portes sont des composants importants de nombreux algorithmes quantiques, notamment l'algorithme de Grover, l'algorithme de Shor, les algorithmes de correction d'erreurs quantiques, QAOA, VQE et bien d'autres. En outre, les portes à longue portée sont nécessaires pour maintenir la connectivité totale des registres à mesure que leur taille augmente.

L'utilisation de résonances d'interaction dans les ensembles atomiques, appelées couramment résonance de Förster, constitue une approche prometteuse pour la réalisation de portes à longue portée. L'augmentation de l'interaction garantie par sa nature résonante permet de réaliser des opérations quantiques entre qubits distants, ce qui surpasse de manière significative toutes les approches concurrentes en matière d'opérations à longue portée. La grande précision des opérations à trois qubits démontrée dans cette étude nous permet d'affirmer que l'approche proposée est prometteuse pour une application dans les registres quantiques modernes.

Dans le cadre de cette thèse, une étude complète de l'applicabilité des résonances de Förster pour la mise en œuvre du calcul quantique dans les registres quantiques à base d'atomes neutres a été réalisée. Le cycle de recherche s'est déroulé en quatre étapes. À chaque étape, différentes variantes de schémas de résonance ont été proposées, ainsi que des approches de leur utilisation pour créer des portes quantiques. Des méthodes supplémentaires ont également été proposées pour améliorer la précision et la stabilité des portes quantiques et pour faciliter leur réalisation expérimentale.

## I. Première étape

Au cours de la première étape des recherches, de nouvelles résonances à trois corps du type (R.1) ont été proposées et modélisées numériquement. Le principal avantage de ces résonances par rapport aux transitions précédemment étudiées (R.2) était la possibilité de les réaliser pour des états atomiques de Rydberg de grand nombre quantique principal avec  $n > 38$  dans le Rb. Cela a été rendu possible par le fait que la première transition à deux corps  $2 \times nP \rightarrow nS + (n+1)S$ , nécessaire à la réalisation du transfert borroméen parallèle, a été remplacée par la transition  $nP + (n+1)P \rightarrow nS + (n+2)S$ , relâchant ainsi la contrainte d'utiliser un seul niveau de Rydberg initial pour tous les atomes. De telles transitions ont un défaut quantique positif à champ électrique nul, et peuvent être utilisées en conjonction avec des sauts d'excitation  $SP$  non résonnants pour réaliser un transfert de population à trois corps. Des oscillations cohérentes de la population ont été démontrées pour ce nouveau schéma d'interaction résonnante dans un ensemble structuré, accompagnées d'un changement de phase des états de registre collectif. Ainsi, il a été démontré que ces résonances sont prometteuses pour la réalisation de portes quantiques à trois qubits.

$$\begin{aligned} nP_{3/2}(m = 3/2) + (n+1)P_{3/2}(m = 3/2) + (n+1)P_{3/2}(m = -3/2) \rightarrow \\ \rightarrow nS_{1/2}(m = 1/2) + (n+2)S_{1/2}(m = 1/2) + (n+1)P_{3/2}(m = 1/2) \end{aligned} \quad (\text{R.1})$$

$$3 \times nP_{3/2}(|m|) \rightarrow nS_{1/2} + (n+1)S_{1/2} + nP_{3/2}(|m^*|) \quad (\text{R.2})$$

Un schéma de porte quantique de Toffoli a été proposé sur la base de la résonance (R.3) dans les atomes de Rb. L'utilisation d'états élevés  $n = 80$  nous a permis d'augmenter significativement les durées de vie des états collectifs de Rydberg et de réduire l'influence des pertes sur la cohérence des oscillations de la population. Dans le cadre des simulations numériques, les atomes ont été disposés linéairement à une distance  $R = 10 \mu\text{m}$  les uns des autres le long de l'axe de quantification  $Z$  coïncidant avec la direction du champ électrique continu externe. Cette configuration permet de réduire considérablement le nombre de canaux d'interaction multiparticulaire en raison de la présence de la règle de sélection sur la projection totale de la quantité de mouvement du système  $\Delta M = 0$ . Pour isoler davantage les pics de résonance à deux et trois corps, un champ magnétique externe a été utilisé. Une haute fidélité de  $\sim 98.3\%$  a été démontrée pour cette porte dans les simulations numériques grâce à une optimisation multiparamétrique réalisée à l'aide de la méthode Nelder-Mead. Le temps de mise en œuvre obtenu pour la porte est de 2.42 microsecondes.

$$\begin{aligned} |80P_{3/2}(3/2) 81P_{3/2}(3/2) 81P_{3/2}(-3/2)\rangle \rightarrow \\ \rightarrow |80S_{1/2}(1/2) 82S_{1/2}(1/2) 81P_{3/2}(1/2)\rangle \end{aligned} \quad (\text{R.3})$$

Parmi les inconvénients significatifs du schéma développé, il convient de noter la complexité de sa réalisation expérimentale. En particulier, l'excitation des atomes dans différents états de Rydberg nécessite l'utilisation de plusieurs sources laser mutuellement cohérentes. De plus, la nécessité d'utiliser un champ magnétique externe pour isoler le processus d'interaction à trois corps complique le dispositif expérimental. La grande sensibilité de la porte aux déviations du

champ électrique statique de contrôle impose des exigences en matière d'isolation du dispositif par rapport à l'environnement. Des recherches supplémentaires sont également nécessaires pour améliorer la précision de la porte quantique jusqu'à des valeurs supérieures à 99% afin de la rendre compatible avec les techniques de correction d'erreurs quantiques. Nous avons conclu que, bien que la porte proposée puisse potentiellement être appliquée à la mise en œuvre d'algorithmes quantiques complexes, des efforts supplémentaires sont nécessaires pour compenser les inconvénients décrits.

## II. Deuxième étape

Comme nous l'avons montré précédemment, l'assouplissement de la contrainte d'utilisation d'un seul niveau de Rydberg conduit à des inconvénients expérimentaux. Par conséquent, un schéma de résonance de Förster différent était nécessaire. Nous avons proposé et étudié numériquement des résonances de Förster à trois corps à changement d'état de structure fine (FSSC) (R.4). Leur principale différence avec les transitions présentées précédemment (R.1) est que pendant le processus FSSC à trois corps, le moment angulaire total du troisième atome passe à une valeur inférieure. Étant donné que le processus de saut d'excitation  $SP$  avec changement de moment angulaire  $J = 3/2 \rightarrow J = 1/2$  présente un défaut d'énergie important, la condition de compensation mutuelle des défauts  $\Delta_1 = \Delta_2$  peut être remplie en utilisant la transition standard à deux corps  $2 \times nP \rightarrow nS + (n + 1)S$ . En même temps, en raison du défaut d'énergie négative, la transition à deux corps ne peut pas être résonante dans un champ externe, comme nous l'avons déjà mentionné. Ainsi, seules les résonances à trois corps sont réalisées dans un système à trois atomes, en l'absence de processus à deux corps. Cela simplifie grandement la dynamique de phase et de population dans le registre quantique.

$$3 \times nP_{3/2} \rightarrow nS_{1/2} + (n + 1)S_{1/2} + nP_{1/2} \quad (\text{R.4})$$

Les résonances (R.4) ont été étudiées numériquement pour des ensembles d'atomes de Rb et de Cs. Nous avons également étudié les résonances de Förster quasi-interdites à plusieurs corps situées près du champ électrique statique résonant du schéma (R.4). La détermination de l'intensité de ces résonances était nécessaire pour évaluer leur influence potentielle sur la cohérence des oscillations de Rabi dans les ensembles atomiques et pour déterminer les éléments atomiques et les états de Rydberg les plus appropriés pour la réalisation de portes quantiques multiqubits. Sur la base des résultats de cette étude, nous avons conclu que les ensembles de rubidium à trois atomes présentent des résonances à trois corps très isolées dont la force est supérieure d'un ordre de grandeur à celle des transitions quasi-interdites voisines pour les états de Rydberg de haute altitude  $n = 70$  ou plus.

Une étude numérique poussée des résonances à plusieurs corps (R.4) a ensuite été réalisée dans des ensembles structurés et non structurés d'atomes de Rb. Dans la configuration spatiale linéaire du registre, seuls deux canaux à trois corps ont été observés pour de grandes distances interatomiques  $R = 10 \mu\text{m}$ , en l'absence totale d'interactions de résonance à deux corps. Des oscillations de population très cohérentes ont également été mises en évidence,

accompagnées de changements de la phase des états du système. Ainsi, nous avons conclu que les résonances FSSC démontrées sont prometteuses pour la mise en œuvre de protocoles de portes quantiques multiqubits et nous avons procédé au développement des portes correspondantes.

### III. Troisième étape

Au cours de la troisième étape de la recherche, un protocole de porte quantique de Toffoli basé sur les résonances FSSC (R.4) pour  $n = 70$  a été proposé et modélisé numériquement. La configuration spatiale linéaire du registre à trois atomes a été choisie de manière similaire au cas précédent. La principale différence entre le nouveau protocole de porte quantique et le protocole considéré précédemment est l'absence de nécessité d'exciter les atomes dans différents états de Rydberg. En outre, l'absence de processus de résonance à deux corps près des interactions à trois corps simplifie considérablement la dynamique de phase du système.

Grâce à une série d'expériences numériques, nous avons démontré de manière convaincante que la précision de notre porte quantique de Toffoli proposée est  $> 99\%$ . Ainsi, une amélioration significative de la précision a été obtenue par rapport au protocole précédent décrit dans la sous-section I.

Nous avons obtenu une réduction significative du temps de porte quantique par rapport au schéma proposé précédemment (jusqu'à  $1.15 \mu\text{s}$  à la distance interatomique  $R = 10 \mu\text{m}$  et jusqu'à  $0.42 \mu\text{s}$  à  $R = 8.5 \mu\text{m}$ ). Cela semble contre-intuitif, puisque la force de l'interaction à trois corps diminue certainement avec la diminution de  $n$ . Néanmoins, grâce à la simplification essentielle de la dynamique de phase du système due à l'absence de processus de résonance à deux corps, nous avons réussi à mettre en œuvre la porte pendant la première période des oscillations de Rabi, ce qui avait été impossible pour le schéma précédent.

Nous avons également étudié l'influence des variations des paramètres du registre atomique sur la précision de la porte quantique. Comme nous l'avons montré, les deux principaux facteurs limitant sont la forte sensibilité de la porte aux variations du champ électrique et à la distance interatomique. Néanmoins, il est possible de parvenir à un compromis qui permette d'assouplir les exigences relatives au contrôle de l'un des paramètres. En particulier, la forte dépendance de la fidélité de la porte aux variations du champ continu peut être réduite lorsque la distance interatomique  $R$  est diminuée en raison de l'augmentation de l'interaction interatomique et de l'élargissement des pics de résonance. Il a été démontré que lorsque la distance interatomique est réduite de  $R = 10 \mu\text{m}$  à  $R = 8.5 \mu\text{m}$ , la sensibilité aux fluctuations du champ diminue d'un facteur d'environ 4. Bien que la réduction de la distance interatomique ne réponde pas aux objectifs de réalisation de portes quantiques entre atomes distants, l'étude présentée permet d'évaluer différentes variantes de l'équilibrage du registre quantique nécessaires pour atteindre la précision expérimentale maximale de la porte.

Malgré l'amélioration significative de la précision de la porte quantique par rapport à la proposition précédente, un certain nombre d'inconvénients du système ont nécessité des efforts supplémentaires. Tout d'abord, la nécessité de modifier le champ de contrôle externe

pendant la porte quantique subsistait, ce qui limitait considérablement la précision possible des réalisations expérimentales. En outre, le nombre insuffisant de paramètres contrôlables du système a considérablement limité la possibilité de compenser les dynamiques de phase et de population indésirables. D'autres études ont donc été nécessaires pour compenser les lacunes décrites.

## IV. Quatrième étape

À ce stade, nous nous sommes concentrés sur la recherche de mécanismes supplémentaires pour contrôler les interactions de résonance multiparticulaire dans les ensembles d'atomes de Rydberg. En particulier, nous avons étudié en détail l'utilisation d'un rayonnement radiofréquence externe pour induire des résonances de Förster. Auparavant, les résonances induites par les radiofréquences (RF) avaient été étudiées en détail dans des systèmes à deux atomes. Cependant, à notre connaissance, aucune étude sur les résonances de Förster induites par des radiofréquences à particules multiples n'a été présentée avant ce travail.

Nous avons proposé et étudié numériquement des résonances FSSC à trois corps induites par des radiofréquences dans des systèmes d'atomes de Rydberg de Rb isolés dans l'espace. Ces résonances sont basées sur l'application d'un champ inducteur composite, qui comprend à la fois un champ électrique continu et un rayonnement de radiofréquence. Les photons RF permettent de compenser le défaut de Förster des états de Rydberg collectifs pour une valeur arbitrairement choisie du champ de contrôle externe. Le rayonnement RF externe permet également d'induire des résonances de Förster à deux corps inaccessibles  $nP + (n + 1)P \rightarrow nS + (n + 1)S$  pour les états de Rydberg élevés. De telles résonances ne peuvent pas être réalisées pour les états de Rydberg collectifs du Rb avec  $n > 38$  en raison des valeurs spéciales des polarisabilités et des défauts quantiques de ces états. Néanmoins, la compensation du défaut d'énergie à deux corps est possible grâce à l'émission ou à l'absorption de radiofréquences. Ainsi, le rayonnement RF externe fournit un outil flexible pour manipuler l'interaction dipôle-dipôle.

Nous avons simulé numériquement des interactions de résonance à deux corps (R.5) et à trois corps (R.6) induites par les radiofréquences dans l'ensemble ordonné d'atomes de Rb pour  $n = 70$ . Il a été montré que pour les deux types de résonances, la position de la première bande latérale de Floquet est effectivement contrôlée par le rayonnement externe. Ainsi, la résonance peut être induite pour une valeur arbitraire du champ électrique continu. Ce fait permet d'isoler de manière significative les pics à trois corps des résonances quasi-interdites environnantes et de réduire leur influence sur la dynamique du système quantique. Selon les conclusions de cette étude, les résonances multiparticules présentent une dynamique de population cohérente dans une configuration spatiale linéaire et conviennent bien à la réalisation de portes quantiques.

$$|70P_{3/2}\rangle^{\otimes 3} \rightarrow |70S_{1/2}; 71S_{1/2}; 70P_{3/2}(|m| = 1/2)\rangle \quad (\text{R.5})$$

$$|70P_{3/2}\rangle^{\otimes 3} \rightarrow |70S_{1/2}; 71S_{1/2}; 70P_{1/2}\rangle \quad (\text{R.6})$$

Nous avons également proposé et étudié numériquement des protocoles de portes *CCPHASE* à trois qubits basés sur les résonances à deux corps et à trois corps induites par la radiofréquence. L'utilisation d'un rayonnement inducteur nous permet de contrôler efficacement la population et la dynamique de phase du système, ce qui offre de nombreuses possibilités de manipulation des états quantiques. Ainsi, nous pouvons utiliser la fréquence et l'amplitude du rayonnement externe comme paramètres de contrôle exclusifs pour contrôler la phase de la porte. Il a été démontré qu'en gardant tous les paramètres du système (distance interatomique, champ électrique continu externe et temps de réalisation de la porte) inchangés, nous pouvons réaliser la porte *CCPHASE* pour une valeur arbitraire de  $\phi$  avec une grande précision en faisant varier uniquement la fréquence et l'amplitude du champ RF. De même, l'activation de la résonance à deux et trois corps peut se produire tout en préservant entièrement tous les paramètres expérimentaux, en faisant varier les paramètres du champ RF. À cet égard, différentes variations des portes proposées peuvent être réalisées dans le même dispositif expérimental. Il convient de noter que la possibilité de mettre en œuvre des portes arbitraires sans modifier la géométrie du registre est cruciale pour l'exécution d'algorithmes dans des installations d'informatique quantique à grande échelle.

Les protocoles proposés pour les portes quantiques font preuve d'une grande fidélité. En particulier, la fidélité moyenne des portes basées sur les résonances à trois corps était de  $\sim 99.3\%$  à température ambiante. La principale source de pertes, comme dans les protocoles proposés précédemment, est représentée par les durées de vie finies des états de Rydberg. Ainsi, en modélisant la réalisation de la porte dans un ensemble cryogénique (avec une température de 4 K), nous avons réussi à atteindre une fidélité de  $\sim 99.7\%$ , ce qui dépasse de manière significative la fidélité de toutes les réalisations expérimentales de portes à trois corps actuellement disponibles.

## V. Conclusion

Ces travaux ont permis de proposer et d'étudier numériquement plusieurs schémas de résonances de Förster à trois particules dans des ensembles structurés d'atomes de Rydberg isolés dans des pinces optiques individuelles. Des schémas pour la réalisation de portes quantiques multicubiques à longue portée basées sur les résonances présentées ont également été proposés. Des techniques supplémentaires pour contrôler l'interaction dipôle-dipôle ont été proposées, y compris l'utilisation d'un rayonnement radiofréquence externe induisant la résonance et d'un champ magnétique externe. Les résultats obtenus nous permettent d'affirmer le potentiel élevé des résonances de Förster pour la réalisation de portes quantiques dans des registres quantiques basés sur des atomes neutres, ainsi que le potentiel d'utilisation de cet effet pour maintenir l'interconnectivité entre des qubits distants et des registres quantiques isolés.

# Bibliography

- [1] M. A. Nielsen and I. L. Chuang, *Quantum Computation and Quantum Information: 10th Anniversary Edition* (Cambridge University Press, 2010) (cit. on pp. 13–16, 23, 28–31, 33–37, 107, 133, 137).
- [2] W. Brinkman, D. Haggan, and W. Troutman, "A history of the invention of the transistor and where it will lead us", *IEEE Journal of Solid-State Circuits* **32**, 1858 (1997) (cit. on p. 13).
- [3] W. Witkowski, "'Moore's Law's dead,' Nvidia CEO Jensen Huang says in justifying gaming-card price hike", (2022) <https://www.marketwatch.com/story/moores-laws-dead-nvidia-ceo-jensen-says-in-justifying-gaming-card-price-hike-11663798618> (cit. on p. 14).
- [4] S. Machkovech, "Intel: 'Moore's law is not dead' as Arc A770 GPU is priced at 329", (2022) <https://arstechnica.com/gadgets/2022/09/the-intel-arc-a770-gpu-launches-october-12-for-329/> (cit. on p. 14).
- [5] J. Shalf, "The future of computing beyond Moore's Law", *Philosophical Transactions of the Royal Society A: Mathematical, Physical and Engineering Sciences* **378**, 20190061 (2020) (cit. on p. 14).
- [6] C. Bernhardt, *Quantum computing for everyone* (Mit Press, 2019) (cit. on p. 14).
- [7] R. LaPierre, "DiVincenzo Criteria", in *Introduction to Quantum Computing* (Springer International Publishing, Cham, 2021), pp. 241–244 (cit. on pp. 14, 16).
- [8] S. Gulde, M. Riebe, G. P. T. Lancaster, C. Becher, J. Eschner, H. Häffner, F. Schmidt-Kaler, I. L. Chuang, and R. Blatt, "Implementation of the Deutsch-Jozsa algorithm on an ion-trap quantum computer", *Nature* **421**, 48 (2003) (cit. on p. 15).
- [9] F. Shi, X. Rong, N. Xu, Y. Wang, J. Wu, B. Chong, X. Peng, J. Knipert, R.-S. Schoenfeld, W. Harneit, M. Feng, and J. Du, "Room-Temperature Implementation of the Deutsch-Jozsa Algorithm with a Single Electronic Spin in Diamond", *Phys. Rev. Lett.* **105**, 040504 (2010) (cit. on p. 15).
- [10] B. Perez-Garcia, J. Francis, M. McLaren, R. I. Hernandez-Aranda, A. Forbes, and T. Konrad, "Quantum computation with classical light: The Deutsch Algorithm", *Physics Letters A* **379**, 1675 (2015) (cit. on p. 15).
- [11] P. Shor, "Polynomial-time algorithms for prime factorization and discrete logarithms on a quantum computer", *SIAM Rev.* **41**, 303 (1999) (cit. on pp. 15, 16, 24, 37, 137).
- [12] L. K. Grover, "A Fast Quantum Mechanical Algorithm for Database Search", in *Proceedings of the Twenty-Eighth Annual ACM Symposium on Theory of Computing*, STOC '96 (1996), pp. 212–219 (cit. on pp. 15, 24, 36).

## Bibliography

---

- [13] M. Sipser, "*Introduction to the Theory of Computation*", *SIGACT News* **27**, 27 (1996) (cit. on p. 15).
- [14] R. E. Ladner, "*On the Structure of Polynomial Time Reducibility*", *J. ACM* **22**, 155 (1975) (cit. on p. 15).
- [15] T. Vidick and J. Watrous, "*Quantum Proofs*", *Foundations and Trends in Theoretical Computer Science* **11**, 1 (2016) (cit. on p. 15).
- [16] T. D. Kieu, "*The travelling salesman problem and adiabatic quantum computation: an algorithm*", *Quantum Information Processing* **18**, 90 (2019) (cit. on p. 16).
- [17] M. T. Khumalo, H. A. Chieza, K. Prag, and M. Woolway, "*An investigation of IBM quantum computing device performance on combinatorial optimisation problems*", *Neural Computing and Applications*, 1 (2022) (cit. on p. 16).
- [18] A. Parra-Rodriguez, P. Lougovski, L. Lamata, E. Solano, and M. Sanz, "*Digital-analog quantum computation*", *Phys. Rev. A* **101**, 022305 (2020) (cit. on pp. 17, 21).
- [19] I. M. Georgescu, S. Ashhab, and F. Nori, "*Quantum simulation*", *Rev. Mod. Phys.* **86**, 153 (2014) (cit. on pp. 17, 73, 137).
- [20] H. J. Briegel, D. E. Browne, W. Dür, R. Raussendorf, and M. Van den Nest, "*Measurement-based quantum computation*", *Nature Physics* **5**, 19 (2009) (cit. on p. 17).
- [21] A. Finnila, M. Gomez, C. Sebenik, C. Stenson, and J. Doll, "*Quantum annealing: A new method for minimizing multidimensional functions*", *Chemical Physics Letters* **219**, 343 (1994) (cit. on p. 17).
- [22] I. Buluta and F. Nori, "*Quantum Simulators*", *Science* **326**, 108 (2009) (cit. on pp. 17, 72).
- [23] R. Raussendorf, J. Harrington, and K. Goyal, "*Topological fault-tolerance in cluster state quantum computation*", *New Journal of Physics* **9**, 199 (2007) (cit. on p. 17).
- [24] A. W. Glaetzle, R. M. W. van Bijnen, P. Zoller, and W. Lechner, "*A coherent quantum annealer with Rydberg atoms*", *Nature Communications* **8**, 15813 (2017) (cit. on p. 17).
- [25] H.-L. Huang, D. Wu, D. Fan, and X. Zhu, "*Superconducting quantum computing: a review*", *Science China Information Sciences* **63**, 180501 (2020) (cit. on p. 17).
- [26] M. Kjaergaard, M. E. Schwartz, J. Braumüller, P. Krantz, J. I.-J. Wang, S. Gustavsson, and W. D. Oliver, "*Superconducting Qubits: Current State of Play*", *Annual Review of Condensed Matter Physics* **11**, 369 (2020) (cit. on p. 17).
- [27] J. Clarke and F. K. Wilhelm, "*Superconducting quantum bits*", *Nature* **453**, 1031 (2008) (cit. on p. 18).
- [28] X.-F. Shi, "*Quantum logic and entanglement by neutral Rydberg atoms: methods and fidelity*", *Quantum Science and Technology* **7**, 023002 (2022) (cit. on pp. 18, 19, 21, 23–25, 37, 38, 53–57, 160).

- [29] F. Arute, K. Arya, R. Babbush, D. Bacon, J. C. Bardin, R. Barends, R. Biswas, S. Boixo, F. G. Brandao, D. A. Buell, et al., "Quantum supremacy using a programmable superconducting processor", *Nature* **574**, 505 (2019) (cit. on p. 18).
- [30] C. Neill, T. McCourt, X. Mi, Z. Jiang, M. Niu, W. Mruczkiewicz, I. Aleiner, F. Arute, K. Arya, J. Atalaya, et al., "Accurately computing the electronic properties of a quantum ring", *Nature* **594**, 508 (2021) (cit. on p. 18).
- [31] P. Bermejo and R. Orús, "Variational quantum non-orthogonal optimization", *Scientific Reports* **13**, 9840 (2023) (cit. on p. 18).
- [32] S. Watabe, M. Serikow, S. Kawabata, and A. Zagorskin, "Scaling Law in Large Quantum Devices with Dissipation", in *APS March Meeting Abstracts, Vol.2021, A30.008* (2021) (cit. on p. 18).
- [33] M. Kjaergaard, M. E. Schwartz, A. Greene, G. O. Samach, A. Bengtsson, M. O'Keeffe, C. M. McNally, J. Braumüller, D. K. Kim, P. Krantz, et al., "Programming a quantum computer with quantum instructions", *arXiv preprint arXiv:2001.08838* (2020) (cit. on p. 18).
- [34] R. Barends, J. Kelly, A. Megrant, A. Veitia, D. Sank, E. Jeffrey, T. C. White, J. Mutus, A. G. Fowler, B. Campbell, et al., "Superconducting quantum circuits at the surface code threshold for fault tolerance", *Nature* **508**, 500 (2014) (cit. on p. 18).
- [35] C. Rigetti, J. M. Gambetta, S. Poletto, B. L. T. Plourde, J. M. Chow, A. D. Córcoles, J. A. Smolin, S. T. Merkel, J. R. Rozen, G. A. Keefe, M. B. Rothwell, M. B. Ketchen, and M. Steffen, "Superconducting qubit in a waveguide cavity with a coherence time approaching 0.1 ms", *Phys. Rev. B* **86**, 100506 (2012) (cit. on p. 18).
- [36] F. Marxer, A. Vepsäläinen, S. W. Jolin, J. Tuorila, A. Landra, C. Ockeloen-Korppi, W. Liu, O. Ahonen, A. Auer, L. Belzane, et al., "Long-Distance Transmon Coupler with cz-Gate Fidelity above 99.8%", *PRX Quantum* **4**, 010314 (2023) (cit. on p. 18).
- [37] L. Ding, M. Hays, Y. Sung, B. Kannan, J. An, A. Di Paolo, A. H. Karamlou, T. M. Hazard, K. Azar, D. K. Kim, et al., "High-Fidelity, Frequency-Flexible Two-Qubit Fluxonium Gates with a Transmon Coupler", *arXiv preprint arXiv:2304.06087* (2023) (cit. on p. 18).
- [38] J.-Y. Ryu, E. Elala, and J.-K. K. Rhee, "Quantum Graph Neural Network Models for Materials Search", *Materials* **16**, 4300 (2023) (cit. on p. 18).
- [39] J. Zhang, G. Pagano, P. W. Hess, A. Kyprianidis, P. Becker, H. Kaplan, A. V. Gorshkov, Z.-X. Gong, and C. Monroe, "Observation of a many-body dynamical phase transition with a 53-qubit quantum simulator", *Nature* **551**, 601 (2017) (cit. on p. 18).
- [40] T. P. Harty, D. T. C. Allcock, C. J. Ballance, L. Guidoni, H. A. Janacek, N. M. Linke, D. N. Stacey, and D. M. Lucas, "High-Fidelity Preparation, Gates, Memory, and Read-out of a Trapped-Ion Quantum Bit", *Phys. Rev. Lett.* **113**, 220501 (2014) (cit. on p. 18).

## Bibliography

---

- [41] J. P. Gaebler, T. R. Tan, Y. Lin, Y. Wan, R. Bowler, A. C. Keith, S. Glancy, K. Coakley, E. Knill, D. Leibfried, and D. J. Wineland, “*High-Fidelity Universal Gate Set for  $^9\text{Be}^+$  Ion Qubits*”, *Phys. Rev. Lett.* **117**, 060505 (2016) (cit. on p. 18).
- [42] G. Semeghini, H. Levine, A. Keesling, S. Ebadi, T. T. Wang, D. Bluvstein, R. Verresen, H. Pichler, M. Kalinowski, R. Samajdar, A. Omran, S. Sachdev, A. Vishwanath, M. Greiner, V. Vuletić, and M. D. Lukin, “*Probing topological spin liquids on a programmable quantum simulator*”, *Science* **374**, 1242 (2021) (cit. on pp. 18, 22).
- [43] S. Ebadi, T. T. Wang, H. Levine, A. Keesling, G. Semeghini, A. Omran, D. Bluvstein, R. Samajdar, H. Pichler, W. W. Ho, et al., “*Quantum phases of matter on a 256-atom programmable quantum simulator*”, *Nature* **595**, 227 (2021) (cit. on pp. 18, 22).
- [44] K.-N. Schymik, B. Ximenez, E. Bloch, D. Dreon, A. Signoles, F. Nogrette, D. Barredo, A. Browaeys, and T. Lahaye, “*In situ equalization of single-atom loading in large-scale optical tweezer arrays*”, *Phys. Rev. A* **106**, 022611 (2022) (cit. on pp. 18, 21, 164).
- [45] I. S. Madjarov, J. P. Covey, A. L. Shaw, J. Choi, A. Kale, A. Cooper, H. Pichler, V. Schkolnik, J. R. Williams, and M. Endres, “*High-fidelity entanglement and detection of alkaline-earth Rydberg atoms*”, *Nature Physics* **16**, 857 (2020) (cit. on pp. 18, 19, 21, 38).
- [46] S. Olmschenk, R. Chicireanu, K. D. Nelson, and J. V. Porto, “*Randomized benchmarking of atomic qubits in an optical lattice*”, *New Journal of Physics* **12**, 113007 (2010) (cit. on p. 18).
- [47] H. Levine, A. Keesling, G. Semeghini, A. Omran, T. T. Wang, S. Ebadi, H. Bernien, M. Greiner, V. Vuletić, H. Pichler, and M. D. Lukin, “*Parallel Implementation of High-Fidelity Multiqubit Gates with Neutral Atoms*”, *Phys. Rev. Lett.* **123**, 170503 (2019) (cit. on pp. 18, 21, 37, 38, 57, 58, 138).
- [48] Z. Fu, P. Xu, Y. Sun, Y.-Y. Liu, X.-D. He, X. Li, M. Liu, R.-B. Li, J. Wang, L. Liu, and M.-S. Zhan, “*High-fidelity entanglement of neutral atoms via a Rydberg-mediated single-modulated-pulse controlled-phase gate*”, *Phys. Rev. A* **105**, 042430 (2022) (cit. on pp. 18, 57, 137).
- [49] S. J. Evered, D. Bluvstein, M. Kalinowski, S. Ebadi, T. Manovitz, H. Zhou, S. H. Li, A. A. Geim, T. T. Wang, N. Maskara, H. Levine, G. Semeghini, M. Greiner, V. Vuletić, and M. D. Lukin, “*High-fidelity parallel entangling gates on a neutral-atom quantum computer*”, *Nature* **622**, 268 (2023) (cit. on pp. 18, 21, 25, 58, 163, 164).
- [50] L. Gyongyosi and S. Imre, “*A Survey on quantum computing technology*”, *Computer Science Review* **31**, 51 (2019) (cit. on p. 18).
- [51] T. Olsacher, L. Postler, P. Schindler, T. Monz, P. Zoller, and L. M. Sieberer, “*Scalable and Parallel Tweezer Gates for Quantum Computing with Long Ion Strings*”, *PRX Quantum* **1**, 020316 (2020) (cit. on p. 18).

- [52] B. Lekitsch, S. Weidt, A. G. Fowler, K. Mølmer, S. J. Devitt, C. Wunderlich, and W. K. Hensinger, "Blueprint for a microwave trapped ion quantum computer", *Science Advances* **3**, e1601540 (2017) (cit. on pp. 18, 19).
- [53] C. D. Bruzewicz, J. Chiaverini, R. McConnell, and J. M. Sage, "Trapped-ion quantum computing: Progress and challenges", *Applied Physics Reviews* **6**, 021314 (2019) (cit. on pp. 18, 19).
- [54] A. H. Myerson, D. J. Szwer, S. C. Webster, D. T. C. Allcock, M. J. Curtis, G. Imreh, J. A. Sherman, D. N. Stacey, A. M. Steane, and D. M. Lucas, "High-Fidelity Readout of Trapped-Ion Qubits", *Phys. Rev. Lett.* **100**, 200502 (2008) (cit. on p. 18).
- [55] S. Crain, C. Cahall, G. Vrijsen, E. E. Wollman, M. D. Shaw, V. B. Verma, S. W. Nam, and J. Kim, "High-speed low-crosstalk detection of a  $171\text{Yb}^+$  qubit using superconducting nanowire single photon detectors", *Communications Physics* **2**, 97 (2019) (cit. on p. 18).
- [56] M. Siegele-Brown, S. Hong, F. R. Lebrun-Gallagher, S. J. Hile, S. Weidt, and W. K. Hensinger, "Fabrication of surface ion traps with integrated current carrying wires enabling high magnetic field gradients", *Quantum Science and Technology* **7**, 034003 (2022) (cit. on p. 19).
- [57] R. Fein, "Quantum Computing with Neutral Atoms", (2023) <https://quantumtech.blog/2023/01/17/quantum-computing-with-neutral-atoms/> (cit. on pp. 19, 20).
- [58] K.-N. Schymik, S. Pancaldi, F. Nogrette, D. Barredo, J. Paris, A. Browaeys, and T. Lahaye, "Single Atoms with 6000-Second Trapping Lifetimes in Optical-Tweezer Arrays at Cryogenic Temperatures", *Phys. Rev. Appl.* **16**, 034013 (2021) (cit. on pp. 19, 151, 164).
- [59] M. Saffman, T. G. Walker, and K. Mølmer, "Quantum information with Rydberg atoms", *Rev. Mod. Phys.* **82**, 2313 (2010) (cit. on pp. 20, 21, 25, 50, 72, 73, 76, 77, 102, 137, 146, 151).
- [60] L. Henriët, L. Beguin, A. Signoles, T. Lahaye, A. Browaeys, G.-O. Reymond, and C. Jurczak, "Quantum computing with neutral atoms", *Quantum* **4**, 327 (2020) (cit. on pp. 20, 22, 53, 54, 57).
- [61] Wintersperger, Karen, Dommert, Florian, Ehmer, Thomas, Hoursanov, Andrey, Klepsch, Johannes, Mauerer, Wolfgang, Reuber, Georg, Strohm, Thomas, Yin, Ming, and Lubner, Sebastian, "Neutral atom quantum computing hardware: performance and end-user perspective", *EPJ Quantum Technol.* **10**, 32 (2023) (cit. on pp. 20, 22, 23).
- [62] M. Schlosser, S. Tichelmann, D. Schäffner, D. O. de Mello, M. Hambach, J. Schütz, and G. Birkel, "Scalable Multilayer Architecture of Assembled Single-Atom Qubit Arrays in a Three-Dimensional Talbot Tweezer Lattice", *Phys. Rev. Lett.* **130**, 180601 (2023) (cit. on p. 20).

## Bibliography

---

- [63] M. Morgado and S. Whitlock, "Quantum simulation and computing with Rydberg-interacting qubits", *AVS Quantum Science* **3**, 023501 (2021) (cit. on pp. 21, 23, 56, 57, 59).
- [64] S. Jandura and G. Pupillo, "Time-Optimal Two- and Three-Qubit Gates for Rydberg Atoms", *Quantum* **6**, 712 (2022) (cit. on pp. 21, 24, 58, 160).
- [65] W. Xu, A. V. Venkatramani, S. H. Cantú, T. Šumarac, V. Klüsener, M. D. Lukin, and V. Vuletić, "Fast Preparation and Detection of a Rydberg Qubit Using Atomic Ensembles", *Phys. Rev. Lett.* **127**, 050501 (2021) (cit. on p. 21).
- [66] M. Endres, H. Bernien, A. Keesling, H. Levine, E. R. Anschuetz, A. Krajenbrink, C. Senko, V. Vuletic, M. Greiner, and M. D. Lukin, "Atom-by-atom assembly of defect-free one-dimensional cold atom arrays", *Science* **354**, 1024 (2016) (cit. on p. 21).
- [67] C. S. Adams, J. D. Pritchard, and J. P. Shaffer, "Rydberg atom quantum technologies", *Journal of Physics B: Atomic, Molecular and Optical Physics* **53**, 012002 (2019) (cit. on pp. 21, 23, 50, 57, 72).
- [68] M. Greiner, O. Mandel, T. Esslinger, T. W. Hänsch, and I. Bloch, "Quantum phase transition from a superfluid to a Mott insulator in a gas of ultracold atoms", *Nature* **415**, 39 (2002) (cit. on p. 22).
- [69] L. W. Cheuk, M. A. Nichols, K. R. Lawrence, M. Okan, H. Zhang, E. Khatami, N. Trivedi, T. Paiva, M. Rigol, and M. W. Zwierlein, "Observation of spatial charge and spin correlations in the 2D Fermi-Hubbard model", *Science* **353**, 1260 (2016) (cit. on p. 22).
- [70] M. Boll, T. A. Hilker, G. Salomon, A. Omran, J. Nespolo, L. Pollet, I. Bloch, and C. Gross, "Spin- and density-resolved microscopy of antiferromagnetic correlations in Fermi-Hubbard chains", *Science* **353**, 1257 (2016) (cit. on p. 22).
- [71] J. P. Hague, P. E. Kornilovitch, and C. MacCormick, "Cold-atom quantum simulator to explore pairing, condensation, and pseudogaps in extended Hubbard-Holstein models", *Phys. Rev. A* **102**, 033333 (2020) (cit. on p. 22).
- [72] M. F. Parsons, A. Mazurenko, C. S. Chiu, G. Ji, D. Greif, and M. Greiner, "Site-resolved measurement of the spin-correlation function in the Fermi-Hubbard model", *Science* **353**, 1253 (2016) (cit. on p. 22).
- [73] J. Eisert, M. Friesdorf, and C. Gogolin, "Quantum many-body systems out of equilibrium", *Nature Physics* **11**, 124 (2015) (cit. on p. 22).
- [74] A. Keesling, A. Omran, H. Levine, H. Bernien, H. Pichler, S. Choi, R. Samajdar, S. Schwartz, P. Silvi, S. Sachdev, P. Zoller, M. Endres, M. Greiner, V. Vuletić, and M. D. Lukin, "Quantum Kibble-Zurek mechanism and critical dynamics on a programmable Rydberg simulator", *Nature* **568**, 207 (2019) (cit. on p. 22).

- [75] V. Lienhard, S. de Léséleuc, D. Barredo, T. Lahaye, A. Browaeys, M. Schuler, L.-P. Henry, and A. M. Läuchli, "Observing the Space- and Time-Dependent Growth of Correlations in Dynamically Tuned Synthetic Ising Models with Antiferromagnetic Interactions", *Phys. Rev. X* **8**, 021070 (2018) (cit. on p. 22).
- [76] S. Giovanazzi, "Hawking Radiation in Sonic Black Holes", *Phys. Rev. Lett.* **94**, 061302 (2005) (cit. on p. 22).
- [77] E. Zohar, J. I. Cirac, and B. Reznik, "Quantum simulations of lattice gauge theories using ultracold atoms in optical lattices", *Reports on Progress in Physics* **79**, 014401 (2015) (cit. on p. 22).
- [78] B. Nachman, D. Provasoli, W. A. de Jong, and C. W. Bauer, "Quantum Algorithm for High Energy Physics Simulations", *Phys. Rev. Lett.* **126**, 062001 (2021) (cit. on p. 22).
- [79] P. Rebentrost, M. Mohseni, and S. Lloyd, "Quantum Support Vector Machine for Big Data Classification", *Phys. Rev. Lett.* **113**, 130503 (2014) (cit. on p. 22).
- [80] V. Havlíček, A. D. Córcoles, K. Temme, A. W. Harrow, A. Kandala, J. M. Chow, and J. M. Gambetta, "Supervised learning with quantum-enhanced feature spaces", *Nature* **567**, 209 (2019) (cit. on p. 22).
- [81] M. Raissi, P. Perdikaris, and G. Karniadakis, "Physics-informed neural networks: A deep learning framework for solving forward and inverse problems involving non-linear partial differential equations", *Journal of Computational Physics* **378**, 686 (2019) (cit. on pp. 22, 23).
- [82] S. Ebadi, A. Keesling, M. Cain, T. T. Wang, H. Levine, D. Bluvstein, G. Semeghini, A. Omran, J.-G. Liu, R. Samajdar, et al., "Quantum optimization of maximum independent set using Rydberg atom arrays", *Science* **376**, 1209 (2022) (cit. on p. 23).
- [83] J. Wurtz, P. L. Lopes, N. Gemelke, A. Keesling, and S. Wang, "Industry applications of neutral-atom quantum computing solving independent set problems", *arXiv preprint arXiv:2205.08500* (2022) (cit. on p. 23).
- [84] M.-T. Nguyen, J.-G. Liu, J. Wurtz, M. D. Lukin, S.-T. Wang, and H. Pichler, "Quantum Optimization with Arbitrary Connectivity Using Rydberg Atom Arrays", *PRX Quantum* **4**, 010316 (2023) (cit. on pp. 23, 152).
- [85] M. F. Serret, B. Marchand, and T. Ayril, "Solving optimization problems with Rydberg analog quantum computers: Realistic requirements for quantum advantage using noisy simulation and classical benchmarks", *Phys. Rev. A* **102**, 052617 (2020) (cit. on p. 23).
- [86] J. Roffe, "Quantum error correction: an introductory guide", *Contemporary Physics* **60**, 226 (2019) (cit. on p. 23).
- [87] C. Figgatt, D. Maslov, K. A. Landsman, N. M. Linke, S. Debnath, and C. Monroe, "Complete 3-Qubit Grover search on a programmable quantum computer", *Nature Communications* **8**, 1918 (2017) (cit. on p. 24).

## Bibliography

---

- [88] I. Cong, H. Levine, A. Keesling, D. Bluvstein, S.-T. Wang, and M. D. Lukin, “*Hardware-Efficient, Fault-Tolerant Quantum Computation with Rydberg Atoms*”, *Phys. Rev. X* **12**, 021049 (2022) (cit. on pp. 24, 137).
- [89] J. M. Baker, A. Litteken, C. Duckering, H. Hoffmann, H. Bernien, and F. T. Chong, “*Exploiting long-distance interactions and tolerating atom loss in neutral atom quantum architectures*”, in *2021 ACM/IEEE 48th Annual International Symposium on Computer Architecture (ISCA)* (IEEE, 2021), pp. 818–831 (cit. on p. 24).
- [90] S. T. Yasuhiro Takahashi and N. Kunihiro, “*Quantum addition circuits and unbounded fan-out*”, *Quantum Information and Computation* **10(910)**, 872 (2010) (cit. on p. 24).
- [91] L. Isenhower, M. Saffman, and K. Mølmer, “*Multibit  $C_k$  NOT quantum gates via Rydberg blockade*”, *Quantum Inf. Process.* **10**, 755 (2011) (cit. on pp. 24, 57, 58).
- [92] X.-F. Shi, “*Deutsch, Toffoli, and cnot Gates via Rydberg Blockade of Neutral Atoms*”, *Phys. Rev. Applied* **9**, 051001 (2018) (cit. on pp. 24, 66).
- [93] H.-Z. Wu, Z.-B. Yang, and S.-B. Zheng, “*Implementation of a multiqubit quantum phase gate in a neutral atomic ensemble via the asymmetric Rydberg blockade*”, *Phys. Rev. A* **82**, 034307 (2010) (cit. on p. 24).
- [94] M. Li, F.-Q. Guo, Z. Jin, L.-L. Yan, E.-J. Liang, and S.-L. Su, “*Multiple-qubit controlled unitary quantum gate for Rydberg atoms using shortcut to adiabaticity and optimized geometric quantum operations*”, *Phys. Rev. A* **103**, 062607 (2021) (cit. on p. 24).
- [95] C.-Y. Guo, L.-L. Yan, S. Zhang, S.-L. Su, and W. Li, “*Optimized geometric quantum computation with a mesoscopic ensemble of Rydberg atoms*”, *Phys. Rev. A* **102**, 042607 (2020) (cit. on p. 24).
- [96] D. Yu, Y. Gao, W. Zhang, J. Liu, and J. Qian, “*Scalability and high-efficiency of an  $(n+1)$ -qubit Toffoli gate sphere via blockaded Rydberg atoms*”, *arXiv preprint arXiv:2001.04599* (2020) (cit. on p. 24).
- [97] R. Li, S. Li, D. Yu, J. Qian, and W. Zhang, “*Optimal Model for Fewer-Qubit CNOT Gates With Rydberg Atoms*”, *Phys. Rev. Appl.* **17**, 024014 (2022) (cit. on p. 24).
- [98] I. I. Beterov, I. N. Ashkarin, E. A. Yakshina, D. B. Tretyakov, V. M. Entin, I. I. Ryabtsev, P. Cheinet, P. Pillet, and M. Saffman, “*Fast three-qubit Toffoli quantum gate based on the three-body Förster resonances in Rydberg atoms*”, *Phys. Rev. A* **98**, 042704 (2018) (cit. on pp. 24, 58, 91–93, 109–111, 124–126, 132, 135, 137, 141).
- [99] M. Khazali and K. Mølmer, “*Fast Multiqubit Gates by Adiabatic Evolution in Interacting Excited-State Manifolds of Rydberg Atoms and Superconducting Circuits*”, *Phys. Rev. X* **10**, 021054 (2020) (cit. on p. 24).
- [100] A. M. Farouk, I. I. Beterov, P. Xu, S. Bergamini, and I. I. Ryabtsev, “*Parallel Implementation of  $CNOT^N$  and  $C^2NOT^2$  Gates via Homonuclear and Heteronuclear Förster Interactions of Rydberg Atoms*”, *Photonics* **10** (2023) (cit. on pp. 24, 137).

- 
- [101] G. Pelegrí, A. J. Daley, and J. D. Pritchard, "High-fidelity multiqubit Rydberg gates via two-photon adiabatic rapid passage", *Quantum Science and Technology* **7**, 045020 (2022) (cit. on p. 24).
- [102] T. H. Xing, X. Wu, and G. F. Xu, "Nonadiabatic holonomic three-qubit controlled gates realized by one-shot implementation", *Phys. Rev. A* **101**, 012306 (2020) (cit. on p. 24).
- [103] H.-D. Yin, X.-X. Li, G.-C. Wang, and X.-Q. Shao, "One-step implementation of Toffoli gate for neutral atoms based on unconventional Rydberg pumping", *Opt. Express* **28**, 35576 (2020) (cit. on p. 24).
- [104] X. Chen, H. Xie, G.-W. Lin, X. Shang, M.-Y. Ye, and X.-M. Lin, "Dissipative generation of a steady three-atom singlet state based on Rydberg pumping", *Phys. Rev. A* **96**, 042308 (2017) (cit. on p. 24).
- [105] C. Yang, D.-X. Li, and X.-Q. Shao, "Dissipative preparation of multipartite Greenberger-Horne-Zeilinger states of Rydberg atoms\*", *Chinese Physics B* **30**, 023201 (2021) (cit. on p. 24).
- [106] T. M. Wintermantel, Y. Wang, G. Lochead, S. Shevate, G. K. Brennen, and S. Whitlock, "Unitary and Nonunitary Quantum Cellular Automata with Rydberg Arrays", *Phys. Rev. Lett.* **124**, 070503 (2020) (cit. on p. 24).
- [107] R. Faoro, B. Pelle, A. Zuliani, P. Cheinet, E. Arimondo, and P. Pillet, "Borromean three-body FRET in frozen Rydberg gases", *Nat. Commun.* **6**, 8173 (2015) (cit. on pp. 25, 61, 66, 68, 70–74, 76, 77, 92, 101, 112, 113).
- [108] T. G. de Brugière, "Methods for optimizing the synthesis of quantum circuits", PhD thesis (Universite Paris-Saclay, 2020) (cit. on pp. 29, 34, 35).
- [109] M. Saffman, "A little bit of quantum information", 2015 (cit. on pp. 30, 34, 35).
- [110] E. Fredkin and T. Toffoli, "Conservative logic", *International Journal of Theoretical Physics* **21**, 219 (1982) (cit. on p. 34).
- [111] A. Peres, "Reversible logic and quantum computers", *Phys. Rev. A* **32**, 3266 (1985) (cit. on p. 34).
- [112] D. Aharonov, "A simple proof that Toffoli and Hadamard are quantum universal", *arXiv preprint quant-ph/0301040* (2003) (cit. on p. 35).
- [113] [https://en.wikipedia.org/wiki/Quantum\\_algorithm](https://en.wikipedia.org/wiki/Quantum_algorithm) (cit. on p. 36).
- [114] A. Montanaro, "Quantum algorithms: an overview", *npj Quantum Information* **2**, 15023 (2016) (cit. on p. 36).
- [115] K. P. Seshadreesan, J. P. Olson, K. R. Motes, P. P. Rohde, and J. P. Dowling, "Boson sampling with displaced single-photon Fock states versus single-photon-added coherent states: The quantum-classical divide and computational-complexity transitions in linear optics", *Phys. Rev. A* **91**, 022334 (2015) (cit. on p. 36).

## Bibliography

---

- [116] S. Kutin, "Quantum Lower Bound for the Collision Problem with Small Range", *Theory of Computing* **1**, 29 (2005) (cit. on p. 36).
- [117] F. Magniez, M. Santha, and M. Szegedy, "Quantum Algorithms for the Triangle Problem", *SIAM Journal on Computing* **37**, 413 (2007) (cit. on p. 36).
- [118] G. Brassard and P. Hoyer, "An exact quantum polynomial-time algorithm for Simon's problem", in *Proceedings of the Fifth Israeli Symposium on Theory of Computing and Systems* (IEEE, 1997), pp. 12–23 (cit. on p. 36).
- [119] E. Farhi, J. Goldstone, and S. Gutmann, "A quantum approximate optimization algorithm", *arXiv preprint arXiv:1411.4028* (2014) (cit. on p. 36).
- [120] A. Peruzzo, J. McClean, P. Shadbolt, M.-H. Yung, X.-Q. Zhou, P. J. Love, A. Aspuru-Guzik, and J. L. O'Brien, "A variational eigenvalue solver on a photonic quantum processor", *Nature Communications* **5**, 4213 (2014) (cit. on p. 36).
- [121] D. Coppersmith, "An approximate Fourier transform useful in quantum factoring", *arXiv preprint quant-ph/0201067* (2002) (cit. on p. 37).
- [122] D. Deutsch and R. Jozsa, "Rapid solution of problems by quantum computation", *Proceedings of the Royal Society of London. Series A: Mathematical and Physical Sciences* **439**, 553 (1992) (cit. on p. 37).
- [123] E. Bernstein and U. Vazirani, "Quantum Complexity Theory", in *Proceedings of the Twenty-Fifth Annual ACM Symposium on Theory of Computing*, STOC '93 (1993), pp. 11–20 (cit. on p. 37).
- [124] D. R. Simon, "On the Power of Quantum Computation", *SIAM Journal on Computing* **26**, 1474 (1997) (cit. on p. 37).
- [125] A. Y. Kitaev, "Quantum measurements and the Abelian stabilizer problem", *arXiv preprint quant-ph/9511026* (1995) (cit. on p. 37).
- [126] I. Ashkarin, I. Beterov, D. Tretyakov, V. Entin, E. Yakshina, and I. Ryabtsev, "Scheme of a hydrogen-molecule quantum simulator based on two ultracold rubidium atoms", *Quantum Electronics* **49**, 449 (2019) (cit. on p. 37).
- [127] L. Isenhower, E. Urban, X. L. Zhang, A. T. Gill, T. Henage, T. A. Johnson, T. G. Walker, and M. Saffman, "Demonstration of a Neutral Atom Controlled-NOT Quantum Gate", *Phys. Rev. Lett.* **104**, 010503 (2010) (cit. on pp. 37, 55, 57).
- [128] S.-L. Su, E. Liang, S. Zhang, J.-J. Wen, L.-L. Sun, Z. Jin, and A.-D. Zhu, "One-step implementation of the Rydberg-Rydberg-interaction gate", *Phys. Rev. A* **93**, 012306 (2016) (cit. on p. 37).
- [129] X. L. Zhang, A. T. Gill, L. Isenhower, T. G. Walker, and M. Saffman, "Fidelity of a Rydberg blockade quantum gate from simulated quantum process tomography", *Phys. Rev. A* **85**, 042310 (2012) (cit. on p. 37).
- [130] A. Gilchrist, N. K. Langford, and M. A. Nielsen, "Distance measures to compare real and ideal quantum processes", *Phys. Rev. A* **71**, 062310 (2005) (cit. on p. 38).

- [131] T. Wilk, A. Gaëtan, C. Evellin, J. Wolters, Y. Miroshnychenko, P. Grangier, and A. Browaeys, "Entanglement of Two Individual Neutral Atoms Using Rydberg Blockade", *Phys. Rev. Lett.* **104**, 010502 (2010) (cit. on pp. 38, 55, 57).
- [132] J. J. Balmer, "Notiz über die Spectrallinien des Wasserstoffs", *Annalen der Physik* **261**, 80 (1885) (cit. on p. 38).
- [133] J. R. Rydberg, "XXXIV. On the structure of the line-spectra of the chemical elements", *The London, Edinburgh, and Dublin Philosophical Magazine and Journal of Science* **29**, 331 (1890) (cit. on p. 38).
- [134] A. L. Schawlow, "Spectroscopy in a new light", *Rev. Mod. Phys.* **54**, 697 (1982) (cit. on p. 38).
- [135] M. Saffman, "Atomic Physics: Structure, Interactions and Entanglement", 2015 (cit. on pp. 38, 40–42, 77, 83, 165, 166, 171).
- [136] N. Bohr, "I. On the constitution of atoms and molecules", *The London, Edinburgh, and Dublin Philosophical Magazine and Journal of Science* **26**, 1 (1913) (cit. on p. 38).
- [137] T. F. Gallagher, *Rydberg Atoms*, Cambridge Monographs on Atomic, Molecular and Chemical Physics (Cambridge University Press, 1994) (cit. on pp. 39, 41, 43, 46, 49, 62, 67, 77, 166, 171).
- [138] J. M. Nipper, "Interacting Rydberg atoms : coherent control at Förster resonances and polar homonuclear molecules", PhD thesis (Physikalisches Institut Universität Stuttgart, 2012) (cit. on pp. 39, 41–44, 47, 50, 166).
- [139] L. D. Landau and E. M. Lifshitz, *Quantum mechanics: non-relativistic theory*, Vol. 3 (Elsevier, 2013) (cit. on pp. 40, 43).
- [140] S. Patsch, "Control of Rydberg atoms for quantum technologies", PhD thesis (Freien Universität Berlin, 2022) (cit. on pp. 41, 49).
- [141] M. J. Seaton, "Quantum defect theory", *Reports on Progress in Physics* **46**, 167 (1983) (cit. on p. 41).
- [142] W. Li, I. Mourachko, M. W. Noel, and T. F. Gallagher, "Millimeter-wave spectroscopy of cold Rb Rydberg atoms in a magneto-optical trap: Quantum defects of the ns, np, and nd series", *Phys. Rev. A* **67**, 052502 (2003) (cit. on p. 41).
- [143] J. Han, Y. Jamil, D. V. L. Norum, P. J. Tanner, and T. F. Gallagher, "Rb *n*f quantum defects from millimeter-wave spectroscopy of cold  $^{85}\text{Rb}$  Rydberg atoms", *Phys. Rev. A* **74**, 054502 (2006) (cit. on p. 41).
- [144] C. Foot, *Atomic physics*, Vol. 7 (OUP Oxford, 2004) (cit. on pp. 42–44, 47).
- [145] H. Weimer, "Quantum many-body physics with strongly interacting Rydberg atoms", PhD thesis (Universität Stuttgart, 2010) (cit. on pp. 43, 46, 48, 49).

## Bibliography

---

- [146] S. Weber, C. Tresp, H. Menke, A. Urvoy, O. Firstenberg, H. P. Büchler, and S. Hofferberth, "Calculation of Rydberg interaction potentials", *Journal of Physics B: Atomic, Molecular and Optical Physics* **50**, 133001 (2017) (cit. on pp. 46, 83).
- [147] J. Deiglmayr, H. Saßmannshausen, P. Pillet, and F. Merkt, "Observation of Dipole-Quadrupole Interaction in an Ultracold Gas of Rydberg Atoms", *Phys. Rev. Lett.* **113**, 193001 (2014) (cit. on p. 49).
- [148] W. Maineult, B. Pelle, R. Faoro, E. Arimondo, P. Pillet, and P. Cheinet, "Dipole-quadrupole Förster resonance in cesium Rydberg gas", *Journal of Physics B: Atomic, Molecular and Optical Physics* **49**, 214001 (2016) (cit. on p. 49).
- [149] G. Cario and J. Franck, "Über Zerlegung von Wasserstoffmolekülen durch angeregte Quecksilberatome", *Zeitschrift für Physik* **11**, 161 (1922) (cit. on p. 49).
- [150] T. Förster, "Zwischenmolekulare energiewanderung und fluoreszenz", *Annalen der physik* **437**, 55 (1948) (cit. on p. 49).
- [151] D. L. Andrews, D. S. Bradshaw, R. Dinshaw, and G. D. Scholes, "Resonance Energy Transfer", in *Photonics* (John Wiley Sons, Ltd, 2015) Chap. 3, pp. 101–127 (cit. on p. 50).
- [152] M. Cardoso Dos Santos, W. R. Algar, I. L. Medintz, and N. Hildebrandt, "Quantum dots for Förster Resonance Energy Transfer (FRET)", *TrAC Trends in Analytical Chemistry* **125**, 115819 (2020) (cit. on p. 50).
- [153] C. S. E. van Ditzhuijzen, A. Tauschinsky, and H. B. van Linden van den Heuvell, "Observation of Stückelberg oscillations in dipole-dipole interactions", *Phys. Rev. A* **80**, 063407 (2009) (cit. on pp. 50, 136, 138, 141, 168, 170).
- [154] I. I. Beterov, G. N. Hamzina, E. A. Yakshina, D. B. Tretyakov, V. M. Entin, and I. I. Ryabtsev, "Adiabatic passage of radio-frequency-assisted Förster resonances in Rydberg atoms for two-qubit gates and the generation of Bell states", *Phys. Rev. A* **97**, 032701 (2018) (cit. on pp. 50, 102, 136, 149).
- [155] S. Ravets, H. Labuhn, D. Barredo, L. Beguin, T. Lahaye, and A. Browaeys, "Coherent dipole-dipole coupling between two single Rydberg atoms at an electrically-tuned Förster resonance", *Nat. Phys.* **10**, 914 (2014) (cit. on pp. 51, 62, 124, 163).
- [156] X. Wu, X. Liang, Y. Tian, F. Yang, C. Chen, Y.-C. Liu, M. K. Tey, and L. You, "A concise review of Rydberg atom based quantum computation and quantum simulation\*", *Chinese Physics B* **30**, 020305 (2021) (cit. on pp. 53, 56, 57, 59, 151).
- [157] N. C. Jones, R. Van Meter, A. G. Fowler, P. L. McMahon, J. Kim, T. D. Ladd, and Y. Yamamoto, "Layered Architecture for Quantum Computing", *Phys. Rev. X* **2**, 031007 (2012) (cit. on p. 53).
- [158] N. Schlosser, G. Reymond, I. Protsenko, and P. Grangier, "Sub-poissonian loading of single atoms in a microscopic dipole trap", *Nature* **411**, 1024 (2001) (cit. on p. 54).

- [159] F. Nogrette, H. Labuhn, S. Ravets, D. Barredo, L. Béguin, A. Vernier, T. Lahaye, and A. Browaeys, "Single-Atom Trapping in Holographic 2D Arrays of Microtraps with Arbitrary Geometries", *Phys. Rev. X* **4**, 021034 (2014) (cit. on p. 54).
- [160] Y.-Y. Jau, A. M. Hankin, T. Keating, I. H. Deutsch, and G. W. Biedermann, "Entangling atomic spins with a Rydberg-dressed spin-flip blockade", *Nature Physics* **12**, 71 (2016) (cit. on p. 54).
- [161] A. M. Hankin, Y.-Y. Jau, L. P. Parazzoli, C. W. Chou, D. J. Armstrong, A. J. Landahl, and G. W. Biedermann, "Two-atom Rydberg blockade using direct  $6S$  to  $nP$  excitation", *Phys. Rev. A* **89**, 033416 (2014) (cit. on p. 54).
- [162] D. Jaksch, J. I. Cirac, P. Zoller, S. L. Rolston, R. Côté, and M. D. Lukin, "Fast Quantum Gates for Neutral Atoms", *Phys. Rev. Lett* **85**, 2208 (2000) (cit. on p. 55).
- [163] K. M. Maller, M. T. Lichtman, T. Xia, Y. Sun, M. J. Piotrowicz, A. W. Carr, L. Isenhower, and M. Saffman, "Rydberg-blockade controlled-not gate and entanglement in a two-dimensional array of neutral-atom qubits", *Phys. Rev. A* **92**, 022336 (2015) (cit. on pp. 55–57).
- [164] X. L. Zhang, L. Isenhower, A. T. Gill, T. G. Walker, and M. Saffman, "Deterministic entanglement of two neutral atoms via Rydberg blockade", *Phys. Rev. A* **82**, 030306 (2010) (cit. on pp. 55, 57).
- [165] D. F. James and J. Jerke, "Effective Hamiltonian theory and its applications in quantum information", *Canadian Journal of Physics* **85**, 625 (2007) (cit. on p. 55).
- [166] D. James, "Quantum Computation with Hot and Cold Ions: An Assessment of Proposed Schemes", *Fortschritte der Physik* **48**, 823 (2000) (cit. on p. 55).
- [167] X.-F. Shi, "Suppressing Motional Dephasing of Ground-Rydberg Transition for High-Fidelity Quantum Control with Neutral Atoms", *Phys. Rev. Appl.* **13**, 024008 (2020) (cit. on p. 56).
- [168] P. Raina and B. Santra, "Exploring multi-level Rydberg excitation schemes for suppressing motional dephasing in optically trapped Cs atom qubits", *Physica Scripta* **96**, 075802 (2021) (cit. on p. 56).
- [169] I. I. Beterov, I. I. Ryabtsev, D. B. Tretyakov, and V. M. Entin, "Quasiclassical calculations of blackbody-radiation-induced depopulation rates and effective lifetimes of Rydberg  $nS$ ,  $nP$ , and  $nD$  alkali-metal atoms with  $n < 80$ ", *Phys. Rev. A* **79**, 052504 (2009) (cit. on pp. 56, 62, 96–98, 126, 141).
- [170] I. I. Ryabtsev, I. I. Beterov, D. B. Tretyakov, V. M. Entin, and E. A. Yakshina, "Doppler- and recoil-free laser excitation of Rydberg states via three-photon transitions", *Phys. Rev. A* **84**, 053409 (2011) (cit. on pp. 56, 128, 147).
- [171] C. Carr, M. Tanasittikosol, A. Sargsyan, D. Sarkisyan, C. S. Adams, and K. J. Weatherill, "Three-photon electromagnetically induced transparency using Rydberg states", *Opt. Lett.* **37**, 3858 (2012) (cit. on p. 56).

## Bibliography

---

- [172] H. Levine, A. Keesling, A. Omran, H. Bernien, S. Schwartz, A. S. Zibrov, M. Endres, M. Greiner, V. Vuletić, and M. D. Lukin, "High-Fidelity Control and Entanglement of Rydberg-Atom Qubits", *Phys. Rev. Lett.* **121**, 123603 (2018) (cit. on p. 57).
- [173] C. Sheng, X. He, P. Xu, R. Guo, K. Wang, Z. Xiong, M. Liu, J. Wang, and M. Zhan, "High-Fidelity Single-Qubit Gates on Neutral Atoms in a Two-Dimensional Magic-Intensity Optical Dipole Trap Array", *Phys. Rev. Lett.* **121**, 240501 (2018) (cit. on p. 57).
- [174] J. H. Lee, E. Montano, I. H. Deutsch, and P. S. Jessen, "Robust site-resolvable quantum gates in an optical lattice via inhomogeneous control", *Nature Communications* **4**, 2027 (2013) (cit. on p. 57).
- [175] E. Brion, L. H. Pedersen, and K. Mølmer, "Adiabatic elimination in a lambda system", *Journal of Physics A: Mathematical and Theoretical* **40**, 1033 (2007) (cit. on p. 57).
- [176] D. D. Yavuz, P. B. Kulatunga, E. Urban, T. A. Johnson, N. Proite, T. Henage, T. G. Walker, and M. Saffman, "Fast Ground State Manipulation of Neutral Atoms in Microscopic Optical Traps", *Phys. Rev. Lett.* **96**, 063001 (2006) (cit. on p. 57).
- [177] M. Saffman, "Quantum computing with atomic qubits and Rydberg interactions: Progress and challenges", *J. Phys. B: At. Mol. Phys.* **49**, 202001 (2016) (cit. on pp. 57, 73, 108).
- [178] T. M. Graham, M. Kwon, B. Grinkemeyer, Z. Marra, X. Jiang, M. T. Lichtman, Y. Sun, M. Ebert, and M. Saffman, "Rydberg-Mediated Entanglement in a Two-Dimensional Neutral Atom Qubit Array", *Phys. Rev. Lett.* **123**, 230501 (2019) (cit. on p. 57).
- [179] J.-Z. Xu, L.-N. Sun, J.-F. Wei, Y.-L. Du, R. Luo, L.-L. Yan, M. Feng, and S.-L. Su, "Two-Qubit Geometric Gates Based on Ground-State Blockade of Rydberg Atoms", *Chinese Physics Letters* **39**, 090301 (2022) (cit. on pp. 57, 152).
- [180] J. T. Young, P. Bienias, R. Belyansky, A. M. Kaufman, and A. V. Gorshkov, "Asymmetric Blockade and Multiqubit Gates via Dipole-Dipole Interactions", *Phys. Rev. Lett.* **127**, 120501 (2021) (cit. on p. 57).
- [181] A. M. Farouk, I. I. Beterov, P. Xu, and I. I. Ryabtsev, "Scalable Heteronuclear Architecture of Neutral Atoms Based on EIT", *Journal of Experimental and Theoretical Physics* **137**, 202 (2023) (cit. on p. 57).
- [182] J.-L. Wu, Y. Wang, J.-X. Han, Y.-K. Feng, S.-L. Su, Y. Xia, Y. Jiang, and J. Song, "One-step implementation of Rydberg-antiblockade SWAP and controlled-SWAP gates with modified robustness", *Photon. Res.* **9**, 814 (2021) (cit. on p. 57).
- [183] X. Tan, J.-L. Wu, C. Deng, W.-J. Mao, H.-T. Wang, and X. Ji, "Implementation of quantum phase gate between two atoms via Rydberg antiblockade and adiabatic passage", *Chinese Physics B* **27**, 100307 (2018) (cit. on p. 57).
- [184] H. Jo, Y. Song, M. Kim, and J. Ahn, "Rydberg Atom Entanglements in the Weak Coupling Regime", *Phys. Rev. Lett.* **124**, 033603 (2020) (cit. on p. 57).

- [185] I. I. Ryabtsev, D. B. Tretyakov, I. I. Beterov, and V. M. Entin, "Observation of the Stark-Tuned Förster Resonance between Two Rydberg Atoms", *Phys. Rev. Lett.* **104**, 073003 (2010) (cit. on pp. 57, 72, 115).
- [186] I. I. Beterov and M. Saffman, "Rydberg blockade, Förster resonances, and quantum state measurements with different atomic species", *Phys. Rev. A* **92**, 042710 (2015) (cit. on pp. 57, 72).
- [187] I. I. Beterov, M. Saffman, E. A. Yakshina, D. B. Tretyakov, V. M. Entin, S. Bergamini, E. A. Kuznetsova, and I. I. Ryabtsev, "Two-qubit gates using adiabatic passage of the Stark-tuned Förster resonances in Rydberg atoms", *Phys. Rev. A* **94**, 062307 (2016) (cit. on pp. 57, 58).
- [188] A. Fuhrmanek, R. Bourgain, Y. R. P. Sortais, and A. Browaeys, "Free-Space Lossless State Detection of a Single Trapped Atom", *Phys. Rev. Lett.* **106**, 133003 (2011) (cit. on p. 59).
- [189] Z. C. Liu, N. P. Inman, T. J. Carroll, and M. W. Noel, "Time Dependence of Few-Body Förster Interactions among Ultracold Rydberg Atoms", *Phys. Rev. Lett.* **124**, 133402 (2020) (cit. on p. 61).
- [190] S. E. Spielman, A. Handian, N. P. Inman, T. J. Carroll, and M. W. Noel, "Slow Thermalization of Few-Body Dipole-Dipole Interactions", *arXiv preprint arXiv:2208.02909* (2022) (cit. on p. 61).
- [191] J. H. Gurian, P. Cheinet, P. Huillery, A. Fioretti, J. Zhao, P. L. Gould, D. Comparat, and P. Pillet, "Observation of a Resonant Four-Body Interaction in Cold Cesium Rydberg Atoms", *Phys. Rev. Lett.* **108**, 023005 (2012) (cit. on pp. 61–64, 70, 72, 74, 77, 92, 112, 113).
- [192] D. B. Tretyakov, I. I. Beterov, E. A. Yakshina, V. M. Entin, I. I. Ryabtsev, P. Cheinet, and P. Pillet, "Observation of the Borromean Three-Body Förster Resonances for Three Interacting Rb Rydberg Atoms", *Phys. Rev. Lett.* **119**, 173402 (2017) (cit. on pp. 61, 73, 75, 76, 84, 87, 89, 92, 93, 111–113, 123, 137).
- [193] I. I. Ryabtsev, I. I. Beterov, D. B. Tretyakov, E. A. Yakshina, V. M. Entin, P. Cheinet, and P. Pillet, "Coherence of three-body Förster resonances in Rydberg atoms", *Phys. Rev. A* **98**, 052703 (2018) (cit. on pp. 61, 73, 76, 77, 81, 85, 87–89, 91–94, 100, 101, 103, 111, 112, 120, 124, 126, 141, 143, 149, 170, 171, 173).
- [194] V. Bendkowsky, B. Butscher, J. Nipper, J. B. Balewski, J. P. Shaffer, R. Löw, T. Pfau, W. Li, J. Stanojevic, T. Pohl, and J. M. Rost, "Rydberg Trimers and Excited Dimers Bound by Internal Quantum Reflection", *Phys. Rev. Lett.* **105**, 163201 (2010) (cit. on p. 62).
- [195] J. von Stecher, J. P. D’Incao, and C. H. Greene, "Signatures of universal four-body phenomena and their relation to the Efimov effect", *Nature Physics* **5**, 417 (2009) (cit. on p. 62).

## Bibliography

---

- [196] F. Ferlaino, S. Knoop, M. Berninger, W. Harm, J. P. D’Incao, H.-C. Nägerl, and R. Grimm, “*Evidence for Universal Four-Body States Tied to an Efimov Trimer*”, *Phys. Rev. Lett.* **102**, 140401 (2009) (cit. on p. 62).
- [197] N. Gross, Z. Shotan, S. Kokkelmans, and L. Khaykovich, “*Observation of Universality in Ultracold  $^7\text{Li}$  Three-Body Recombination*”, *Phys. Rev. Lett.* **103**, 163202 (2009) (cit. on p. 62).
- [198] S. Jochim, M. Bartenstein, A. Altmeyer, G. Hendl, C. Chin, J. H. Denschlag, and R. Grimm, “*Pure Gas of Optically Trapped Molecules Created from Fermionic Atoms*”, *Phys. Rev. Lett.* **91**, 240402 (2003) (cit. on p. 62).
- [199] T. Weber, J. Herbig, M. Mark, H.-C. Nägerl, and R. Grimm, “*Three-Body Recombination at Large Scattering Lengths in an Ultracold Atomic Gas*”, *Phys. Rev. Lett.* **91**, 123201 (2003) (cit. on p. 62).
- [200] T. Vogt, M. Viteau, J. Zhao, A. Chotia, D. Comparat, and P. Pillet, “*Dipole Blockade at Förster Resonances in High Resolution Laser Excitation of Rydberg States of Cesium Atoms*”, *Phys. Rev. Lett.* **97**, 083003 (2006) (cit. on pp. 62, 115, 163).
- [201] T. Vogt, M. Viteau, A. Chotia, J. Zhao, D. Comparat, and P. Pillet, “*Electric-Field Induced Dipole Blockade with Rydberg Atoms*”, *Phys. Rev. Lett.* **99**, 073002 (2007) (cit. on p. 62).
- [202] D. Comparat and P. Pillet, “*Dipole Blockade in a Cold Rydberg Atomic Sample*”, *J. Opt. Soc. Am. B* **27**, A208 (2010) (cit. on pp. 62, 73).
- [203] T. F. Gallagher and P. Pillet, in *Advances in Atomic, Molecular, and Optical Physics*, Vol. 56 (Academic Press, 2008), pp. 161–218 (cit. on p. 62).
- [204] M. Kiffner, W. Li, and D. Jaksch, “*Three-Body Bound States in Dipole-Dipole Interacting Rydberg Atoms*”, *Phys. Rev. Lett.* **111**, 233003 (2013) (cit. on p. 66).
- [205] D. S. Petrov, “*Three-Body Interacting Bosons in Free Space*”, *Phys. Rev. Lett.* **112**, 103201 (2014) (cit. on p. 66).
- [206] I. I. Ryabtsev, D. B. Tretyakov, I. I. Beterov, V. M. Entin, and E. A. Yakshina, “*Stark-tuned Förster resonance and dipole blockade for two to five cold Rydberg atoms: Monte Carlo simulations for various spatial configurations*”, *Phys. Rev. A* **82**, 053409 (2010) (cit. on p. 72).
- [207] E. A. Yakshina, D. B. Tretyakov, I. I. Beterov, V. M. Entin, C. Andreeva, A. Cinins, A. Markovski, Z. Iftikhar, A. Ekers, and I. I. Ryabtsev, “*Line shapes and time dynamics of the Förster resonances between two Rydberg atoms in a time-varying electric field*”, *Phys. Rev. A* **94**, 043417 (2016) (cit. on pp. 72, 74, 136).
- [208] I. Ryabtsev, I. Beterov, D. Tretyakov, V. Entin, and E. Yakshina, “*Spectroscopy of cold rubidium Rydberg atoms for applications in quantum information*”, *Phys. Usp.* **59**, 196 (2016) (cit. on pp. 73, 74).

- [209] H. Weimer, M. Müller, I. Lesanovsky, P. Zoller, and H. P. Büchler, "A Rydberg quantum simulator", *Nature Physics* **6**, 382 (2010) (cit. on p. 73).
- [210] J. P. Hague and C. MacCormick, "Quantum simulation of electron-phonon interactions in strongly deformable materials", *New Journal of Physics* **14**, 033019 (2012) (cit. on p. 73).
- [211] A. Dauphin, M. Müller, and M. A. Martin-Delgado, "Rydberg-atom quantum simulation and Chern-number characterization of a topological Mott insulator", *Phys. Rev. A* **86**, 053618 (2012) (cit. on p. 73).
- [212] J. P. Hague and C. MacCormick, "Bilayers of Rydberg Atoms as a Quantum Simulator for Unconventional Superconductors", *Phys. Rev. Lett.* **109**, 223001 (2012) (cit. on p. 73).
- [213] A. W. Glaetzle, M. Dalmonte, R. Nath, I. Rousochatzakis, R. Moessner, and P. Zoller, "Quantum Spin-Ice and Dimer Models with Rydberg Atoms", *Phys. Rev. X* **4**, 041037 (2014) (cit. on p. 73).
- [214] M. Mattioli, A. W. Glätzle, and W. Lechner, "From classical to quantum non-equilibrium dynamics of Rydberg excitations in optical lattices", *New Journal of Physics* **17**, 113039 (2015) (cit. on p. 73).
- [215] J. Gelhausen, M. Buchhold, A. Rosch, and P. Strack, "Quantum-optical magnets with competing short- and long-range interactions: Rydberg-dressed spin lattice in an optical cavity", *SciPost Phys.* **1**, 004 (2016) (cit. on p. 73).
- [216] A. Dauphin, M. Müller, and M. A. Martin-Delgado, "Quantum simulation of a topological Mott insulator with Rydberg atoms in a Lieb lattice", *Phys. Rev. A* **93**, 043611 (2016) (cit. on p. 73).
- [217] K. A. Safinya, J. F. Delpéch, F. Gounand, W. Sandner, and T. F. Gallagher, "Resonant Rydberg-Atom-Rydberg-Atom Collisions", *Phys. Rev. Lett.* **47**, 405 (1981) (cit. on p. 73).
- [218] D. B. Tretyakov, I. I. Beterov, V. M. Entin, I. I. Ryabtsev, and P. L. Chapovsky, "Investigation of cold rubidium Rydberg atoms in a magneto-optical trap", *Journal of Experimental and Theoretical Physics* **108**, 374 (2009) (cit. on p. 74).
- [219] I. I. Ryabtsev, D. B. Tretyakov, and I. I. Beterov, "Stark-switching technique for fast quantum gates in Rydberg atoms", *Journal of Physics B: Atomic, Molecular and Optical Physics* **36**, 297 (2003) (cit. on p. 74).
- [220] I. I. Ryabtsev, D. B. Tretyakov, I. I. Beterov, and E. V. M., "Effect of finite detection efficiency on the observation of the dipole-dipole interaction of a few Rydberg atoms", *Phys. Rev. A* **76**, 012722 (2007) (cit. on p. 75).
- [221] B. Kaulakys, "Consistent analytical approach for the quasi-classical radial dipole matrix elements", *J. Phys. B: At. Mol. Opt. Phys.* **28**, 4963 (1995) (cit. on pp. 83, 95, 139, 166, 168).

## Bibliography

---

- [222] L. Du, P. Barral, M. Cantara, J. de Hond, Y.-K. Lu, and W. Ketterle, “Atomic physics on a 50 nm scale: Realization of a bilayer system of dipolar atoms”, arXiv preprint arXiv:2302.07209 (2023) (cit. on pp. 88, 152).
- [223] P. Cheinet, K.-L. Pham, P. Pillet, I. Beterov, I. Ashkarin, D. Tretyakov, E. Yakshina, V. Entin, and I. Ryabtsev, “Three-body Förster resonance of a new type in Rydberg atoms”, *Quantum Electronics* **50**, 213 (2020) (cit. on pp. 91, 110, 111, 119, 125, 126, 139, 140, 143, 149).
- [224] K.-L. Pham, S. Lepoutre, P. Pillet, P. Cheinet, I. Ashkarin, I. Beterov, D. Tretyakov, V. Entin, E. Yakshina, and I. Ryabtsev, “Searching optimal conditions for quantum gates application with the new 3-body Förster resonances in Rb and Cs Rydberg atoms”, arXiv preprint arXiv:2012.12845 (2020) (cit. on pp. 91, 113, 131).
- [225] I. N. Ashkarin, I. I. Beterov, E. A. Yakshina, D. B. Tretyakov, V. M. Entin, I. I. Ryabtsev, P. Cheinet, K.-L. Pham, S. Lepoutre, and P. Pillet, “Toffoli gate based on a three-body fine-structure-state-changing Förster resonance in Rydberg atoms”, *Phys. Rev. A* **106**, 032601 (2022) (cit. on pp. 91, 125, 135, 137, 139, 140, 146, 149, 152).
- [226] I. Ashkarin, S. Lepoutre, P. Pillet, I. Beterov, I. Ryabtsev, and P. Cheinet, “High-fidelity  $CCR_z(\phi)$  gates via RF-induced Förster resonances”, arXiv preprint arXiv:2307.12789 (2023) (cit. on pp. 91, 136, 137).
- [227] T. G. Walker and M. Saffman, “Consequences of Zeeman degeneracy for the van der Waals blockade between Rydberg atoms”, *Phys. Rev. A* **77**, 032723 (2008) (cit. on pp. 94, 126, 139, 141, 149).
- [228] M. L. Zimmerman, M. G. Littman, M. M. Kash, and D. Kleppner, “Stark structure of the Rydberg states of alkali-metal atoms”, *Phys. Rev. A* **20**, 2251 (1979) (cit. on p. 99).
- [229] T. Toffoli, “Reversible computing”, in *Automata, Languages and Programming*, edited by J. de Bakker and J. van Leeuwen (1980), pp. 632–644 (cit. on p. 102).
- [230] I. I. Ryabtsev, D. B. Tretyakov, and I. I. Beterov, “Applicability of Rydberg atoms to quantum computers”, *J. Phys. B: At. Mol. Phys.* **38**, S421 (2005) (cit. on p. 102).
- [231] G. K. Brennen, C. M. Caves, P. S. Jessen, and I. H. Deutsch, “Quantum Logic Gates in Optical Lattices”, *Phys. Rev. Lett.* **82**, 1060 (1999) (cit. on p. 103).
- [232] C. Weitenberg, M. Endres, J. F. Sherson, M. Cheneau, P. Schaub, T. Fukuhara, I. Bloch, and S. Kuhr, “Single-spin addressing in an atomic Mott insulator”, *Nature* **471**, 319 (2011) (cit. on p. 103).
- [233] C. Zhang, S. L. Rolston, and S. Das Sarma, “Manipulation of single neutral atoms in optical lattices”, *Phys. Rev. A* **74**, 042316 (2006) (cit. on p. 103).
- [234] T. Xia, M. Lichtman, K. Maller, A. W. Carr, M. J. Piotrowicz, L. Isenhower, and M. Saffman, “Randomized Benchmarking of Single-Qubit Gates in a 2D Array of Neutral-Atom Qubits”, *Phys. Rev. Lett.* **114**, 100503 (2015) (cit. on p. 103).

- [235] E. Brion, A. S. Mouritzen, and K. Mølmer, "Conditional dynamics induced by new configurations for Rydberg dipole-dipole interactions", *Phys. Rev. A* **76**, 022334 (2007) (cit. on p. 103).
- [236] D. M. Olsson and L. S. Nelson, "The Nelder-Mead Simplex Procedure for Function Minimization", *Technometrics* **17**, 45 (1975) (cit. on p. 107).
- [237] M. D. Bowdrey, D. K. L. Oi, A. J. Short, K. Banaszek, and J. A. Jones, "Fidelity of single qubit maps", *Phys. Lett. A* **294**, 258 (2002) (cit. on pp. 107, 132).
- [238] W. Liu, J. Zhang, Z. Z. Deng, and G. Long, "Simulation of general three-body interactions in a nuclear magnetic resonance ensemble quantum computer", *Sci. China Ser. G* **51**, 1089 (2008) (cit. on p. 108).
- [239] X. Peng, J. Zhang, J. Du, and D. Suter, "Quantum Simulation of a System with Competing Two- and Three-Body Interactions", *Phys. Rev. Lett* **103**, 140501 (2009) (cit. on p. 108).
- [240] H.-W. Hammer, A. Nogga, and A. Schwenk, "Colloquium: Three-body forces: From cold atoms to nuclei", *Rev. Mod. Phys.* **85**, 197 (2013) (cit. on p. 108).
- [241] K. Jachymski, P. Bienias, and H. P. Büchler, "Three-Body Interaction of Rydberg Slow-Light Polaritons", *Phys. Rev. Lett.* **117**, 053601 (2016) (cit. on p. 108).
- [242] W.-L. You, Y.-C. Qiu, and A. M. Oleś, "Quantum phase transitions in a generalized compass chain with three-site interactions", *Phys. Rev. B* **93**, 214417 (2016) (cit. on p. 108).
- [243] A. Derevianko, P. Komar, T. Topcu, R. M. Kroeze, and M. D. Lukin, "Effects of molecular resonances on Rydberg blockade", *Phys. Rev. A* **92**, 063419 (2015) (cit. on pp. 109, 135).
- [244] B. Pelle, R. Faoro, J. Billy, E. Arimondo, P. Pillet, and P. Cheinet, "Quasiforbidden two-body Förster resonances in a cold Cs Rydberg gas", *Phys. Rev. A* **93**, 023417 (2016) (cit. on pp. 112–115).
- [245] R. Kachru, T. F. Gallagher, F. Gounand, P. L. Pillet, and N. H. Tran, "Resonant collisions of Na  $nS$  and  $nD$  Rydberg atoms", *Phys. Rev. A* **28**, 2676 (1983) (cit. on p. 113).
- [246] M. J. Renn, W. R. Anderson, and T. F. Gallagher, "Resonant collisions of K Rydberg atoms", *Phys. Rev. A* **49**, 908 (1994) (cit. on p. 113).
- [247] I. Mourachko, D. Comparat, F. de Tomasi, A. Fioretti, P. Nosbaum, V. M. Akulin, and P. Pillet, "Many-Body Effects in a Frozen Rydberg Gas", *Phys. Rev. Lett* **80**, 253 (1998) (cit. on p. 115).
- [248] J. Nipper, J. B. Balewski, A. T. Krupp, B. Butscher, R. Löw, and T. Pfau, "Highly Resolved Measurements of Stark-Tuned Förster Resonances between Rydberg Atoms", *Phys. Rev. Lett.* **108**, 113001 (2012) (cit. on p. 115).

## Bibliography

---

- [249] W. R. Anderson, J. R. Veale, and T. F. Gallagher, “Resonant Dipole-Dipole Energy Transfer in a Nearly Frozen Rydberg Gas”, *Phys. Rev. Lett* **80**, 249 (1998) (cit. on p. 115).
- [250] S. Westermann, T. Amthor, A. L. de Oliveira, J. Deiglmayr, M. Reetz-Lamour, and M. Weidemuller, “Dynamics of resonant energy transfer in a cold Rydberg gas”, *Eur. Phys. J. D* **40**, 37 (2006) (cit. on p. 115).
- [251] T. G. Walker and M. Saffman, “Zeros of Rydberg–Rydberg Förster interactions”, *Journal of Physics B: Atomic, Molecular and Optical Physics* **38**, S309 (2005) (cit. on p. 123).
- [252] S. de Léséleuc, D. Barredo, V. Lienhard, A. Browaeys, and T. Lahaye, “Analysis of imperfections in the coherent optical excitation of single atoms to Rydberg states”, *Phys. Rev. A* **97**, 053803 (2018) (cit. on pp. 128, 147).
- [253] J. A. Nelder and R. Mead, “A Simplex Method for Function Minimization”, *The Computer Journal* **7**, 308 (1965) (cit. on p. 132).
- [254] M. Delvecchio, F. Petiziol, E. Arimondo, and S. Wimberger, “Atomic interactions for qubit-error compensation”, *Phys. Rev. A* **105**, 042431 (2022) (cit. on p. 134).
- [255] M. Mack, J. Grimm, F. Karlewski, L. ő. Sárkány, H. Hattermann, and J. Fortágh, “All-optical measurement of Rydberg-state lifetimes”, *Phys. Rev. A* **92**, 012517 (2015) (cit. on p. 134).
- [256] C. S. E. van Ditzhuijzen, A. Tauschinsky, and H. B. van Linden van den Heuvell, “Radio-frequency-driven dipole-dipole interactions in spatially separated volumes”, *Phys. Rev. A* **78**, 063409 (2008) (cit. on p. 136).
- [257] D. B. Tretyakov, V. M. Entin, E. A. Yakshina, I. I. Beterov, C. Andreeva, and I. I. Ryabtsev, “Controlling the interactions of a few cold Rb Rydberg atoms by radio-frequency-assisted Förster resonances”, *Phys. Rev. A* **90**, 041403 (2014) (cit. on p. 136).
- [258] J. Lee, J. Iqbal, and T. F. Gallagher, “Microwave transitions of pairs of cold Rb Rydberg atoms as Förster resonances of Floquet states”, *Phys. Rev. A* **96**, 012507 (2017) (cit. on p. 136).
- [259] X.-R. Huang, Z.-X. Ding, C.-S. Hu, L.-T. Shen, W. Li, H. Wu, and S.-B. Zheng, “Robust Rydberg gate via Landau-Zener control of Förster resonance”, *Phys. Rev. A* **98**, 052324 (2018) (cit. on p. 136).
- [260] S. Hollerith, K. Srakaew, D. Wei, A. Rubio-Abadal, D. Adler, P. Weckesser, A. Kruckenhauser, V. Walther, R. van Bijnen, J. Rui, C. Gross, I. Bloch, and J. Zeiher, “Realizing Distance-Selective Interactions in a Rydberg-Dressed Atom Array”, *Phys. Rev. Lett.* **128**, 113602 (2022) (cit. on p. 137).
- [261] J. Ramette, J. Sinclair, Z. Vendeiro, A. Rudelis, M. Cetina, and V. Vuletić, “Any-To-Any Connected Cavity-Mediated Architecture for Quantum Computing with Trapped Ions or Rydberg Arrays”, *PRX Quantum* **3**, 010344 (2022) (cit. on p. 137).

- [262] C. Daska, K. Ender, G. B. Mbeng, A. Kruckenhauser, W. Lechner, and R. van Bijnen, "Quantum Optimization via Four-Body Rydberg Gates", *Phys. Rev. Lett.* **128**, 120503 (2022) (cit. on pp. 137, 152).
- [263] D. G. Cory, M. D. Price, W. Maas, E. Knill, R. Laflamme, W. H. Zurek, T. F. Havel, and S. S. Somaroo, "Experimental Quantum Error Correction", *Phys. Rev. Lett.* **81**, 2152 (1998) (cit. on p. 137).
- [264] D. Crow, R. Joynt, and M. Saffman, "Improved Error Thresholds for Measurement-Free Error Correction", *Phys. Rev. Lett.* **117**, 130503 (2016) (cit. on p. 137).
- [265] S. Tang, C. Yang, D. Li, and X. Shao, "Implementation of Quantum Algorithms via Fast Three-Rydberg-Atom CCZ Gates", *Entropy* **24**, 10.3390/e24101371 (2022) (cit. on p. 137).
- [266] E. Dennis, "Toward fault-tolerant quantum computation without concatenation", *Phys. Rev. A* **63**, 052314 (2001) (cit. on p. 137).
- [267] J.-F. Wei, F.-Q. Guo, D.-Y. Wang, Y. Jia, L.-L. Yan, M. Feng, and S.-L. Su, "Fast multi-qubit Rydberg geometric fan-out gates with optimal control technology", *Phys. Rev. A* **105**, 042404 (2022) (cit. on p. 137).
- [268] D. Yu, H. Wang, J.-M. Liu, S.-L. Su, J. Qian, and W. Zhang, "Multiqubit Toffoli Gates and Optimal Geometry with Rydberg Atoms", *Phys. Rev. Appl.* **18**, 034072 (2022) (cit. on p. 137).
- [269] M. Li, J.-Y. Li, F.-Q. Guo, X.-Y. Zhu, E. Liang, S. Zhang, L.-L. Yan, M. Feng, and S.-L. Su, "Multiple-Qubit  $C_k U^m$  Logic Gates of Rydberg Atoms via Optimized Geometric Quantum Operations", *Annalen der Physik* **534**, 2100506 (2022) (cit. on p. 137).
- [270] J.-L. Wu, Y. Wang, J.-X. Han, S.-L. Su, Y. Xia, J. Song, and Y. Jiang, "Fast and Robust Multiqubit Gates on Rydberg Atoms by Periodic Pulse Engineering", *Advanced Quantum Technologies* **5**, 2200042 (2022) (cit. on p. 137).
- [271] P. Maity and M. Purkait, "Implementation of a holonomic 3-qubit gate using Rydberg superatoms in a microwave cavity", *The European Physical Journal Plus* **137**, 1299 (2022) (cit. on p. 137).
- [272] A. D. Hill, M. J. Hodson, N. Didier, and M. J. Reagor, "Realization of arbitrary doubly-controlled quantum phase gates", *arXiv preprint arXiv:2108.01652* (2021) (cit. on p. 138).
- [273] I. I. Beterov, E. A. Yakshina, D. B. Tretyakov, V. M. Entin, U. Singh, Y. V. Kudlaev, K. Y. Mityanin, K. A. Panov, N. V. Alyanova, C. Andreeva, and I. I. Ryabtsev, "Trapping, detection and manipulation of single Rb atoms in an optical dipole trap using a long-focus objective lens", *Journal of Physics: Conference Series* **1859**, 012049 (2021) (cit. on p. 146).
- [274] Y. Zeng, P. Xu, X. He, Y. Liu, M. Liu, J. Wang, D. J. Papoular, G. V. Shlyapnikov, and M. Zhan, "Entangling Two Individual Atoms of Different Isotopes via Rydberg Blockade", *Phys. Rev. Lett.* **119**, 160502 (2017) (cit. on p. 148).

## Bibliography

---

- [275] B. Ximenez Rodrigues Alves, "Scaling up 2D atom array platform with 87Rb Rydberg atoms", *Bulletin of the American Physical Society* (2023) (cit. on p. 151).
- [276] B. Suman and P. Kumar, "A survey of simulated annealing as a tool for single and multiobjective optimization", *Journal of the Operational Research Society* **57**, 1143 (2006) (cit. on p. 151).
- [277] B. T. Torosov and N. V. Vitanov, "Smooth composite pulses for high-fidelity quantum information processing", *Phys. Rev. A* **83**, 053420 (2011) (cit. on pp. 152, 162).
- [278] B. T. Torosov, S. Guérin, and N. V. Vitanov, "High-Fidelity Adiabatic Passage by Composite Sequences of Chirped Pulses", *Phys. Rev. Lett.* **106**, 233001 (2011) (cit. on p. 152).
- [279] W. S. Warren, H. Rabitz, and M. Dahleh, "Coherent Control of Quantum Dynamics: The Dream Is Alive", *Science* **259**, 1581 (1993) (cit. on p. 152).
- [280] A. Larrouy, S. Patsch, R. Richaud, J.-M. Raimond, M. Brune, C. P. Koch, and S. Gleyzes, "Fast Navigation in a Large Hilbert Space Using Quantum Optimal Control", *Phys. Rev. X* **10**, 021058 (2020) (cit. on p. 152).
- [281] A. F. Ali, "Hybrid simulated annealing and Nelder-Mead algorithm for solving large-scale global optimization problems", *International Journal of Research in Computer Science* **4**, 1 (2014) (cit. on p. 152).
- [282] J. Vankka and K. A. Halonen, *Direct digital synthesizers: theory, design and applications*, Vol. 614 (Springer Science & Business Media, 2001) (cit. on p. 152).
- [283] A. Facon, E.-K. Dietsche, D. Grosso, S. Haroche, J.-M. Raimond, M. Brune, and S. Gleyzes, "A sensitive electrometer based on a Rydberg atom in a Schrödinger-cat state", *Nature* **535**, 262 (2016) (cit. on p. 152).
- [284] W. Bowden, R. Hobson, P. Huillery, P. Gill, M. P. A. Jones, and I. R. Hill, "Rydberg electrometry for optical lattice clocks", *Phys. Rev. A* **96**, 023419 (2017) (cit. on p. 152).
- [285] D. H. Meyer, P. D. Kunz, and K. C. Cox, "Waveguide-Coupled Rydberg Spectrum Analyzer from 0 to 20 GHz", *Phys. Rev. Appl.* **15**, 014053 (2021) (cit. on p. 152).
- [286] J. A. Sedlacek, A. Schwettmann, H. Kübler, R. Löw, T. Pfau, and J. P. Shaffer, "Microwave electrometry with Rydberg atoms in a vapour cell using bright atomic resonances", *Nature physics* **8**, 819 (2012) (cit. on p. 152).
- [287] K.-Y. Liao, H.-T. Tu, S.-Z. Yang, C.-J. Chen, X.-H. Liu, J. Liang, X.-D. Zhang, H. Yan, and S.-L. Zhu, "Microwave electrometry via electromagnetically induced absorption in cold Rydberg atoms", *Phys. Rev. A* **101**, 053432 (2020) (cit. on p. 152).
- [288] Y. Chew, T. Tomita, T. P. Mahesh, S. Sugawa, S. de Léséleuc, and K. Ohmori, "Ultra-fast energy exchange between two single Rydberg atoms on a nanosecond timescale", *Nature Photonics* **16**, 724 (2022) (cit. on p. 152).

- 
- [289] N. Chen, L. Li, W. Huie, M. Zhao, I. Vetter, C. H. Greene, and J. P. Covey, "Analyzing the Rydberg-based optical-metastable-ground architecture for  $^{171}\text{Yb}$  nuclear spins", *Phys. Rev. A* **105**, 052438 (2022) (cit. on p. 152).
- [290] D. Litinski, "How to compute a 256-bit elliptic curve private key with only 50 million Toffoli gates", *arXiv preprint arXiv:2306.08585* (2023) (cit. on p. 160).
- [291] É. Gouzien, D. Ruiz, F.-M. Le Régent, J. Guillaud, and N. Sangouard, "Performance Analysis of a Repetition Cat Code Architecture: Computing 256-bit Elliptic Curve Logarithm in 9 Hours with 126 133 Cat Qubits", *Phys. Rev. Lett.* **131**, 040602 (2023) (cit. on p. 160).
- [292] I. I. Beterov, E. A. Yakshina, D. B. Tret'yakov, N. V. Al'yanova, D. A. Skvortsova, G. Suliman, T. R. Zagirov, V. M. Entin, and I. I. Ryabtsev, "Three-Photon Laser Excitation of Single Rydberg Rubidium Atoms in an Optical Dipole Trap", *Journal of Experimental and Theoretical Physics* **137**, 246 (2023) (cit. on p. 163).
- [293] B. Butscher, "A Rydberg interferometer: from coherent formation of ultralong-range Rydberg molecules to state tomography of Rydberg atoms", PhD thesis (Universität Stuttgart, 2011) (cit. on p. 166).
- [294] J. M. Blatt, "Practical points concerning the solution of the Schrödinger equation", *Journal of Computational Physics* **1**, 382 (1967) (cit. on p. 166).